Development of a modular interferometric microscopy system for characterization of MEMS

A Thesis
Submitted to the Faculty
of the

Worcester Polytechnic Institute

in partial fulfillment of the requirements for the
Degree of Master of Science
in
Mechanical Engineering

by

Adam R. Klempner

19 December 2006

Approved:

Prof. Ryszard J. Pryputniewicz, Major Advisor

Prof. Nancy A. Burnham, Member, Thesis Committee

Dr. Thomas F. Marinis, Draper Laboratory, Cambridge, MA
Member, Thesis Committee

Prof. John M. Sullivan, Member, Thesis Committee

Prof. Yiming Rong, Graduate Committee Representative

NEST – NanoEngineering, Science, and Technology
CHSLT – Center for Holographic Studies and Laser micro-mechaTronics
Mechanical Engineering Department
Worcester Polytechnic Institute
Worcester, MA 01609

SUMMARY

One of the key measurement devices used in characterization of microelectromechanical systems (MEMS) at WPI is the interferometric microscope. This device allows remote, noninvasive measurements of the surface shape and deformations of MEMS in full-field-of-view with high spatial resolution and nanometer accuracy. These abilities make MEMS characterization an ideal application of the interferometric microscope because of the need for non destructive, non invasive, and high accuracy measurements. However, an improved system needs to be developed so that measurements can be performed faster, setup time is reduced, the quality of results are improved, and the general capabilities of the system are increased. With MEMS becoming more prevalent in the market, national defense agencies developing high performance MEMS at an ever increasing rate, and the new Lufkin MEMS fabrication facility at WPI opening, the demand for such a system on campus is very high.

Therefore, a new modular high stability interferometric microscopy system is being developed to facilitate accurate measurements of MEMS. This system will have the ability to characterize the shape and deformation of MEMS ranging in size from sub-micrometer features to inch size packaging. The system will have nanometer out of plane resolution and a high spatial resolution with a scan depth of up to 250 μm. MEMS samples can be subjected to a variety of operational and loading conditions, including thermal variations, vibrational loading, and vacuum and pressure environments, while the MEMS shape and deformation are being measured.

In order to perform these tasks, the new system is designed as a modular structure where each module has a specific function and is easily interchangeable with other

modules, as required by specific applications. The measurement and loading capabilities are divided into two subsystems, which include their respective modules. The measurement subsystem consists of three main interferometer modules, one designed for small MEMS, one for larger MEMS, and one for time domain vibrational measurements. The loading device subsystem consists of a climate chamber module that has vacuum capabilities, a thermoelectric cooler (TEC) module, and several piezoelectric (PZT) shaker modules for various size measurement samples. Many combinations of the modules can be achieved. For example, the system can be configured to measure very small vibrationally excited MEMS in a vacuum environment, then, in a matter of minutes, be switched over to measuring the thermal deformations of a large MEMS.

Each of these modules has been extensively tested and calibration results are presented herein. Representative MEMS measurements have been performed for thermally loaded samples, devices that have been vibrationally excited, and devices that have been exposed to both vacuum and atmospheric pressure. Coefficient of thermal expansion (CTE) mismatch between MEMS structural material causes devices to bend as they are thermally loaded. Devices that are vibrationally excited show significant performance differences depending on whether they are excited in vacuum or air. Quantitative results using this new modular interferometric microscopy system are described and show the importance of characterization of MEMS in various test environments. This is especially important and timely, as assessment of MEMS reliability is being required for a major thrust in advancing the emerging MEMS technology.

ACKNOWLEDGMENTS

I would like to thank Prof. Ryszard J. Pryputniewicz for giving me the opportunity to pursue this Thesis in such a unique area of Mechanical Engineering. With his guidance over the years, "Prof." has allowed me to be part of many projects, all of them giving me the experience and knowledge necessary to develop the system reported in this Thesis.

I would also like to thank everyone at CHSLT for their support, guidance, and friendship over the years. I would especially like to thank Ryan Marinis for all of his contributions in every phase of this project, Peter Hefti for teaching me everything I needed to know about the set up of interferometers, for performing numerous experiments with me, and teaching me how to use the machines in the machine shop. I would also like to thank Shivananda Mizar for helping me acquire all of the necessary equipment, the "CS guys" Curt Ferguson and Darren Tropey for writing such versatile image acquisition software, Krzysztof Nowakowski for his help manufacturing some of the interferometer components, and Wei Han for being a good friend and colleague. Without you guys, I would never have been able to complete this Thesis to the extent at which I have, and it would have been a heck of a lot less fun. Thanks!

TABLE OF CONTENTS

LIST OF FIGURES

LIST OF TABLES

NOMENCLATURE

a	amplitude of modulation
$A_o(u,v)$	object beam amplitude
$A_r(u,v)$	reference beam amplitude
$A_{to}(u,v)$	time varying object beam amplitude
$A'_o(u,v)$	object beam amplitude, state 2
$A'_r(u,v)$	reference beam amplitude, state 2
AFM	atomic force microscope
AMD	Advanced Micro Devices, Inc.
BS	beam splitter
c	speed of light
CCD	charge coupled device
CD	compact disc
CHSLT	Center for Holographic Studies and Laser micro-mechaTronics
CMOS	complementary metal oxide semiconductor
CNC	computer numerical control
CTE	coefficient of thermal expansion
DBS	directional beam splitter
DLP	digital light processing
ESD	electrostatic discharge
f_B	frequency shift generated by an acousto-optic modulator (Bragg cell)
f_D	Doppler frequency
f_o	resonant frequency
FWHM	full width at half maximum
GPIB	general purpose interface bus, (IEEE-488 standard)
GPS	global positioning system
HeNe	helium-neon
HEX	heat exchanger
I	intensity
$I(u,v)$	intensity distribution captured by the camera
$I_b(u,v)$	background intensity
$I_m(u,v)$	modulation intensity
$I_n(u,v)$	image set, state 1
$I'_n(u,v)$	image set, state 2
$I_{tn}(u,v)$	image from a time-average sequence
$I_{to}(u,v)$	time varying object beam intensity
I_1	intensity of wave 1
I_2	intensity of wave 2
I_{max}	intensity of the brightest fringe
I_{min}	intensity of the darkest fringe
$I_o(u,v)$	object beam intensity
$I_r(u,v)$	reference beam intensity
IC	integrated circuit
IEEE	Institute of Electrical and Electronics Engineers
$\boldsymbol{K}$	sensitivity vector

$\boldsymbol{K}_1$	illumination vector
$\boldsymbol{K}_2$	observation vector
L1	lens 1
L2	lens 2
$\boldsymbol{L}$	vector describing surface of object in space
L_c	coherence length
LVPZT	low voltage piezoelectric transducer
LCD	liquid crystal display
LDV	laser Doppler vibrometry
LED	light emitting diode
LS	light source
M	characteristic function of time-average modulation
MEMS	microelectromechanical systems
MRI	magnetic resonance imaging
n	increment, fringe order
NI DAQ	National Instruments data acquisition
NIST	National Institute of Standards and Technology
OBJ	objective
OEH	opto-electronic holography
OELIM	optoelectronic laser interferometric microscope
PBS	proximal beam splitter
PC	personal computer
PID	proportional-integral-derivative feedback controller
PSI	phase stepped interferometry
PZT	piezoelectric transducer
Q	quality factor
Q_d	live static display of OEH
Q_{tD}	live time-average display
REF	reference mirror
SEM	scanning electron microscope
SSM	sacrificial surface machining
SWLI	scanning white light interferometry
TAS	Thermal Analysis System
TEC	thermoelectric cooler
(u,v)	pixel coordinates of an image
UNF	unified fine (thread standard)
V	fringe visibility
VLSI	very large scale integration
VSI	vertical scanning interferometry
z	vertical scan position
$\Delta\phi(u,v)$	phase difference
$\Delta\nu$	frequency bandwidth of a light source
δ	width of modulation
λ	wavelength
λ_1	wavelength 1
λ_2	wavelength 2

Ω	fringe-locus function
Ω_t	time varying fringe-locus function
τ	exponential decay factor
τ_c	temporal coherence
θ_n	phase step increment
θ_R	calculated actual phase step increment

OBJECTIVES

The intent of this Thesis is to design, build, and implement a complete system for characterization of MEMS shape and deformations under various operational and loading conditions. More specifically, the CHSLT laboratories at WPI have a need for a non-contact measurement system that can characterize surface topography of MEMS with the following requirements:

1) nanometer out of plane resolution,
2) completely noninvasive,
3) ability to measure components with overall lateral dimensions ranging from 20 by 20 μm to 20 by 20 mm,
4) ability to measure static shape including samples with step heights > 150 nm,
5) ability to measure static deformation,
6) ability to measure vibrating objects both spatially and temporally,
7) reduce the set up and alignment time from days to hours,
8) provide at least 20 cm of working space around the MEMS in the measurement apparatus to ensure ample room for loading devices.

Along with being able to measure the MEMS with the above requirements, the system also has to be able to drive and load the MEMS in the following ways:

1) supply necessary power sources and signals for the MEMS
2) thermally cycle MEMS from -30°C to 100°C
3) dynamically excite samples from 1,000 Hz to 1.0 MHz
4) subject the MEMS to vacuum and dry gas environments

These are the requirements of the system. At the time of initiation of this Thesis, no such cohesive system existed in the CHSLT.

1. INTRODUCTION

Throughout history, the ability to accurately measure has been a leading factor in the development of new technologies. Egyptian surveying techniques allowed for construction of the pyramids, thousands of years later still considered some of the greatest structures on Earth. The design and construction of ancient Roman aqueducts would have required large scale advanced measurements to ensure proper flow of water to the cities, allowing the population centers to develop. Inaccurate measurements of the circumference of the Earth led Christopher Columbus to believe that he had sailed to India when instead he had only made it to the Americas. His measurements and calculations had greatly underestimated the distance from the Canary Islands to Japan by about 15,000 km (Encarta, 2006). This measurement blunder led to the eventual colonization of the Americas.

Since then, nearly every technological advancement can be, in some way, attributed to the ability to accurately measure. The American industrial revolution was in large part brought about by the introduction of quality controls and precision machining, both of which are tolerance measurement based processes. Modern medicine is based on the ability to accurately diagnose problems often using measurement techniques such as MRI and ultrasound. Computers are constantly using sensors to measure the surface of the storage media for the presence of data bits: in the case of a hard drive this is a magnetic measurement, for a CD this is an optical measurement.

The number of examples of how measurement processes are used in technology and their influence on technological advancements are endless. One particular area of great contemporary interest is that of the measurement of microelectromechanical

systems (MEMS) to aid in their rapidly advancing development.

1.1. MEMS

Continued advances in miniaturization, largely due to improvements in sacrificial surface machining (SSM), have led recently to development of micoelectromechanical systems (MEMS). Today, MEMS defines both the technology to make these systems and the systems themselves (Pryputniewicz and Furlong, 2003). From consumer products to military defense systems, MEMS are allowing devices to be more accurate, smaller, faster, consume lower power than their larger counterparts, and less expensive. MEMS play key roles in recent technological advancements in aerospace, telecommunications, safety, medical applications, consumer electronics, and biotechnology. Some common applications of MEMS are as automotive stability control and roll over prevention, commercial and military guidance systems, biological and chemical sensors, video projectors, and motion sensors for video game consoles.

MEMS are typically considered to be electromechanical devices of characteristic dimensions ranging from 1 μm to 1,000 μm. MEMS are fabricated using similar processes as in the integrated circuit (IC) industry, which are based on silicon wafer technologies. These processes utilize very large scale integration (VLSI) techniques that allow fabrication of multiple mechanical structures, that are integrated with controlling electronics, in large batches (Pryputniewicz, 2003a). The ability to batch produce MEMS in large numbers is a key advantage that MEMS have over functionally similar macro-sized devices: batch production allows for the cost-per-unit to be significantly lower. In fact, many different organizations have realized this potential for profit and in the year

2000, experts estimate that nearly $82 billion in revenue was generated by microsystem industries (Hsu, 2002). By 2004, Texas Instruments alone was generating a revenue of $880 million with the sales of its MEMS micromirror based DLP device for projectors and televisions (In-Stat, 2006). Funding for MEMS companies has increased 43.9% from 2003 to 2004 and the number of MEMS produced is expected to grow by 20% per year through 2009, (In-Stat, 2006). Typical MEMS products included in this revenue figure are accelerometers (airbag deployment sensors), gyroscopes (vehicle stability control, aerospace), micromirrors and arrays (telecommunications, high definition visual displays, directable automotive headlamps), chemical and biological sensors (micro-chem lab), pressure sensors (process control), etc. The number of applications for MEMS are ever increasing as they become mainstream and new industries are adopting their advantageous and far reaching technology.

In many applications, MEMS have significant advantages over older, non-MEMS based technologies. As mentioned previously, MEMS are fabricated in large batches using existing silicon wafer technology and fabrication facilities which helps to minimize their cost. Also aiding the total cost of the MEMS-based products are fabrication techniques, which allow components to be manufactured in an already assembled state, meaning that no assembly is required for the actual MEMS device (MEMS packaging is another issue and will be discussed shortly). For example, 6,000 MEMS accelerometers are fabricated on a single six inch diameter silicon wafer and 20 wafers are processed simultaneously at Analog Devices Inc., meaning that 120,000 accelerometers are manufactured in one batch. In addition, traditional mechanical airbag accelerometers cost more than $15 each, while batch fabricated MEMS accelerometers cost less than $4

(Sulouff, 2003).

MEMS devices typically have high operational mechanical frequencies due to their high stiffness and small mass of moving parts. This allows MEMS to have significantly faster response times than larger mechanical devices. RF MEMS switches can achieve frequencies of 40 GHz or greater (Pacheco et al., 2000) in comparison to mechanical switches, which operate at up to several thousand Hz.

Possibly the most obvious key advantage that MEMS have over macro-scale technology is size. Since the actual MEMS component is one millimeter or less in length and width, when fully packaged with controlling electronics, this device itself is typically the size of an IC chip or smaller. Such miniaturized sizes allow high precision sensors and actuators to be utilized in all types of applications. Consumer electronics such as cell phones, GPS, and handheld games benefit from miniature inertial sensors, (Sulouff, 2003, Pryputniewicz et al., 2001a). Miniaturization in terms of dimensions and mass are of significant concern to spacecraft and satellite engineering, making the applications for MEMS technology highly desirable in these fields (Hsu, 2002; Pryputniewicz et al., 2001b). The list of advantages of MEMS components is very long and continues well past what is discussed herein. There are, however, many challenges in MEMS design that, usually, may not be an issue for larger devices.

Packaging of MEMS involves integration of electronic and micromechanical components in an enclosure to ensure proper interconnection with other components as well as protection from unfavorable environmental conditions. However, this is not a trivial engineering problem, since the primary purpose of the package is in direct conflict with the purpose of the MEMS: the package shields the sensitive MEMS parts from the

environment, while these parts attempt to interact with the environment as sensors or actuators. For example, a MEMS pressure sensor has a thin membrane that is used to measure pressure of an environment relative to a reference pressure (or vacuum). Such a membrane, however, is very delicate and any contaminates from the environment can adversely affect operation of the device. Therefore, a pressure sensor package must be able to protect the membrane from the environment while still allowing enough contact with the environment to facilitate measurements. In general, packaging challenges make packaging the cost-dominating factor in the development of MEMS. Typically about 80% of the cost of a finished MEMS-based product is related to the packaging (Hsu, 2002).

It is important to test new MEMS designs as the product is being developed. Often, computational and analytical models are used in the development of new MEMS designs. Usually, these models are based on limited knowledge of material properties, process conditions, and tolerances. Because of the difficulty in measuring properties of such small devices with high accuracy (Pryputniewicz et al., 2001c), the analytical and computational models are often not validated and may lead to serious repercussions on the performance and reliability of MEMS products. Pryputniewicz (2003a), describes this notion as:

> *Research into MEMS testing… has received [little] attention, which, given that MEMS are no different from their macro world counterparts in terms of reliability, is a somewhat disturbing oversight. If a sensor fails to deploy an airbag during an automobile crash, it matters not if the sensor is the size of a grapefruit or smaller than a pinhead. Clearly, reliable test methodologies must be developed for MEMS devices*.

One such methodology for non-invasively characterizing shape and deformations of

MEMS is based on optical interferometry.

Conventional “interactive”, i.e., invasive testing methods for macro sized mechanical components cannot be applied to microsystems. For example, a strain gage cannot be applied to a two micrometer thick MEMS component without adversely affecting its performance, or even damaging it. Nor can point-by-point contact measurements be made to measure the geometry of this two micrometer thick component without severely distorting or destroying it. The most common method for testing MEMS is to check the electrical output of a device and see if it is within tolerance. However this method often lets one (merely) know that a particular device is non-functional, but it does not reveal the cause of the problem. As MEMS are mechanical in nature, occasionally there are mechanical problems. For example, a MEMS gyroscope, similar to the one shown in Fig. 1, arrived to our testing facility in an electrically non-functional state, i.e., the output signal of the gyroscope was not what was expected. A visual inspection of the package and optical microscope images could not find any anything wrong with the device.

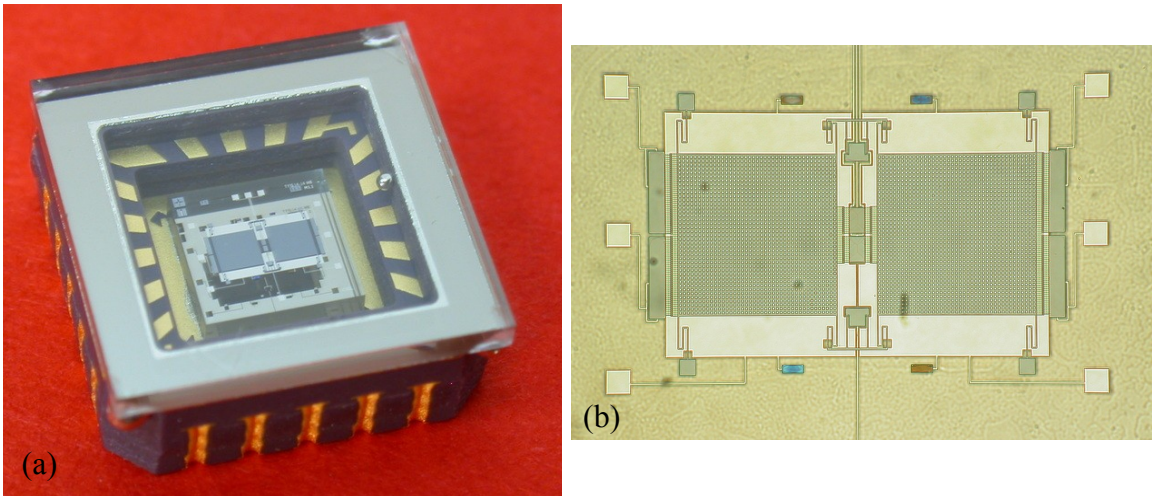

Fig. 1. Representative packaged MEMS gyroscope:
(a) visual inspection, (b) an optical microscope image.

As something was obviously wrong with the output of this device, it was placed under the interferometer for further inspection. The interferometric analysis, shown in Fig. 2, clearly indicates a mechanical problem with this device. Ideally the measured surface of this particular type of a device should be planar, but interferometric analysis shows that the left proof mass (i.e., shuttle) has been deformed downwards. (What happened was that the left proof mass, a square plate – of about 300 microns on a side - supported by 4 folded springs, had stuck to the underlying substrate at some point in time prior to its arrival at CHSLT).

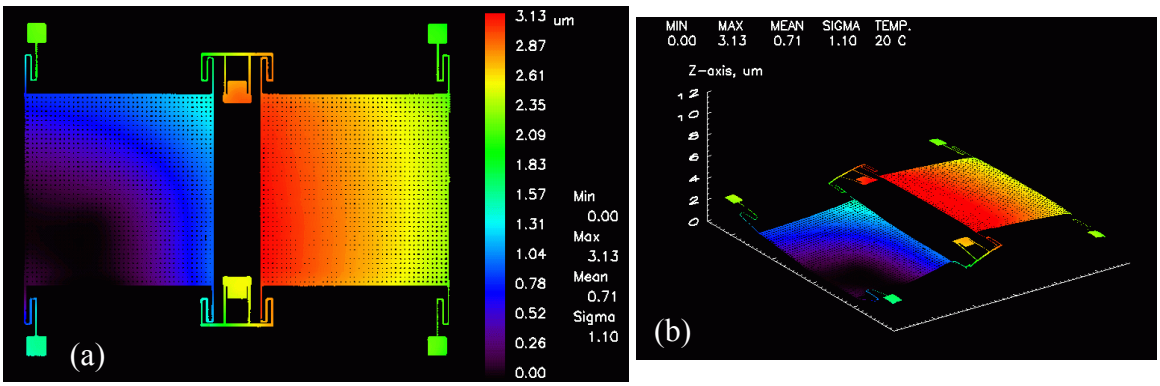

Fig. 2. Interferometric analysis of a packaged MEMS gyroscope showing a defect: (a) 2D representation of measured shape of the top surface of the microgyro, (b) 3D representation of measured shape of the top surface.

This example graphically illustrates that there is a need for developing effective methodologies for full-field-of-view characterization of MEMS, particularly mechanical structures, and that interferometry is an ideal tool for many MEMS testing applications.

1.2. What is interferometry?

In general, interferometry is utilization of the interference of two waves to perform some sort of measurement. Typically there is a comparison between a

"reference" wave and an "experimental" wave to achieve a measurement (Pryputniewicz, 1976). The type of wave depends on what sort of measurement is desired. For example, sound waves are used in acoustic interferometers to measure properties of gases and liquids, radio and microwaves are used to measure the surface of the Earth and other large bodies with synthetic aperture radar systems, and light waves are used most commonly in laboratories using optical interferometers to measure the shape and deformation of various types of objects ranging from MEMS to bridges, planes, and buildings.

1.3. A brief history of interferometry

Interferometry was not originally developed for measurements of micron sized objects. In fact, interferometry was first used for astronomical measurements. It was in 1880 when Albert A. Michelson showed through mathematics and experiments that the interference of two beams of light from a distant source allows more accurate measurement of the remote object than any then-current methods (Lowell, 2003). Michelson was an American physicist who received the Nobel Prize in 1907 for his discoveries and experiments. It was not until 1920 that the technique had been perfected enough to make significant scientific measurements. At that time Michelson used interferometry to measure the diameter of the first star outside our solar system (Lowell, 2003).

Interferometry, however, was not discovered by Michelson. In fact, the principle was nearly a century old by the time Michelson began his measurements. At the beginning of the 19th century, Young experimentally demonstrated the phenomenon of interference and Fresnel explained it analytically using wave theory (Pryputniewicz,

2003b). It was these pioneering physicists who laid the theoretical frame work for Michelson to base his research on.

Since the time of Michelson, numerous advancements and discoveries have been made in the field of interferometry. Many different methods for shape and deformation measurement have been developed including laser interferometry, white light interferometry, and speckle interferometry. A derivative of interferometry, holography, has also been extensively utilized within the past five decades for precision measurements (Pryputniewicz, 2003b). Holography also allows the measurement of deformations of objects over time and is described in detail by Vest (1979) and Pryputniewicz (2003b).

Recently, measurement systems have been improving significantly both in terms of range of applications and quality of results. With the commercialization of the diode laser over the past two decades, interferometric and holographic measurement systems have dramatically reduced in size since the diode laser is a fraction of the size of a gas and other lasers used heretofore. Also, the use of computers with CCD and CMOS cameras has allowed measurements to be done in near real-time, with no need for developing photographic films or plates. By directly importing the data into a computer, analysis can be performed and results obtained in a minimal amount of time, minutes rather than hours or days. Computers also provide the ability to display/output quantitative results where absolute shape and deformation fields can be characterized. With over two centuries of development, it is only now that these nondestructive and noninvasive measurement techniques are sufficiently advanced to be applied to characterize micron scale components of the emerging technologies.

1.4. Current state of the art interferometry

As time progresses the interferometers get smaller, faster, more sensitive, and easier to use. Interferometers have been utilized heavily in the educational and research fields and are traditionally built in-house, but recently numerous commercially available interferometers are being marketed. There have been many advances recently in this field, but two of the most significant are those of (i) scanning white light interferometry (SWLI) and (ii) the computer interface.

With advances in computer technology and software control, interferometric measurements can be made with just a few clicks of a mouse on some of these systems. For example, Zygo Corp. is one of the largest companies to develop, produce, and market interferometric metrology equipment. Zygo manufactures several different types of interferometers and one type is an automated white light interferometer that can be utilized for characterization of micro-scale components, such as MEMS. Depending on the options purchased, interferometers such as this can cost several hundred thousand dollars. With an in-plane field of view of 0.04 to 21.9 mm and a vertical scan range of 150 μm, the Zygo NewView 6300 is the current state-of-the-art of commercially available systems (Zygo, 2006).

2. PRINCIPLES OF INTERFEROMETRY

Interferometry refers to utilization of the interference of two waves (from this point forward we will consider only optical interferometry). There are many interferometric apparatus for producing interference between two light waves, but all of them follow two basic rules: light waves will only interfere if they come from the same source, and at the point of interference, they must be coherent; coherence being a measure of the ability of waves to interfere. There are two fundamental groups of interferometers: (i) wavefront dividing and (ii) amplitude dividing. Correspondingly, there are two types of coherence: (i) spatial and (ii) temporal.

2.1. Wavefront dividing interferometers

The oldest known demonstration of interferometer operation is in a wavefront division experiment set up by Young in the early 1800's. It is commonly referred to as "Young's double slit experiment", Fig. 3. In this setup, light passes through two separate holes and is divided into two similar wavefronts which then expand and interfere. This interference results in a fringe pattern that is then observable on a screen. This type of interferometer is not used in the modular interferometric microscopy system, therefore it will not be discussed in detail.

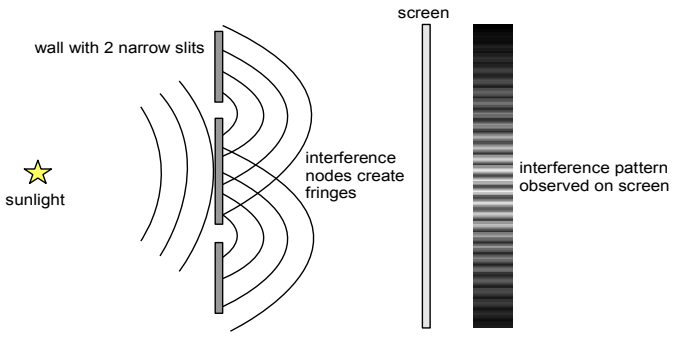

Fig. 3. Young's double slit experiment: a wavefront dividing interferometer.

2.2. Amplitude dividing interferometers

Amplitude dividing interferometers, such as the Michelson interferometer shown in Fig. 4, are more commonly used in interferometric measurement systems. In a simplistic case, a collimated monochromatic wavefront is directed into a beam splitter (BS) that allows 50% of the light to pass through, the remaining 50% of the light is reflected orthogonally. The beams are then reflected off of mirrors 1 and 2 and recombined in the BS. At the point that the beams are recombined, interference may occur and is observed by the detector.

The key distinction to make between this configuration and that of a wavefront dividing interferometer is that this configuration does not interfere two separate parts of a wavefront, rather the interference occurs between two partial (i.e., amplitude divided) waves that have originated from a single original wave.

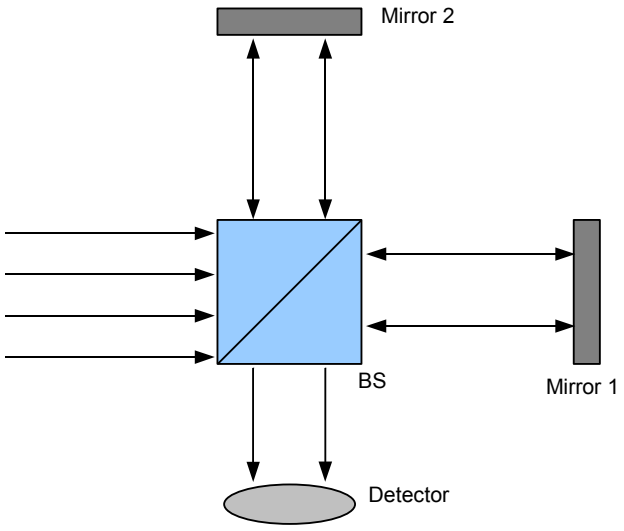

Fig. 4. The Michelson amplitude dividing interferometer.

2.3. Interference

Interferometry is based on the wave nature of light. Using the superposition principle, it can be said that two waves overlapping in the same space will have their amplitudes combined to form a new wave. Consider the waves shown in Fig. 5. When waves 1 and 2 are nearly in phase, Fig. 5a, they are said to constructively interfere to form wave 3. When the waves are nearly in antiphase, Fig. 5b, they are said to be destructively interfering. Mathematically, we can say that the intensity of each wave is proportional to the square of its amplitude. This allows us to say that the intensity (I) of the combined wave 3 is (Robinson and Reid, 1993)

$$I = I_1 + I_2 + 2\sqrt{I_1 I_2}\cos\Delta\phi \quad , \tag{1}$$

where the intensities I_1 and I_2 are from waves 1 and 2, respectively, and $\Delta\phi$ is the phase difference between these two waves. The term $2\sqrt{I_1 I_2}\cos\Delta\phi$ is known as the interference term. In the case of Fig. 5a, $\Delta\phi$ is nearly zero making the interference term significant. In the case of Fig. 5b, $\Delta\phi$ is approximately $\pi/2$ causing the interference to be about zero.

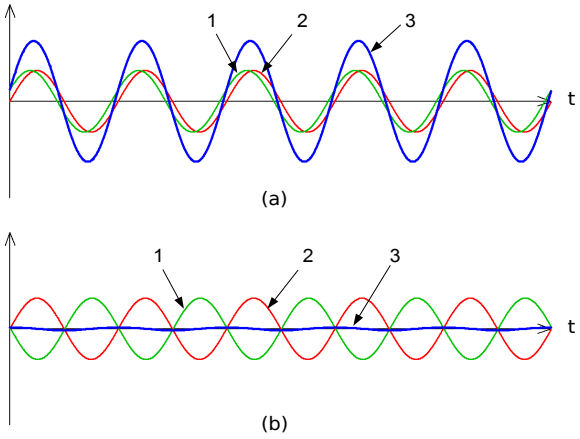

Fig. 5. Interference of two infinite waves of a single frequency: (a) constructive interference, (b) destructive interference.

2.4. Coherence

Coherence is the ability of light waves to interfere. There are two fundamental types of coherence: spatial and temporal. Spatial coherence basically describes how well the wavefront dividing interferometers will form fringe patterns. More precisely, spatial coherence describes the ability of two distinct points of a wave in space to interfere when averaged over time. Temporal coherence is a description of how well a wave can correlate with itself at a different time instant (Kreis, 1996). This type of coherence is an indication of how well an amplitude dividing interferometer will produce fringe patterns.

As the interferometers used in the modular interferometric microscopy system are amplitude dividing interferometers, let us consider temporal coherence. Remembering the Michelson interferometer of Fig. 4 and the description of interference in Fig. 5 it could be easily said that this interferometer *will* produce and interference pattern. However, that may not always be the case. The assumption in Fig. 5 is that the two interfering waves are of infinite length and of one constant frequency. This, however, is an idealization as no light source is this perfect. Even single mode lasers which are described as "monochromatic" have a finite spectral bandwidth.

To represent these real light sources we can say that they output wave trains of finite length with random phase shifts between each train (Gåsvik, 2002). Figure 6a shows two sets of wave trains, such as those reflected back by both mirrors in the Michelson interferometer, prior to being recombined by the BS. The figure only shows two wave trains for each arm of the interferometer, but as the detector which records the intensity information runs at only video rates, a very large number of wave trains are averaged together (since they are traveling at the speed of light) to make one recording.

Note that the length of each wave train is the coherence length, L_c, of the light source. Also note that between wave trains there is a random phase shift or discontinuity simulating a "real" light source.

In the case of Fig. 6a, the interferometer is aligned perfectly: the distances from the BS to each mirror are identical. The abrupt and random phase shifts occur at the same instant in time. The box surrounding all of the wave trains indicates that interference will occur with the highest visibility. Because of the perfect alignment, the intensity observed by the detector is still the ideal case, given by Eq. 1.

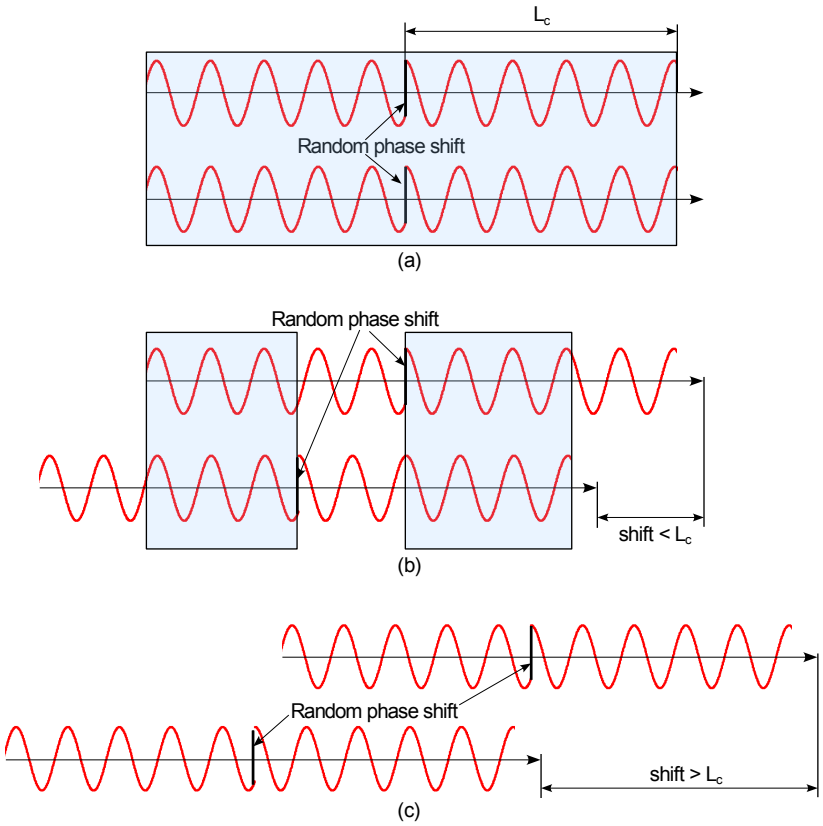

Fig. 6. How coherence length affects interference with different phase shifts, areas that will reliably interfere are highlighted in blue:
(a) both wave trains are aligned and will completely interfere;
(b) a shift less than the coherence length has been introduced, only a portion of the wave trains will consistently interfere;
(c) a shift longer than the coherence length has been introduced, only random interference will occur.

Figure 6b represents the case when the interferometer is partially misaligned by having one of the mirrors a different distance from the BS than the other. In this case, however, the path length difference is less than the coherence length of the light source. This allows some interference to occur. The highlighted regions are the only areas where the first wave trains align and the second wave trains align. These are the only areas where the interference will be constant through time. Outside of these areas there will still be interference between wave trains, but as the phase shift between wave trains is random, the interference will be random through time. Having this random interference reduces the contrast of the fringe pattern. For the ideal case where $I_1 = I_2$, Eq. 1 becomes:

$$I = I_1 + I_2 + 2V\sqrt{I_1 I_2}\cos\Delta\phi \quad , \tag{2}$$

where V is known as the fringe visibility that ranges from 0 to 1. The fringe visibility is also defined as (Gåsvik, 2002)

$$V = \frac{I_{max} - I_{min}}{I_{max} + I_{min}} \quad , \tag{3}$$

where I_{max} and I_{min} are the intensities of the brightest and darkest fringes, respectively. Looking at Fig. 6b, one might guess that $V \approx 0.6$ meaning that the fringe contrast of this interferometer alignment is roughly 60% of that of the ideal alignment in Fig. 6a.

Figure 6c is a case where the path length difference in the two arms of the interferometer is greater than the coherence length of the light source. When this situation occurs no fringes are generated. As no portion of the wave trains line up, complete random interference is occurring. The $\Delta\phi$ term is varying randomly from 0 to 2π and when averaged over time the cosine of this term goes to zero, changing Eq. 2 into:

$$I = I_1 + I_2 \tag{4}$$

and the result is constant intensity where no interference takes place.

It is often desirable to know what the coherence length of a light source is when setting up an interferometer. For this purpose, it can be said that the temporal coherence, τ_c, at the point where the path length difference brings the fringe visibility to zero is (Gåsvik, 2002)

$$\tau_c = \frac{L_c}{c} = \frac{1}{\Delta v} \quad , \tag{5}$$

where L_c is the coherence length, c is the speed of light, and Δv is the frequency bandwidth of the light source. The coherence length L_c can also be thought of as the distance the wave travels in time τ_c. Anything shorter than this coherence length or time will interfere. For the set up of interferometers, the coherence length is what needs to be known, therefore Eq. 5 can be rewritten using the bandwidth wavelengths λ_1 and λ_2 to become

$$L_c = \frac{c}{\Delta v} = \left| \frac{1}{\lambda_1} - \frac{1}{\lambda_2} \right|^{-1} \quad . \tag{6}$$

Equation 6 is used to determine how precisely the path lengths of the interferometer need to be aligned in order for interference to be observed. Properties of some common light sources are summarized in Table 1.

Table 1. Typical properties of common light sources for interferometers.

Light source	***Bandwidth,* $\lambda_2 - \lambda_1$**	**Δv**	**Peak λ, nm**	**Coherence length, L_c**
Solid state laser	1×10^{-15} m	1.0 MHz	532	300 m
HeNe laser	0.1 pm	150 MHz	633	2 m
Diode laser	1 nm	700 GHz	650	420 μm
LED	30 nm	3×10^{13} Hz	640	13 μm
White light	300 nm	3×10^{14} Hz	550	1 μm

Figure 7 is a representation of the visibility of a fringe as one arm of the interferometer is scanned through the temporal coherence range. This plot is representative of what a LED coherence range looks like. When using a LED in the interferometer, the two arms need to be aligned within a few fringes to maintain high contrast. The temporal coherence range would be shorter for a white light source and much longer for the lasers.

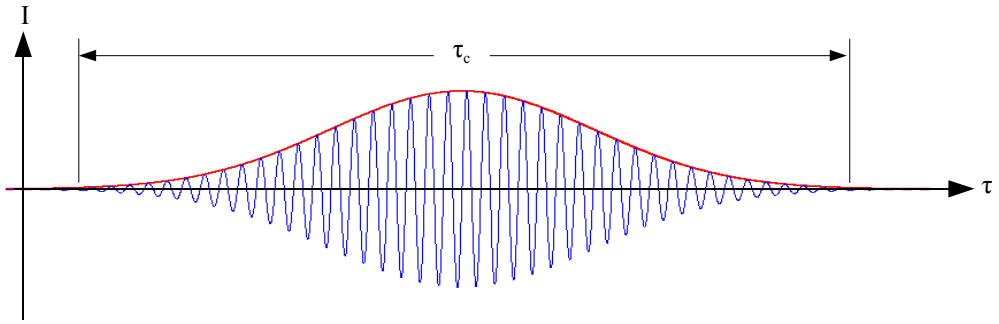

Fig. 7. Plot of the visibility of a fringe across the temporal coherence range.

3. INTERFEROMETER CONFIGURATIONS

MEMS are typically fabricated out of silicon which is highly reflective in the visible spectrum (Jones and Jones, 2000). Therefore, retro-reflective interferometers have been implemented. Retro-reflective type interferometers use the direct reflection of light off of the object being measured, or stated differently, the object being measured is both illuminated and observed through the same axis which is normal to the object surface. This type of interferometer is best suited to nearly flat, highly reflective objects such as MEMS. There are many other types of interferometers (diffuse reflective, transmissive, etc.), but as they are not well suited to the study of MEMS, they will not be discussed in detail. This Chapter gives a general description of each type of interferometer that is implemented in the modular interferometric microscopy system of this Thesis.

3.1. The Michelson interferometer

The Michelson interferometer is one of the most versatile interferometers ever developed. Developed by and named after Albert Michelson, this is also one of the oldest designs. Antiquity, however, does not mean that this configuration has outlived its usefulness. On the contrary, variations of the Michelson interferometer are some of the most common interferometers today. The phase stepping Michelson interferometer is able to very accurately measure the surface shape of components that are highly reflective with a surface that is continuous. Shown in Fig. 8 is one possible configuration of a modern Michelson interferometer in use today. A monochromatic coherent light source (LS) such as a laser or LED, outputs a beam that is expanded by one lens (L1) and collimated by a second lens (L2). This expanded and collimated beam is then divided

into two parts/beams by the BS each sent along two orthogonal paths – to the MEMS, and to a reference mirror (REF). These two beams are then reflected back and recombined by the BS to form an interference pattern that is imaged by the imaging objective (OBJ) and recorded by the camera. When the path that one beam travels varies with respect to the other, there is a phase difference when they are recombined. The phase difference results in constructive and/or destructive interference producing light and dark bands, known as interference fringes. The interference fringes have a similar meaning to contour lines on a topographical map – they represent deviations in elevation (shape) of the object. In order to get quantitative data out of these interference fringes, phase stepping of one arm of the interferometer is performed. Phase stepping is a known minute movement in a known direction of one component determining the path/trajectory of a light beam. This is usually done by means of a piezoelectric transducer (PZT) attached to the object or reference mirror. Phase steps and analysis will be discussed in detail in Chapter 4. A typical phase step requires a highly repeatable controlled linear motion of < 70 nm.

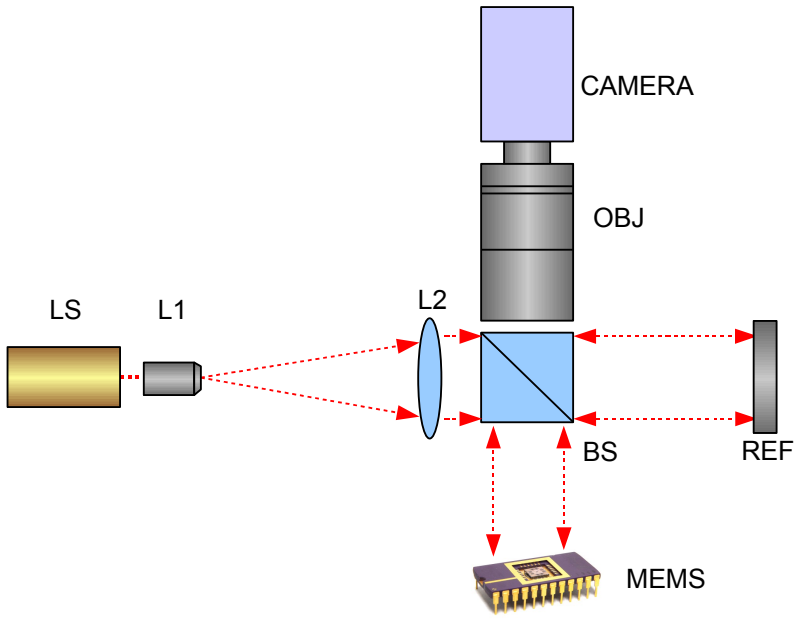

Fig. 8. Schematic of a Michelson interferometer.

3.2. The Mirau interferometer

The Mirau interferometer is a common design used in high magnification microscopes. This configuration can have an optical magnification of 50x or more, in contrast to the Michelson which is usually limited to around 5x magnification. Shown in Fig. 9 is a schematic of a Mirau interferometer. The light source (LS) is usually a LED or white light lamp with a diverging output. The light is collimated by a lens or lens system (L1) and is direct downward by a BS. The light is focused by lens L2 toward the MEMS being investigated. A beam splitter plate reflects half of the light to a small reference mirror (REF) and transmits half of the light to the MEMS. Both the REF and the MEMS reflect light back to the beam splitter plate where the two beams are recombined to form an interference pattern with the same meaning as that of the Michelson interferometer. This image is reflected upward through L2, BS, and focused by lens L3 onto an imaging device such as a camera.

The Mirau interferometer is commonly used in vertical scanning interferometers because it can be readily aligned. The lens L2, the REF, and the beam splitter plate can be contained inside a microscope objective. Because that part of the system is neatly packaged, alignment is not much more difficult than focusing a microscope onto a MEMS. Microscope objectives with magnifications of 10x or greater typically have a shallow depth of field, several micrometers or less, thus when the Mirau objective is focused, the path length that the light travels from the MEMS to the beam splitter plate is the same as that of the REF to the beam splitter plate. When the path lengths are accurately aligned, a non-monochromatic light source can still achieve interference over a limited range. This principle is utilized for vertical scanning interferometry.

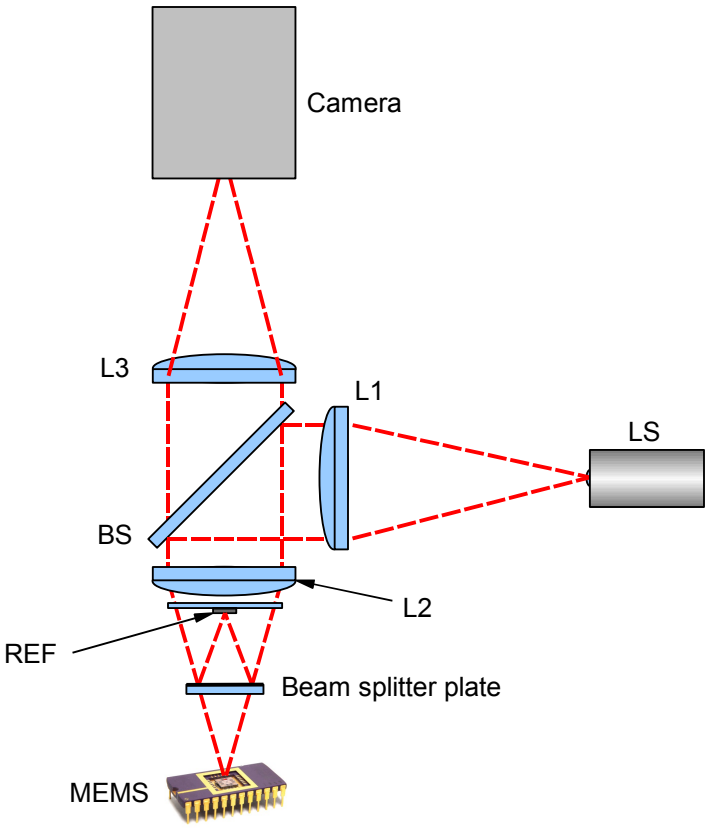

Fig. 9. Schematic of a Mirau interferometer.

3.3. The scanning white light interferometer

Scanning white light interferometry (SWLI) is a form of vertical scanning interferometry (VSI) that utilizes a broadband white light source and a coherence tracking method to measure the shape of objects with larger step heights than conventional phase stepped interferometers can accommodate (Harasaki et al., 2000). The advantage a SWLI system has over a phase stepped Michelson or Mirau system is that it can measure steps in the sample, such as multiple layers of a MEMS device in one measurement. This is often very important in the characterization of MEMS and the key reason for developing this SWLI system.

In SWLI, fringes are only generated when the path length of both the object and

reference arms of the interferometer match to within the coherence length of the light source. The coherence length of a white light source is very short, typically a micrometer or less. It is this limited coherence length that is exploited for SWLI measurements.

One SWLI configuration is shown in Fig. 10. This particular configuration shows the use of a Michelson interferometer built into a microscope objective, achieving optical magnifications of 2.5x or 5x. Higher magnifications are possible using Mirau interferometer objectives and lower magnifications (or even demagnifications) are possible using a modified version of the Michelson interferometer shown in Fig. 8.

Light is output from a halogen (white) light bulb, directed down into the interferometric objective (OBJ) via the BS. The PZT scans the objective downward a maximum of 250 µm at a constant rate. As different layers of the sample come into focus, pixels imaging them begin to modulate (see A and B in the lower right of the figure). Images are acquired at constant intervals as the PZT is scanned. This produces an image stack that is analyzed for full 3D representation of the surfaces of a MEMS.

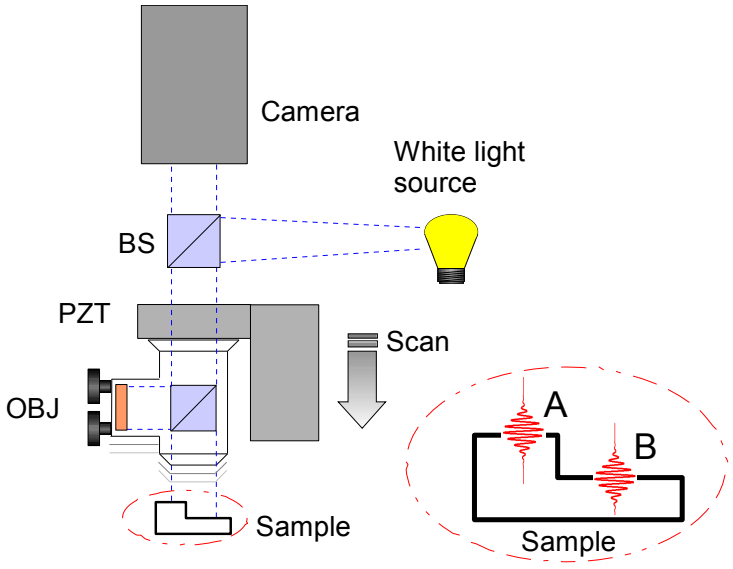

Fig. 10. Schematic of a vertical scanning interferometer.

3.4. The vibrometer

The vibrometer is an interferometer based on the Michelson configuration. Employing a technique known as a Laser Doppler Vibrometry (LDV), the vibrometer that is used in this system is a commercially available unit, the *Polytec OFV 502 Fiber vibrometer system*. Utilizing the Doppler shift of light reflected off of a vibrating object, this technique allows a point wise measurement of the velocity of a vibrating object. Because of the very high frequency of laser light, about 4.74×10^{14} Hz, direct measurement of this minute Doppler shift is not easy. The system uses an interferometer to demodulate the Doppler frequency of the object beam by interfering it with a static reference beam.

Shown in Fig. 11, the fundamental vibrometer configuration is similar to that of the Michelson interferometer. The laser beam is split into two arms acting as a reference and an object beams, respectively. The object beam is pointed at a vibrating object and reflected light is recombined in the beam splitter with the reference light.

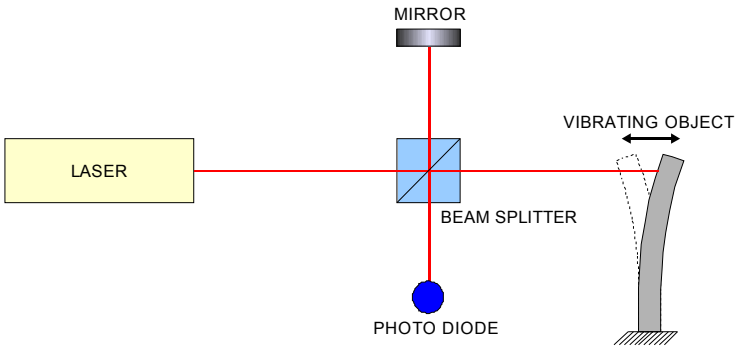

Fig. 11. Schematic of the vibrometer interferometer.

As the object vibrates there is a Doppler shift in the frequency of the laser light of the object beam. Interfering this light with the reference light will cause a beat frequency that is equal to the difference of the reference signal from the object signal. This is

measured by the photo diode as variations in intensity, Fig. 12. Changes of intensity of this light with respect to time are due to the beat frequency caused by a vibrating object. And, as with the Michelson interferometer, the peak to peak distance of this signal is equal to half of the wavelength (λ), of the laser. For a description of the analysis of this signal, see Section 4.5.

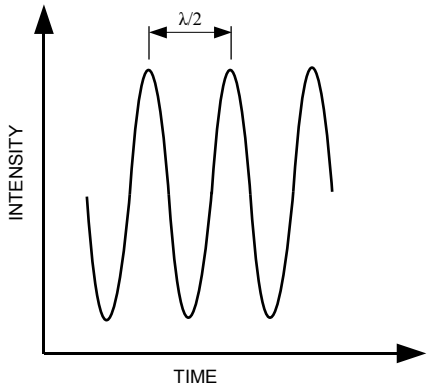

Fig. 12. Changes of intensity with respect to time.

4. QUANTITATIVE INTERFEROMETRIC ANALYSIS

All of the interferometers used in this system will generate some form of phase information that relates to the measurement of relative location on an object. In three-dimensional space this information can be used to determine the fringe-locus function (Ω) which defines the fringe loci on the objects surface. The fringe locus function relates directly to the fringe orders (n) by (Pryputniewicz, 1995)

$$\Omega = 2\pi n \quad . \tag{7}$$

The values of Ω relate to system geometry and the unknown vector $\boldsymbol{L}$ describing the location of the surface of an object in space according to (Pryputniewicz, 2003b)

$$\Omega = (\boldsymbol{K}_2 - \boldsymbol{K}_1)\cdot\boldsymbol{L} = \boldsymbol{K}\cdot\boldsymbol{L} \quad , \tag{8}$$

where $\boldsymbol{K}$ is the sensitivity vector of the interferometer, defined in terms of the illumination vector $\boldsymbol{K}_1$ and the the observation vector $\boldsymbol{K}_2$, both representing the geometry of the system. The solution to Eq. 8 in full three-dimensional space with arbitrary locations for the illumination and observation vectors is quite lengthy and well described (Pryputniewicz, 1995, 2003b). Fortunately, the interferometers utilized by the modular interferometric microscopy system are of the retro-reflective type meaning that the illumination and observation vectors follow the same path and the interferometer is only sensitive along one axis. This greatly simplifies the quantitative analysis of the interferometric data because instead of having to deal with x, y, and z space, there is only the z-axis to consider. Equation 8 can then be solved for $\boldsymbol{L}$ in the z direction (L_z) and rewritten as (Pryputniewicz, 2003b)

$$L_z = \frac{\lambda}{4\pi}\Omega \quad . \tag{9}$$

4.1. Phase stepped interferometry

Phase stepped interferometry (PSI) is a methodology that is utilized to measure the absolute shape of an object with a precision of up to λ/1000, where λ is the wavelength of the light source being used (Harasaki et al., 2000). This technique relies on a set of fringe patterns recorded by a camera in the interferometer. Interferometers such as the Michelson and Mirau are commonly used as phase stepping interferometers with the addition of a PZT for modulation of the object or reference beam. Mathematically, the intensity distribution $I(u,v)$ captured by the camera during an acquisition of a single image is (Brown, 1999)

$$I(u,v) = I_b(u,v) + I_m(u,v)\cos[\Delta\phi(u,v)] \quad , \tag{10}$$

where $I_b(u,v)$ and $I_m(u,v)$ are the background and modulation intensities, respectively, and $\Delta\phi(u,v)$ is the interference phase information. These three quantities are functions of the pixel coordinates across the entire image (u,v) and are unknown. Looking at a single image of a fringe pattern, Fig. 13, it is clear that surface being measured is spherically curved, but the direction, concave or convex, is unknown.

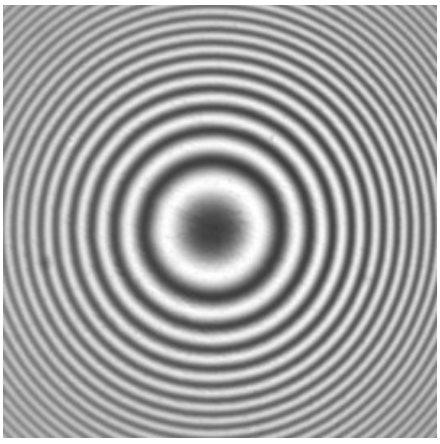

Fig. 13. Fringe pattern of a curved (spherical) mirror.

As we have no way of determining the phase of the light with one image we are unable to determine if the shape of the surface is concave or convex. Of the three quantities in Eq. 10, the phase information is needed to calculate the absolute shape of an object. However, there is only one equation and three unknowns which makes it necessary to introduce phase stepping, which is the process of shifting the path length of one arm of the interferometer by discrete known amounts, to generate a solvable system of equations of the type

$$I_n(u,v) = I_b(u,v) + I_m(u,v)\cos[\Delta\phi(u,v) + \theta_n] \quad , \quad n = 1,\ldots,5 \quad , \tag{11}$$

that will allow for the phase information to be extracted subject to the known phase step increments of θ_n (Kreis, 1996; Robinson and Reid, 1993). In our case, five phase steps are utilized, n = 1,…,5, with an increment of π/2 for each n. This process generates an over determined system of five equations to be solved for the three unknowns. Other algorithms are available such as three and four phase step methods, but the five step algorithm is far less sensitive to phase step errors (Schwider et al., 1983).

For simplification of the equation system shown in Eq. 11, let us use phase steps θ_n of -π, -π/2, 0, π/2, and π. The five phase step images acquired by the camera can be represented as

$$I_1 = I_b + I_m\cos(\Delta\phi - \pi) = I_b - I_m\cos(\Delta\phi) \quad , \tag{12}$$

$$I_2 = I_b + I_m\cos(\Delta\phi - \frac{\pi}{2}) = I_b + I_m\sin(\Delta\phi) \quad , \tag{13}$$

$$I_3 = I_b + I_m\cos(\Delta\phi + 0) = I_b + I_m\cos(\Delta\phi) \quad , \tag{14}$$

$$I_4 = I_b + I_m\cos(\Delta\phi + \frac{\pi}{2}) = I_b - I_m\sin(\Delta\phi) \quad , \tag{15}$$

$$I_5 = I_b + I_m\cos(\Delta\phi + \pi) = I_b - I_m\cos(\Delta\phi) \quad . \tag{16}$$

In Eqs 12 to 16, the pixel coordinates (u,v) have been omitted for clarity. A series of five

phase step images corresponding to a data acquisition sequence is shown in Fig. 14. Note that the first image captured, I_1, and the last image, I_5, end up with identical terms in Eqs 12 and 16, respectively, indicating that the images will look the same provided a true phase step of $\pi/2$ per image was achieved. Visually comparing the fringe pattern of image one to image five is a common way for an operator of the interferometer to determine if the appropriate phase step is being achieved. A keen eye will note that the phase step was slightly off $\pi/2$ or 90° per image in Fig. 14.

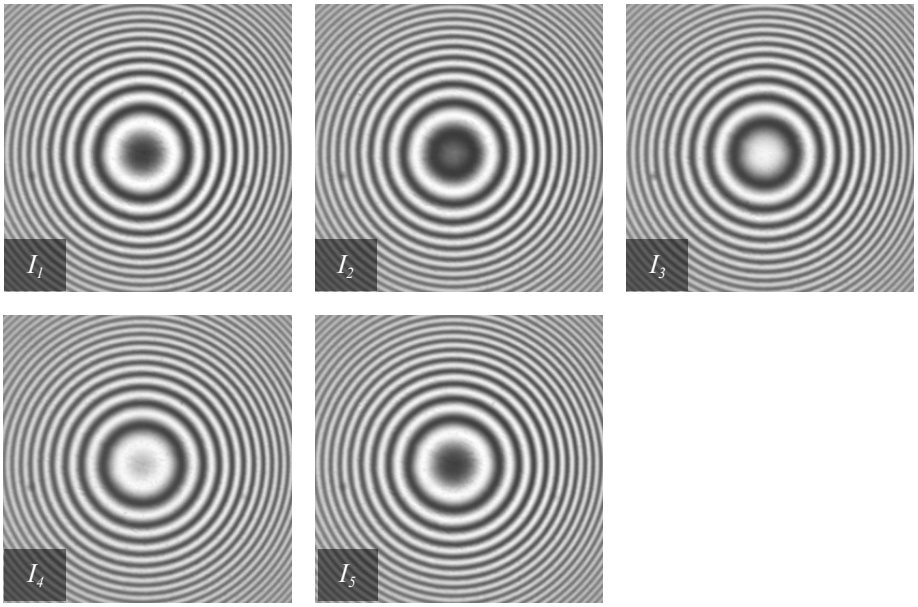

Fig. 14. A series of 5 phase steps, each approximately $\pi/2$, of a curved mirror.

Solving the system of Eqs 12 to 16 for the phase information $\Delta\phi$ yields (Robinson and Reid, 1993)

$$\Delta\phi = \tan^{-1}\left(\frac{2(I_2 - I_4)}{2I_3 - I_5 - I_1}\right) , \tag{17}$$

where the pixel coordinates (u,v) have again been omitted for clarity. The actual phase step θ_R can be calculated to find out the error by (Kreis, 1996)

$$\theta_R = \cos^{-1}\left(\frac{I_1 - I_2 + I_3 - I_4}{2(I_2 - I_3)}\right) , \tag{18}$$

on a per pixel basis. Statistical removal of any outlying points is performed, then the actual phase step of each pixel is averaged to find a quantitative result. In the case of Fig. 14, the actual phase step was 91.89° which is acceptable with the 5 phase step method (Robinson and Reid, 1993).

The phase in Eq. 17 relates to the object shape but it is wrapped modulo 2π due to the discontinuous arctangent function, Fig. 15. To extract the continuous spatial phase directly relating to the actual shape of the object, phase unwrapping is required (Furlong, 1999). Scaling of the unwrapped phase image by $\lambda/(4\pi)$ per pixel yields the physical shape of the object in the out of plane direction. In-plane scaling based on the interferometer optical magnification allows for a full three-dimensional shape to be displayed.

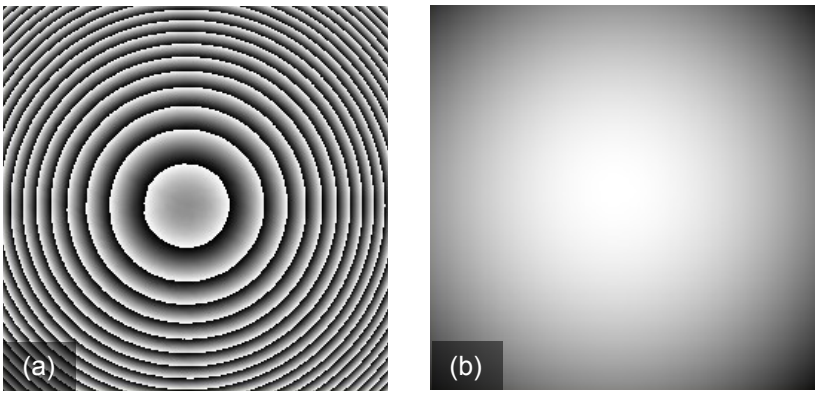

Fig. 15. Shape of a curved mirror: (a) wrapped phase, (b) unwrapped phase.

The interferometric procedure, as presented in this Section, has a measurement range that depends on the number of fringes that can be resolved by an imaging system. Using a high resolution CCD or CMOS digital camera and a highly reflective object, out

of plane measurements can have a range of approximately 0 to 50 μm, with a resolution on the order of a few nanometers or better provided that the surface is smooth and continuous (Klempner, 2003). A major limitation of the PSI technique is that phase errors will occur if there is a surface discontinuity (step) greater than λ/4 (Harasaki et al., 2000).

4.2. Opto-electronic holography

Opto-electronic holography, also referred to as OEH, is a modern adaptation of holographic interferometry. Holographic interferometry is a technique that was developed in 1965 by Stetson and Powell that utilizes holograms (photographic plates that capture both intensity and phase of light) to perform deformation measurements (Stetson and Powell, 1966). As holograms require chemical photographic processing, making measurements with this technique is time consuming. With the introduction of video cameras with outputs that could be digitized by computers, the field of holographic interferometry took a great leap forward. OEH systems could now perform measurements in near real-time with no chemical processing required (Pryputniewicz, 2003b).

Holographic interferometry is primarily used for a precise comparison of two states of an object, for example, before and after an object is subjected to a load. Said differently, holographic techniques are commonly utilized for precise measurement of a deformation of an object. OEH accomplishes this by recording two sets of phase stepped images and then making a comparison between the "reference" set to the "deformed" set. This mode of OEH is often termed "static". Customarily, OEH techniques are utilized with speckle interferometers (Yokum et al., 2001), but for this system it is used with the

Michelson and Mirau configurations.

The first set recorded by the camera, $I_n(u,v)$, is usually of the object in its undeformed, unstressed state and is of the form (Pryputniewicz, 2003b)

$$I_n(u,v) = I_o(u,v) + I_r(u,v) + 2\,A_o(u,v)\,A_r(u,v)\cos[\Delta\phi(u,v) + \theta_n] \quad , \tag{19}$$

where I_o and I_r are the object and reference beam intensities as a function of pixel coordinates (u,v), which are the square of the object and reference beam amplitudes A_o and A_r, respectively. The finite known phase step increments are θ_n. The second set of phase stepped images, $I'_n(u,v)$, is of the object after a some change Ω has occurred:

$$\begin{aligned} I'_n(u,v) &= I'_o(u,v) + I'_r(u,v) \\ &+ 2\,A'_o(u,v)\,A'_r(u,v)\cos[\Delta\phi(u,v) + \Omega(u,v) + \theta_n] \quad . \end{aligned} \tag{20}$$

Using a four phase step method, a series of equations are generated. Using a phase step of $\pi/2$ and leaving out the pixel coordinates (u,v) for clarity, two sets of four simultaneous equations are generated which are (Pryputniewicz and Stetson, 1990)

$$I_1 = I_o + I_r + 2\,A_o\,A_r\cos(\Delta\phi + 0) \quad , \tag{21}$$

$$I_2 = I_o + I_r + 2\,A_o\,A_r\cos(\Delta\phi + \frac{\pi}{2}) \quad , \tag{22}$$

$$I_3 = I_o + I_r + 2\,A_o\,A_r\cos(\Delta\phi + \pi) \quad , \tag{23}$$

$$I_4 = I_o + I_r + 2\,A_o\,A_r\cos(\Delta\phi + \frac{3\pi}{2}) \quad , \tag{24}$$

and

$$I'_1 = I'_o + I'_r + 2\,A'_o\,A'_r\cos(\Delta\phi + \Omega + 0) \quad , \tag{25}$$

$$I'_2 = I'_o + I'_r + 2\,A'_o\,A'_r\cos(\Delta\phi + \Omega + \frac{\pi}{2}) \quad , \tag{26}$$

$$I'_3 = I'_o + I'_r + 2\,A'_o\,A'_r\cos(\Delta\phi + \Omega + \pi) \quad , \tag{27}$$

$$I'_4 = I'_o + I'_r + 2\,A'_o\,A'_r\cos(\Delta\phi + \Omega + \frac{3\pi}{2}) \quad . \tag{28}$$

Evaluating Eqs 21 to 28 yields

$$I_1 = I_o + I_r + 2\,A_o\,A_r \cos(\Delta\phi) \quad , \tag{29}$$

$$I_2 = I_o + I_r + 2\,A_o\,A_r \sin(\Delta\phi) \quad , \tag{30}$$

$$I_3 = I_o + I_r - 2\,A_o\,A_r \cos(\Delta\phi) \quad , \tag{31}$$

$$I_4 = I_o + I_r - 2\,A_o\,A_r \sin(\Delta\phi) \quad , \tag{32}$$

and

$$I'_1 = I'_o + I'_r + 2\,A'_o\,A'_r \cos(\Delta\phi + \Omega) \quad , \tag{33}$$

$$I'_2 = I'_o + I'_r + 2\,A'_o\,A'_r \sin(\Delta\phi + \Omega) \quad , \tag{34}$$

$$I'_3 = I'_o + I'_r - 2\,A'_o\,A'_r \cos(\Delta\phi + \Omega) \quad , \tag{35}$$

$$I'_4 = I'_o + I'_r - 2\,A'_o\,A'_r \sin(\Delta\phi + \Omega) \quad . \tag{36}$$

Simplification of Eqs 29 to 36 allows the computer to calculate a fringe pattern which is essentially a subtraction of the reference state from the deformed state and display it live as (Pryputniewicz, 2003b)

$$Q_d = \sqrt{D_1^2 + D_2^2} = 8\,A_o\,A_r \cos\left(\frac{\Omega}{2}\right) \quad , \tag{37}$$

where

$$D_1 = (I_1 - I_3) + (I'_1 - I'_3) \quad , \text{ and} \tag{38}$$

$$D_2 = (I_2 - I_4) + (I'_2 - I'_4) \quad . \tag{39}$$

Q_d is called the "live static" display mode of OEH. As fringes indicating deformations are generated live on a video display, this is useful for real-time assessment of how loads affect certain objects. Thermal or mechanical loads are commonly applied to objects when using the OEH technique.

To perform quantitative measurements of the deformations of the object, Ω must be extracted from the system of equations. Up until this point, the OEH technique has

been for the live display mode, Q_d, where acquisition and processing speed is important to ensure a smooth updated live display of the calculated fringe patterns. For the live display, a four phase step algorithm is an acceptable compromise between speed and error tolerance (Pryputniewicz, 2003b). When the OEH technique is switched into the data acquisition mode, speed becomes less important and quality of the results becomes more important. In this case, five phase steps of both the reference and deformed state are utilized. Equation sets 21 to 24 and 25 to 28 both have an additional phase step of $\pi/2$ for the recording of I_5 and I'_5 respectively. Using an adaptation of equations derived in (Kreis, 1996 and Pryputniewicz 2003b), we can define

$$A = 2(I_2 - I_4) \quad , \tag{40}$$

$$B = 2I_3 - I_5 - I_1 \quad , \tag{41}$$

$$C = 2(I'_2 - I'_4) \quad , \tag{42}$$

$$D = 2I'_3 - I'_5 - I'_1 \quad , \tag{43}$$

which are utilized to form what is known as the "sin" and "cosine" images

$$sin = B \cdot C - A \cdot D \quad , \tag{44}$$

$$cosine = B \cdot D + A \cdot C \quad . \tag{45}$$

The deformations, Ω, are then calculated by

$$\Omega = \tan^{-1}\left(\frac{sin}{cosine}\right) \quad , \tag{46}$$

which is wrapped modulo 2π the same as Eq. 17 is. Unwrapping and scaling, as described in Section 4.1, is performed outputting quantitative measurements of the deformations of the object.

4.3. Time-average holography

Up until this point we have been dealing with measurements of static objects. Time-average holography is a mode of OEH that facilitates visualization of the motion of sinusoidally vibrating objects. The time-average mode takes advantage of the fact that objects vibrating sinusoidally spend more time at the physical extremes of the motion where the velocity is at or near zero, than the rest of the motion where the velocity is high. Figure 16 illustrates this point by showing that the object will spend nearly half of the time for the extreme 10 to 15 % of motion (highlighted in blue in a few locations). When averaged over many periods, the optical phase information that comes from these extremes overpowers that of the rest of the motion, resulting in the calculation of a fringe pattern that is indicative of the maximum amplitude of vibration of an object.

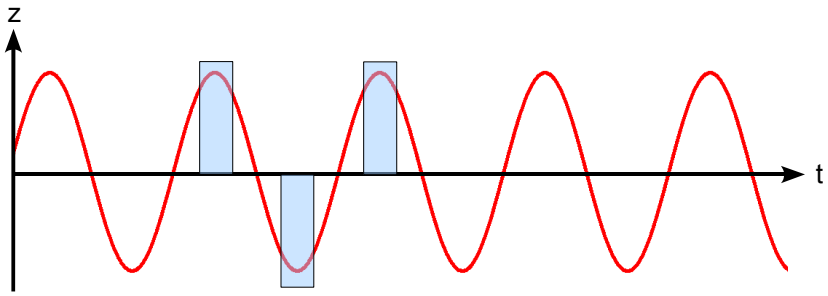

Fig. 16. Motion of an object vibrating harmonically.

For a sinusoidally vibrating object being captured in time-average mode a constant running series of images is acquired. The *n-th* sequential image, I_{tn}, can be represented by (Pryputniewicz, 2003b)

$$I_{tn} = I_{to} + I_r + 2 A_{to} A_r \cos(\Delta\phi_t + \theta_n) M(\Omega_t) \quad , \tag{47}$$

where the pixel coordinates (u,v) have been omitted for clarity as before, I_{to} represents

the time varying object beam intensity, I_r is the reference beam intensity, A_{to} is the time varying amplitude of the object beam, A_r is the amplitude of the reference beam, $\Delta\phi$ is the optical phase information, θ_n represents the *n-th* sequential phase step of $\pi/2$, Ω_t is the time varying fringe locus function, and M is the characteristic function of the modulation that is of the form of a zero-order Bessel function of the first kind (Vest, 1979; Pryputniewicz, 2003b; Nakadate, 1986). To be able to solve Eq. 47, a system of equations is generated similar to that of Eqs 21 to 24 and likewise is evaluated as Eqs 29 to 32 to form

$$I_{t1} = I_{to} + I_r + 2\,A_{to}\,A_r \cos(\Delta\phi_t)\,M(\Omega_t) \quad , \tag{48}$$

$$I_{t2} = I_{to} + I_r + 2\,A_{to}\,A_r \sin(\Delta\phi_t)\,M(\Omega_t) \quad , \tag{49}$$

$$I_{t3} = I_{to} + I_r - 2\,A_{to}\,A_r \cos(\Delta\phi_t)\,M(\Omega_t) \quad , \tag{50}$$

$$I_{t4} = I_{to} + I_r - 2\,A_{to}\,A_r \sin(\Delta\phi_t)\,M(\Omega_t) \quad . \tag{51}$$

This sequence of images is constantly repeated at video rates and is displayed live as Q_{tD} (Pryputniewicz, 2003b)

$$Q_{tD} = \sqrt{(I_{t1} - I_{t3})^2 + (I_{t2} - I_{t4})^2} = 4\,A_o\,A_r\,M(\Omega_t) \quad . \tag{52}$$

Due to the zero-order Bessel function of the first kind of M, the interference pattern generated by Eq. 52 is not sinusoidal in nature, as the fringe patterns of the previous Sections were. Instead, bright fringes form along the nodes on the vibrating object, and the fringes get darker as they move onto areas of greater motion. In Fig. 17, a micro cantilever is fixed on the left side and is vibrating at its second bending mode, note the bright node out on the right side of the beam.

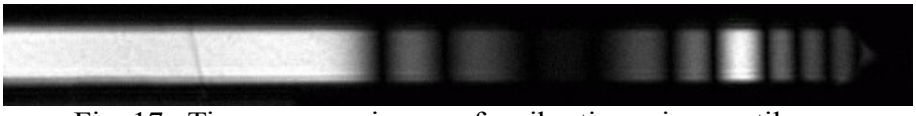

Fig. 17. Time-average image of a vibrating microcantilever.

Quantitative analysis of the time-average image data is possible by modulating the reference wave at the same frequency that the object is being excited (Kreis, 1996; Pryputniewicz, 2003b). This, however, can be challenging when the object is vibrating at very high frequencies. Often times MEMS can be vibrating at hundreds of kHz or even more, and it is difficult to reliably modulate the reference beam at high frequencies. One solution to this problem is to utilize stroboscopic illumination with the OEH mode. In this case, the reference image can be taken while the object is at rest, then the object can be excited and strobed at the excitation frequency – effectively freezing its position in the oscillation – when the deformed state recording is made. As laser diodes can be modulated at several MHz and LEDs can be modulated at tens of kHz or higher, this is an effective method for making quantitative measurements of vibrating objects (Marinis et al., 2005).

4.4. Vertical scanning white light interferometry

Scanning white light interferometry (SWLI) is a form of vertical scanning interferometry (VSI) that utilizes a broadband white light source and a coherence tracking method to measure the shape of objects with larger step heights than PSI can accommodate (Harasaki et al., 2000). In SWLI, fringes are only generated when the path length of both the object and reference beams of the interferometer match to within the coherence length of the light source. The coherence length of a white light source is very short, typically a micrometer or less. It is this limited coherence length that is exploited for SWLI measurements.

To perform a SWLI measurement one arm of the interferometer is scanned at a

constant rate of speed as images are recored at constant intervals. As the path length of the reference beam approaches that of the object beam, the image begins to modulate in the form

$$\omega(\varphi)=\sin(\varphi)\,a\,e^{-\frac{(\varphi-z)^2}{\delta^2}}, \tag{53}$$

where ω is the modulation amplitude as a function of the scan phase, φ, or vertical position. The constants a, z, and δ correspond to amplitude, position, and width of the modulation, respectively. Equation 53 is plotted in Fig. 18 simulating response of a SWLI system with an 8-bit camera. The scan phase as a function of pixel intensity for one pixel of the CMOS array, traced through the scanned image stack, is shown by the dashed line.

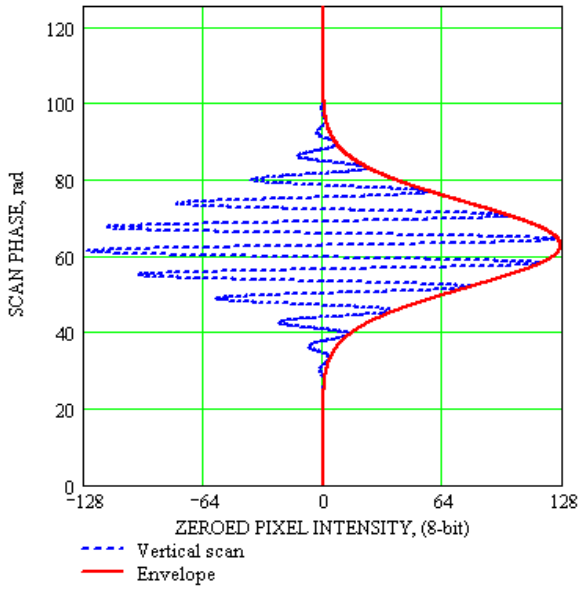

Fig. 18. Simulation of the modulation of one pixel in a VSI measurement.

The solid line in Fig. 18 is the envelope of the signal that is used to find the peak modulation. The scan phase position of the peak modulation directly corresponds to the

location of the surface that this pixel is imaging. Determining the physical location of the peak modulation is a simple conversion from scan phase to distance based on the number of images and scan velocity at which the images were recorded during the SWLI measurement. Each individual pixel will generate a similar curve, but the location of the peak will vary directly with position of the surface of the object being imaged. Because there is no phase unwrapping performed in SWLI as there is in PSI, the shape measurement is not affected by surface steps or discontinuities (PSI is limited to a step < $\lambda/4$). The step height limitation for SWLI is only constrained by the limitations of the scanning hardware.

4.5. Vibrometry

Section 3.3 describes the fundamental configuration of a laser Doppler vibrometer. Unlike the interferometer configurations, this system does not use a camera for acquisition of the data, instead, it used a photo diode. The implication of this is that the results are not full-field-of-view, i.e. the intensity I is not a function of (u,v). The intensity captured by the photo diode is a function of time, not space, and can be represented as

$$I(t) = I_b + I_m \cos(2\pi f_D t + \Delta\phi(t)) \quad , \tag{54}$$

where $I_b(u,v)$ and $I_m(u,v)$ are the background and modulation intensities respectively, $\Delta\phi(t)$ is the time varying interference phase information, and f_D is the Doppler frequency generated by the vibrating object. The equation for the Doppler frequency is

$$f_D = \frac{2v}{\lambda} \quad , \tag{55}$$

where λ is the wavelength of the laser, in this case 633 nm, and v is the velocity of the vibrating object which is to be solved for.

As the situation with Eq. 10, in Eq. 55 are more variables than can be solved for with a single equation. To generate a solvable system of equations a frequency shift is added into one arm of the interferometer with the use of an acousto-optic modulator, sometimes called a Bragg cell. This frequency shift, f_B, is 40 MHz or higher (Polytec, 2006), and affects Eq. 54 as

$$I(t) = I_b + I_m \cos(2\pi(f_B - f_D)t + \Delta\phi(t)) \quad . \tag{56}$$

The Doppler frequency, and thus the object velocity, is now carried in the ~40 MHz signal and can be decoded using temporal heterodyne techniques as described by Dändliker and Thalmann (1985), and Pryputniewicz (1985, 1986).

5. THE INTERFEROMETRIC MICROSCOPE

As the development of new MEMS has increased dramatically over the last two decades, so did the need to characterize their shape and mechanical response to various loadings and operating conditions. To ensure the MEMS meet fabrication tolerances and function within design specifications, optoelectronic laser interferometric microscope (OELIM) methodology has been developed at WPI and is continually being optimized to keep abreast of the state-of-the-art technology.

5.1. Legacy interferometric microscopes of CHSLT

The development of interferometric microscopy has been an ongoing development at WPI for nearly the past 30 years. Although the development has been an evolutionary process with many changes, there were three significant improvements that warrant designation. As these systems were never officially named at CHSLT, I will designate them simply as Mark 1, Mark 2, and Mark 3. The following subsections will serve as a brief description of each.

5.1.1. The Mark 1 interferometric microscope

In the Mark 1 configuration shown in Fig. 19, a beam of collimated coherent light is brought into the system and is directed into a spatial filter assembly consisting of a microscope objective and a spatial filter. The filtered and expanding beam is then collimated by a lens and redirected by the directional beam splitter (DBS) through the microscope objective (MO) to illuminate the object. The proximal beam splitter (PBS) is placed over the object and inclined by a small angle with respect to the object.

Interference occurs between the bottom surface of the PBS and the top surface of the MEMS. The interference pattern is then transmitted back through MO, DBS, and the relay lens to be imaged by the CCD camera (Brown, 1999).

In the configuration of Fig. 19, the wavefronts are planar and parallel interference fringes result when the PBS is introduced into the path. As these fringes are carriers of the MEMS shape information rather than a pure representation, visual inspection with this technique before quantitative analysis can be challenging. Also, phase stepping for this configuration is performed by shifting the MEMS rather than the PBS due to the space constraints of this microscope chassis. Detailed description of the technique, system setup, analysis, and applications is given by Brown (1999), or Brown and Pryputniewicz (2000).

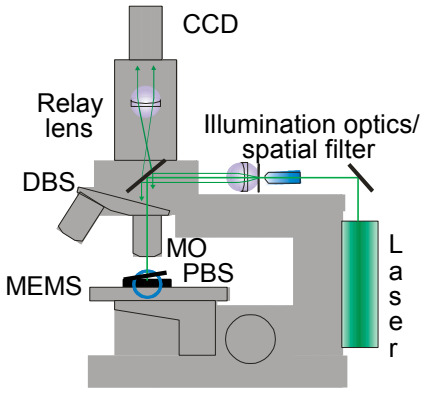

Fig. 19. The Mark 1 interferometric microscope.

5.1.2. The Mark 2 interferometric microscope

The Mark 1 configuration was modified to allow for the shape and deformation of MEMS to be more readily measured. This Mark 2 interferometric microscope, Fig. 20, is built using many of the same components as the Mark 1, however the optical interference is by a miniature Michelson interferometer. The purchase of super long working distance

microscope objectives allows the use of a cube beam splitter (BS) instead of the thin PBS of the Mark 1. The flat reference mirror (REF) has phase stepping capabilities instead of phase stepping the object as in the Mark 1. Moving the phase stepping to the reference allowed for new loading devices to be used such as a heater block to thermally cycle the MEMS. In the Mark 2 configuration the fringes are directly related to the MEMS shape or deformation. Analysis of these interference patterns are performed as described in Sections 4.1 and 4.2.

Although the Mark 2 design provided many improvements over the original, it had several short comings. First, the working distance between the MEMS and the BS was only a few millimeters, limiting the size of packages and loading devices that could be utilized. Secondly, due to the limited space on the microscope platform and the miniature size of the interferometric components, proper alignment was a challenge.

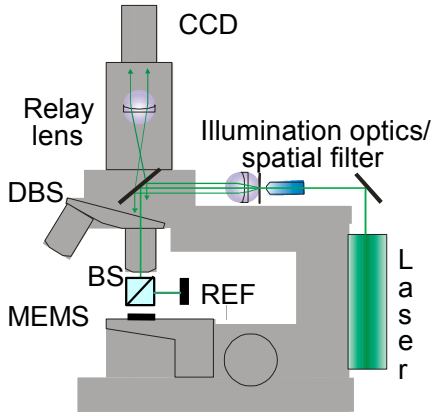

Fig. 20. The Mark 2 interferometric microscope.

5.1.3. The Mark 3 interferometric microscope

In order to remedy these problems, the Mark 3 interferometric microscope was developed, Fig. 3. It was based on a newer, commercially available microscope chassis, which offers up to 50 mm of vertical working space with less than 20 mm of vertical

travel. Additionally, the interferometer itself was now built into the microscope objectives. This created more working distance, and allowed the MEMS to be placed on a platform that has tilting abilities, allowing for easier interferometric alignment.

With the Mark 3, the addition of high resolution digital CCD camera dramatically increased quality of the measurements in terms of spatial resolution. The previous generations systems operated with analog CCDs that had approximately ¼ million pixels. Using the digital CCD that contained 3 million pixels, the Mark 3 provided for an increase in spatial resolution of 12 times compared to that of the Mark 1 and Mark 2. However, this 3 mega pixel camera was a digital photography camera, not a video camera so live processing modes such as OEH and time-average were not possible. For these modes, the old analog cameras had to be used.

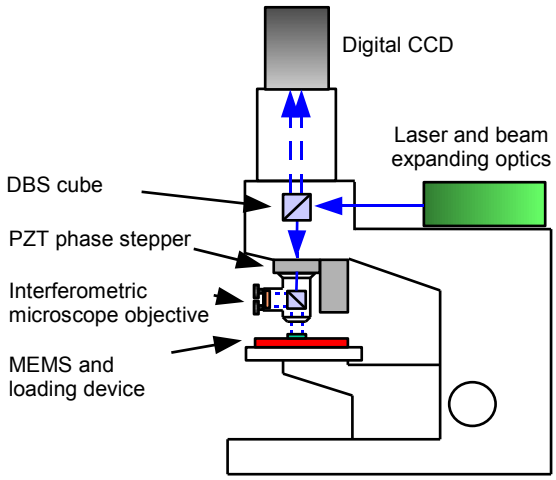

Fig. 21. The Mark 3 interferometric microscope.

The Mark 3 interferometer was the first interferometer at CHSLT to implement the use of a LED instead of a laser in certain situations. This improved image quality greatly, but did not increase the measurement range, resolution, or accuracy. As with the Mark 1 and Mark 2, the Mark 3 was only a phase stepping interferometer. This technique, as

described in Chapter 4, only allows surfaces with step heights less than approximately 150 nm to be measured. As MEMS are typically fabricated out of multiple layers several micrometers thick, this is a major limitation.

Also, the Mark 3 version of the interferometric microscope was developed specifically to work with low profile setups, i.e., setups not exceeding 50 mm in height. Often, however, experiments require the use of large or multiple PZT drives, heating plates, or other loading devices that simply can not fit within the working space of the Mark 3. Overall it was the limitations of these systems that was the deciding factor to pursue a new interferometric measurement system.

5.2. Commercially available interferometric microscopes

Purchasing a complete system from a commercial manufacturer of interferometric instruments was briefly considered. Companies such as Zygo, Veeco, and Wyko (Veeco and Wyko recently merged) have been producing interferometric systems for years. They offer complete packages with very nicely integrated hardware, software, and controls, for a very expensive price that is measured in hundreds of thousands of dollars, depending upon the configuration.

Currently, the top of the line system for the measurement of MEMS is Zygo's "New View 6000" series of microscopes. They are scanning white light interferometers with phase shifting capabilities. The general system specifications and capabilities are listed in Table 2. While the total package that Zygo makes is very well engineered and is complete, there were several major drawbacks. First, the maximum object height is limited to 3.5 inches, which would not allow us to utilize several of our PZT loading

devices for vibration excitation. Second, measurement of samples in an environmental chamber is not easily performed because the system is based solely on closed microscope objectives (as were the Mark 1 – Mark 3). Lastly, the standard imaging camera only has a resolution of 640 x 480 pixels (with an optional camera having 992 x 992 pixels). From our previous testing, many MEMS have such intricate and narrow features, they can only be resolved with multi-mega pixel cameras.

Table 2. Capabilities of the Zygo *New View 6000* interferometric microscope.

Measurement technique	SWLI and PSI
Scanner	Closed loop PZT
Magnification	1x to 100x
Light source	LED
Camera (standard)	Digital CDD, 640 x 480
Vertical scan range (standard)	150 μm
Sample stage	X-Y: ±2", 2 axes of tilt ±6°
Maximum sample height	3.5"
Measurement repeatability	0.1 nm
Total system weight	950 lbs.

5.3. Preliminary design of the Mark 4 interferometer

To continue improvements in the Mark series, the Mark 4 interferometric microscope has been developed with several significant improvements. Shown in Fig. 22 is a preliminary system design that is a departure from the previous Mark interferometers in that it is not based upon a commercially available microscope chassis. Instead, a massive piece of granite, cut in an "L" shape, is used as the microscope chassis. It sits on a table that is isolated from building vibrations via pneumatic isolation legs. A chamber was designed to be constructed around the microscope to reduce air currents and

acoustical vibrations. Some of the imaging optics are the same as those utilized in the Mark 3 system and are attached to a *Z*-axis stage that provides effective working space of up to 60 cm. An *X*-*Y* axis of the 4 dof platform stage allows for in-plane travel of 4 in., in either direction. A 10 bit digital CMOS camera with 6.6 mega pixel resolution is able to acquire full resolution measurements at 7 Hz providing for near real-time measurements.

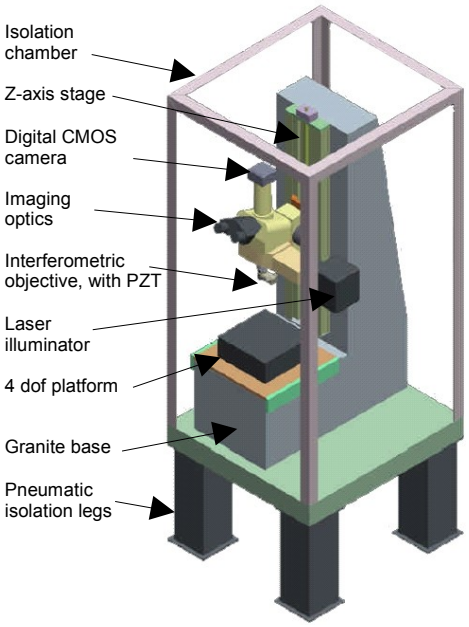

Fig. 22. Solid model of a preliminary design of the Mark 4.

Granite was chosen as the structural material for the chassis due to its availability, ability to be precision ground, damping characteristics compared to metals, and its overall mass. The stages provide increased positioning range in all directions, and the digital CMOS camera provides an improved resolution, frame rate, and bit depth compared to the Mark 3 system. These improvements increase the overall versatility of the interferometric microscope.

6. THE MARK 4 MODULAR INTERFEROMETRIC MICROSCOPE

As the limitations of the Mark 3 interferometer became more and more obvious over time, the demand at CHSLT for a better system increased dramatically. For example, devices to thermally load MEMS, vibrationally excite larger MEMS packages, and subject MEMS to vacuum environments, physically did not fit in the Mark 3. With these limitations in mind, we determined some design parameters for a new interferometric microscopy system that would alleviate these problems, summarized in Table 3.

Table 3. Design goals for the Mark 4 interferometric microscope.

Out of plane resolution	1 nm
In plane resolution	better than 1% of the lateral viewing area
Lateral viewing area	20 × 20 μm to 20 × 20 mm*
Lateral sample translation	at least 2 inches in X and Y*
Vertical measurement head translation	at least 200 mm*
Maximum step height measurement	at least 50 μm*
Thermal loading range	-30°C to 100°C*
Vibrational loading range	1,000 Hz to 1.0 MHz (reliable)*
Vacuum or dry gas environment?	Yes*

* Indicates a new ability or a significant improvement over the Mark 3 interferometer.

After approximately three years of design, fabrication, purchasing, assembling, and testing, the modular interferometric microscopy system for the characterization of MEMS was completed. The system, shown schematically in Fig. 23, (and enlarged in APPENDIX A), consists of three major subsystems. The first subsystem is the operator interface table, consisting of components 1 through 5. This is where the operator spends most of the time acquiring and processing data. The second subsystem, components 6 through 13, is the measurement station where the MEMS are loaded and measured. The third subsystem, components 14 through 21, is the instrumentation mounted in a rack.

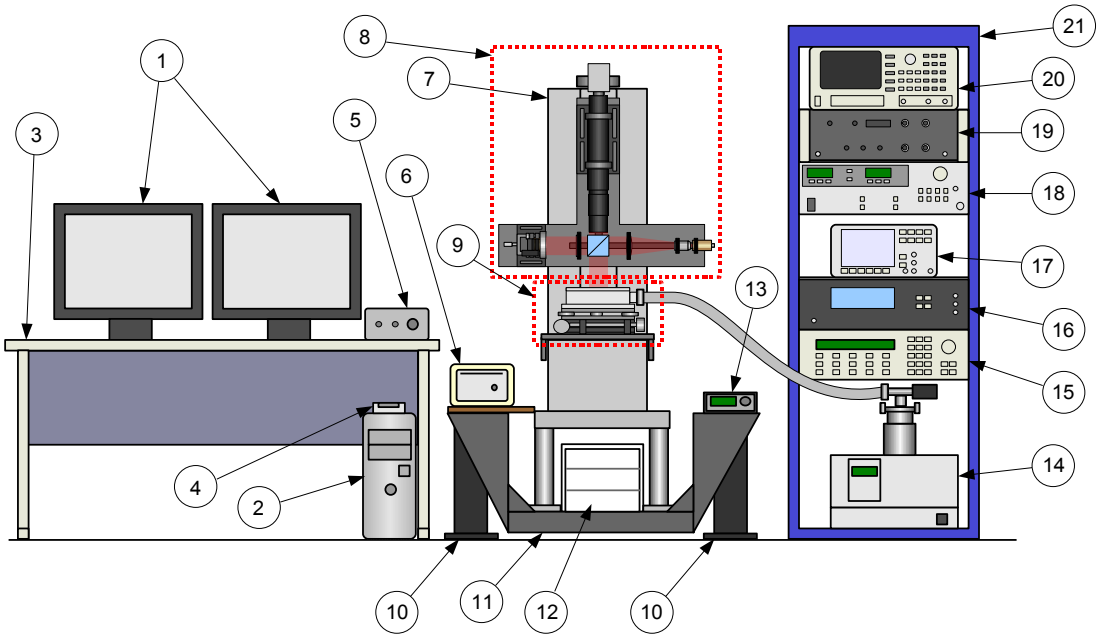

Fig. 23. Schematic of the Mark 4 modular interferometric microscopy system.

Table 4. Component list of the Mark 4 modular interferometric microscopy system.

Component #	Description
1	dual LCD monitors
2	host computer
3	desk
4	National Instruments I/O terminal
5	PZT controller/amplifier
6	vibrometer interferometer unit
7	granite microscope chassis
8	interferometer module, (low magnification module shown)
9	MEMS loading module, (environmental chamber module shown)
10	vibration isolator legs
11	cradle
12	storage bin for system modules, tools, and components
13	light source controller
14	turbomolecular vacuum pump system
15	signal generator
16	vibrometer controller
17	digital oscilloscope
18	TEC and LED controller
19	strobe pulse generator
20	spectrum analyzer
21	instrumentation rack

The system is currently located in HL-145 in the CHSLT labs of the Mechanical Engineering building at WPI. This laboratory, shown in Fig.24, includes all of the necessary feeds for the modular interferometric microscopy system: compressed air, electrical hookups, and chilled glycol. The room ventilation system is a "laminar flow" system designed to reduce air currents, and is tightly controlled for temperature and humidity. Figure 24 shows the system set up in the laboratory with the low magnification interferometer module and environment loading chamber attached.

This Chapter will serve as a description of each subsystem, modules, and components, that together make up a complete interferometric system for quantitative characterization of MEMS. Frequent references to the Appendices may be made for system schematics and mechanical drawings that do not fit within the text.

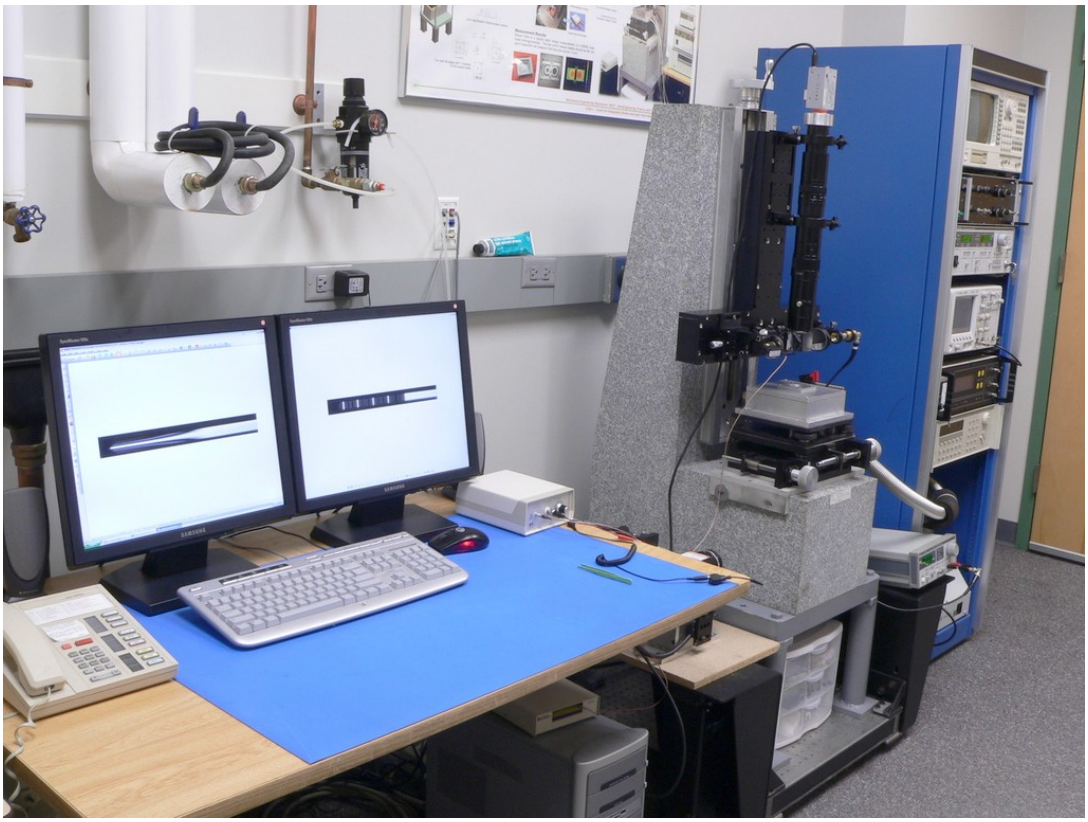

Fig. 24. Photograph of the modular interferometric microscopy system.

6.1. Operator interface subsystem

The operator interface subsystem, highlighted in Fig. 25, is where the operator will sit for majority of the experiment and analysis, once the system is set up and aligned. This subsystem consists of two 19" LCD monitors (1) connected to a currently top-of-the-line PC (2) for control and processing. Having dual monitors allows the operator to have one screen displaying full screen live video while the other screen is available for controls and system operations. The PC features a dual core AMD processor, 2 GB of system memory, Firewire interface for the interferometer digital cameras, GPIB interface for communications to older instruments, and a NI DAQ system (4) for control of the 0-100 V phase stepping PZT amplifier (5). The desk (3), is a standard bench-type desk with an ESD mat complete with an operator grounding strap for the safe handing of statically sensitive MEMS devices. The operator interface subsystem is by far the most simple of the subsystems, yet it allocated the most floor space to ensure proper ergonomics for the operator.

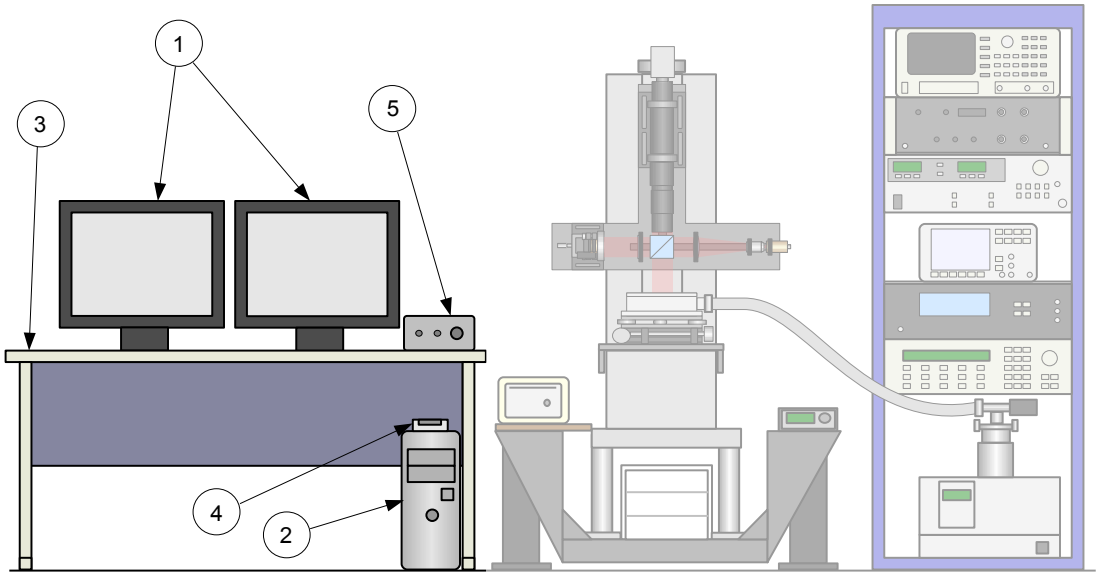

Fig. 25. The operator interface subsystem.

6.2. The measurement station subsystem

The measurement station subsystem is the location where all of the measurements take place, Fig. 26 and Fig. 27. The measurement station, weighing over 1,000 lbs, is supported by a low center of gravity cradle (11) that is pneumatically supported by four vibration isolation legs (10). A three drawer storage bin (12), situated underneath the granite microscope chassis (7), allows for easy access to storage of electrical, mechanical, and optical loading devices, measurement modules, tools, fasteners, and general parts for the system. The interchangeable interferometer modules (8) (low magnification interferometer module shown), are the "heart" of the system. These modules allow full field of view measurements to be performed on MEMS and devices ranging in size from a few micrometers to 20 mm. When the vibrometer interferometer head (not shown) is connected to the vibrometer interferometer (6) point wise temporal vibration measurements can be made with sub-nanometer resolution at frequencies up to 2.0 MHz.

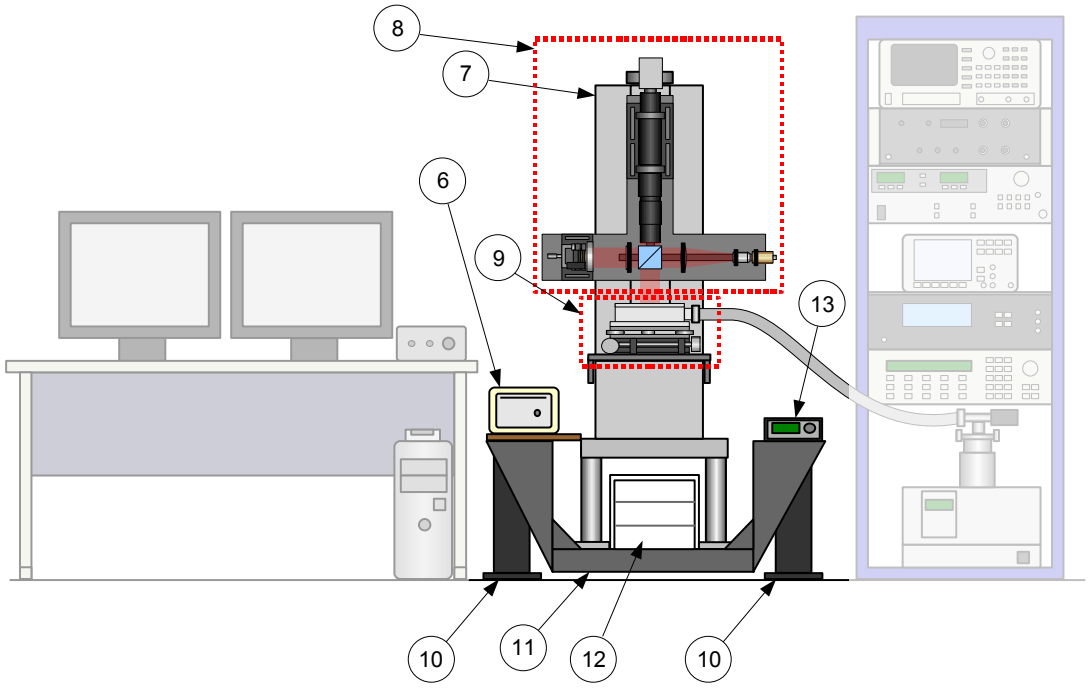

Fig. 26. The measurement station subsystem.

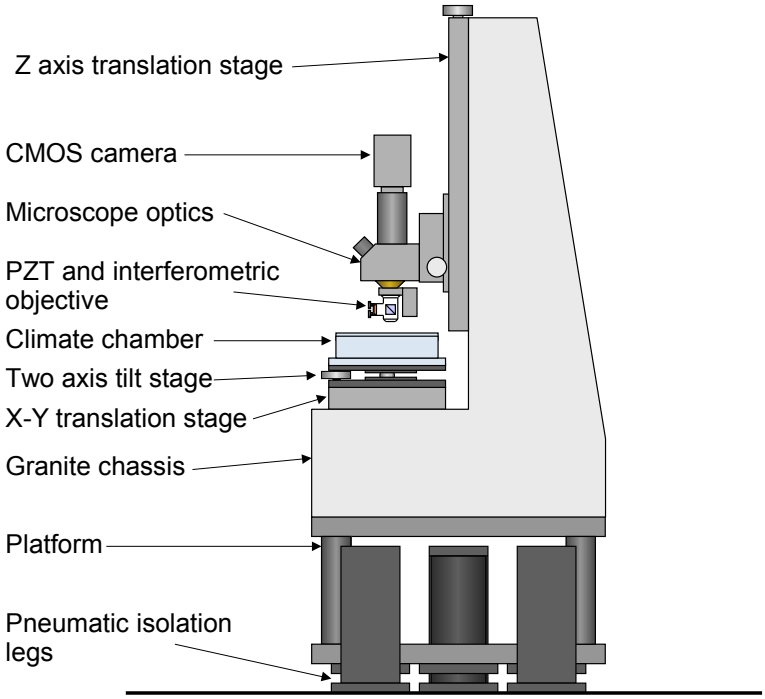

Fig. 27. Profile view of a configuration of the measurement station subsystem.

6.2.1. Vibration isolation and the microscope chassis

The repeatability of most interferometers is greatly affected by the stability of the system. Any vibrations that are "felt" by the interferometer or sample will cause fringe pattern jitter that adversely affects measurements. Initially, the measurement station subsystem was supported by a set of three large pneumatic isolation legs that originally came from a decommissioned scanning electron microscope (SEM). These legs came with three supports for a cradle system that would allow the base structure to be merely one inch above the floor. The cradle platform was cut from an extra piece of two inch thick optical breadboard measuring approximately two feet by three feet. A consultation with engineers of the breadboard manufacturer in California, Newport, Inc., confirmed that this component can withstand the >1,000 lb. load imposed by the measurement station subsystem.

The cradle was assembled on the three pneumatic legs, and the granite microscope chassis and its solid steel support structure were lifted onto the cradle. When the system was pressurized, it became evident that these legs might pose a problem: because they were designed to support an SEM that was much larger, they had a long travel of two inches that caused the granite block to sway back and forth nearly six inches at the top. To prevent this rocking motion, restricter plates were fabricated and placed on the leveling valves, reducing the travel to approximately ½ inch. At this point, the legs appeared to be functioning properly for the interferometric measurement station. When an interferometer was assembled and mounted on the microscope, jitter was noticed in the fringe patterns. The legs were not performing as well as was hoped. As the SEM that the legs were originally designed to support was possibly at least five times more massive, these legs could not provide sufficient damping for the new, much lighter station.

Replacement legs that were better suited for this application were purchased from Newport, Inc. These legs, a set of four IMS-325A would provide better than 98% isolation at frequencies greater than 10 Hz, (most building vibrations occur at frequencies higher than 30 Hz). The IMS-325A vertical damping capabilities, for loads up 1,300 lbs, are shown in Fig. 28 (Newport, 2006a). This isolation system works well but required fabrication of another cradle support as this system requires four legs instead of three.

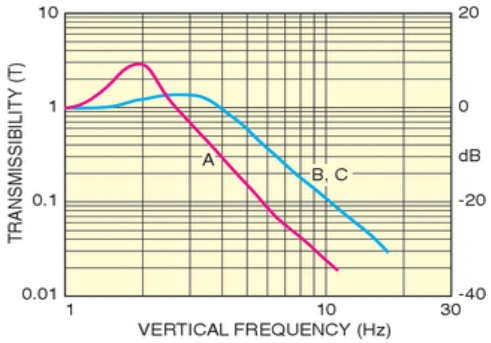

Fig. 28. I-325A pneumatic isolator frequency transmissibility, “A”.

The granite microscope chassis (aka “rock”), Fig. 29, was a donation by a long term sponsor and is the foundation (and motivation) for this Thesis. The “rock” arrived at CHSLT around 2001, and not much was initially done with it. As the challenges with the Mark 3 interferometric microscope arose, the idea to make use of the “rock” for a microscope chassis seemed like a good idea. However, it posed a challenge as all of our previous microscopes were based on commercially available microscope chassis and were far less massive. At that point I decided this would be an excellent project for this Thesis.

The granite structure was originally fabricated as a microscope chassis with holes running up the spine allowing for mounting of a rail and optics. The rail was removed and a 750 mm manual stage was modified and attached. This is a manual lead-screw driven stage that has a pitch of 1 mm per revolution. A large custom handle was fabricated and mounted on the top to allow the stage to be easily positioned. This stage has a travel range of 600 mm, far greater than the 20 mm allowed by the Mark 3.

This granite “L-shaped” block has a weight of approximately 700 lbs. Granite is an ideal structural material for optical systems (in fact, some optical tables are made of granite slabs and were widely used to support apparatus in early stages of development of optical holographic interferometry), hence its original application. Granite has better vibration damping characteristics than common metals and less than half the thermal expansion when compared with 300 series stainless steel and less than 1/3 the thermal expansion in comparison with 6061 aluminum (Newport, 2006b). The granite block was donated with the solid steel support structure that weighs about 300 lbs. When assembled and seated in the cradle as shown in Fig. 29, the working surface is an ergonomic height.

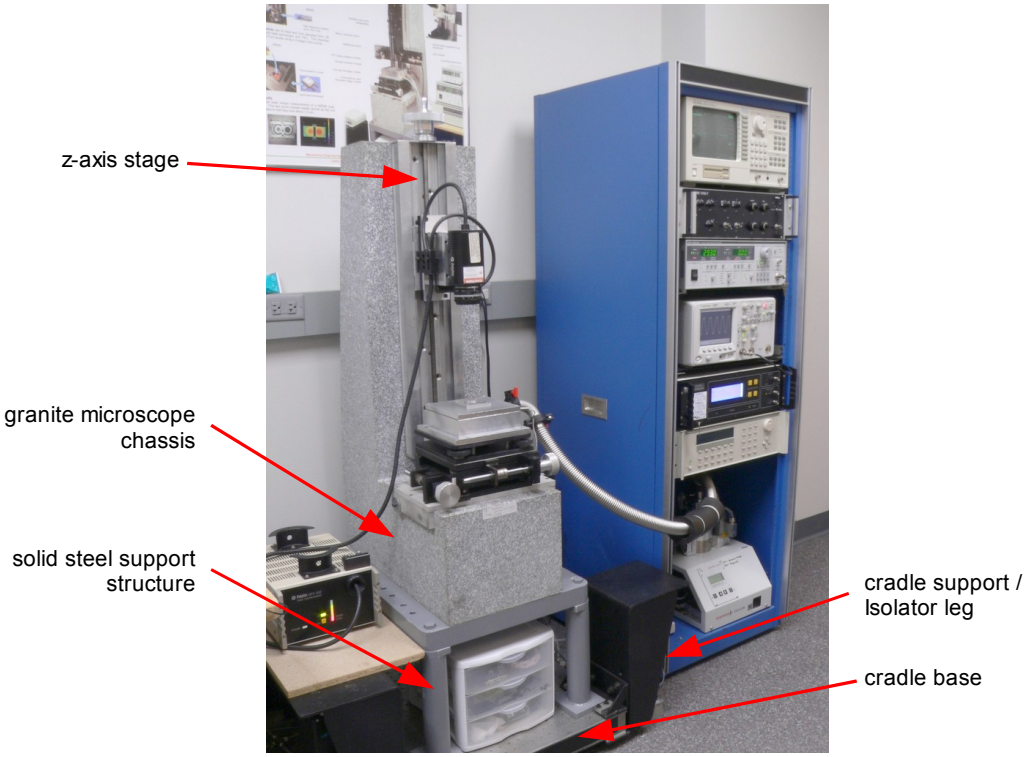

Fig. 29. Photograph of the vibration isolation system and microscope chassis.

6.2.2. High magnification interferometer module

The high magnification interferometer module allows for sub-micron lateral features to be imaged and measured. This system is based on commercially available Nikon microscope optics, shown in Fig. 30 and Appendix B, Fig. B.1. The module is based on a duplicate set of optics of those utilized in the Mark 3. This optic system consists of a halogen illuminator (Nikon *Universal Epi-illuminator10*) with two apertures and options for bandpass optical filters to filter the light to a nearly monochromatic state. Typically, 10 to 20 nm bandpass filters are used in the red 630 nm range. There is an eyepiece (Nikon *TI/ER trinocular observation tube*) that allows the operator to visually inspect the sample and align the interferometer; sometimes more easily accomplished with the eyepiece than with the camera. This microscope head is mounted on a Nikon

modular focusing unit that allows both coarse and fine focus which, in turn, is mounted on the *z*-axis stage allowing a very large range of motion to accommodate nearly any size MEMS loading device.

The microscope objectives, Fig. 31, are limited-production-run Nikon series of interferometric objectives consisting of a 2.5x magnification Michelson objective, a 5x magnification Michelson objective, and 10x, 20x, and 50x magnifications Mirau objectives. The specifications of these objectives are summarized in Table 5.

Table 5. Nikon specifications for the interferometric microscope objectives.

	2.5x	**5x**	**10x**	**20x**	**50x**
interferometer type	Michelson	Michelson	Mirau	Mirau	Mirau
numerical aperture	0.075	0.13	0.3	0.4	0.55
working distance, mm	10.3	9.3	7.4	4.7	3.4
focal length, mm	80	40	19.8	9.96	4.0
depth of focus, μm	48.5	16.2	3.03	1.71	0.90

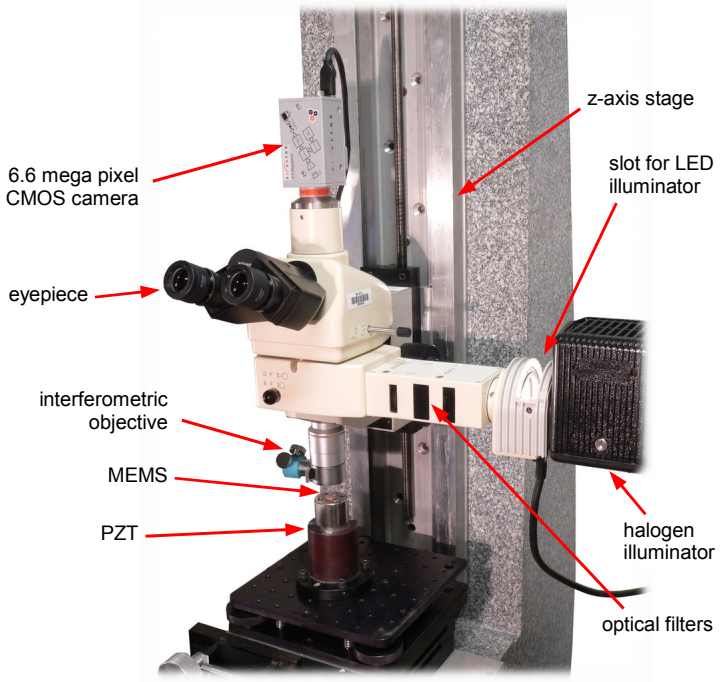

Fig. 30. The high magnification interferometer module.

Fig. 31. Nikon interferometric microscope objectives: 2.5x, 5x, 10x, 20x, 50x.

When a packaged MEMS is hermetically sealed with a glass lid, such as the device in Fig. 1a, and placed under the interferometer, the path length difference caused by the index of refraction of the glass lid must be taken into consideration (Marinis et al., 2005). To ensure the path length of both the object beam and the reference beam match, a compensation window corresponding to that of the packaged device is inserted into the reference arm of the Michelson interferometric objectives, Fig. 32. Unfortunately, there is no such ability for the Mirau objectives so measuring devices through a window with a low coherence light source (filtered white light, or LED) is not possible.

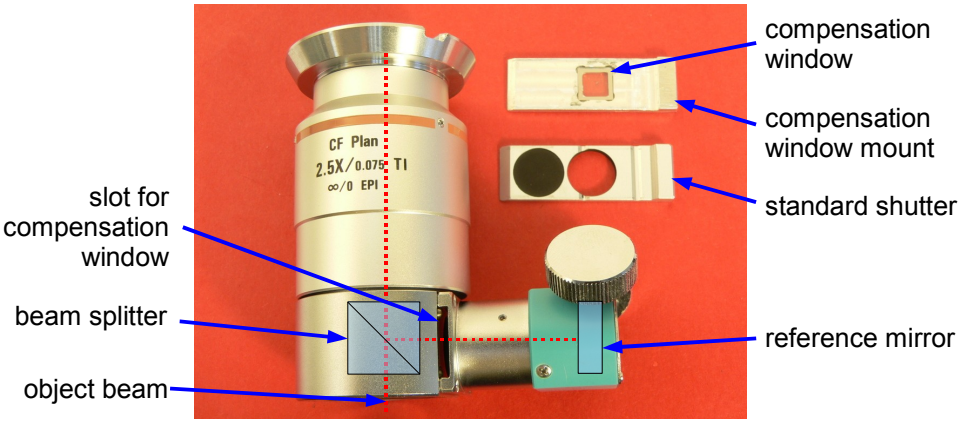

Fig. 32. 2.5x objective with a compensation window and interferometer overlay.

The standard illuminator source for the microscope is a white light halogen source. An optional LED module for the high magnification interferometer, Fig. 33, can be installed in the LED illuminator slot, Fig. 30. The LED allows for dynamic measurements to be performed when strobing of the light source is required. This LED module is fabricated out of Plexiglas so as to not damage the microscope illuminator, has a serial connection for power control, and utilizes a Opto-Diode *OD620-L* LED with a specified peak wavelength of 620 nm, FWHM of 25 nm, 50 mW optical power output, with a rise and fall time of 100 ns for strobing.

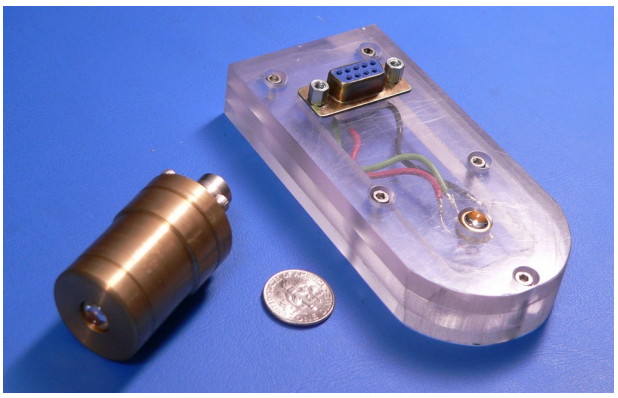

Fig. 33. LED modules for the high and low magnification interferometers.

There are two possible cameras that can be utilized with the high magnification interferometer module: a 1.3 mega pixel camera and a 6.6 mega pixel camera (shown in Fig. 30), although their appearance is nearly identical, both manufactured by PixeLink. The specifications of these cameras are listed in Table 6. Both cameras can be sub sampled so as to increase the frame rate at a lower resolution. In general, for dynamic experiments, the 1.3 mega pixel camera works better than the 6.6 mega pixel one because it is faster. The 6.6 mega pixel camera is utilized for measuring static shape of MEMS that have many intricate features that require high pixel resolution to image.

Table 6. Properties of the PixeLink digital cameras for the interferometer.

	1.3 mega pixel	6.6 mega pixel
model number	PL-741	PL-781
sensor	CMOS	CMOS
resolution	1280 × 1024	2208 × 3000
pixel pitch	6.7 μm	3.5 μm
bit depth	8 or 10	8 or 10
frame rate at full res.	27 Hz	5 Hz
interface	Firewire	Firewire

Phase stepping in the high magnification interferometer module is performed by modulating the object beam as the reference beams are completely enclosed in the interferometric microscope objectives. A PZT can either be placed under the sample, as in Fig. 30, essentially shifting the object upward toward the interferometer, or a PZT can be attached above the interferometric objective, Fig. 34, which steps the objective downward toward the sample. Both are acceptable solutions as they accomplish the same thing: modulating the path length of the object beam.

The high magnification interferometer module is capable of performing full-field-of-view, static shape, static deformation, vibrational, and vertical scanning measurements of MEMS. This interferometer module is capable of measuring MEMS subjected to any of the loading devices available, except those that utilize the environmental chamber (the current chamber window is too thick to compensate for in the interferometric objective).

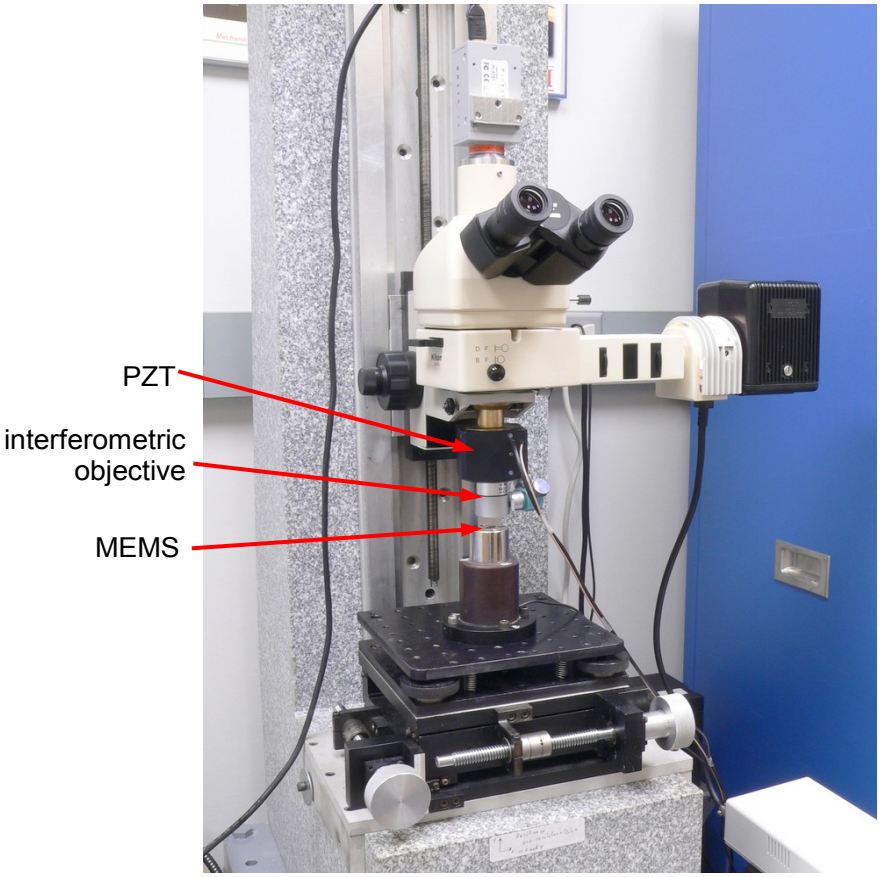

Fig. 34. PZT phase stepping the microscope objective.

6.2.3. Low magnification interferometer

A low magnification interferometer module has been developed to measure objects that are too large for the high magnification interferometer module, or objects that need to be placed a distance further away from the objective than the working distance would allow, such as objects placed in the environmental chamber module. The low magnification interferometer module, shown detached from the system for clarity in Fig. 35, is a phase stepping Michelson interferometer.

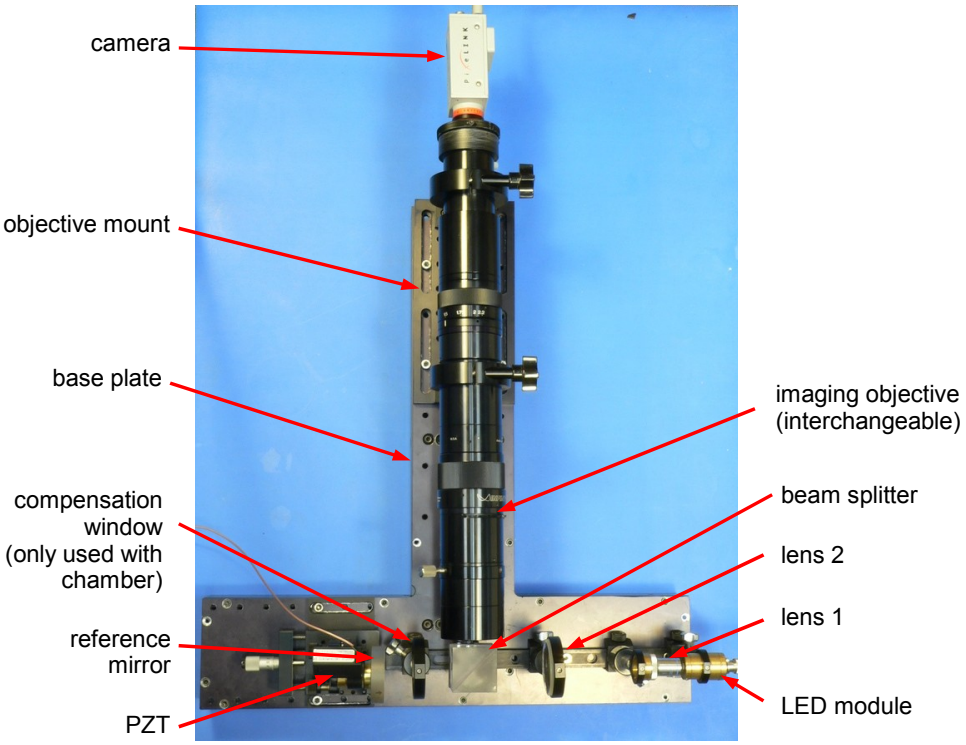

Fig. 35. The low magnification interferometer module, (detached from the system).

The beam splitter is a 40 mm cube and the optics are 2 in. diameter, allowing for objects of 20 mm square to be easily imaged. Alternative views of this module are shown in Appendix B (Figs B.2 and B.3). The base plate, objective mount, PZT mount, and base plate stiffening structure (not shown) all were designed and fabricated to maximize system performance and versatility, mechanical drawings are shown in Appendix C. The base plate has a pattern of 1/4-20 threaded holes to allow easy future upgrades, and sliding objective mount plate has a similar pattern for the same reason. The PZT mount can be slid fore and back, up to 6 inches, to match the reference path length to that of the object beam based on the imaging objective being utilized. All of the optical components are mounted on a rail to ensure they are linearly aligned. Each component has its own rail carrier that allows it to be individually aligned. Once the interferometric components are

aligned, a process that takes an experienced operator less than 30 minutes, they can be locked down with thumb screws or set screws to ensure the system remains aligned even after removing it from the measurement station. The PZT and reference mirror are together mounted on a two axis tilt stage, (better visible in Appendix B, Fig. B.3,) to allow for orthogonal alignment of the reference beam to the object beam when a sample is placed in the measurement station.

The PZT shown in the low magnification interferometer module is one of two PZTs that can be utilized for both phase stepping and/or vertical scanning. These PZTs are manufactured by Physik Instrumente to have a very long scan range. One PZT has an open loop scan range of 100 μm while the other PZT has a closed loop scan range of 250 μm; both have a resolution of 1 nm. Both are intended for microscope objective positioning, thus are well suited for the application of phase stepping and scanning microscope components.

Like the high magnification interferometer module, the low magnification interferometer module has an assortment of objectives that offer varying degrees of magnification. Shown in Fig. 36 are five of the most commonly utilized objectives on this interferometer module. The specifications of these objectives are listed in Table 7. These objective provide an overall field-of-view range of 1.6 to approximately 35 mm in the low magnification interferometer module.

Fig. 36. Standard assortment of imaging objectives for the low mag. interferometer.

Table 7. Specifications of the imaging objectives for the low mag. interferometer.

	A	B	C	D	E
manufacturer	Infinity	Edmund Opt.	Edmund Opt.	Edmund Opt.	Edmund Opt.
model number	K2+CF-3	T52-271	T52-274	T55-350	T55-349
magnification	4.0 - 5.8x	0 - 1.0x	0.066 - 1.0x	1.0x	0.25x
field-of-view, mm	1.1 - 1.6	6.4 - 16	6.4 - 97	8.8	35.2
working distance	90 - 125 mm	5.25 - 11.25”	140 - 280 mm	98 - 123 mm	132 - 182 mm
telecentric?	no	yes	no	yes	yes
zoom?	yes	no*	yes	no	no

*field of view changes as working distance changes, there is no other control of zoom.

The LED module used in the low magnification interferometer is shown in Fig. 33 and utilizes a Opto-Diode *OD620-L* LED with a specified peak wavelength of 620 nm, full width at half max (FWHM) of 25 nm, 50 mW optical power output, with a rise and fall time of 100 ns for strobing. LED module was fabricated out of brass with a one inch

diameter so it mounts easily in standard optic holders. It has a simple BNC connector for the power signal.

Similar to the high magnification module, the low magnification interferometer module is capable of performing full-field-of-view, static shape, static deformation, vibrational, and vertical scanning measurements of MEMS while they are being subjected to any of the loading devices available. This interferometer module imposes no loading restrictions as the high magnification interferometer did.

6.2.4. Vibrometer

The vibrometer is a commercially available system from Polytec that allows high speed and high resolution point-wise vibrational measurements taken in the time domain, i.e., this system directly measures the velocity (distance over time) of a point on a vibrating object. To mount the vibrometer sensor head module to the vertical stage a mounting device was designed, Fig. 37. This mounting device holds the sensor head and its various fiber optic components, it also aligns the optical axis of the sensor to the center of the sample mounting platform. Mechanical drawings are in Appendix C.

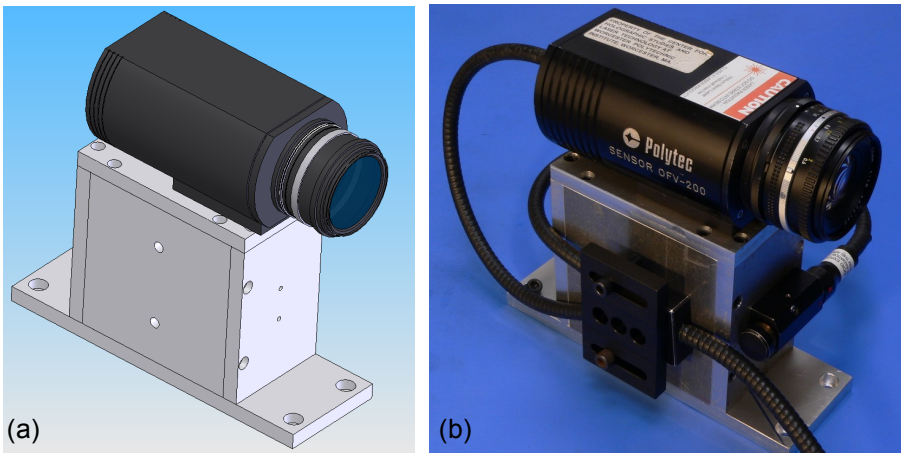

Fig. 37. Vibrometer sensor module. (a) CAD model, (b) assembled unit.

Once mounted to the measurement station subsystem, the vibrometer module consists of three parts, Fig. 38. The vibrometer sensor head, a Polytec *OFV-200*, is connected to the fiber interferometer, *OFV-502*, which is controlled by the vibrometer controller, *OFV 3001*, in the instrumentation subsystem.

The vibrometer module is a relatively simple system to operate. Alignment of the sensor head is little more than focusing a laser spot on a vibrating object (minimum spot size is on the order of 30 μm) and ensuring sufficient signal is being received to make a measurement. The vibrometer controller outputs a modulated voltage corresponding directly to the vibrational velocity or displacement of an object, depending on the mode chosen by the operator. The displacement output voltage is scaled by a factor of 50 nm per volt, and the velocity is scaled by a range of factors selected by the operator: 1.0 mm/s/V to 5000 mm/s/V.

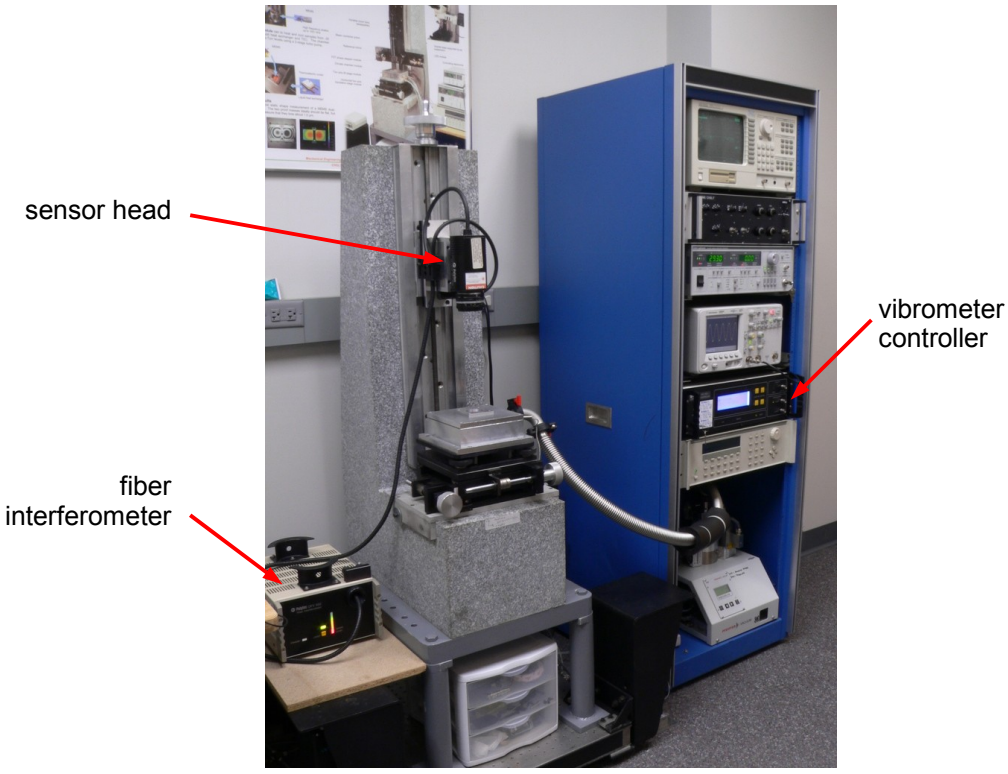

Fig. 38. Vibrometer measurement module.

6.3. MEMS positioning and loading modules

The MEMS loading modules occupy position (9) of the system schematic, Fig. 23. The loading modules are mounted on top of sample positioners and include thermal loading devices, a vacuum system, and vibration excitation PZTs. The loading modules consist of two "large sample" PZTs for vibrational excitation ("large sample" indicates samples with lateral dimensions greater than 5 by 5 mm), a high frequency low voltage PZT (LVPZT) chip, and a low profile PZT array for large samples in the vacuum chamber loading module, a thermoelectric cooler (TEC) and liquid heat exchanger (HEX), and an electrical loading system for powering the MEMS. The loading modules are designed to be interchangeable and as interoperable as possible. The loading module interoperability is summarized in Table 8. Although the table is limited to indicating the interoperability of two modules at once, combinations comprising three or four levels of loading are possible. For example, the vacuum module can be utilized with the TEC module while a MEMS is being powered by the electrical loading system, a combination 3 levels deep.

Table 8. Loading module interoperability chart.
✓ = modules are compatible, o = compatible but not recommended.

	large PZT1	large PZT2	LVPZT chip	low profile PZT	TEC Liq. HEX	vacuum chamber	electrical loading
large PZT1	--		✓				✓
large PZT2		--	✓				✓
LVPZT chip	✓	✓	--	✓	o	✓	✓
low profile PZT			✓	--	o	✓	✓
TEC/Liq. HEX			o	o	--	✓	✓
vacuum chamber			✓	✓	✓	--	✓
electrical loading	✓	✓	✓	✓	✓	✓	--

6.3.1. Positioning subsystem

The positioning subsystem consists of two stages providing four degrees of freedom, Fig 39. The *x*-*y* stage was originally a servo-motor controlled stage, but the motors had seized and the lead screws frozen. After some renovation and some minor modifications, knobs were fabricated to fit the jack shafts, and the stage became useful again. The lead screws on the two translational axes are fairly coarse for this application at 0.1”/rev., but because they are very smooth with no detectable backlash, they work well.

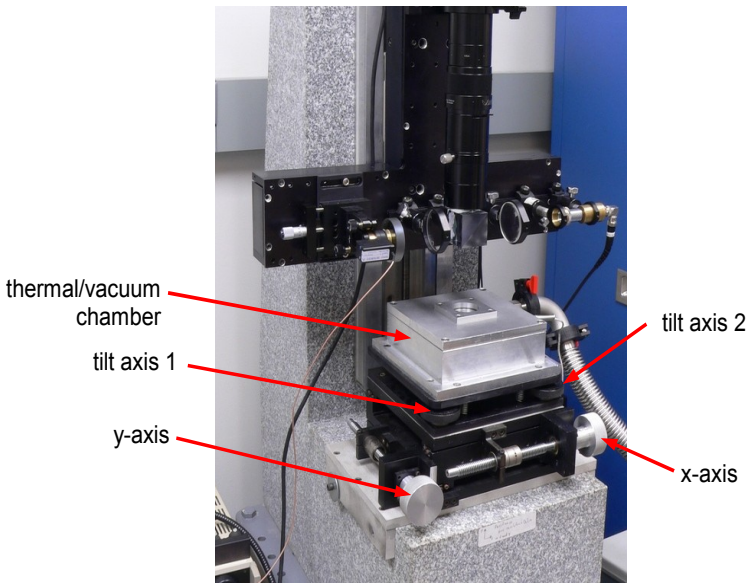

Fig. 39. Sample positioning subsystem with the thermal/vacuum chamber module.

The two axis tilt stage was designed and fabricated because no suitable low profile tilt stage could be found commercially, Fig. 40. Functionally similar stages were available from several vendors, but the cost was unjustifiably high. Therefore, a simple hand screw driven tilt stage was developed. The mechanical drawings can be found in Appendix C, and the tilt stage design calculations can be found in Appendix D. The tilt

stage upper and lower plates, as well as the control knobs, are fabricated out of 6061 aluminum, with a steel pivot ball and pressed in threaded sleeves, visible in Appendix B (Fig B.4). The tilt stage as designed has a manual resolution on the order of one micro-degree, which corresponds to controlling tilt of a 100 μm long MEMS by 1.7 nm out of plane. This level of control is more than sufficient for interferometric alignment. The top plate of the stage has a 1 in. on center pattern of 1/4-20 threaded holes to allow for mounting of most standard loading devices. Since the fabrication of this tilt stage for the modular interferometric microscopy system, two more identical stages have been fabricated for the CHSLT because they work very well and are easy to fabricate.

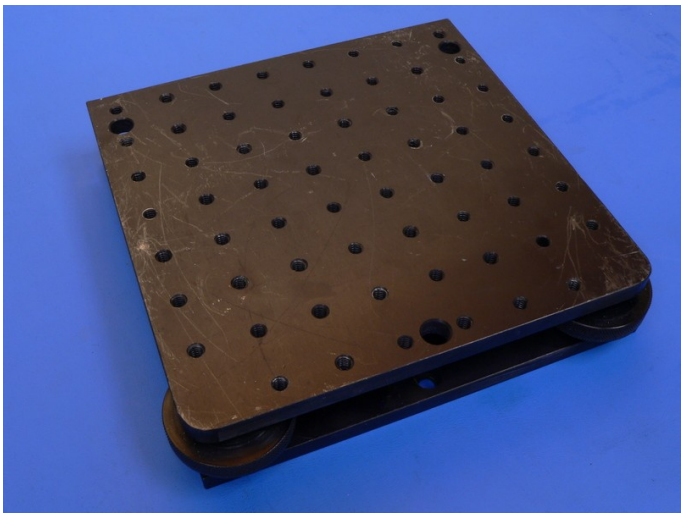

Fig. 40. Photograph of the two axis tilt stage.

6.3.2. Environmental chamber

The environmental chamber was designed and fabricated to subject MEMS to thermal loading and vacuum environments. Shown in Fig. 41 are the major components of the environmental chamber (named such because both the vacuum and temperature can be modulated via the TEC/liquid HEX module in the sealed chamber; also inert dry gas

environments can be achieved with argon or nitrogen). Additional photographs can be found in Appendix B (Figs B.5 and B.6).

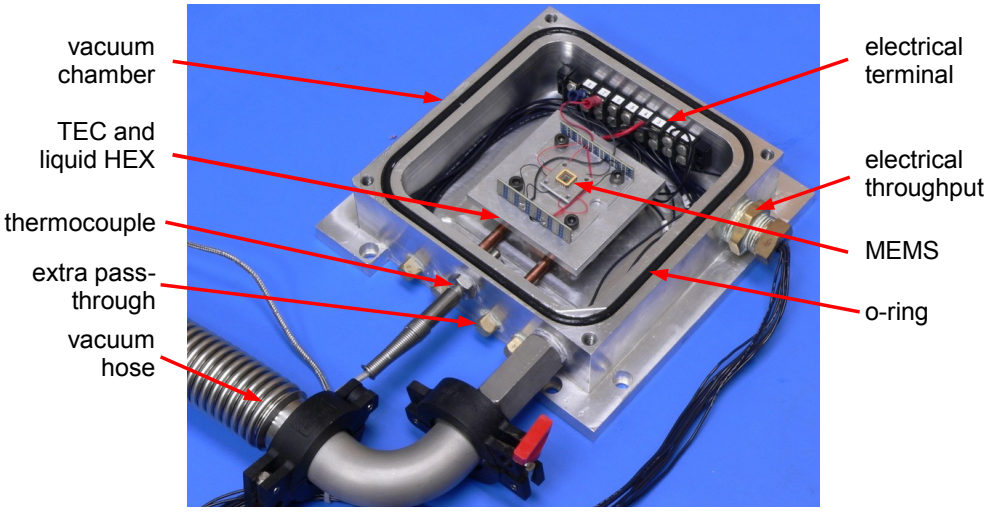

Fig. 41. The environmental chamber.

The chamber base (pictured) was designed and fabricated with a CNC machine out of a solid piece of aluminum. The interior volume is approximately $5.4 \times 5.4 \times 1.625$ inches. The chamber cover (not pictured) has a $\lambda/4$ flatness window with a clear aperture of 1.5 inches. Mechanical drawings of the environmental chamber are found in Appendix C.

The chamber was originally designed to be able to hold a vacuum of 1 mbar, corresponding to the maximum vacuum that the CHSLT piston vacuum pump could pull. As the modular interferometric microscopy system was being utilized for measurements on various pre-production MEMS engineering samples, it became necessary to pull a higher vacuum. A two-stage turbomolecular vacuum pump was purchased and all of the vacuum fittings were resealed with Teflon paste as opposed to the original Teflon tape. The chamber can now sustain approximately 1 μbar, a vacuum three orders of magnitude

higher then possible heretofore.

Thermal management of the chamber is provided by a combination of a TEC and a liquid HEX, Fig. 42. A TEC was chosen as the primary temperature loading device because TECs have very good response time, control, and thermal consistency across the heating/cooling surfaces (Klempner et al., 2005). The liquid HEX is the secondary cooling system that is utilized to pump heat away from the hot side of the TEC when the TEC is employed to maintain sub-zero temperatures for extended periods of time. Without the liquid HEX, the TEC would pump a significant amount of heat into the aluminum chamber when attempting to chill the chamber environment. This was determined by performing computational thermal analysis in the design phase of the chamber.

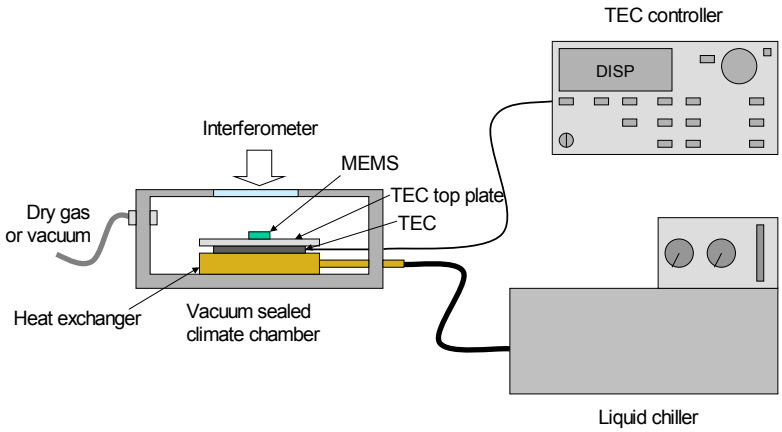

Fig. 42. Schematic of the thermal loading system of the environmental chamber.

A finite difference model of the climate chamber, TEC, and liquid cooled heat exchanger (HEX) was developed using Harvard Thermal's, *Thermal Analysis System* (TAS). The model is shown in Fig. 43, and assumes there is a perfect vacuum in the chamber, convection to the surrounding air from the exposed outside surfaces, the

indicated surfaces are insulated, and there is liquid flowing through the heat exchanger entering at a temperature of -15°C. TAS provides a model for the manufacturer specific TECs (based on nominal operating specifications).

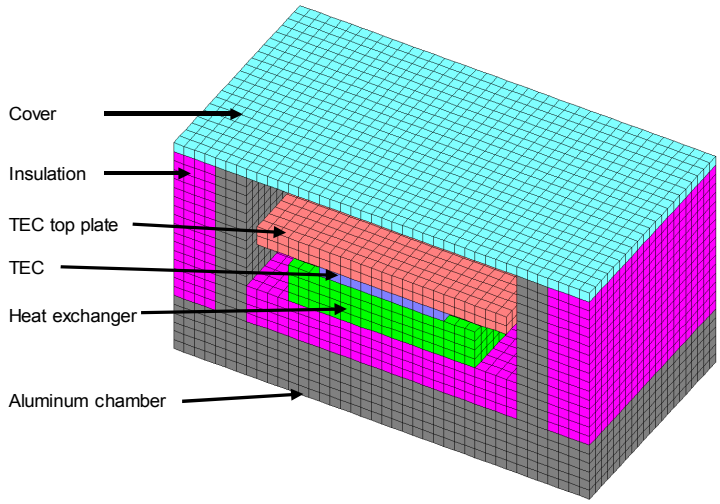

Fig. 43. TAS model of the environmental chamber.

The thermal response of the system is computed by the TAS model and the temperature of the TEC top plate is plotted as a function of time in Fig 44. To cool to below -40ºC, both the HEX and TEC are utilized, resulting in a 200 sec cool down time (3D steady state results are shown in Appendix E, Figs E.1 and E.2). To heat to 100ºC, the liquid flow in the HEX is stopped and the TEC alone heats to the temperature in 120 sec.

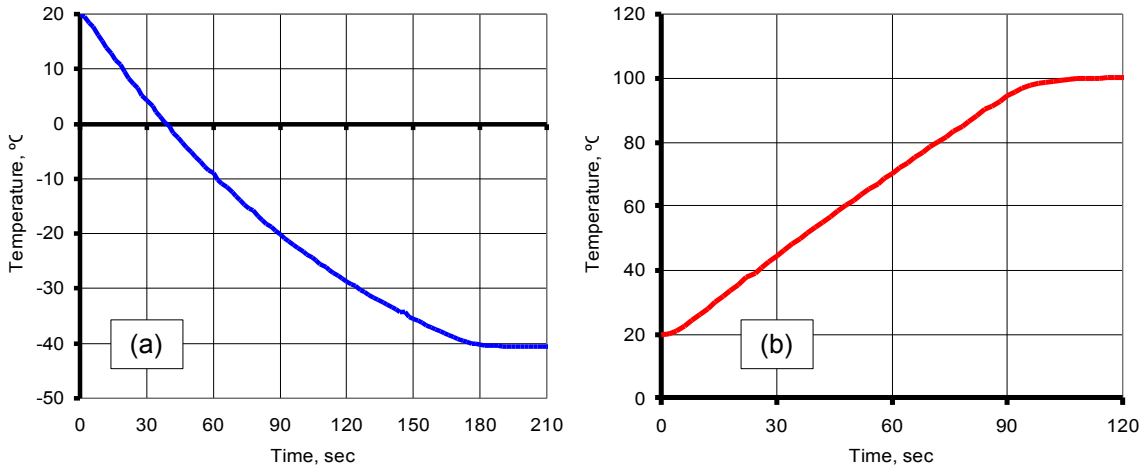

Fig. 44. TAS simulation results of thermal response of the environmental chamber: (a) TEC top plate cooling, (b) TEC top plate heating.

The TEC units utilized in the actual chamber are supplied by both Marlow, Inc. (*DT12*-6) and Melcore, Inc. (*HT-6-12-40*). These TECs have an active thermal surface that is 1.5 by 1.5 inches, a maximum temperature difference from the hot side to the cold side of 60°C at room temperature, and a maximum thermal pumping ability of 54 Watts. Together with the liquid HEX and an aluminum top plate, this thermal management system is 0.9 inches tall and easily fits within the environmental chamber, Fig. 45 without a top plate.

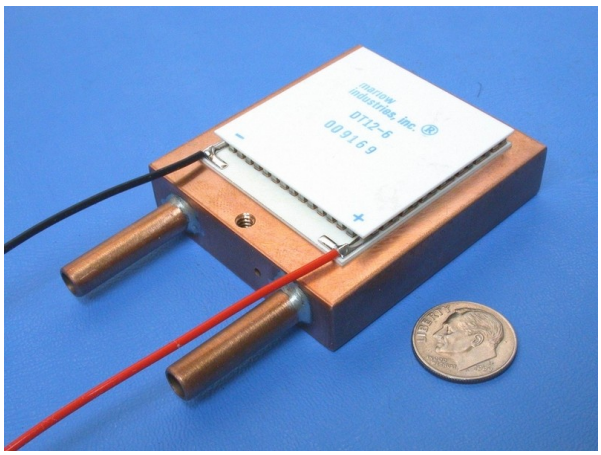

Fig. 45. TEC and liquid HEX.

Referring back to Fig. 41, the environmental chamber is equipped with an electrical feed through that permits up to 8 conductors to be connected to the device in the chamber. These wires are connected to an electrical screw terminal that allows easy electrical connection. Four gas or liquid pass throughs are also available for use with the liquid HEX or connection to dry gas canisters, or various other fluid devices. A sealed thermocouple is affixed to the chamber to measure temperature of the inside atmosphere when the chamber is not being used in vacuum mode. The vacuum pump is connected to the environmental chamber via a high vacuum hose utilizing NW-25 o-ring sealed fittings to make the system as seal tight as possible.

6.3.3. Vibration excitation

Inducing mechanical vibrations into MEMS is a common operation to test for system resonances (Hart et al., 2000; Klempner et al., 2004), material properties (Mizar and Pryputniewicz, 2000; D. R. Pryputniewicz et al., 2001), potential failure modes (Pryputniewicz et al., 2000), and system performance/quality (Pryputniewicz and Furlong, 2003). Customarily, we subject the MEMS to periodic mechanical vibration generated by a sinusoidally driven PZT. PZTs are chosen due to their ability to rapidly and accurately expand and contract with the input signal, up through frequencies of several hundred kHz. To characterize MEMS and MEMS in packaging ranging in size from several micrometers to 20 mm, we have an assortment of various sized PZTs, typical values are summarized in Table 9.

Table 9. Vibration excitation PZT module properties.

	max. sample size	linear freq. response	max. freq.	max. load	environmental chamber compatible?
large object PZT1	3” dia.	0 – 12 kHz	150 kHz	2200 N	No
large object PZT2	1.5” dia.	0 – 18 kHz	150 kHz	445 N	No
low profile PZT array	0.8” x 0.8”	1 – 28 kHz	500 kHz	250 N	Yes
PZT chip	5 mm x 5 mm	1 – 180 kHz	1.2 MHz	100 N	Yes

The large object PZT1 is designed by Jodon, Inc., as a “shaker” for holographic systems, model *EV-100*. This PZT, shown in Fig. 46, is a module for shaking the largest of packages that we receive. It has a three inch diameter top working surface with four 1/4-20 threaded mounting holes. The large object PZT1 has a limited linear response, but high non linear response of up to 150 kHz. With a maximum load capacity of 2200 N or approximately 500 lb_f, this PZT module can easily handle even the largest MEMS package. However, the large object PZT1 module is too large to fit within the environmental chamber. The maximum displacement this PZT is capable of is 4.8 µm at 2000 V. We typically only drive this PZT with a maximum 25 V sine wave, enough to cause about 60 nm of motion. This amount of motion is normally more than sufficient to excite most samples to be measured by the OEH system.

Fig. 46. Large object PZT1.

The large object PZT2 is also designed by Jodon, Inc., as a holographic shaker. Its model number is *EV-30*. The top surface to this PZT, Fig. 47, also has four 1/4-20 threaded mounting holes to mount packages. The linear response of this PZT is better than that of the large object PZT1 and the maximum frequency is also 150 kHz. Load capacity with this PZT is also very high at 100 lb_f, but it also does not fit within the environmental chamber. The maximum vibrational amplitude generated by this PZT are half that of the large object PZT1 at 2.4 μm at 2000 V and 30 nm at 25 V.

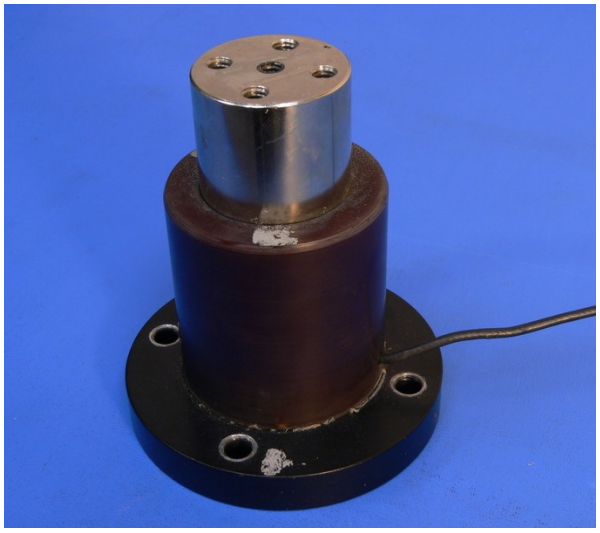

Fig. 47. Large object PZT2.

The low profile PZT array was developed to accommodate MEMS packages in the environmental chamber. This PZT module is an array of four bare Physik Instrumente *PL055.30 LVPZT chips* mechanically and electrically connected to a specially designed module. The PZT chips chosen are low voltage PZTs with a maximum amplitude of 2.2 μm at 100 V. Using our 25 V signal generator, amplitudes of up to 550 nm are possible at low frequencies. The maximum usable frequency of this low profile PZT array is on the order of 500 kHz. The design of this PZT array, Figs 48 and 49, is less than ½ inch thick

including a detachable mounting plate for easy sample mounting. These mounting plates are 0.8 in. by 0.8 in. square made out of 16 gauge aluminum and are mechanically fastened to the PZT array via four 1-80 UNF machine screws. The intention of this mounting plate is to have the ability to mount and unmount MEMS from the PZT array with out permanent attachment. Typically, bare MEMS are liquid "super-glued" to these removable mounting plates (we manufactured a supply of them), to ensure proper coupling of mechanical excitation, but non-permanent attachment to the PZT array itself. The low profile PZT array is utilized when samples are larger than 5 mm by 5 mm square.

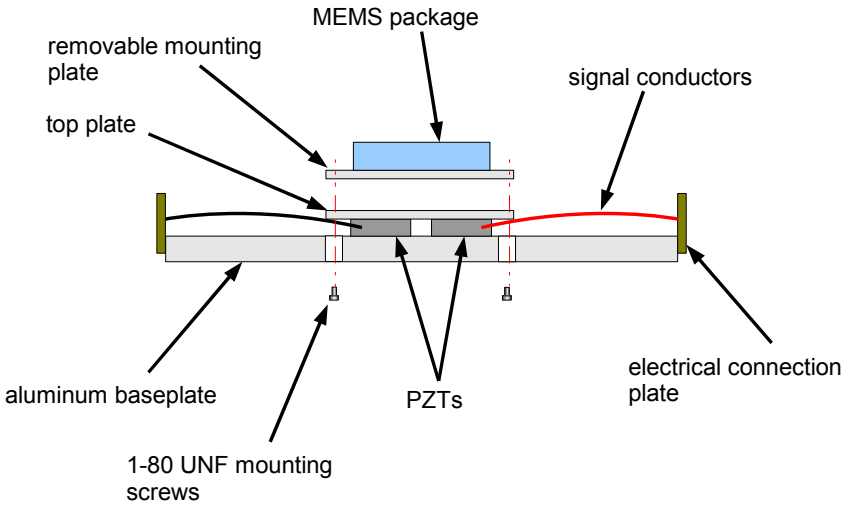

Fig. 48. Schematic of the low profile PZT array module.

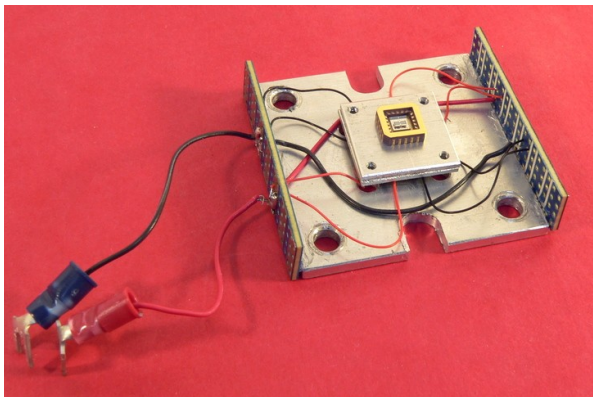

Fig. 49. Photograph of the low profile PZT array module.

The PZT chip utilized in the low profile PZT array module can also be used by itself provided the MEMS is smaller than 5 mm by 5 mm square. The bare chip, Fig 50, is a Physik Instrumente *PL055.30 LVPZT monolithic multilayer piezo actuator.* At 25 V the displacement is approximately 550 nm in low frequencies. This PZT chip has a very high linear response, up to 180 kHz unloaded, and a maximum operational frequency higher than 1 MHz. Above the linear range, these chips are the most linear of all of the PZT modules and are generally chosen favored for experiments whenever possible.

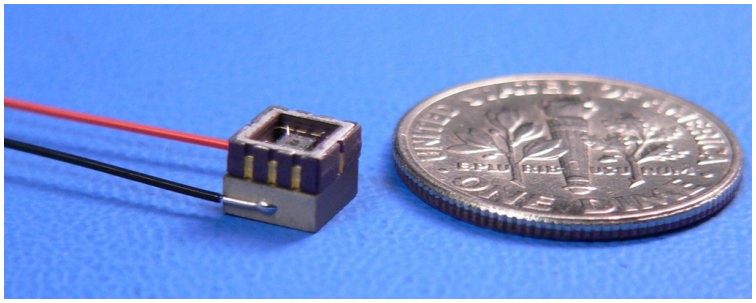

Fig. 50. Photograph of a *PL055.30* LVPZT chip with a MEMS attached.

6.4. Instrumentation subsystem

The instrumentation subsystem consists of an instrumentation rack and all of the rack-mountable controlling electronics and the turbomolecular vacuum pump, Figs 51 and 52. The rack itself (21) is a standard instrumentation rack and all of the components that it contains are commercially available. As such, this Section will serve as a simple description of each component as purchased, implemented, and utilized.

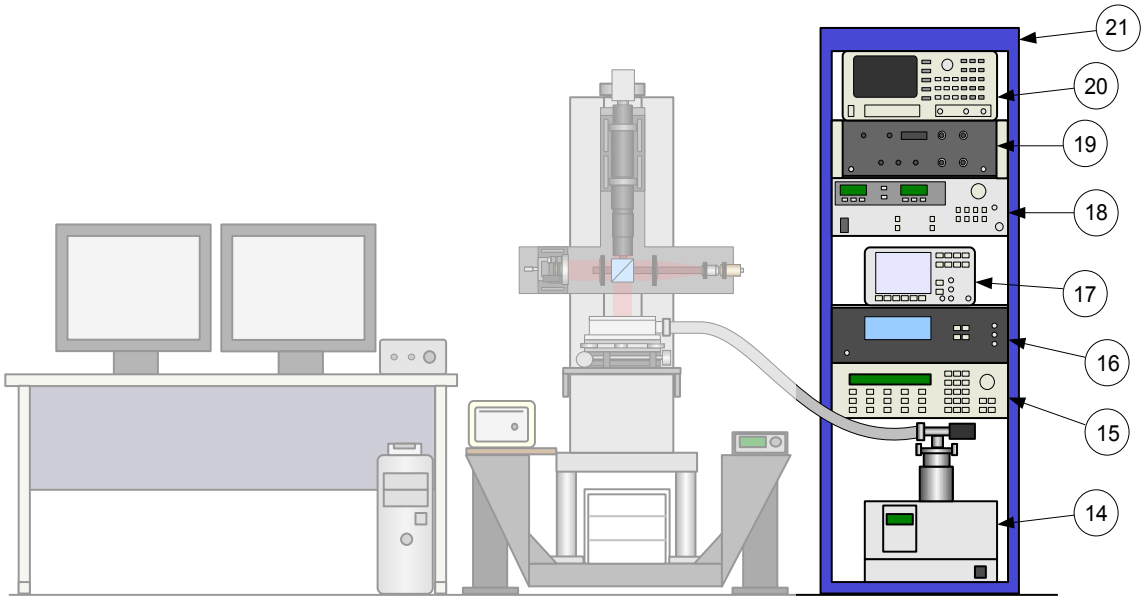

Fig. 51. The instrumentation subsystem.

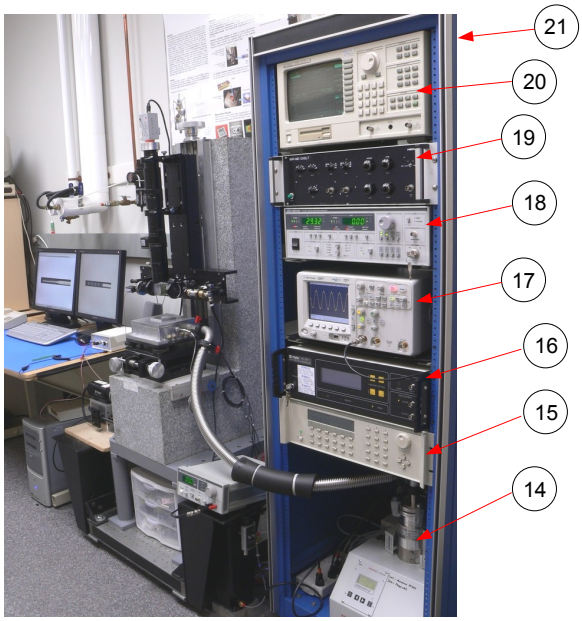

Fig. 52: Photograph of the instrumentation subsystem.

The turbomolecular vacuum pump (14) is a fully integrated, dual-stage, controlled system with a high vacuum gauge from Pfeiffer Vacuum of Germany. The pump system

has a diaphragm backing pump followed by the turbomolecular unit that can reach an ultimate vacuum of 7.5×10^{-7} torr, (1×10^{-7} mbar) according to the manufacturer. It has a free-flow pumping rate of 33 L/s, enough to evacuate the chamber to our best vacuum of 1×10^{-3} mbar in about five minutes. This turbo is quite for a vacuum and operates very smoothly: the pump can be running and connected via the steel hose to the chamber, and measurements can be made as no significant vibrational interference is transferred.

The Wavetek analog signal generator (15) is the instrument that is utilized to generate signals to drive vibration excitation PZTs, strobe the LED light source, and drive certain live MEMS. The Wavetek is a four channel unit that can be computer interfaced via GPIB, although for most experiments it is controlled manually. Each channel has a 30 mV to 25 V p-p output that has a frequency range of 0.01 Hz to 2 MHz.

The vibrometer controller (16) is an integral part of the Polytec vibrometer system. When controlling the rest of the system, the vibrometer controller outputs a modulated voltage corresponding directly to the measured objects' vibrational velocity or displacement, depending on the mode chosen by the operator. The displacement output voltage is scaled by a factor of 50 nm per volt, and the velocity is scaled by a range of factors selected by the operator: 1.0 mm/s/V to 5000 mm/s/V. The typical output signal is a sinusoid scaled by the above factors. This sine signal is then input to either the oscilloscope or spectrum analyzer for analysis.

The digital oscilloscope (17) is an Agilent 6000 scope that is utilized for signal analysis and for recording vibrometer data. This oscilloscope has a digital sampling rate of 2 GSa/s and has a memory for one million data points. It is computer interfaced and measurement data are captured by a PC. This oscilloscope was purchased due to its

ability to store a significant amount of data, required for certain vibrometer measurements such as ring-down of vibrating objects in vacuum. In experiments such as these, vibrations at frequencies of tens of kHz need to be recorded for several seconds at a time, requiring hundreds of thousands of data points to be able to smoothly resolve the sinusoidal motion.

The ILX diode and TEC controller (18) is utilized to control both the TEC module and the LED module for illumination in the high magnification interferometer. This controller has PID adjustable feedback control of the thermistor readings of the TEC. With this unit, control of temperature of the top plate of the TEC module can be achieved with resolution of 0.1°C. Control of the LED module is achieved with a constant current source, adjustable from 0 to 200 mA, with the ability to be externally modulated for strobing of the diode.

The custom made pulse generator (19) is used to stroboscopically illuminate vibrating objects for quantitative vibration analysis. This instrument takes a sinusoidal signal from the signal generator and outputs pulses that can be finely controlled in terms of duration and phase with respect to the input signal. In some cases it is desirable to strobe the object at two points during one period of oscillation: at the maximum and minimum points. This allows for quantitative measurement of the amplitude of vibration.

The instrument at the top of the rack is the spectrum analyzer (20). The spectrum analyzer, an Agilent unit, allows for visualization of the vibrational response of objects measured with the vibrometer in the frequency domain (as opposed to the time domain with the oscilloscope). This is particularly useful for determining and visualizing resonant modes of measurement samples.

7. TESTING AND CALIBRATION

Testing and calibration of the Mark 4 interferometric system is an integral part of its implementation as a tool for the CHSLT. Each individual module was tested and calibrated (where applicable) to ensure that the performance characteristics are well known. This Chapter serves as a reference for the calibration results of each module and the methodology utilized for the calibration.

7.1. LED calibration

The LEDs utilized as light sources for high and low magnification interferometer modules are manufactured by Opto Diode. These are 50 mW red LEDs, that have a manufacturer specified peak wavelength of 620 nm with a FWHM of 25 nm. Since the wavelength of the light directly affects the accuracy of the results per Eq. 9, calibration of these LEDs was performed. An Oriel monochrometer was utilized to measure the spectrum of the LEDs. The monochrometer itself was calibrated against a HeNe laser which inherently has a very well known and defined peak at 632.8 nm (Kuhn, 1998).

Three LED modules have been assigned for duty with the modular interferometric microscopy system at CHSLT and they have have designated LED “B”, “C”, and “D”. Referring back to Fig. 33, LED “B” is mounted in the high magnification interferometer module, LEDs “C” and “D” are mounted in low magnification interferometer modules, with LED “D” being a spare unit. For the initial spectral calibration, the LEDs were powered and the spectrum was measured with the monochrometer. The spectral plots (output power as a function of wavelength) of each LED are shown in Appendix F. The results of these plots are summarized in Table 10.

Table 10. Spectral calibration of the LEDs.

	Specification	LED “B”	LED “C”	LED “D”
peak wavelength, nm	620	636	634	635
FWHM, nm	25	19	19	18

It was also noted that the peak wavelength varies according to the LED driving current. This is very significant as the driving current controls the LED brightness, which is routinely varied based on the interferometer utilized, the imaging objective selected, and the surface properties of the measurement sample. Figures 53 to 55 should be used by the operator to determine the appropriate wavelength, based on the driving current utilized in the experiment, to properly scale the processed data. The characteristic shape and FWHM of the spectral curves remain constant, there is just a wavelength offset as the driving current varies. The wavelength varies linearly with respect to driving current, as can be seen by a R^2 value very near 1.0. These figures have been reproduced in Appendix F, along with the spectral curves, for easy operator reference.

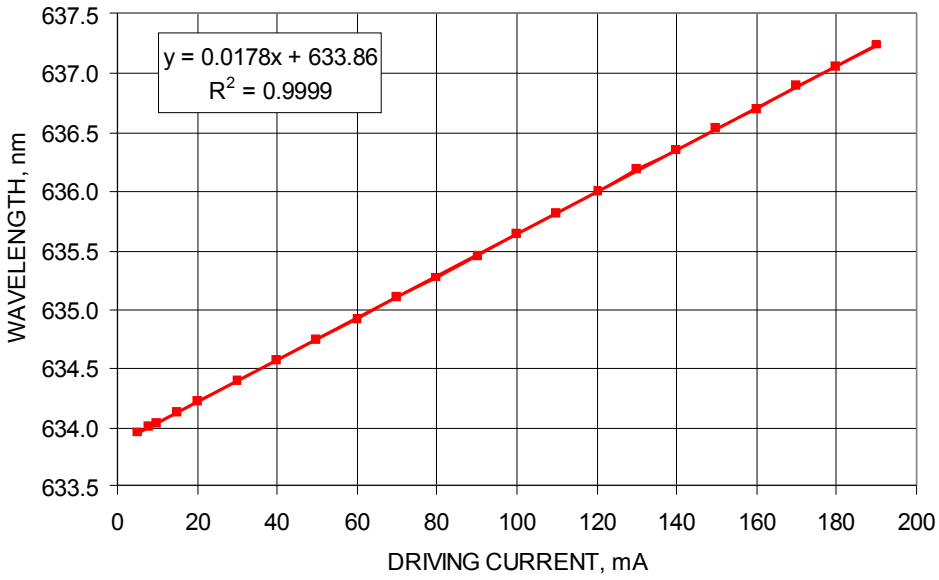

Fig. 53. Peak wavelength of LED "B" as a function of driving current.

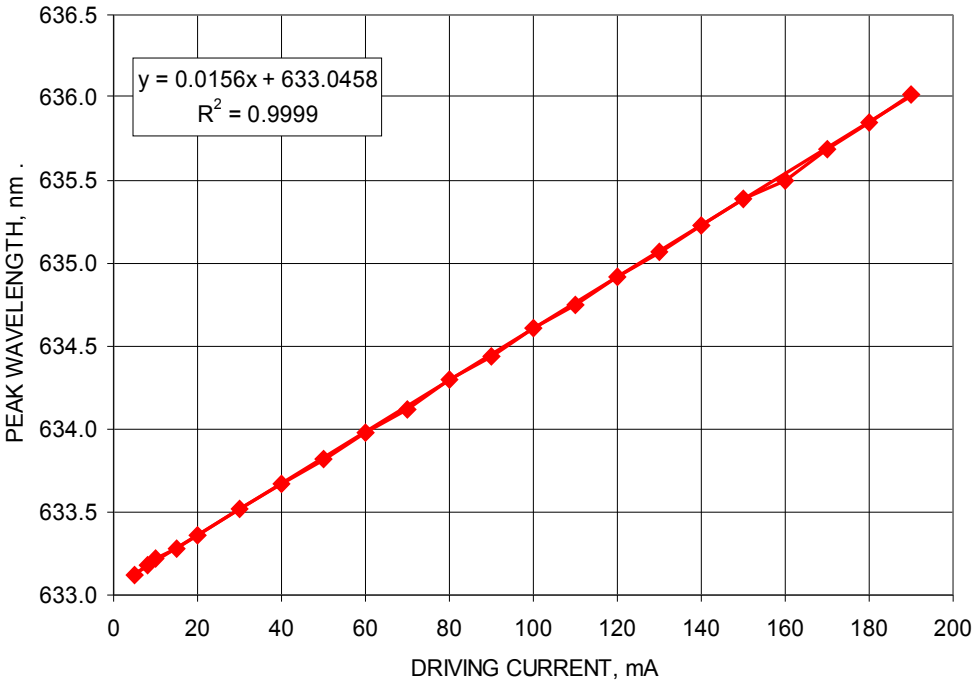

Fig. 54. Peak wavelength of LED "C" as a function of driving current.

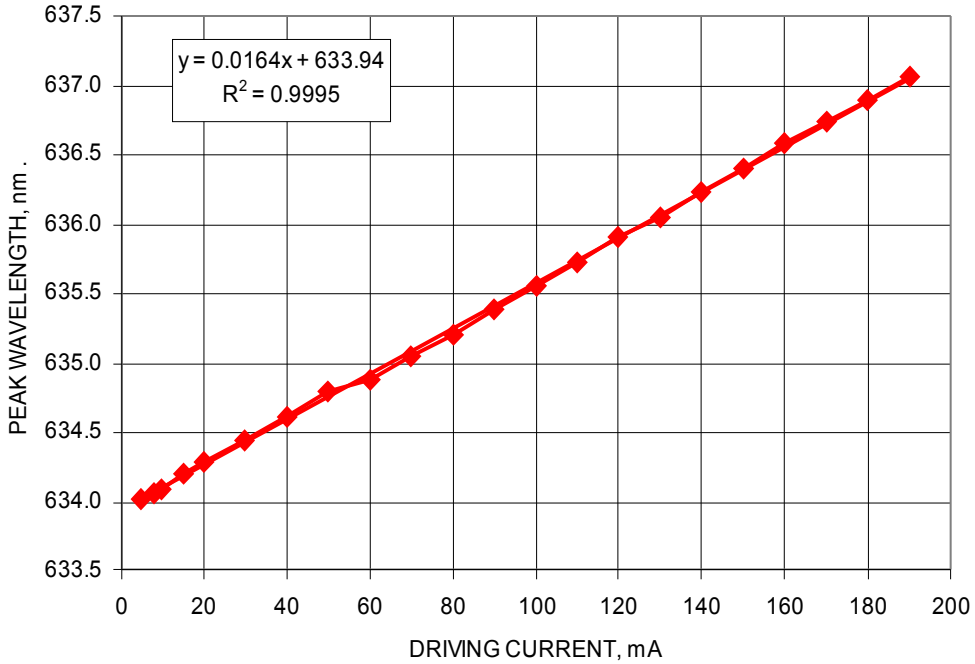

Fig. 55. Peak wavelength of LED "D" as a function of driving current.

7.2. Scanning PZT calibration

Calibration of the scanning PZT is important for the accuracy of the vertical scanning mode of the interferometers. The PZT is calibrated in both open and closed loop modes of operation. The calibration consists of measuring the displacement of the PZT with a high precision (0.0001 in., i.e., 2.5 μm) dial indicator and determining the range at which the PZT behaves linearly. It is important to determine the linearity of the PZT because the assumption is made that the PZT scan is linear when performing VSI.

In the open loop PZT operation of VSI, Fig. 56, the useful PZT scan range is while increasing the preamplifier voltage from 2.5 V to 8.5 V. The curve in Fig. 56 is typical of a PZT hysteresis curve and is very repeatable. VSI measurements are made on the increasing voltage curve because the behavior is more linear than it is in the decreasing curve. Open loop operation is the most simple method for scanning as only a linear ramping signal is required to perform the scan which can be generated by a signal generator or a computer.

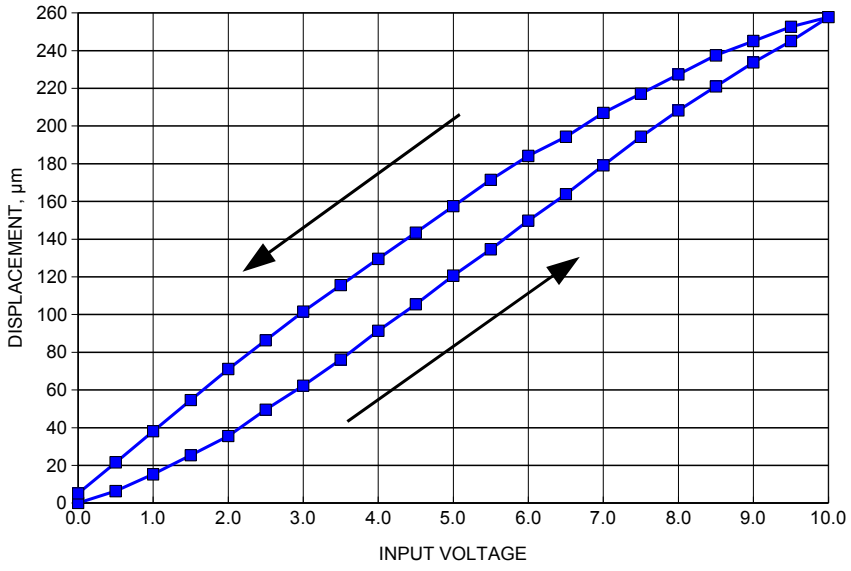

Fig. 56. Open loop calibration of the scanning PZT.

The closed loop operation of the PZT for VSI measurements is also possible using a PZT with a built in position feedback. Using this mode, commands are sent to the PZT controller telling it to move to a specified position. This mode requires the use of a computer and software designed to perform this type of scan. Calibration of the closed loop operation of the PZT was also performed with the high precision dial indicator and shows that the entire scan is linear with no hysteretic affects, Fig. 57.

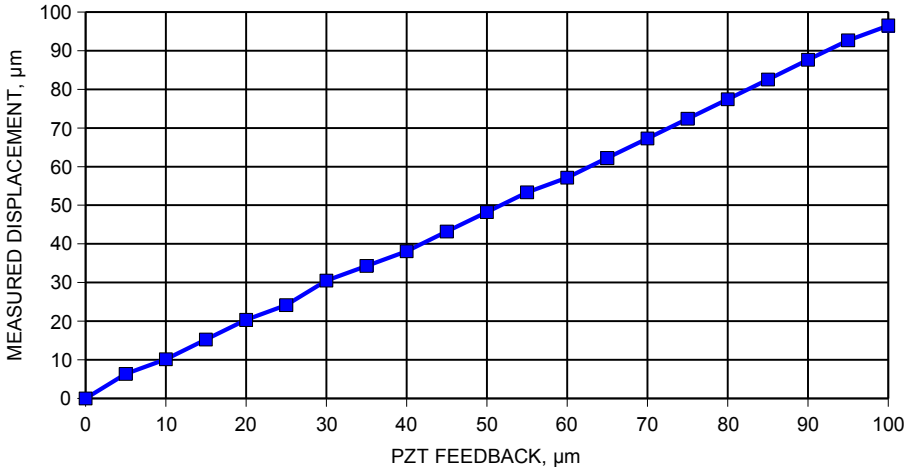

Fig. 57. Closed loop calibration of the scanning PZT.

7.3. Excitation PZT calibration

Calibrations of the excitation PZTs are required to determine the frequency range in which each PZT responds. Determination of this frequency response will allow the operator of the system to choose the optimal PZT for each specific application. The calibration was performed using the vibrometer module to measure the velocity of the top surface of the PZT as a frequency swept sinusoidal signal was used as the driving function. The goal of this calibration is to develop characterization curves of the response of each PZT to a range of frequencies, shown in this Section and reproduced in Appendix G for easy operator reference.

Three ranges were chosen based on the instrumentation that we commonly utilize for experiments: 0 to 20 kHz is the audio range where high-power audio amplifiers can be utilized to drive the PZTs; 0 to 100 kHz is approximately the range in which the LEDs can strobe; and 0 to 1 MHz is the maximum expected range that a response will be achieved by any of the PZTs. The vibrometer was utilized to characterize the response in each range of each PZT. While the amplitude of the PZT response varies with respect to input power, the frequency response curves do not significantly. Therefore the measurements were made at a nominal input power level and the measured PZT velocity will follow the trends presented here, but will be relative the the amount of input power.

7.3.1. Large object PZT1

The large object PZT1 is a Jodon *EV-100*, with a manufacturer specified response of 0 to 150 kHz. The actual response, Figs 58-60, is highly nonlinear and little motion is produced above 46 kHz, although it is detectable through 140 kHz.

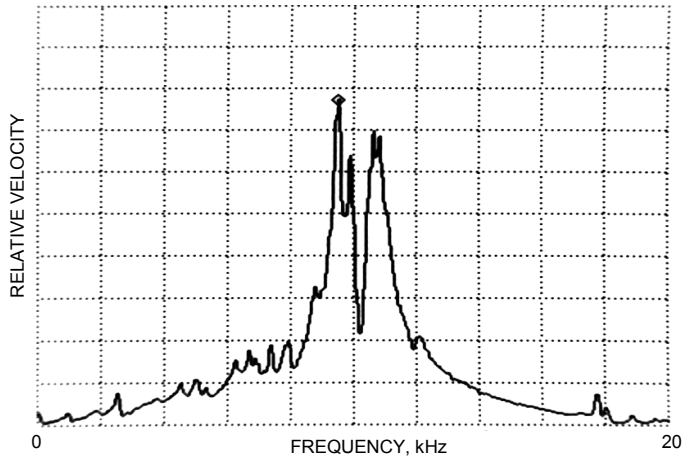

Fig. 58. Frequency response of PZT1 in the audio range, 0 to 20 kHz.

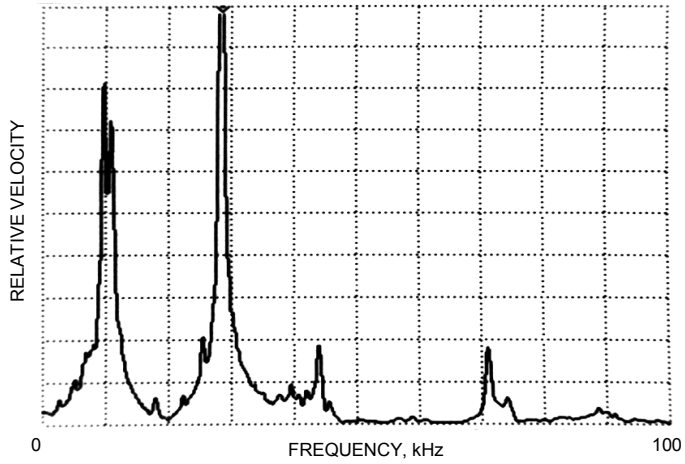

Fig. 59. Frequency response of PZT1 in the LED strobe range, 0 to 100 kHz.

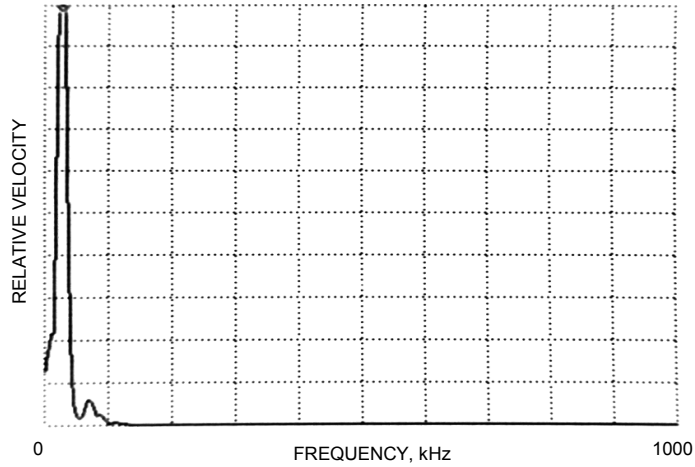

Fig. 60. Frequency response of PZT1 across the maximum range, 0 to 1 MHz.

7.3.2. Large object PZT2

The large object PZT2 is a Jodon *EV-30* with a manufacturer specified response also through 150 kHz. This PZT is also nonlinear, even in the audio range, Fig 61. It has an overall lower response than PZT1, Fig. 62, which rapidly falls off at 110 kHz, Fig. 63.

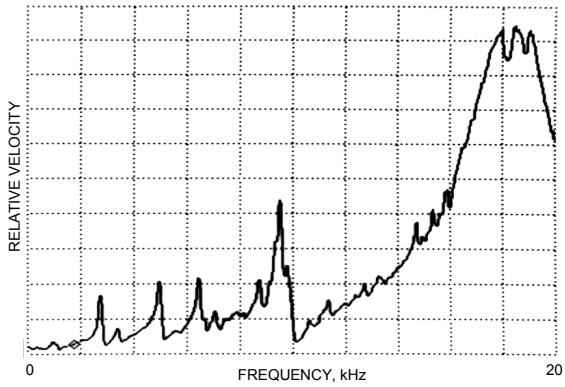

Fig. 61. Frequency response of PZT2 in the audio range, 0 to 20 kHz.

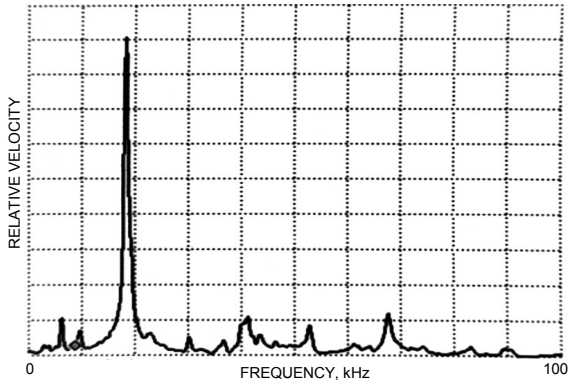

Fig. 62. Frequency response of PZT2 in the LED strobe range, 0 to 100 kHz.

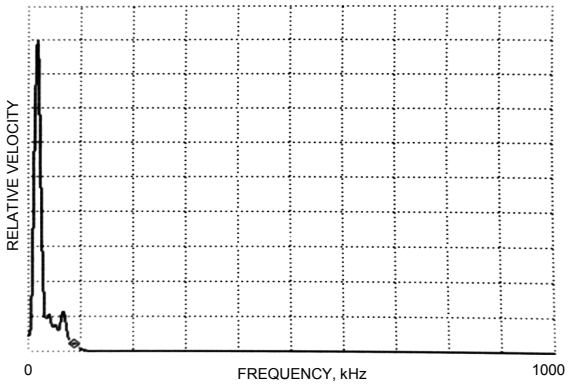

Fig. 63. Frequency response of PZT2 across the maximum range, 0 to 1 MHz.

7.3.3. Small object PZT

The small object PZT chip is a single *PL055.30* PZT chip manufactured by Physik Instrumenté. The small object PZT has the best response of four PZT modules, as it is reasonably linear from 10 kHz to 120 kHz, Figs 64 and 65. This PZT shows no resonances until 130 kHz, Fig. 66, and responds through 1 MHz.

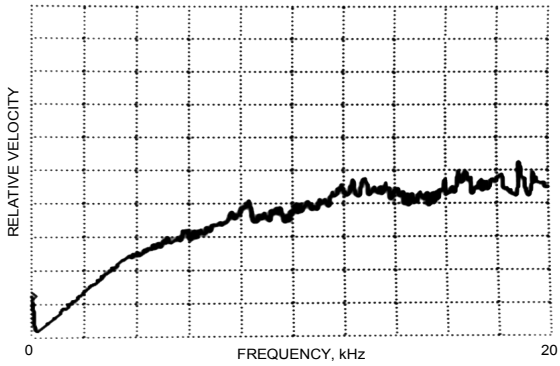

Fig. 64. Frequency response of PZT chip in the audio range, 0 to 20 kHz.

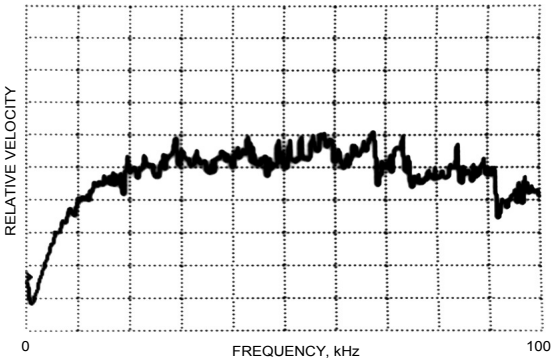

Fig. 65. Frequency response of PZT chip in the LED strobe range, 0 to 100 kHz.

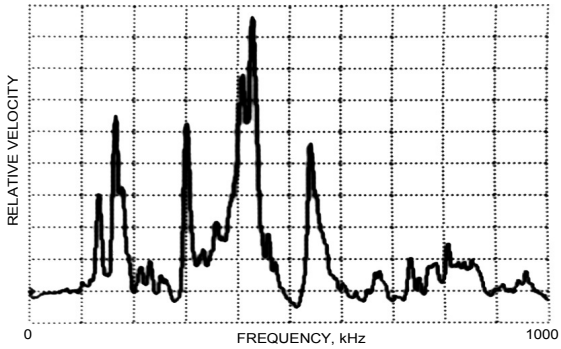

Fig. 66. Frequency response of PZT chip across the maximum range, 0 to 1 MHz.

7.3.4. Low profile PZT module

The low profile PZT module is an array of four of the *PL055.30* PZT chips. The design intention was to keep some of the high frequency response of the single PZT chips, but allow larger objects to be excited. Figures 67 and 68 show that this PZT module has a nonlinear response, contains a "dead zone" from 63 to 100 kHz, but it does respond to 1 MHz, Fig. 69. This PZT module is capable of exciting larger MEMS or MEMS in packaging at frequencies greater than 100 kHz, where the Jodon PZTs stop responding.

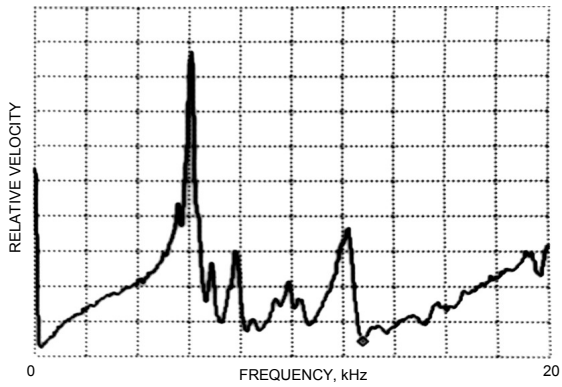

Fig. 67. Frequency response of PZT module in the audio range, 0 to 20 kHz.

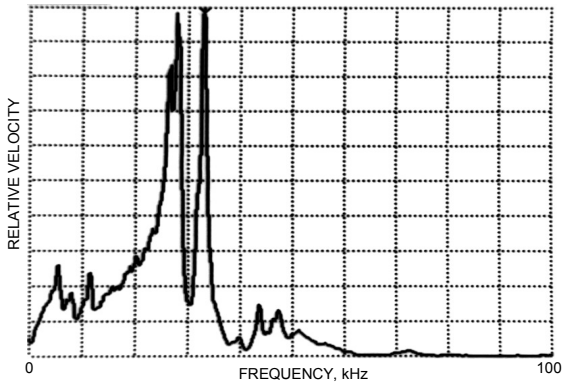

Fig. 68. Frequency response of PZT module in the LED strobe range, 0 to 100 kHz.

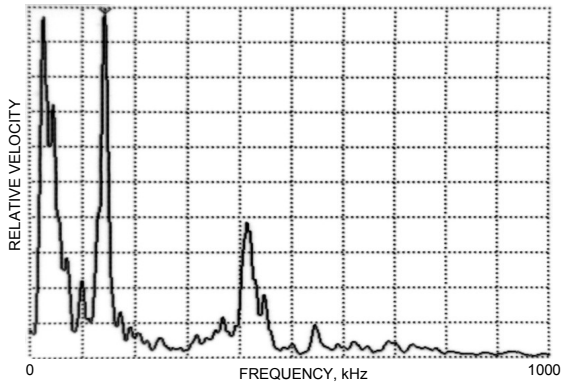

Fig. 69. Frequency response of PZT module across the maximum range, 0 to 1 MHz.

7.4. Phase stepping interferometer calibration

It is important to characterize the performance of any measurement system to gauge the quality of the results that will be generated. To ensure that the modular interferometric microscopy system performs as expected, several overall system calibration experiments were conducted.

First, the precision, or repeatability, of the system had to be determined. For this experiment, a flat optical mirror was the sample and its surface flatness was measured in a series of 12 individual repeated measurements recorded in short succession, Fig. 70. Figure 71 shows the shape of the mirror extracted along the trace (one pixel wide) of Fig. 70, for each of the 12 successive measurements.

It is evident from Fig. 71 that the test sample is not ideal, but instead deviates up to 27 nm from flat along this trace. Of more importance, however, are how the 12 traces repeat. At no point along these traces are there any instances where the measurements vary by more than 2.5 nm. To quantify the system repeatability, precision is calculated by taking the standard deviation about the mean of the traces 1 through 12, Fig. 72. The precision of the system is better than 0.88 nm, with the mean precision being 0.485 nm.

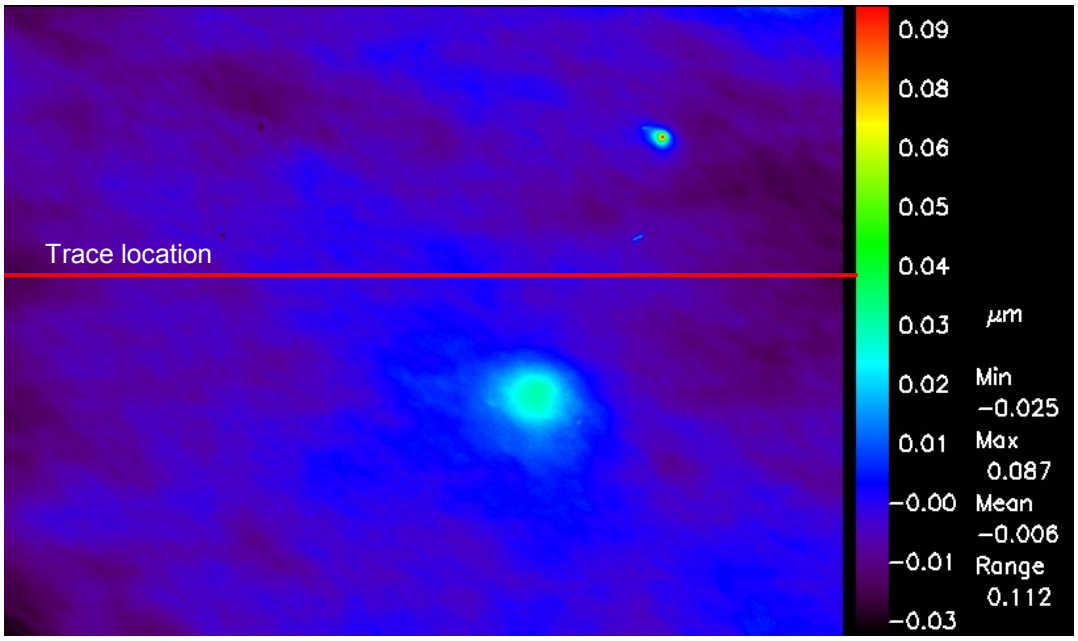

Fig. 70. Interferometric measurement of a mirror surface, 1 of a series of 12.

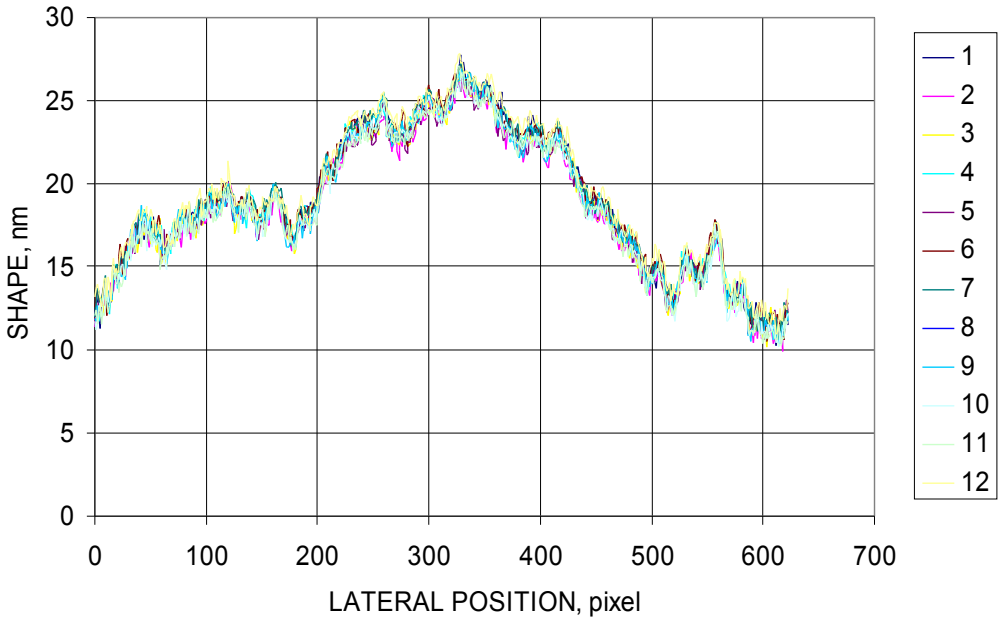

Fig. 71. Repeatability measurement of a mirror surface, 12 horizontal traces.

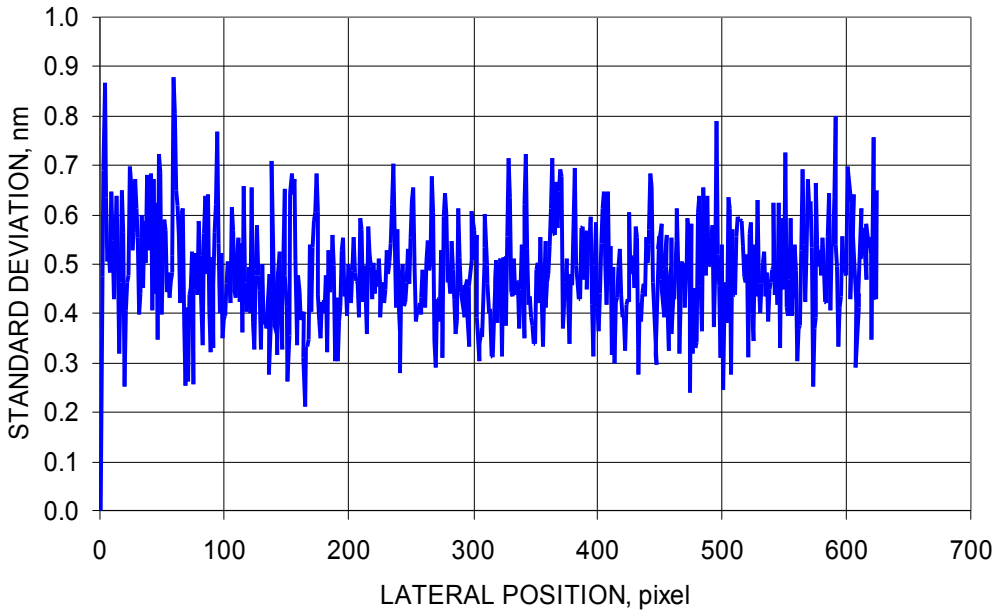

Fig. 72. The precision of the system is one standard deviation of the 12 traces.

Accuracy calibration measurements have also been conducted with the modular interferometric microscopy system. A National Institute of Standards and Technology (NIST) test sample is the calibration piece utilized. Shown in Fig. 73, a number 2075 "sinusoidal roughness specimen" has a 3.0 μm amplitude sine wave formed on the top surface. A portion of the surface of this test sample was measured interferometrically, Fig. 74, then a trace in the same area was performed with a Dektak surface profilometer that has sub-nanometer measurement accuracy. A trace was extracted from the interferometric measurements, as close to the location of the profilometer trace as possible, and the two traces are compared in Fig. 75. The profilometer measures a mean peak to peak amplitude of the surface to be 3012.3 nm, and the interferometer measures a mean peak to peak amplitude of 3010.8 nm, both measurements being within the NIST-certified traceability of the test sample.

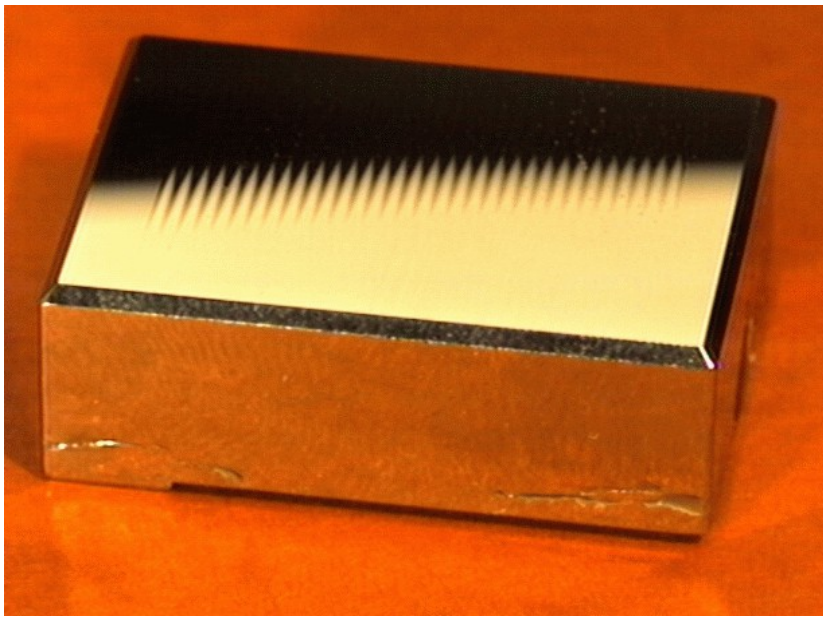

Fig. 73. NIST sinusoidal roughness specimen #2075, for accuracy calibration.

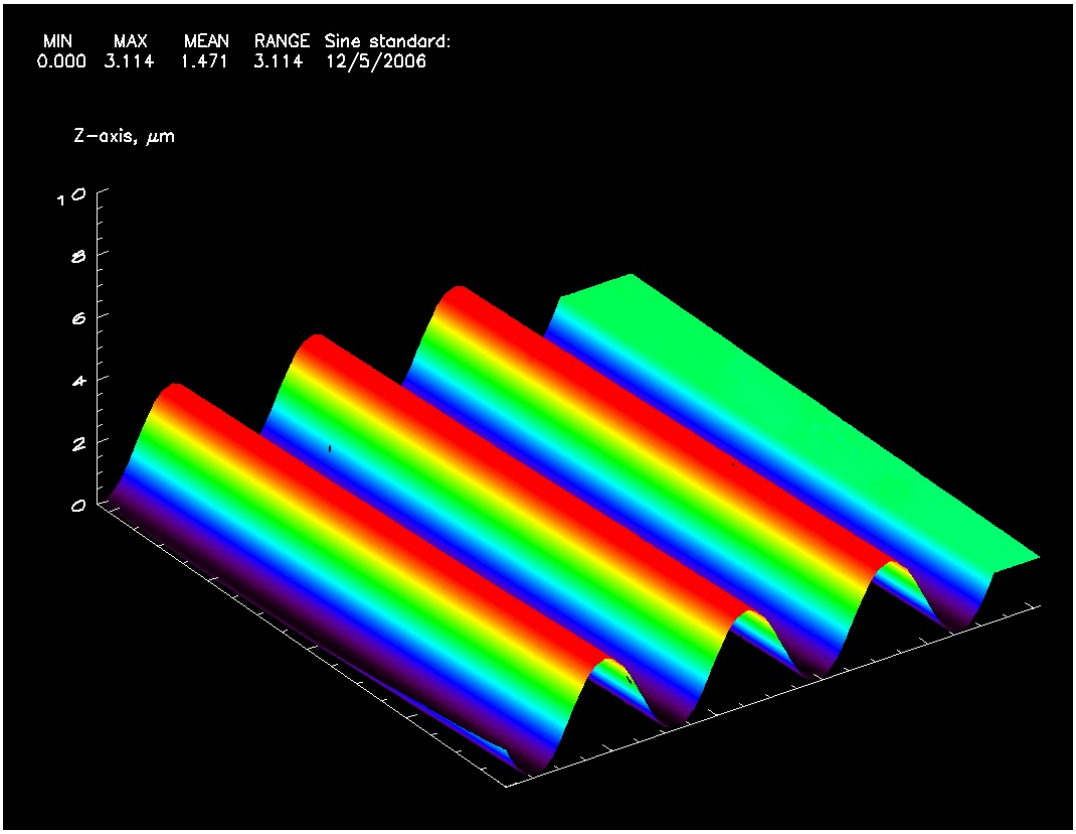

Fig. 74. Interferometric measurement of the surface of the sinusoidal test sample.

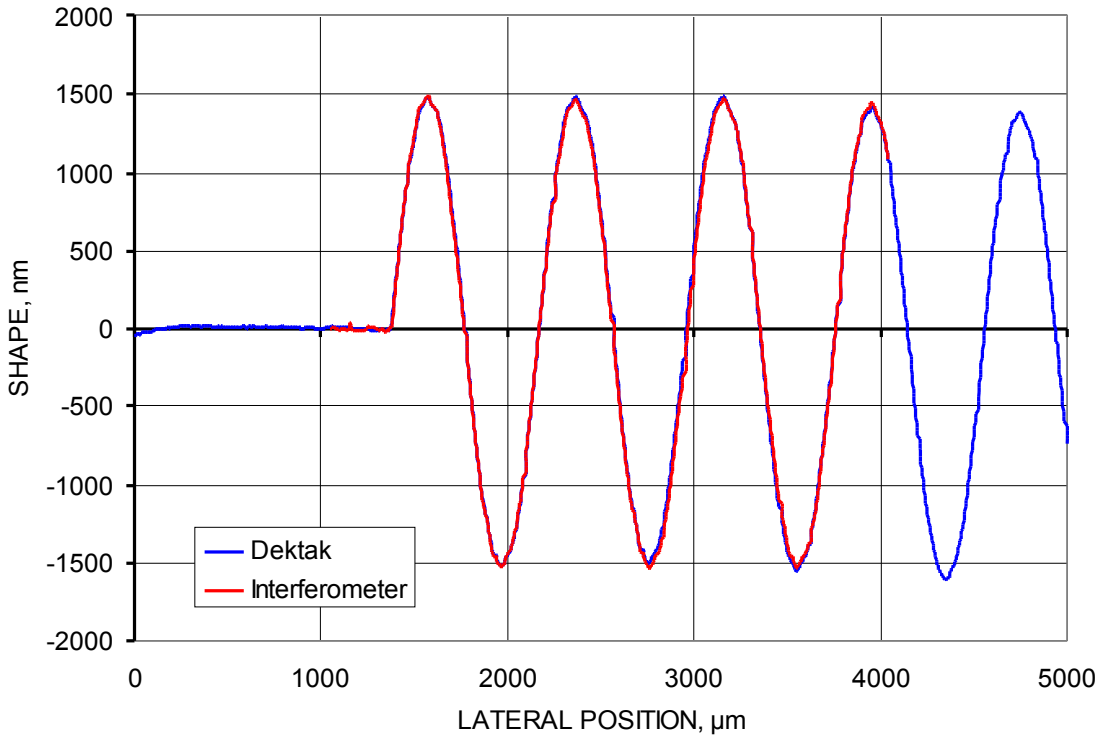

Fig. 75. Interferometer and Dektak profilometer measurements of the test sample.

7.5. Vibrometer calibration

The vibrometer module is a commercial system adapted to work on the modular interferometer chassis and, as such, is periodically returned to the manufacturer for calibration. The latest calibration was performed by Polytec in September, 2006. The entire vibrometer system, including the sensor head, fiber interferometer, and controlling electronics, were serviced and calibrated to manufacturer specification.

7.6. Scanning white light interferometer calibration

Calibration of the scanning white light interferometer is performed in three phases. First, a secondary light source with a coherence length longer than that of the white light source, such as a LED or laser, is calibrated to determine its wavelength (the

results of Section 7.1 are available). Second, the scanning PZT needs to be calibrated to ensure that it is being operated in a linear range (Section 7.2). Third, a scanning measurement is performed with the white light source and then again with a calibrated secondary light source. The reason for repeating the scan with a longer coherence length and well calibrated light source is so that the scanning rate (distance per image step) can be accurately determined.

For example, let us say that a scan was performed with a white light source and LED "B" as the secondary light source. LED "B" was set to a driving current of 120 mA, which according to Fig. 53 corresponds to the wavelength of 636.0 nm. Tracking one pixel through the LED scan shows that modulation is clearly visible for 40 fringes through exactly 320 frames of the image stack. Knowing that one fringe period indicates a displacement half that of the wavelength of the light source, as is the case with any retro-reflective interferometer, it can be said that the distance between fringes is 318 nm or the distance across 40 fringes is 12.72 μm. Dividing this scan distance by the number of image frames showing the modulation, the step per frame is 39.75 nm for this example. When the images are analyzed and stacked in 3D space, the vertical offset between images is set to this calibrated step per frame. Unlike the calibrations of the other modules that are performed periodically, this calibration is performed with every scan that has a different scan depth or scan rate.

8. REPRESENTATIVE MEASUREMENTS OF MEMS

This Chapter contains a set of representative examples of how the different modules of the modular interferometric microscopy system can be utilized to measure various aspects of MEMS. An atomic force microscope (AFM) cantilever is studied in detail in this Chapter. Although it is a simple structure, it clearly demonstrates the need for characterization of (much more complex) MEMS. Also, measurements of microgears and a microgyroscope illustrate system capabilities for measurement of complex MEMS.

8.1. Static shape of a microcantilever

Most measurement processes start with a baseline static shape measurement of a device. For this example, six AFM microcantilevers are examined to determine if coating MEMS with a metallic layer affects the structure. It is common to apply a metallic coating onto areas of MEMS to allow electrical conduction or to fabricate electrodes for electrostatic actuation and/or sensing.

The characteristic dimensions of the microcantilevers are: length = 450 ± 10 μm, width = 50 ± 7.5 μm, and thickness = 2.0 ±1 μm, with the resonant frequency specified by the manufacturer being 6 to 21 kHz. The microcantilevers, one shown in Fig. 76, are fabricated out of silicon and may be coated with aluminum. Individual samples have one or two sides aluminum coated, with coating thicknesses ranging from 5 to 30 nm.

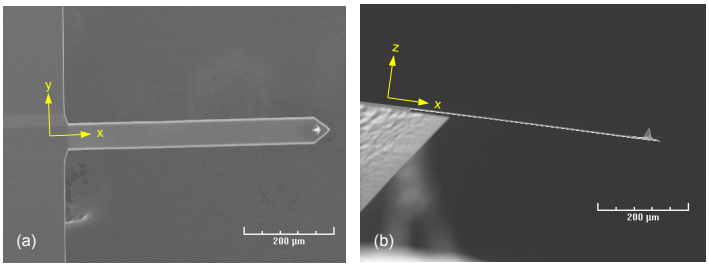

Fig. 76. SEM images of an AFM microcantilever: (a) top view, (b) side view.

The modular interferometric microscopy system was configured with the high magnification interferometer and the microcantilevers were characterized before they were removed from the manufacturer's gel-pak for the baseline measurement. Full-field-of-view measurements were taken of the top surface of each microcantilever, viewing a similar area as Fig 76a. Each microcantilever was analyzed and a trace was taken along the center of each beam, plotted in Fig. 77. Examining the results, coating the beam on a single side and the thickness of this coating greatly affect the static shape. This is expected as the aluminum coating is deposited at an elevated temperature and because there is a coefficient of thermal expansion mismatch between the silicon beam and aluminum coating, residual stresses are introduced into the structure as it cools. Residual stresses are a challenging issue with MEMS as thermal expansion mismatch between various structural layers, coatings, and packaging are common (Klempner et. al, 2002).

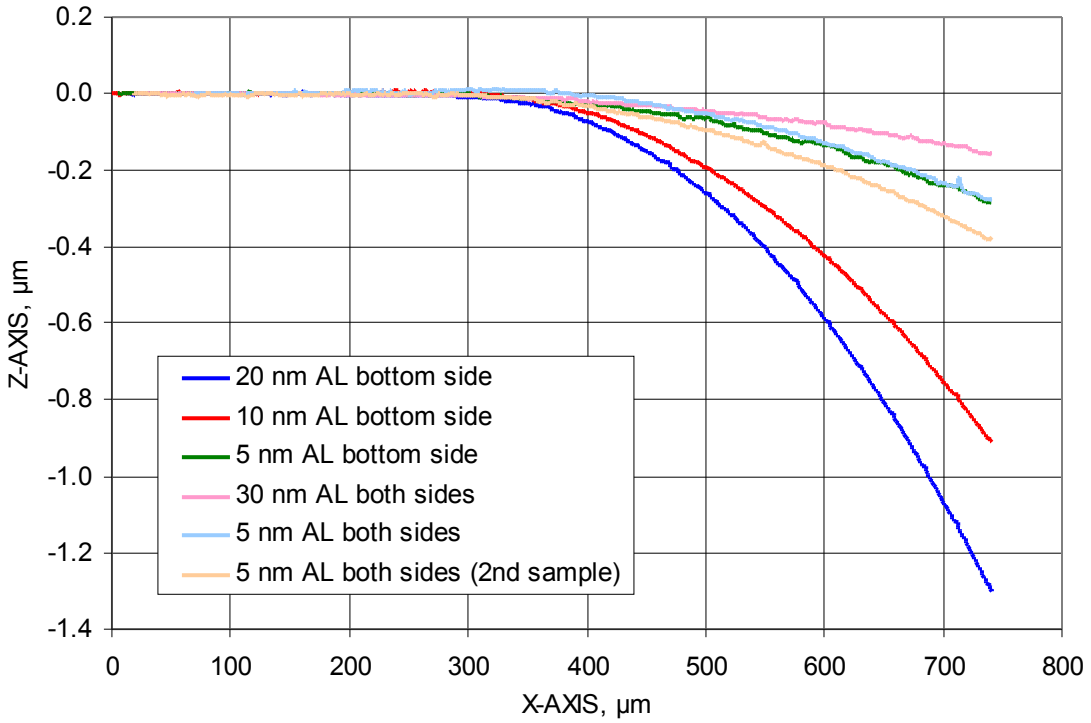

Fig. 77. Baseline shape measurement of 6 coated microcantilevers.

8.2. Thermal deformations of coated and uncoated microcantilevers

To further investigate the behavior of residual stresses due to coefficient of thermal expansion mismatch, a microcantilever coated on one side with 30 nm of aluminum is compared to an uncoated microcantilever at various temperatures. For this experiment, the TEC thermal loading module is added to the measurement system. The microcantilever chips are placed on the aluminum TEC top plate and allowed to reach a steady state temperature before measurements are recorded. The results, shown in Fig. 78, indicate that as temperature is increased, the residual stresses in the coated beam (shown in blue tones) decrease resulting in a straightening out of the beam. The uncoated beam (shown in red tones) has no residual stresses and thus no significant deformation of the beam occurs. This clearly illustrates potential problems (or applications) for MEMS structures that utilize materials with varying coefficients of thermal expansion. Care must be taken in the design of such structures.

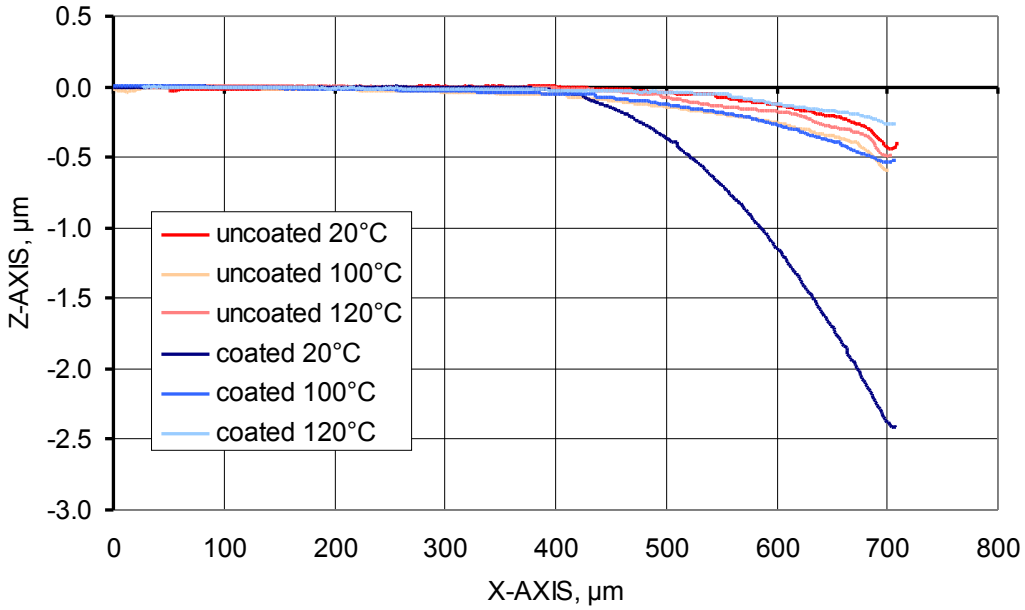

Fig. 78. Shape of an uncoated and a 30 nm AL coated beam at various temperatures.

8.3. Dynamic measurements of microcantilevers

To investigate the dynamic properties of the microcantilevers the interferometric microscopy system was reconfigured to use the vacuum chamber with a single PZT for vibration excitation. The microcantilever chip was super glued onto the PZT for good boundary conditions and the low magnification interferometer module was installed to look into the vacuum chamber. Measurements were performed at both atmospheric pressure and a vacuum of 3 μbar. The microcantilever used for this experiment is of the same dimensions of the previous beams, except it has no AFM tip, Fig. 79.

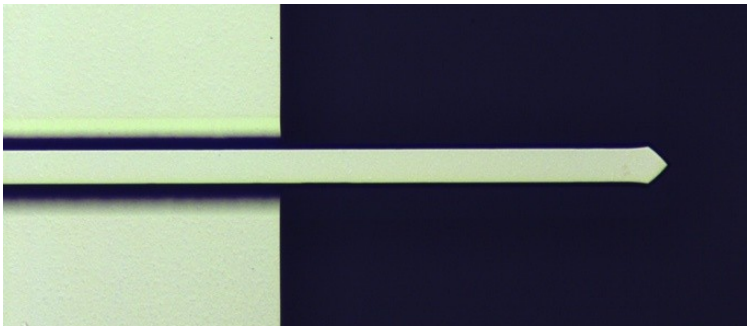

Fig. 79. Photograph of the microcantilever used for dynamic experiments.

The mode shapes and frequencies identified with time-average measurements are illustrated in Figs 80 and 81 for atmospheric pressure and vacuum, respectively. The frequency and amplitude of the driving signal is shown for each mode shape. The measurements include the first five fundamental bending modes for both air and vacuum environments.

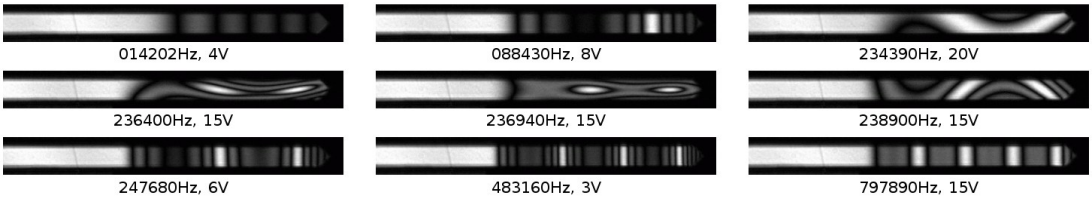

Fig. 80. Time-average recording of the microcantilever resonant modes in air.

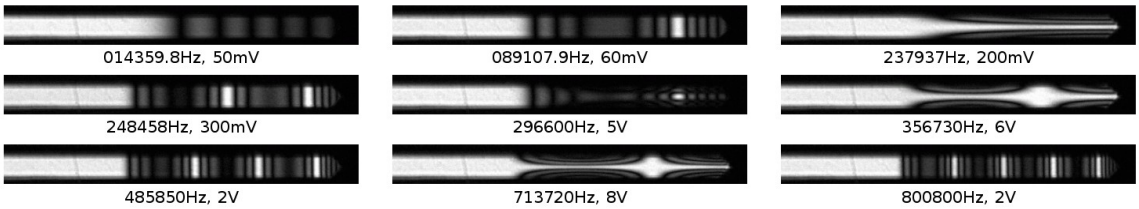

Fig. 81. Time-average recording of the microcantilever resonant modes in vacuum.

Once the fundamental bending modes are identified with time-average measurements, the system is switched to stroboscopic mode to perform quantitative analysis of the fundamental modes. The results of this analysis are shown in Fig. 82.

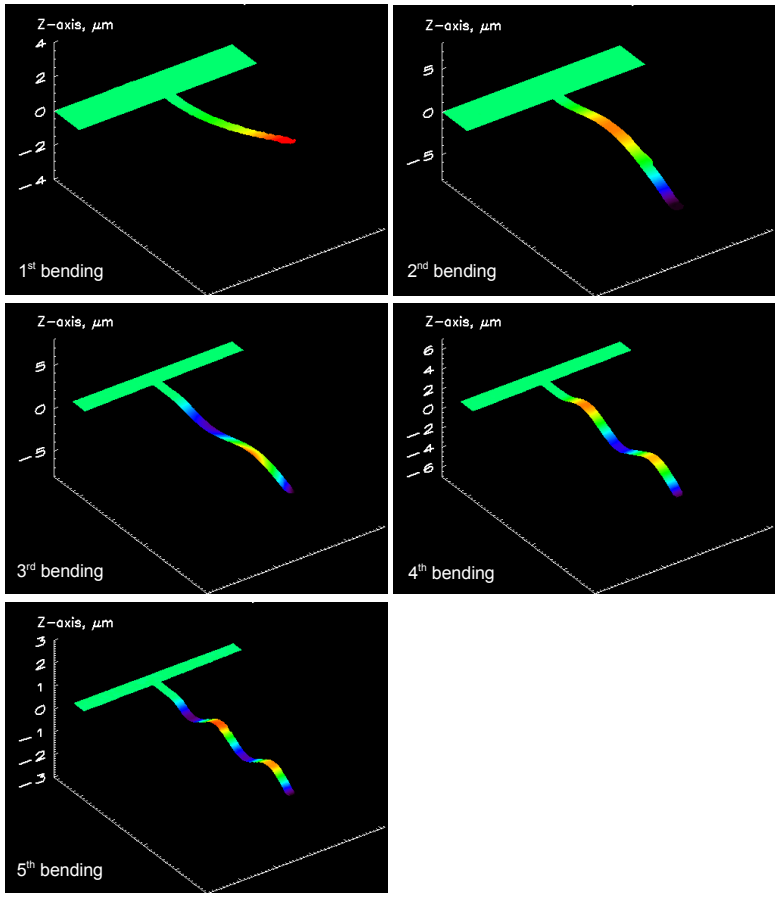

Fig. 82. Measurements of the fundamental bending modes of a microcantilever.

While characterizing dynamic behavior of the microcantilevers several observations were made. First, the frequency range at which the beams vibrate is much wider in air than it is in vacuum. Typically, the range was hundreds to thousands of Hz in air, but only a few Hz in vacuum for basically the same nominal frequencies characteristic of a given mode. Said another way, the resonant frequency peak is broad in air, but very narrow in vacuum. This is indicative of an increase in the quality factor of the cantilevers when they are in vacuum, and is further investigated in Section 8.4. Second, because of the broad resonant frequency range of the cantilevers in air, several complex modes were observed with time-average. This is because the frequency range of two fundamentally defined modes partially overlap. For example, the resonant modes observed in air between the frequencies of 234,390 Hz and 238,900 Hz are a combination of the 1st torsion and the 3rd bending modes. Another observation that can be made is that the resonant frequency shifts slightly from air to vacuum environments. In the case of the 1st bending mode, this shift is 158 Hz out of 14,202 Hz; the 2nd bending mode shifts 638 Hz from 88,430 Hz in air to 89,108 Hz in vacuum; and a similar comparison can be made for all of the fundamental bending modes. Also, in vacuum the 2nd torsion mode appears twice in the measurements, at 356,730 Hz and again at 713,720 Hz (double frequency) which indicates the sample is being excited in a second harmonic. The vibrometer can be utilized to verify that there is indeed a harmonic frequency acting on the sample.

8.4. Quality factor measurements of microcantilevers

The quality factor, Q, of a mechanical system indicates the amount of damping that is present (i.e., loss of energy per cycle of vibration). Determining the Q of many micro-structures, such as MEMS or AFM cantilevers, is often part of the methodology

used to quantify the performance of, or calibration of a specific device. In the case of AFM cantilevers, several calibration methods rely on the accurate knowledge of the Q factor (Burnham et al., 2003).

To measure the Q factor of the microcantilevers the ring down method (Yasumura et al., 2000) was utilized. This involves exciting the cantilever to resonance, abruptly stopping the excitation, and measuring the ring down of the cantilever. Once the exponential decay function is known, Q can be calculated as (Yasumura et al., 2000),

$$Q = \pi \cdot \tau^{-1} \cdot f_o \quad , \tag{57}$$

where f_o is the resonant frequency and τ is the exponential decay factor.

To measure the exponential decay, i.e., the ring down of the microcantilever, the vibrometer module was mounted on the interferometer. The microcantilevers with various coatings were mounted two chips per single PZT and excited in both vacuum and air. Typical excitation and ring down data, as recorded by the oscilloscope, are shown in Figs 83 and 84 for air and vacuum, respectively. The curves are sinusoidal but it is difficult to distinguish that fact because thousands of periods were recored; the resonance is in the 14 kHz range and the entire event can take several seconds in vacuum.

The ring down of the curve is of utmost interest. Extracting these data and fitting an exponential decay function allows the determination of Q per Eq. 57. The fitted exponential decay functions are plotted in Figs 85 and 86 for air and vacuum, respectively. Note that the microcantilevers ring nearly 200 time longer in vacuum than they do in air.

Based on the curves of figs 85 and 86, Q is calculated and plotted in Figs 87 and 88 for each microcantilever in air and vacuum, respectively. With the exception of the

two microcantilevers that have AFM tips, they are arranged from left to right in increasing aluminum coating thickness. With this arrangement, it is evident that the coating thickness reduces the Q of the microsystem.

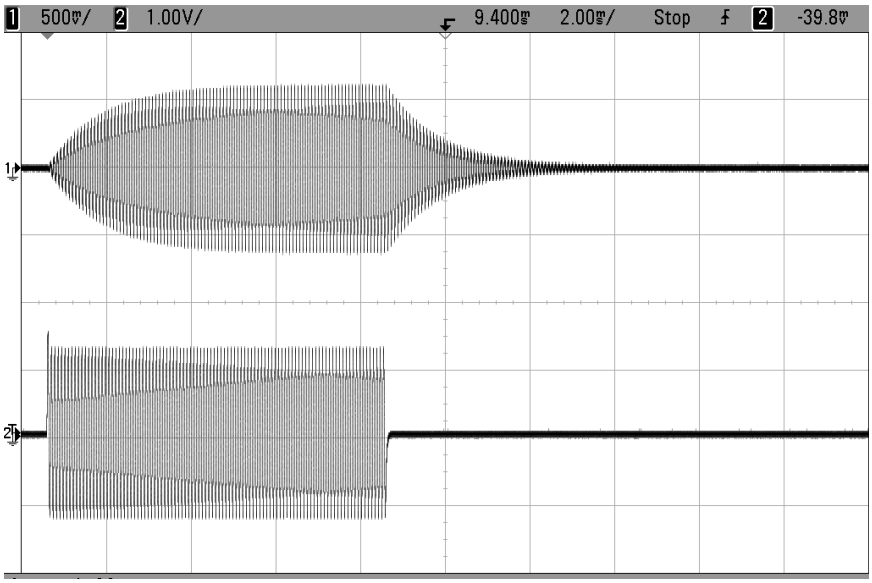

Fig. 83. Typical excitation and ring down of a microcantilever in air. Top: microcantilever velocity. Bottom: PZT excitation signal.

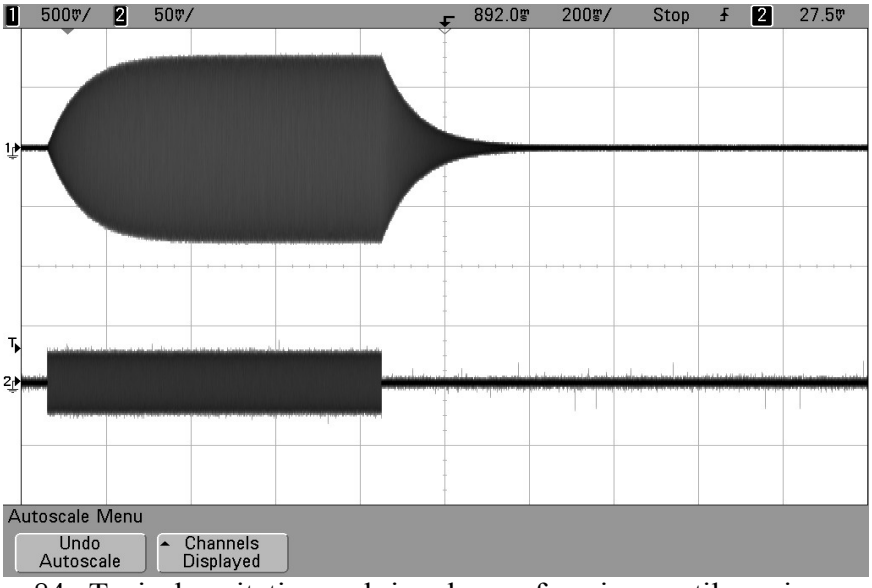

Fig. 84. Typical excitation and ring down of a microcantilever in vacuum. Top: microcantilever velocity. Bottom: PZT excitation signal.

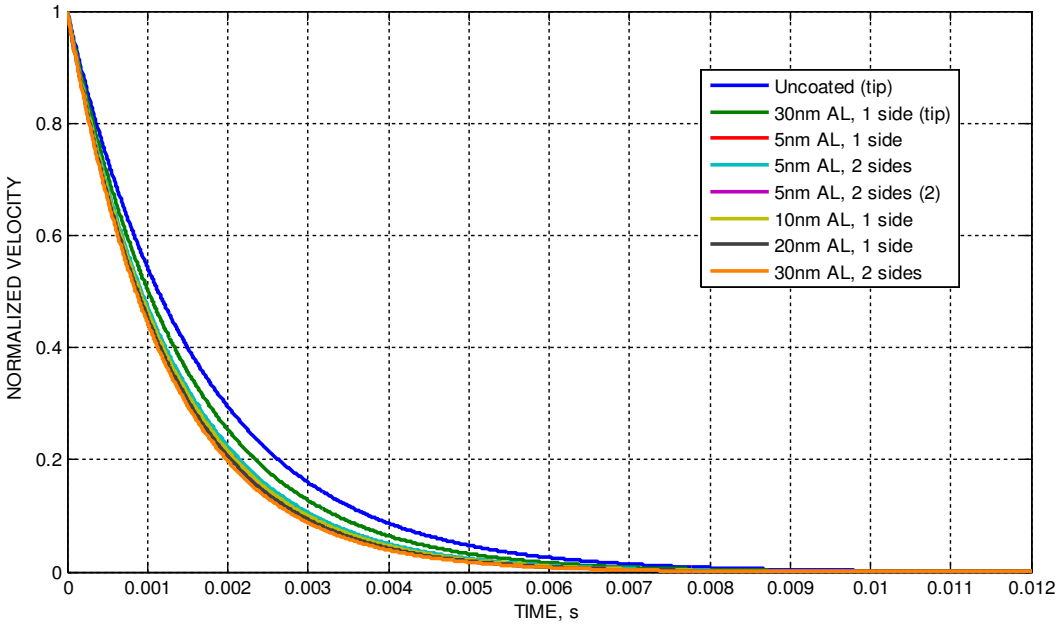

Fig. 85. Ring down curves of microcantilevers in air.

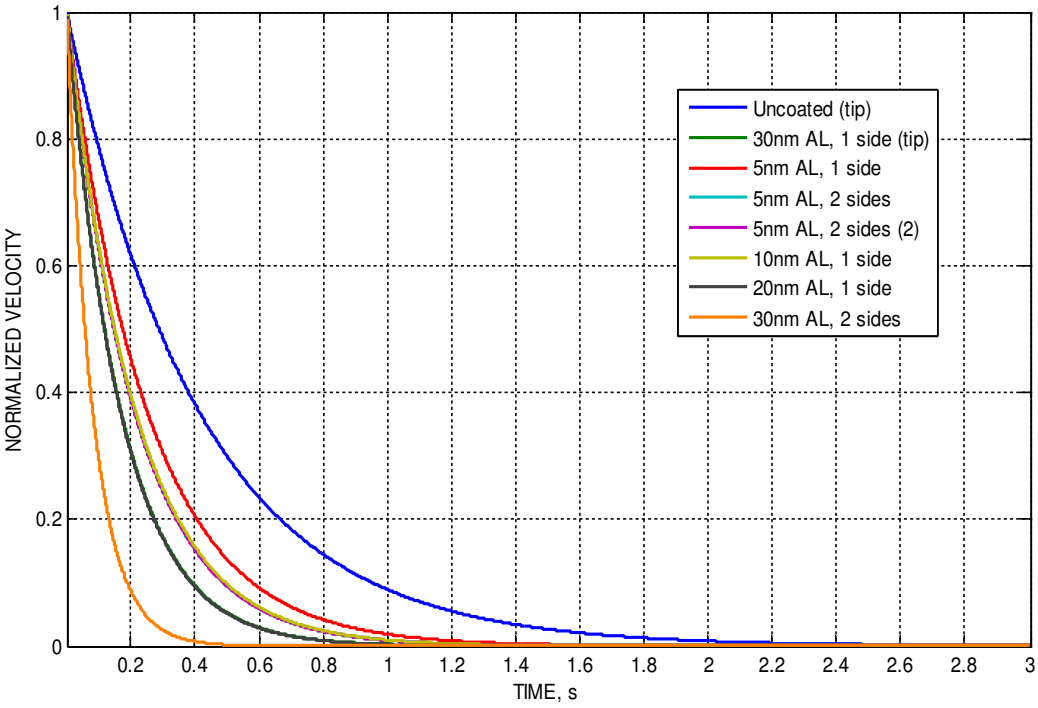

Fig. 86. Ring down curves of microcantilevers in vacuum.

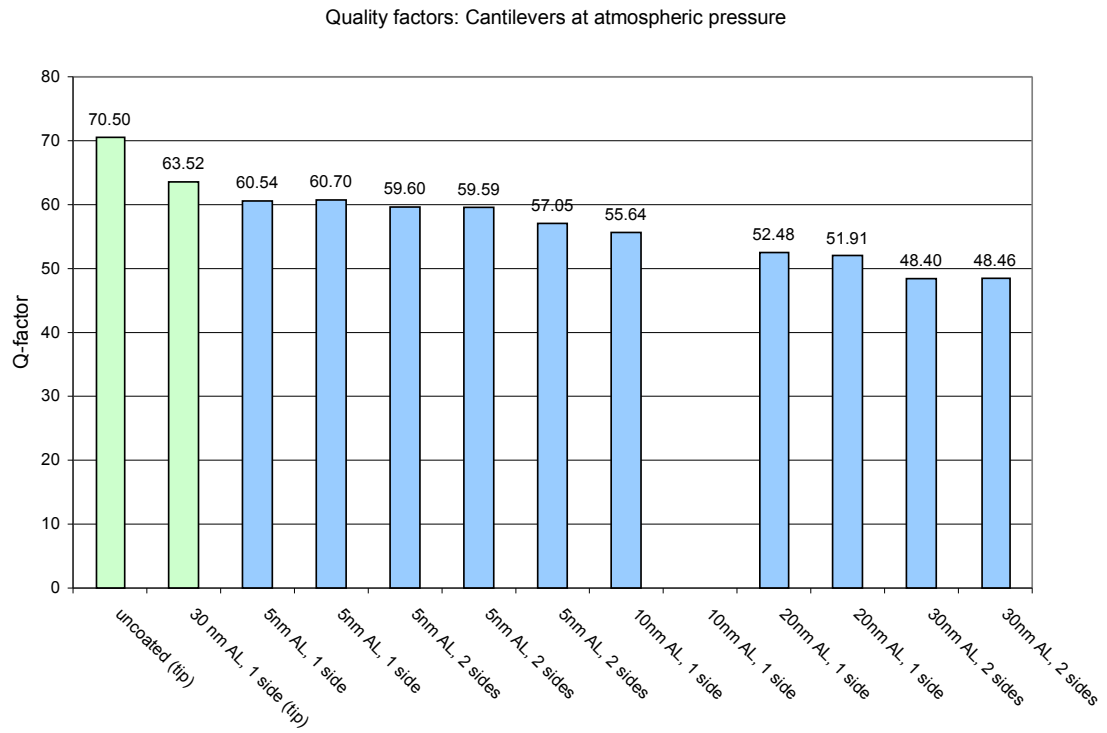

Fig. 87. Microcantilever Q factors based on ring down measurements in air. (All microcantilevers are tipless except as noted).

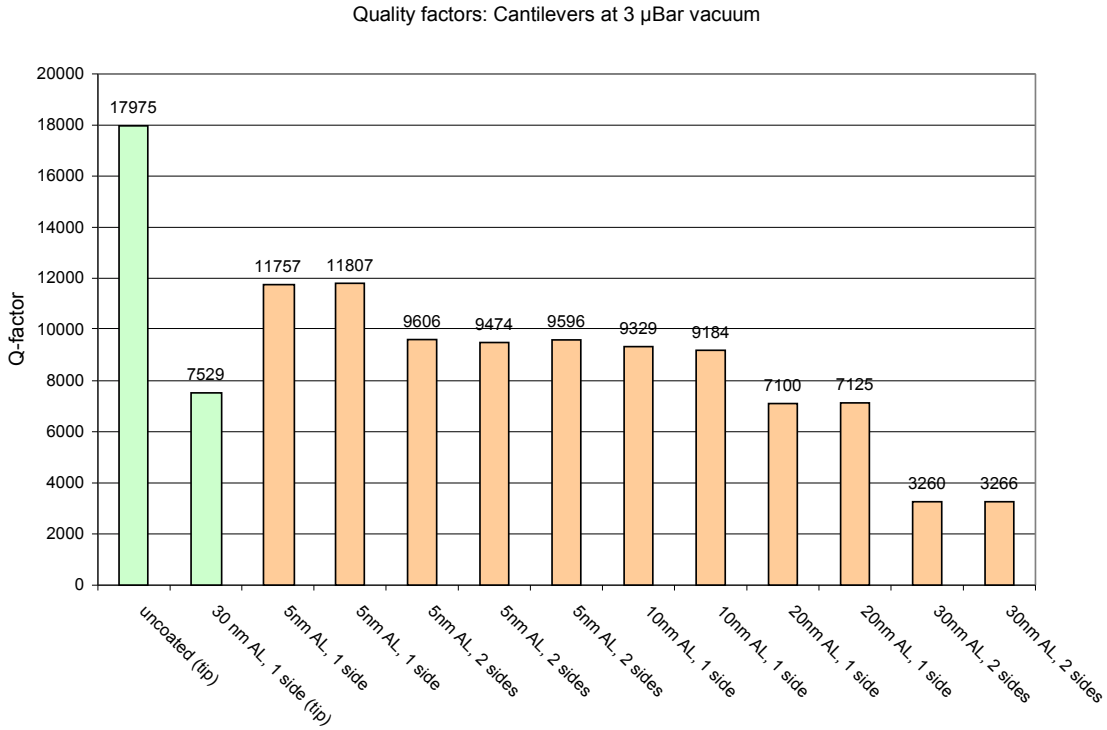

Fig. 88. Microcantilever Q factors based on ring down measurements in vacuum. (All microcantilevers are tipless except as noted).

8.5. Static shape measurements of a microgyroscope

To measure the shape of the proof masses of a microgyroscope, Fig. 89, the interferometer was configured with the high magnification interferometer module using a Michelson objective with the compensation window in place since the package was hermetically sealed with a clear glass cover. The phase steps were recorded in high resolution to resolve the narrow spring structures. Analysis of the recorded data show that the proof masses have residual stresses that cause them to deform approximately 700 nm from flat. Ideally, the proof masses should be flat as there is a capacitive sensor plate very precisely measuring the gap underneath each proof mass to determine rotational accelerations of the package. Any deformations of the proof masses could adversely affect performance of this device (Klempner et al., 2002).

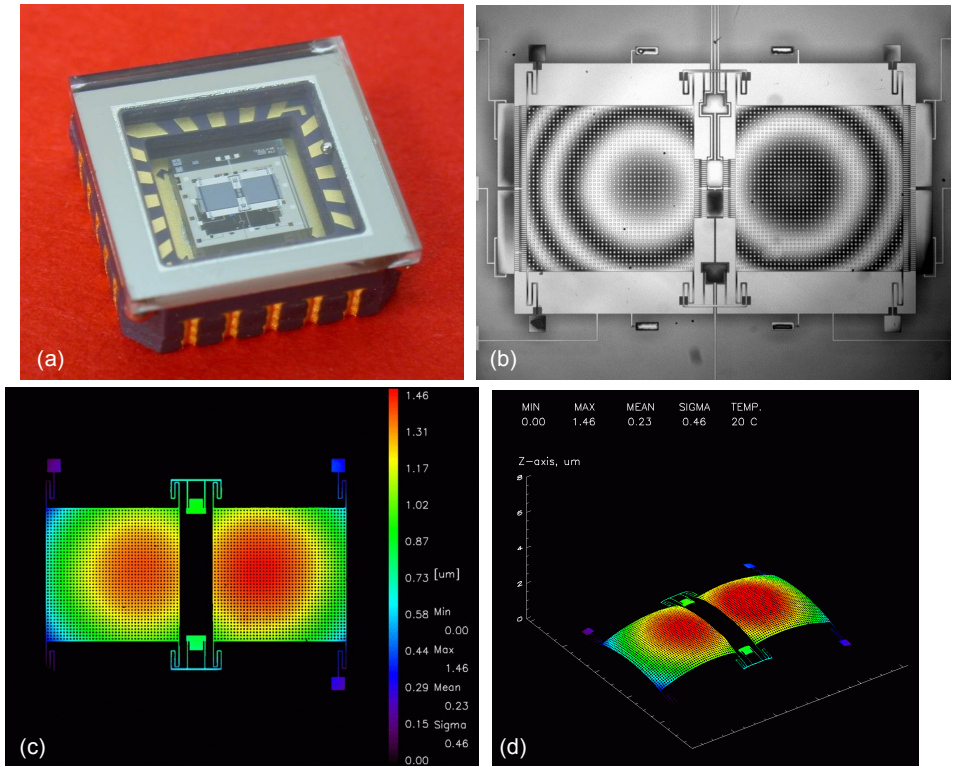

Fig. 89. Static shape measurement of a packaged dual proof mass microgyroscope. (a) Photograph of the packaged device with a clear lid, (b) interferometric fringe pattern, (c) 2D surface map of the measured proof mass structure, (d) 3D representation of (c).

8.6. SWLI measurements of a microengine

A microengine, Fig. 90, was placed under the high magnification interferometer and a series of vertically stepped measurements were performed. More specifically, 500 images were acquired at a step distance of 35 nm/step for a total scan depth of 17.5 µm. Three sample images from a scan of the microengine are shown in Fig. 91. From left to right the images represent a scan starting at the top of the device all the way through the substrate. Note how the fringes only appear on one surface at a time.

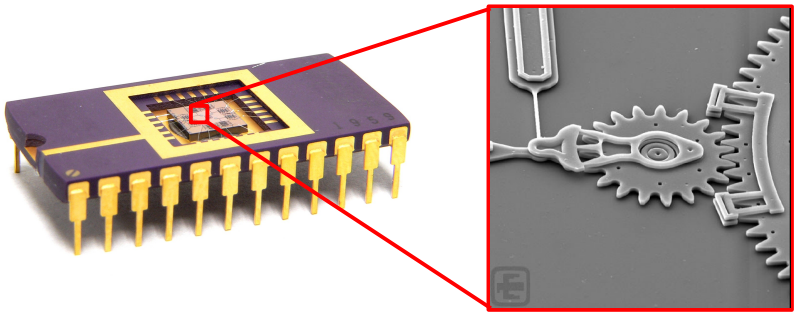

Fig. 90. A packaged microengine and a close-up of the gear train.

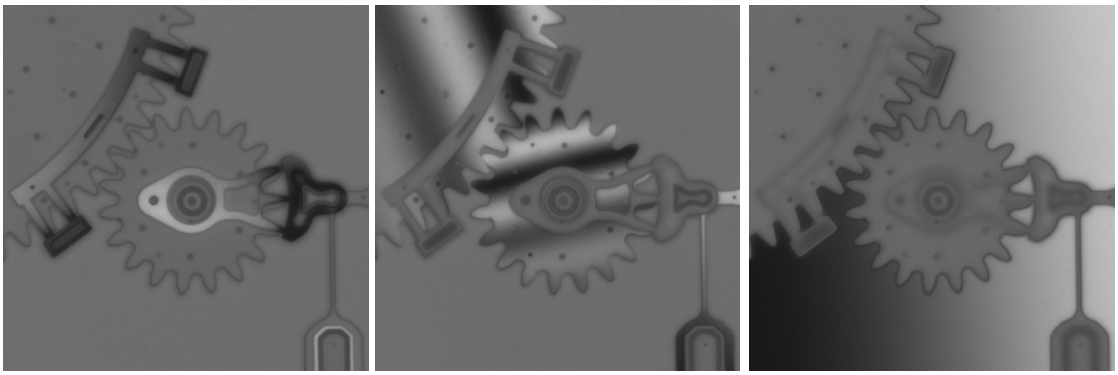

Fig. 91. Sample images from a SWLI image stack.

These 500 images are fed into a 3D array in Matlab for processing. If we trace one pixel through the entire scan we can track the modulation to show where the coherence peak is located, Fig. 92. A Hilbert filter is then applied to this signal to determine the

envelope. Once the envelope is found, the maximum is determined which corresponds to the height at which that pixel measured the surface to be located. Accuracy better than our 35 nm step is achieved by interpolating a spline between envelope points calculated by the Hilbert function.

This process is performed for every pixel in the imaging array to build a full 3D surface map of the microengine, Figs 92 and 93.

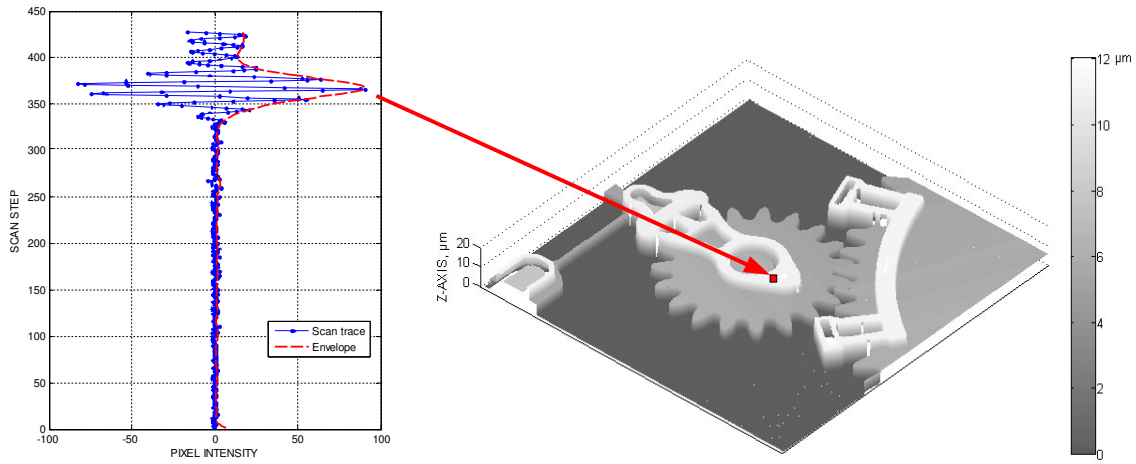

Fig. 92. A trace of one pixel through the image stack and the 3D measured surface.

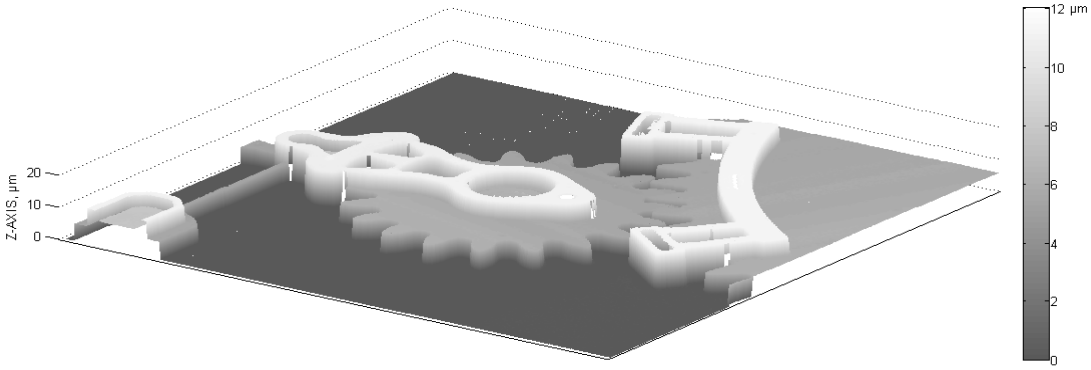

Fig. 93. An alternate view of the 3D measured surface of the microengine.

The results shown in Fig. 93 clearly indicate that SWLI is capable of measuring steps and discontinuities when characterizing MEMS. Traditional PSI methods would have only been able to analyze one continuous region at a time, and there would be no way to relate the various surfaces at different elevations.

9. CONCLUSIONS AND FUTURE WORK

A modular interferometric microscopy system has been developed and implemented as a measurement tool at the CHSLT. The system is comprised of a number of interchangeable modules to accommodate various size MEMS and packaging. Specifically, three interferometer modules have been developed to allow noninvasive point-wise measurement up to full-field-of-view measurement of objects 35 by 35 mm. The combined specifications of these interferometers are:

1) sub-nanometer out of plane resolution with a mean standard deviation of 0.485 nm across 12 calibration measurements,
2) accuracy has been demonstrated to be within 1.5 nm on a 3.0 μm test sample when compared to a Dektak surface profilometer,
3) the system is fully noninvasive in that no contact with the MEMS is ever required,
4) components with sub-micrometer features can be resolved with the high magnification interferometer module,
5) components as large as 35 by 35 mm can be measured full-field-of-view with the low magnification interferometer,
6) SWLI brings new measurement abilities to CHSLT by allowing the measurement of discontinuous surfaces with step heights greater than 200 μm (in comparison to the previous measurements systems which could only measure steps on the order of 150 nm, more than three orders of magnitude less),
7) using time-average and stroboscopic OEH modes, the high and low magnification interferometers can perform measurements of static and dynamic deformations spatially,

8) and using the vibrometer module, dynamic vibrations can be characterized temporally,
9) the vertical stage travel distance has improved from 20 mm to 600 mm allowing for almost any size measurement sample or loading device to be mounted,
10) the entire measurement station is mounted on a 700 lb. granite chassis that is pneumatically isolated from building vibrations, ensuring system stability while measurements are performed.

As the measurement specifications and abilities are listed above, a complete modular loading system has also been developed. The loading modules have the following capabilities:

1) a vacuum chamber with electrical and fluid pass-throughs can subject MEMS to vacuum as low as 3 μbar,
2) the chamber can be backfilled with dry gas to ensure a dry atmosphere,
3) a liquid HEX and TEC module can cool samples to -30°C or heat them to 120°C,
4) a set of PZT modules can dynamically excite MEMS from 100 Hz to 1.0 MHz,
5) an instrumentation rack complete with a signal generator, power source, oscilloscope, and spectrum analyzer can drive MEMS and measure electrical responses.

Having all of these capabilities in one location has greatly reduced the amount of experimental set up time and improved efficiency of the measurement process. What could take hours to days to set up and align with past interferometers, now can be completed in as little as five minutes with the modular system.

Future work that should be performed on the modular interferometric microscopy

system pertains to three areas.

First, improvements to the software utilized to record and analyze the data would be very beneficial. The current software, all developed in-house at the CHSLT, needs improvements in the user interface as a lot of the analysis is performed in command line scripts in various programs. This implies that there is a very steep learning curve and the user needs to be familiar with both the IDL and Matlab programing languages. Integration of all of the recording and analysis routines into one stand alone application with a user friendly interface would be very beneficial.

Second, the microscope chassis developed in this Thesis would lend itself quite nicely to the addition of a Fizeau large area interferometer. Such an interferometer would allow the measurement of entire wafers that MEMS are fabricated on. A Fizeau interferometer module that has a 4 in. diameter field of view could be a useful tool to characterize wafers at various stages of processing in the on-campus MEMS fabrication facility.

Third, improvements to the new SWLI system could speed up the measurement process and accuracy. Currently, the preliminary results shown herein were realized by recording and analyzing approximately 500 images that were each 500 by 500 pixels in size. The recording of the scan took on the order of 20 seconds, however a significant amount of time, nearly 20 minutes, was required to analyze the images in Matlab on a dual P4 3.4 Ghz computer with 2 GB of RAM. For comparison, an analysis of a single set of phase stepped interferometric measurements takes less than one minute of processing time on images one mega pixel or larger. If the SWLI were to be utilized to record multi-mega pixel arrays, processing could take many hours. For this reason,

optimization of the SWLI analysis code is desired. Also, it would be beneficial to obtain a NIST traceable step standard with steps ranging from sub-micrometer to 200 micrometers to verify our preliminary calibration.

10. REFERENCES

G. C. Brown, 1999, *Laser interferometric methodologies for characterizing static and dynamic behavior of microelectromechanical systems (MEMS)*, Ph.D. Dissertation, Worcester Polytechnic Institute, Worcester, MA.

G. C. Brown and R. J. Pryputniewicz, 2000, "New test methodology for static and dynamic shape measurements of microelectromechanical systems" *Opt. Eng.*, 39:127-136.

N. A. Burnham, X. Chen, C. S. Hodges, G. A. Matei, E. J. Thoreson, C. J. Roberts, M. C. Davies, and S. J. B. Tendler, 2003, "Comparison of calibration methods for atomic-force microscopy cantilevers," *Nanotechnology*, 14:1-6.

R. Dändliker and R. Thalmann, 1985, "Heterodyne and quasi-heterodyne holographic interferometry," *Opt. Eng.*, Vol. 25 No. 5, pp 824-831.

Encarta Online Encyclopedia, 2006, *Christopher Columbus*, http://encarta.com/encyclopedia_761568472_2/Christopher_Columbus.html, accessed 11/06.

C. Furlong, 1999, *Hybrid, experimental and computational, approach for the efficient study and optimization of mechanical and electro-mechanical components*, Ph.D. Dissertation, Worcester Polytechnic Institute, Worcester, MA.

K. J. Gåsvik, 2002, *Optical Metrology 3rd Ed.*, Wiley, W. Sussex, England, pp. 37-41, 165-167.

A. Harasaki, J. Schmit, and J. C. Wyant, 2000, "Improved vertical-scanning interferometry," *Applied Optics*, Vol. 39, No. 13, pp 2107-2110.

M. R. Hart, R. A. Conant, K. Y. Lau, and R. S. Muller, 2000, "Stroboscopic interferometer system for dynamic MEMS characterization," J. MEMS, 9, pp. 409-418.

T. R. Hsu, 2002, *MEMS & microsystems, design and manufacture*, McGraw-Hill, New York, NY, pp. 390-393.

In-Stat, 2006, *MEMS shipments to grow 20% per year through 2009*, http://www.instat.com/newmk.asp?ID=1426, accessed 11/06.

M. H. Jones and S. H. Jones, 2000, *Optical properties of silicon*, Virginia Semiconductor, Fredericksburg, VA, pp-1-10.

A. R. Klempner, T. F. Marinis, J. W. Soucy, C. Furlong, and R. J, Pryputniewicz, 2002, "OELIM characterization of thermal deformations of a MEMS package", *Proc. IMAPS-NE 29th Annual Symp.*, Boxboro, MA, pp. 149-154.

A. R. Klempner, 2003, *Development of a compact interferometer for MEMS package characterization*, Major Qualifying Project, Worcester Polytechnic Institute, Worcester, MA.

A. R. Klempner, P. Hefti, R. T. Marinis, R. J. Pryputniewicz, 2004, "Development of a high stability optoelectronic laser interferometric microscope for characterization and optimization of MEMS," *Proc. 15th Internat. Invitational UACEM Symp.,* Springfield, MA, pp. 275-285.

A. R. Klempner, R. T. Marinis, P. Hefti, and R. J. Pryputniewicz, 2005, "Development of a thermal loading system for OELIM characterization of MEMS,"*Proc. IMAPS-NE 32nd Annual Symp.,* Boxboro, MA, pp. 89-92.

T. Kreis, 1996, *Holographic interferometry principles and methods*, Akademie Verlag GmbH, Berlin, pp. 21-26, 123-138, 201-207.

K. J. Kuhn, 1998, *Laser engineering*, Prentice Hall, Upper Saddle River, NJ, pp. 275.

Lowell Observatory, 2003, "History of interferometry", Press Release, Flagstaff, AZ, http://www.lowell.edu/Press/interfer.html, accessed 4/03.

R. T. Marinis, A. R. Klempner, S. P. Mizar, P. Hefti, and R. J. Pryputniewicz, 2005, "Stroboscopic illumination using LED light source," *Proc. IMAPS N.E. 32nd Annual Symp.,* Boxboro, MA, pp. 392-396.

S. P. Mizar and R. J. Pryputniewicz, 2000, "New approach to measurements of shape memory alloys by ACES methodology," *Proc. IX Internat. Congress on Exp. Mech.*, SEM, Bethel, CT, pp. 1013-1016.

S. Nakadate, 1986, "Vibration measurement using phase-shifting time-average holographic interferometry," *Appl. Opt.,* Vol. 25, No. 22, pp. 4155-4161.

Newport, 2006a, "I-325A vertical frequency transmissibility graph," http://www.newport.com/images/webclickthru-EN/images/1377000.gif, accessed 11/06.

Newport, 2006b, "Vibration control technical reference," http://www.newport.com/store/genproduct.aspx?id=168093&lang=1033&Section=Detail, accessed 11/06.

S. P. Pacheco, L. P. B. Katehi, and C. T.-C. Nguyen, 2000, "Design of low actuation voltage RF MEMS switch", *Proc. Microwave Symp. Digest. 2000 IEEE MIT-S Internat.*, pp. 165-168.

Polytec, 2006, "Principles of laser Doppler vibrometry" http://www.polytec.com/usa/158_942.asp, accessed 10/06.

D. R. Pryputniewicz, C. Furlong, and R. J. Pryputniewicz, 2001, "ACES approach to the study of material properties of MEMS," *Proc. Internat. Symp. on MEMS: Mechanics and Measurements*, Portland, OR, pp. 80-83.

R. J. Pryputniewicz, 1976, *Holographic analysis of body deformations*," Ph.D. Dissertation, University of Connecticut, Storrs, CT.

R. J. Pryputniewicz, 1985, "Laser method for studies of energy systems," in: *Handbook of energy systems engineering*, L. C. Wilbur, ed., Wiley, pp. 1498-1512.

R. J. Pryputniewicz, 1986, "Computer-aided fringe analysis," *Proc. SPIE Internat. Conf. on Holography Applications*, Vol. 673, pp. 250-257.

R. J. Pryputniewicz and K. A. Stetson, 1990, "Measurement of vibration patterns using elecrooptic holography," *SPIE*, 1162:456-467.

R. J. Pryputniewicz, 1995, "Quantitative determination of displacements and strains from holograms," Ch. 3 in *Holographic interferometry*, Vol. 68 of Springer Series in Sciences, Springer-Verlag, Berlin, Germany, pp. 33-72.

R. J. Pryputniewicz, M. P. de Boer, and G. C. Brown, 2000, "Advances in optical methodology for studies of dynamic characteristics of MEMS microengines rotating at high speeds," *Proc. IX Internat. Congress on Exp. Mech.*, SEM, Bethel, CT, pp. 1009-1012.

R. J. Pryputniewicz, C. Furlong, G. C. Brown, E. J. Pryputniewicz, and M. E. Seta, 2001a, "ACES methodology for studies of MEMS," *Proc. 28th Annual Symp. & Exhibition of IMAPS-NE*, Boxboro, MA, pp. 208-217.

R. J. Pryputniewicz, C. Furlong, G. C. Brown, E. J. Pryputniewicz, and M. E. Seta, 2001b, "Optoelectronic method for studies of MEMS," *Proc. Internat. Congress on Experimental and Applied Mechanics for Emerging Technologies*, Portland, OR, pp. 817-820.

R. J. Pryputniewicz, 2003a, *Thermomechanical design and analysis of microsystems*, Worcester Polytechnic Institute, Worcester, MA, Chapter 8, p. 1.

R. J. Pryputniewicz, 2003b, *Holographic numerical analysis,* Worcester Polytechnic Institute, Worcester, MA, pp. 5-2 – 5-12, 10-2 – 10-13.

R. J. Pryputniewicz and C. Furlong, 2003, "Novel optoelectronic methodology for testing of MOEMS," *Proc. Internat. Symp. on MOEMS and Miniaturized Systems III*, SPIE-4982:11-25.

D. W. Robinson and G. T. Reid, 1993, *Interferogram Analysis*, Institute of Physics Publishing, Bristol, England, pp. 23-29, 109-110.

J. Schwider, R. Burow, K. E. Elssner, J. Grzanna, R. Spolaczyk, and K. Merkel, 1983, "Digital wave-front measuring interferometry: some systematic error sources," *Appl. Opt.*, Vol. 22 , pp. 3421-3432.

K. A. Stetson and R. L. Powell, 1966, "Hologram interferometry," *J. Opt. Soc. Am.* Vol. 56, pp. 1161-1166.

R. Sulouff, 2003, "Taking inertial MEMS products to the market place", Seminar at Worcester Polytechnic Institute, Micromachined Products Division, Analog Devices Cambridge, MA 02139.

C. M. Vest, 1979, *Holographic Interferometry,* Wiley, New York, pp. 1-30.

K. Y. Yasumura, T. D. Stowe, E. M. Chow, T. Pfafman, T. W. Kenny, B. C. Stipe, and D. Rugar, 2000, "Quality factor in micron- and submicron-thick cantilevers," *J. MEMS*, Vol. 9(1), pp. 117-125.

J. S. Yokum, C. Furlong, K. W. Franklin, G. D. Cockrell, and R. J. Pryputniewicz, 2001, "Fiber optic based optopelectronic holographic system for shape measurements,", *J. Practical Failure Analysis*, Vol. 1(6), pp. 63-70.

Zygo Corp., 2006, "NewView 6300 Specifications", http://www.zygo.com/products/nv6000/nv6300spec.pdf, accessed 3/06.

APPENDIX A. SCHEMATIC OF THE MODULAR INTERFEROMETRIC MICROSCOPY SYSTEM

The schematic of the modular interferometric microscopy system is reproduced at a larger scale, Fig. A.1, in this Appendix. A description of all of the components follows the figure in Table A.1.

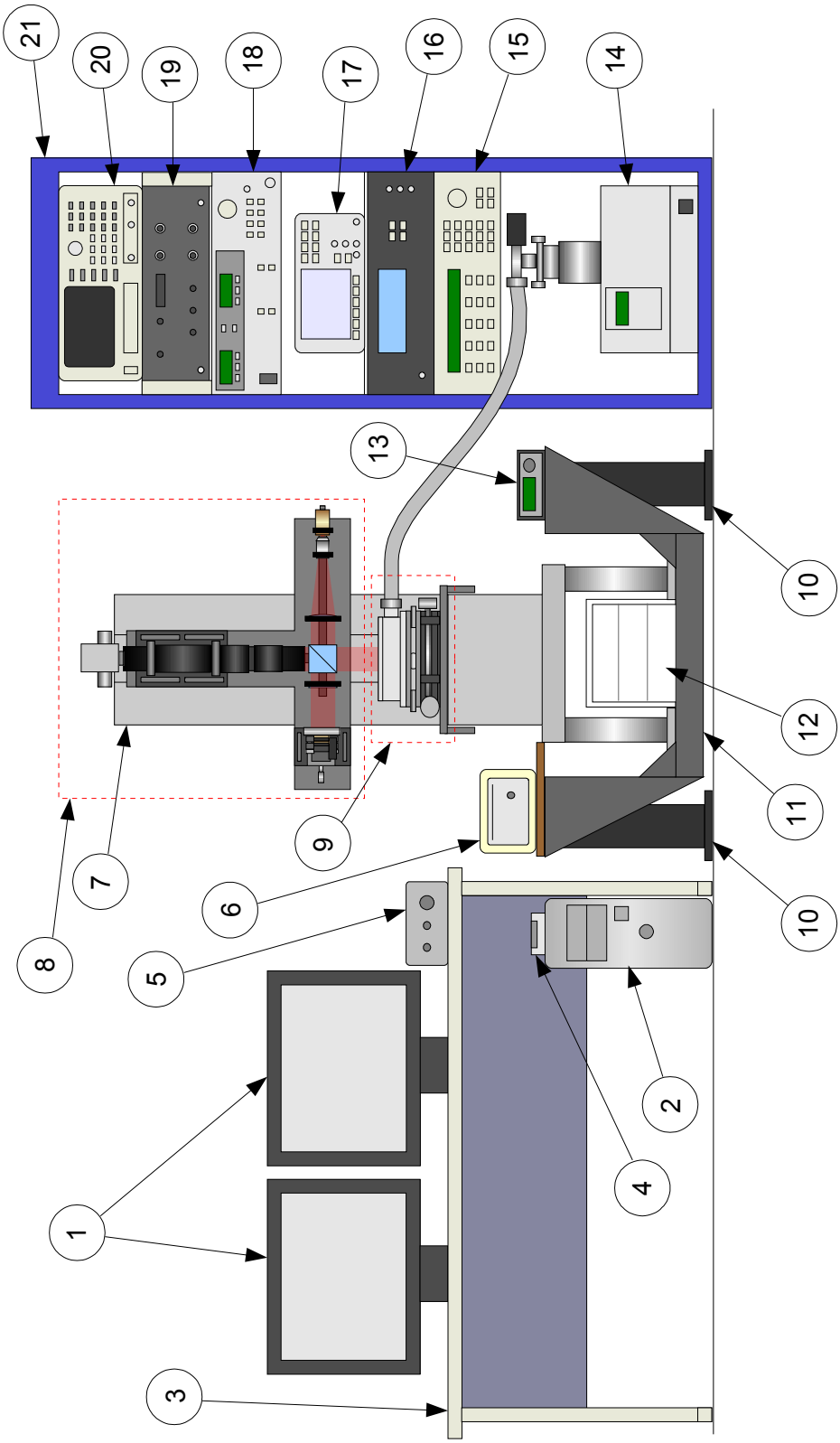

Fig. A.1. Enlarged schematic of the modular interferometric microscopy system.

Table A.1. Component list of the modular interferometric microscopy system.

Component #	Description
1	dual LCD monitors
2	host computer
3	desk
4	National Instruments I/O terminal
5	PZT controller/amplifier
6	vibrometer interferometer unit
7	granite microscope chassis
8	interferometer module, (low magnification module shown)
9	MEMS loading module, (environmental chamber module shown)
10	vibration isolator legs
11	cradle
12	storage bin for system modules, tools, and components
13	light source controller
14	turbomolecular vacuum pump system
15	signal generator
16	vibrometer controller
17	digital oscilloscope
18	TEC and LED controller
19	strobe pulse generator
20	spectrum analyzer
21	instrumentation rack

APPENDIX B. VARIOUS SYSTEM PHOTOGRAPHS

Figures B.1 and B.2 show the measurement station with the high magnification interferometer module and low magnification module mounted, respectively.

Fig. B.1. High magnification interferometer module.

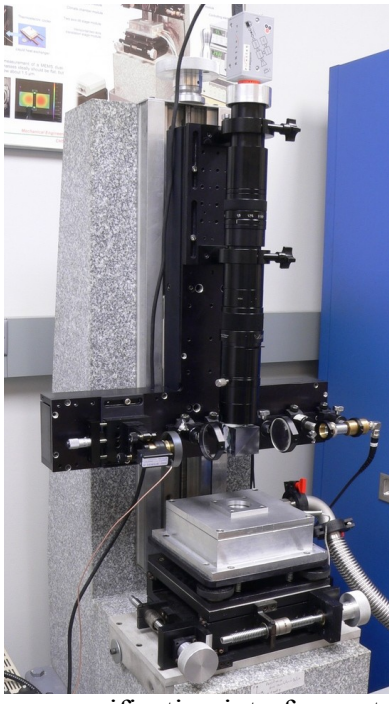

Fig. B.2. Low magnification interferometer module.

Figure B.3 is a photograph illustrating the optics utilized in the low magnification interferometer and the environmental chamber. Figure B.4 is a front view of the tilt stage showing its inner components.

Fig. B.3. Enlarged view of the low magnification interferometer module.

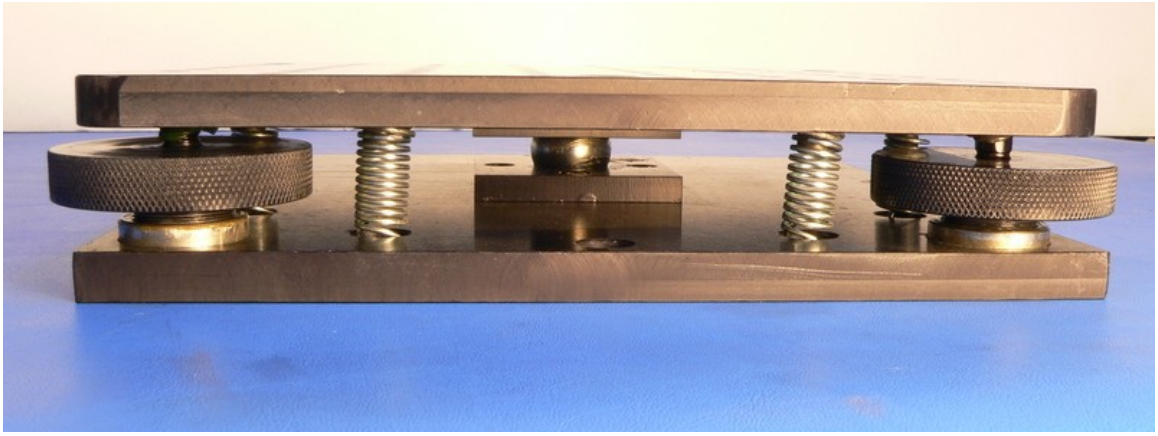

Fig. B.4. Side view of the custom designed and fabricated tilt stage.

Figures B.5 and B.6 illustrate the environmental chamber with the cover removed and affixed, respectively. In these photographs, a MEMS is mounted on the low profile PZT array. Note the electrical pass-throughs allowing a device to be powered if need be.

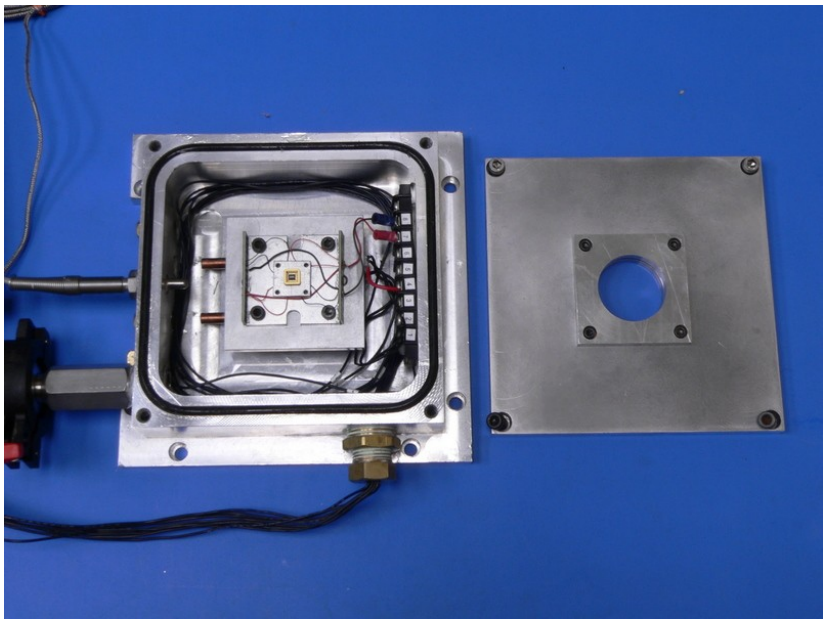

Fig. B.5. Photograph of the environmental chamber with cover off.

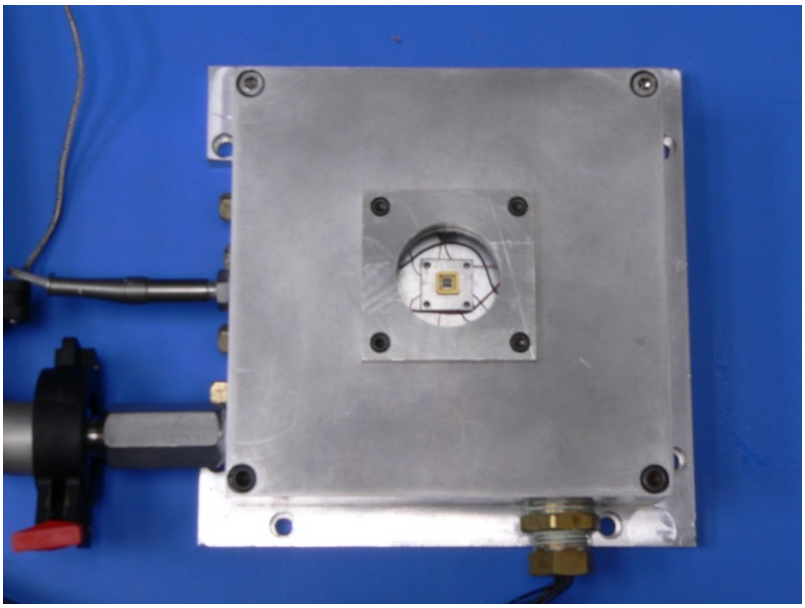

Fig. B.6. Photograph of the environmental chamber with cover in place.

APPENDIX C. MECHANICAL DRAWINGS

This Appendix includes mechanical drawings of all of the components that were developed for the modular interferometric microscopy system. Each of these components were fabricated and treated as noted on the drawings. Components were designed and fabricated for the low magnification interferometer, tilt stage, environmental chamber, vibrometer, and pneumatic isolation leg assembly, as noted on each drawing.

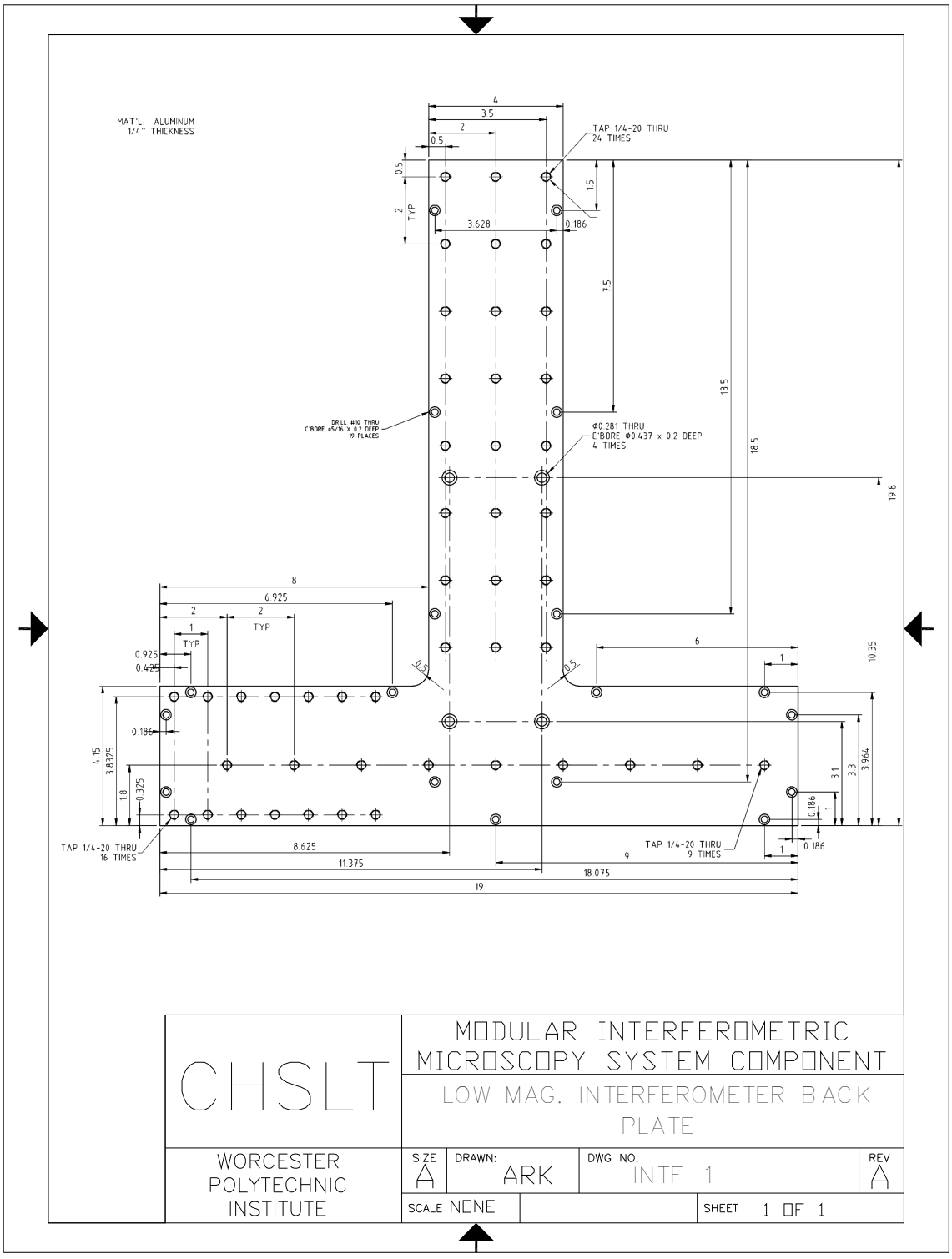

Fig. C.1. Low magnification interferometer back plate.

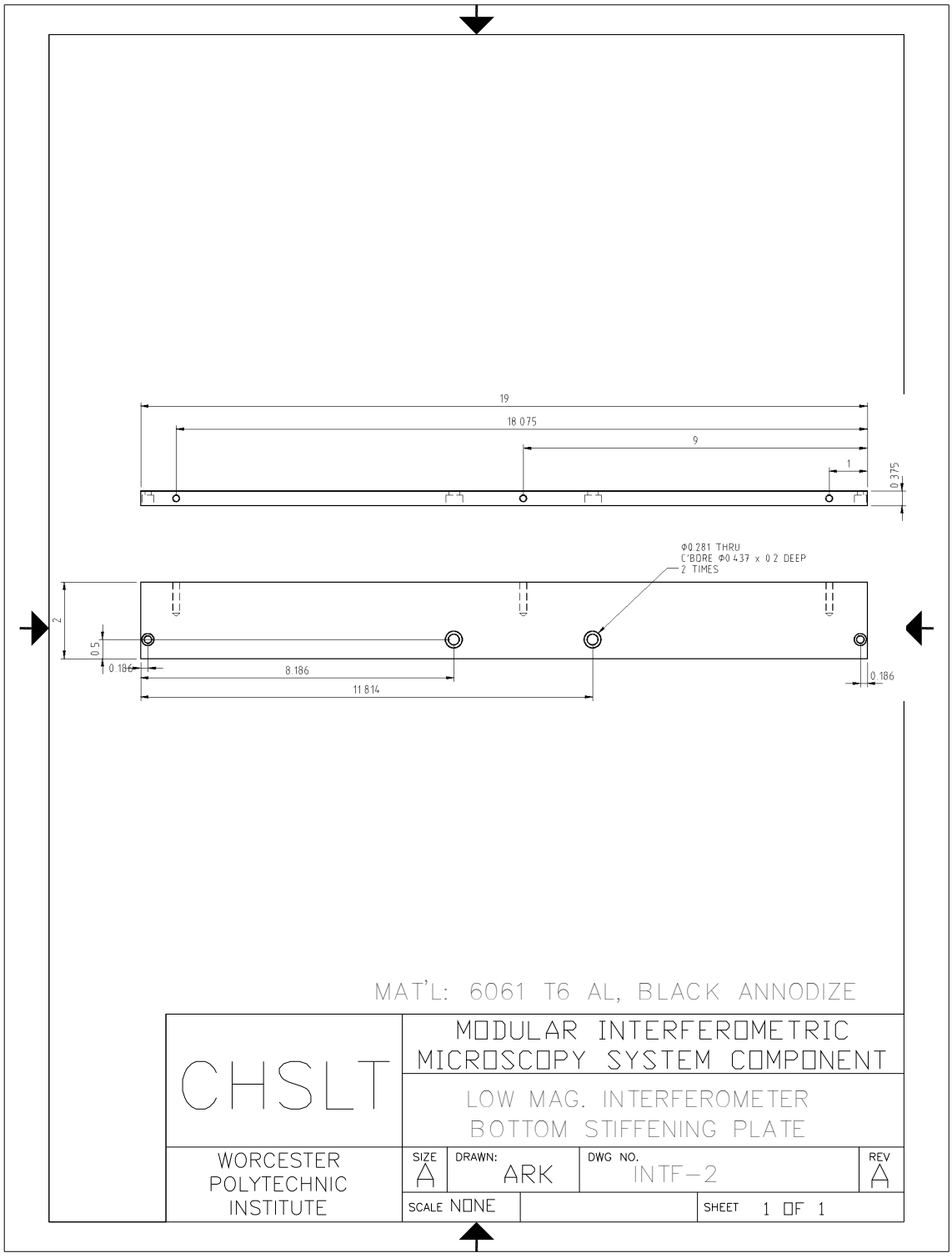

Fig. C.2. Low magnification interferometer bottom stiffening plate.

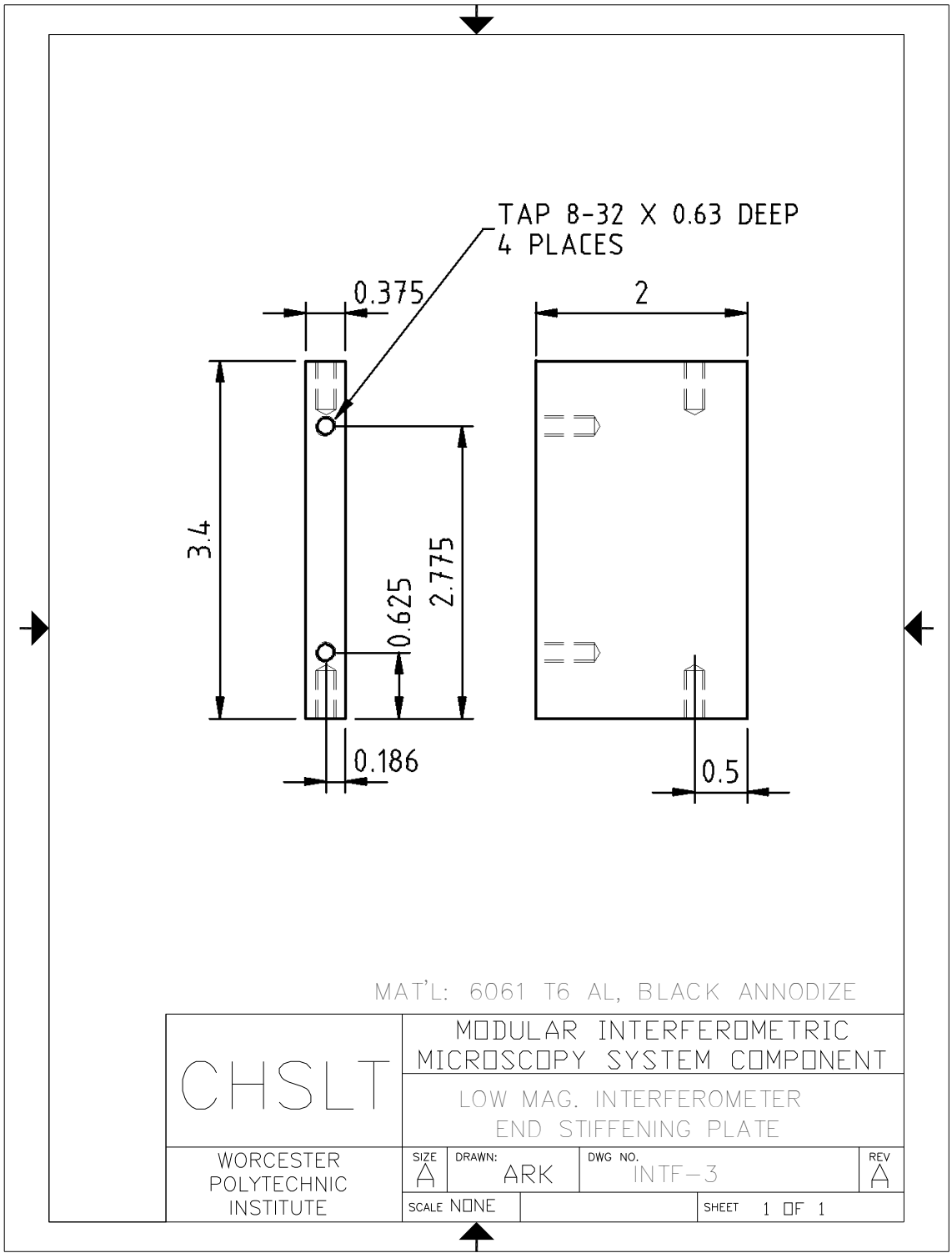

Fig. C.3. Low magnification interferometer end stiffening plate.

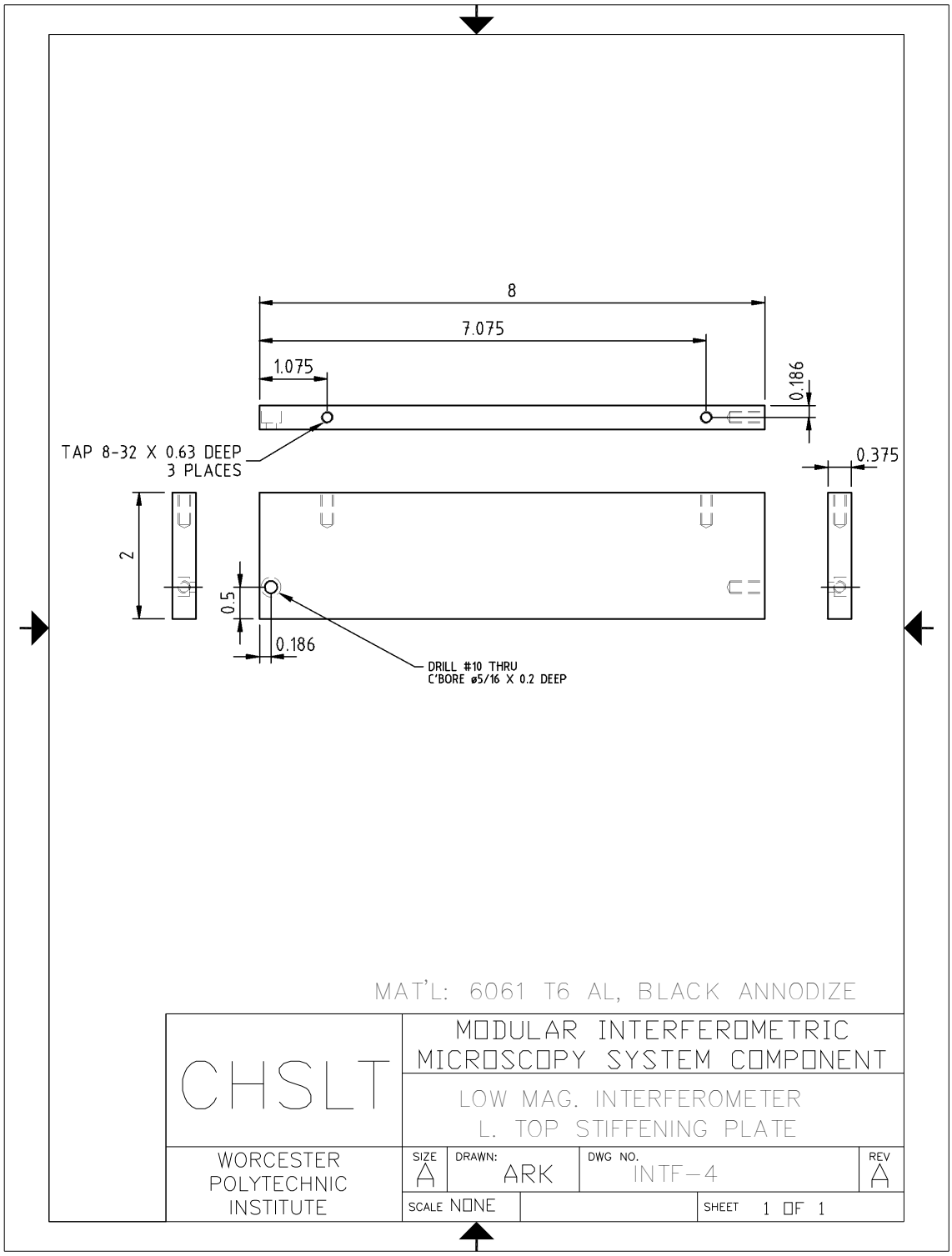

Fig. C.4. Low magnification interferometer left top stiffening plate.

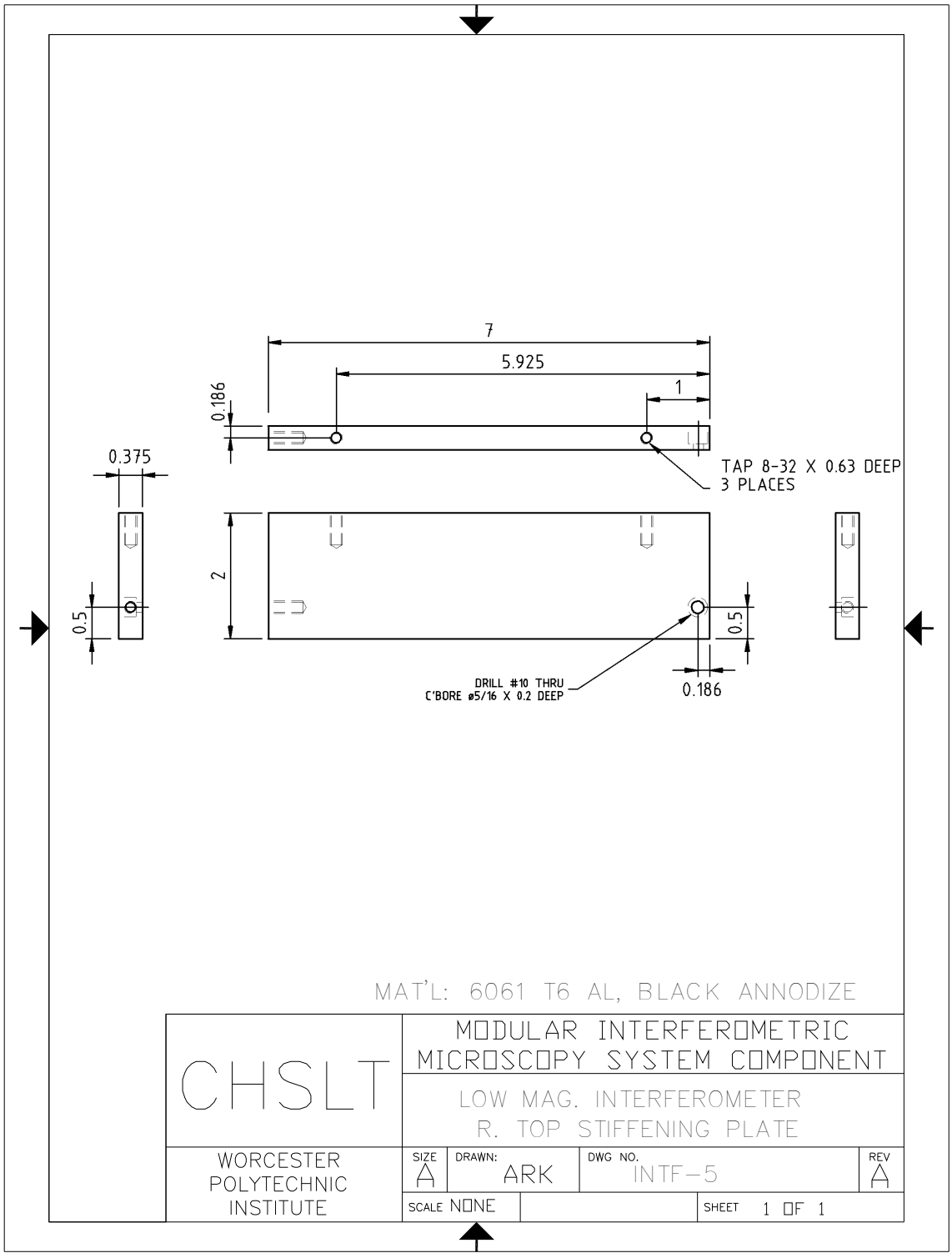

Fig. C.5. Low magnification interferometer right top stiffening plate.

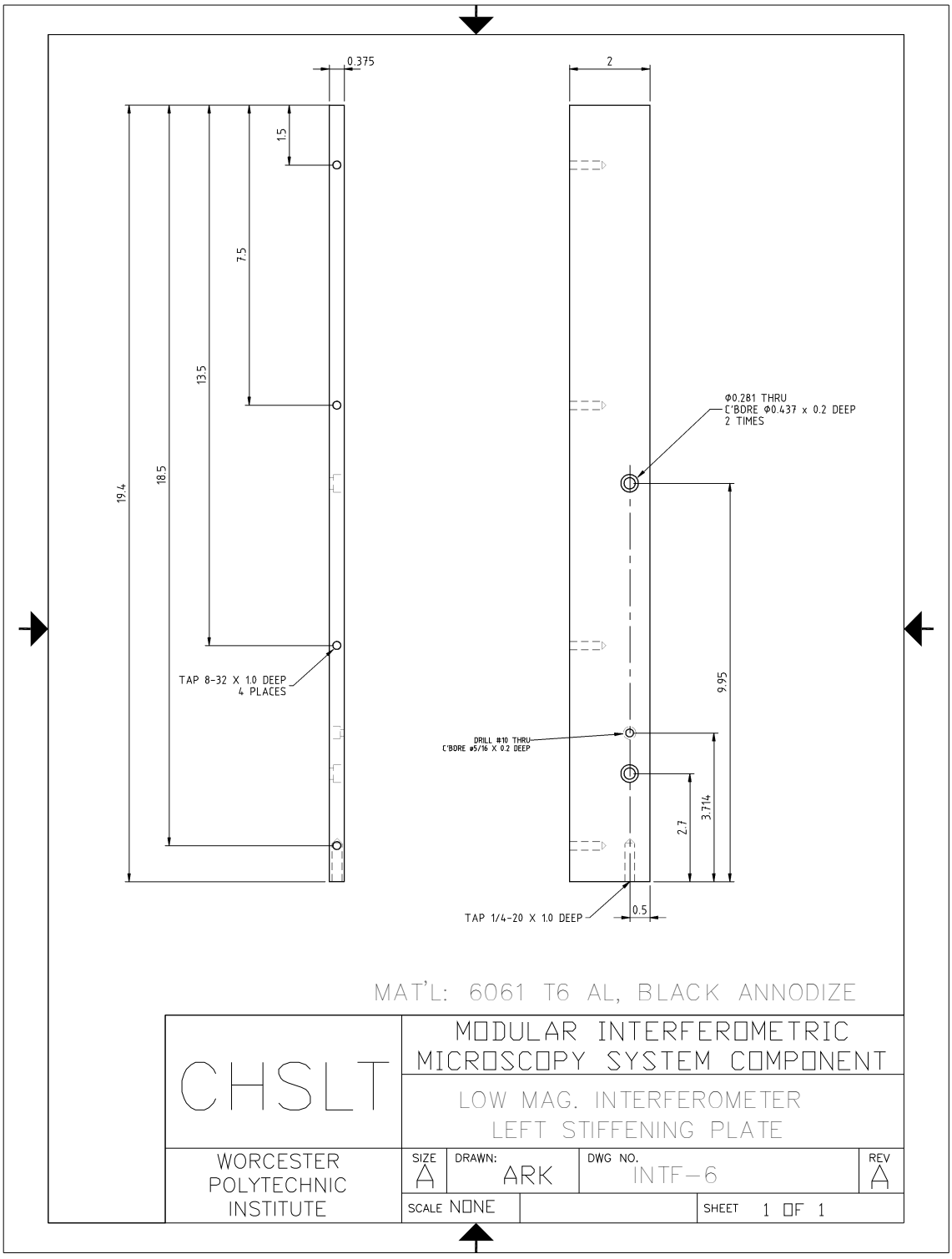

Fig. C.6. Low magnification interferometer left stiffening plate.

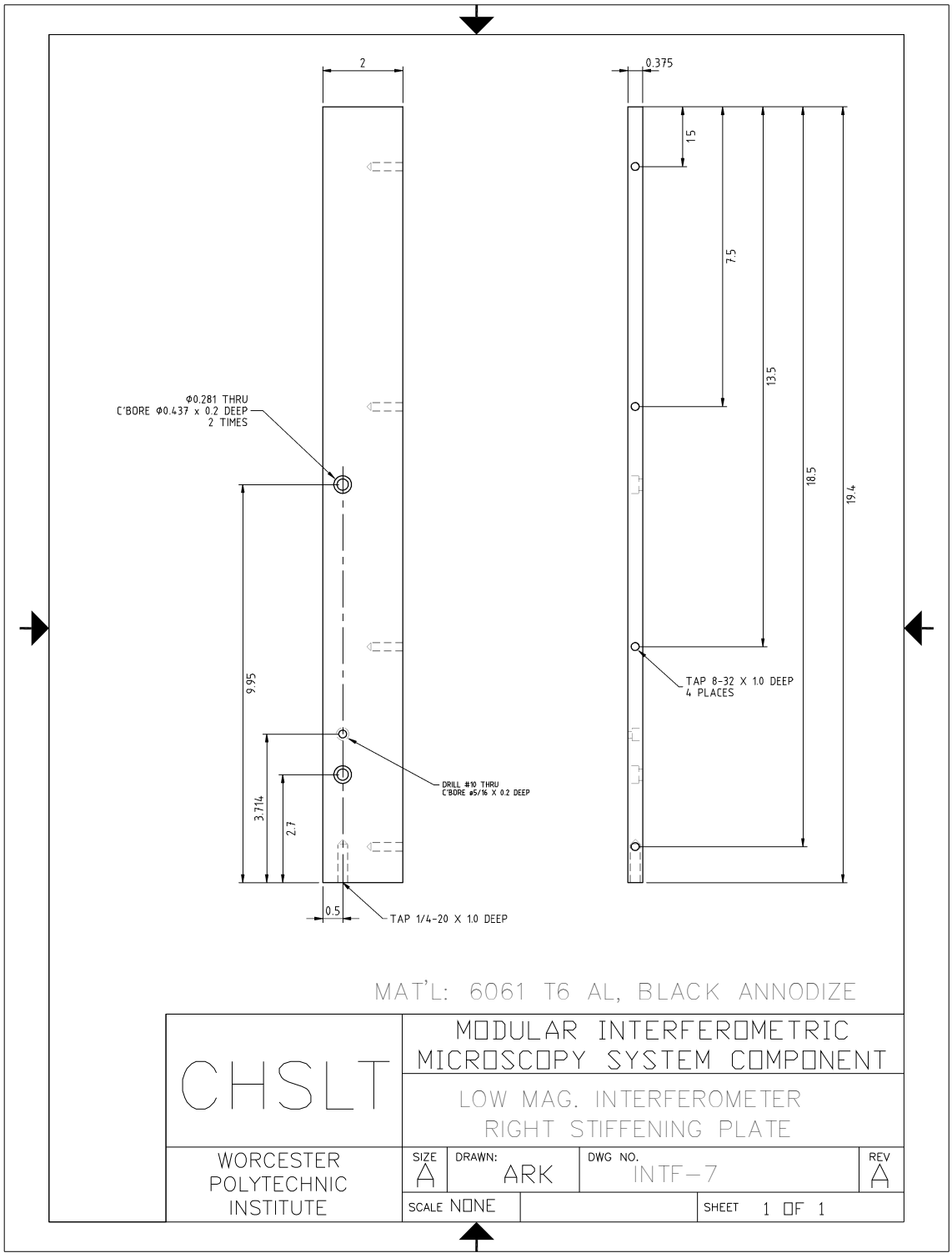

Fig. C.7. Low magnification interferometer right stiffening plate.

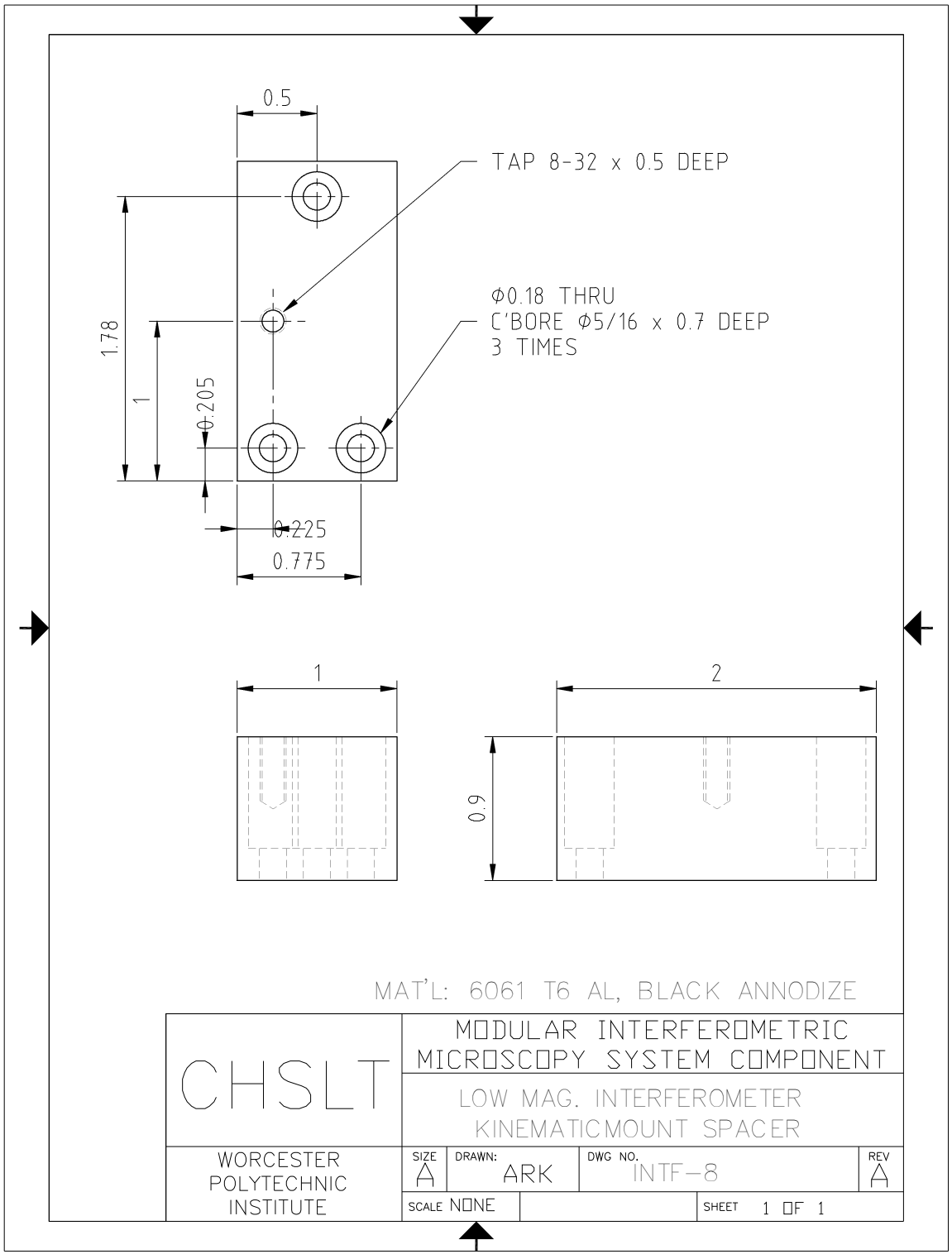

Fig. C.8. Low magnification interferometer kinematic mount spacer.

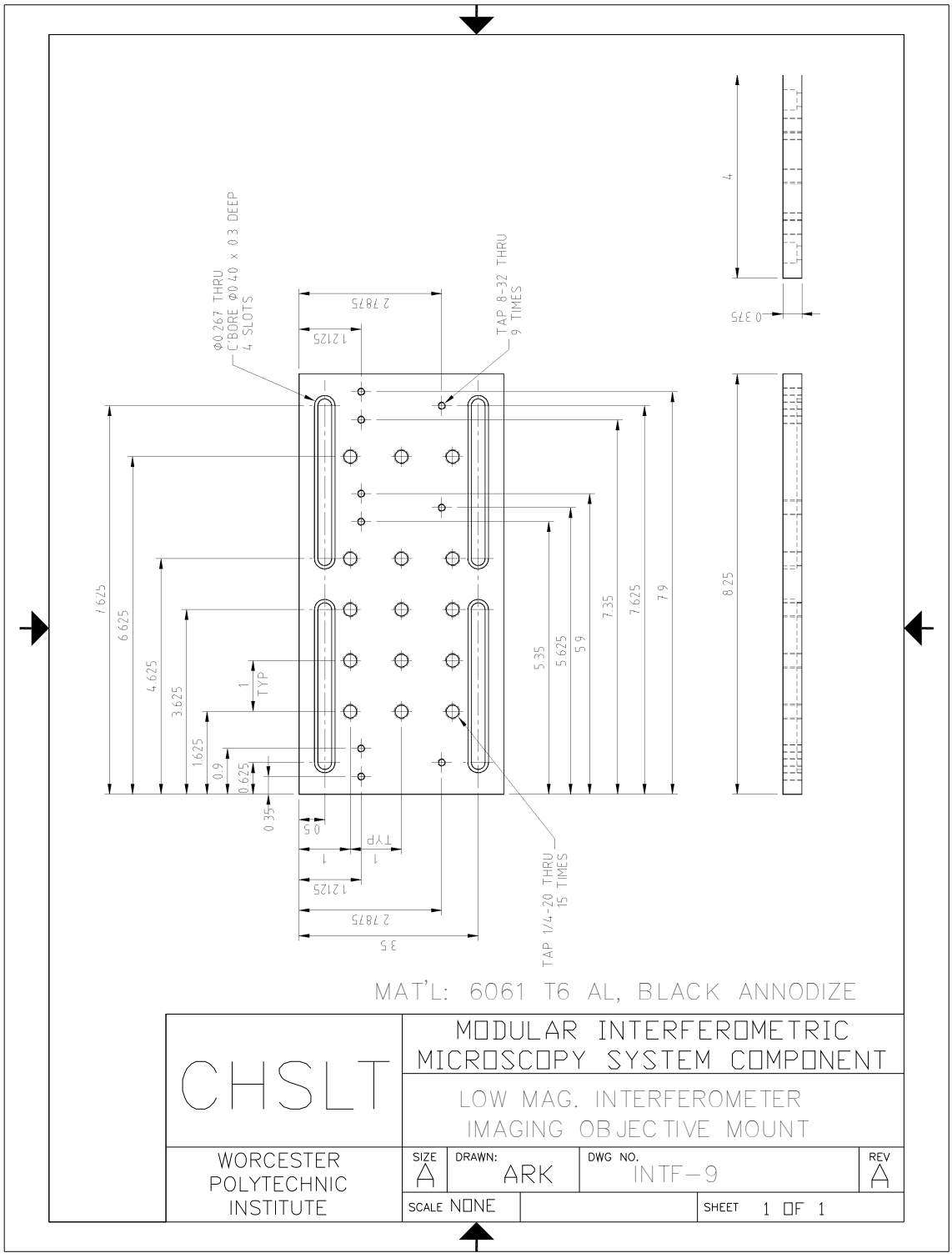

Fig. C.9. Low magnification interferometer imaging objective mount.

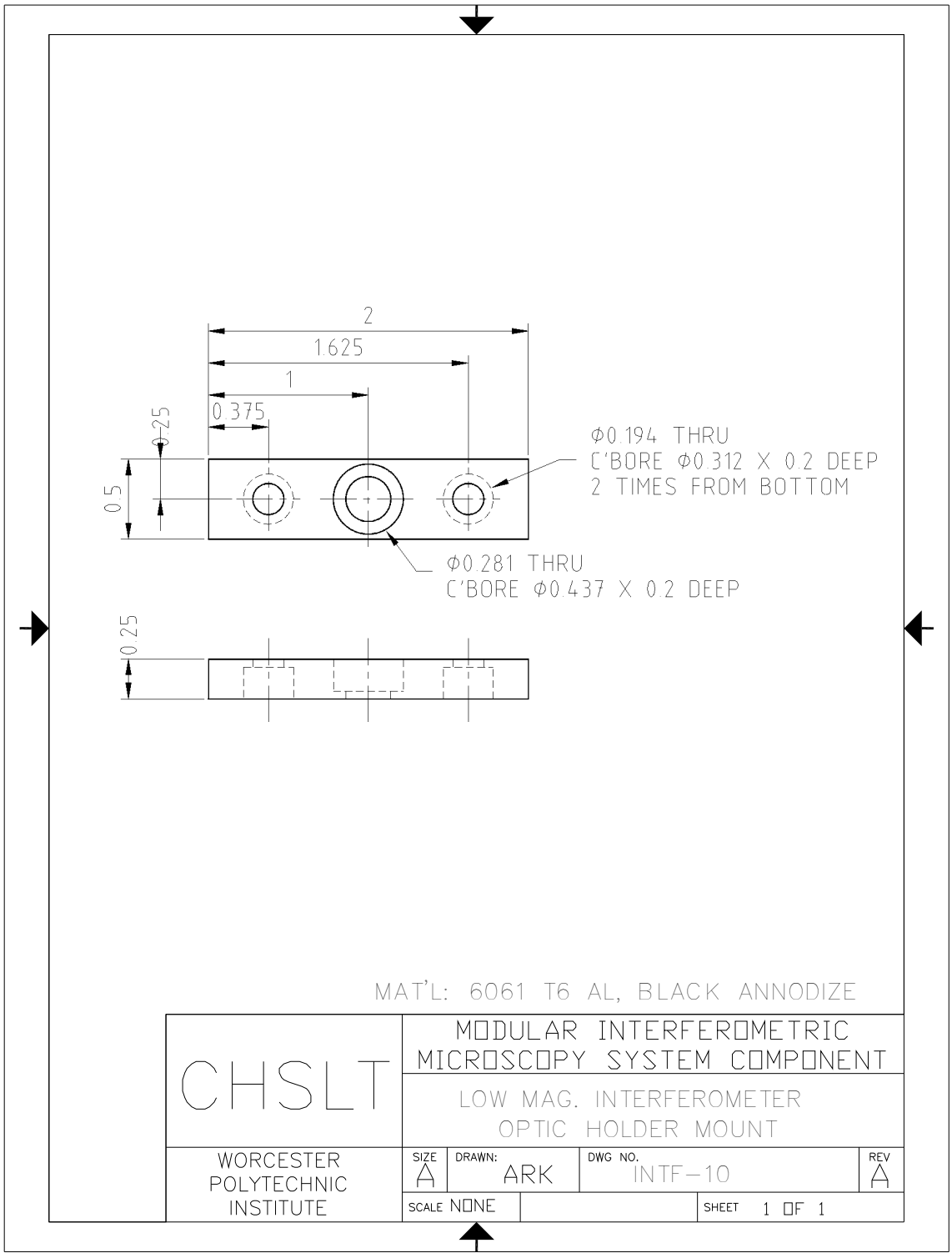

Fig. C.10. Low magnification interferometer optic holder mount.

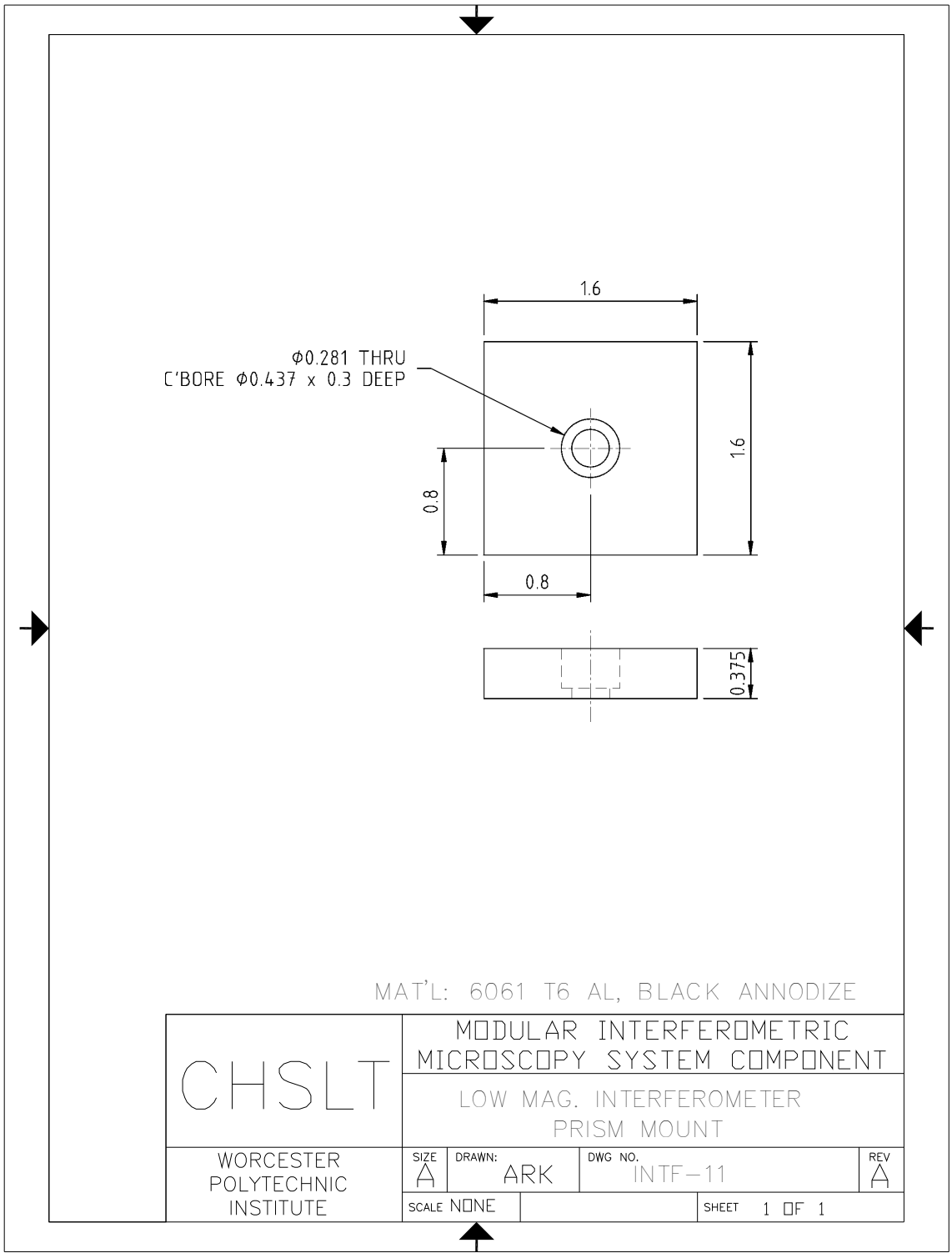

Fig. C.11. Low magnification interferometer prism mount.

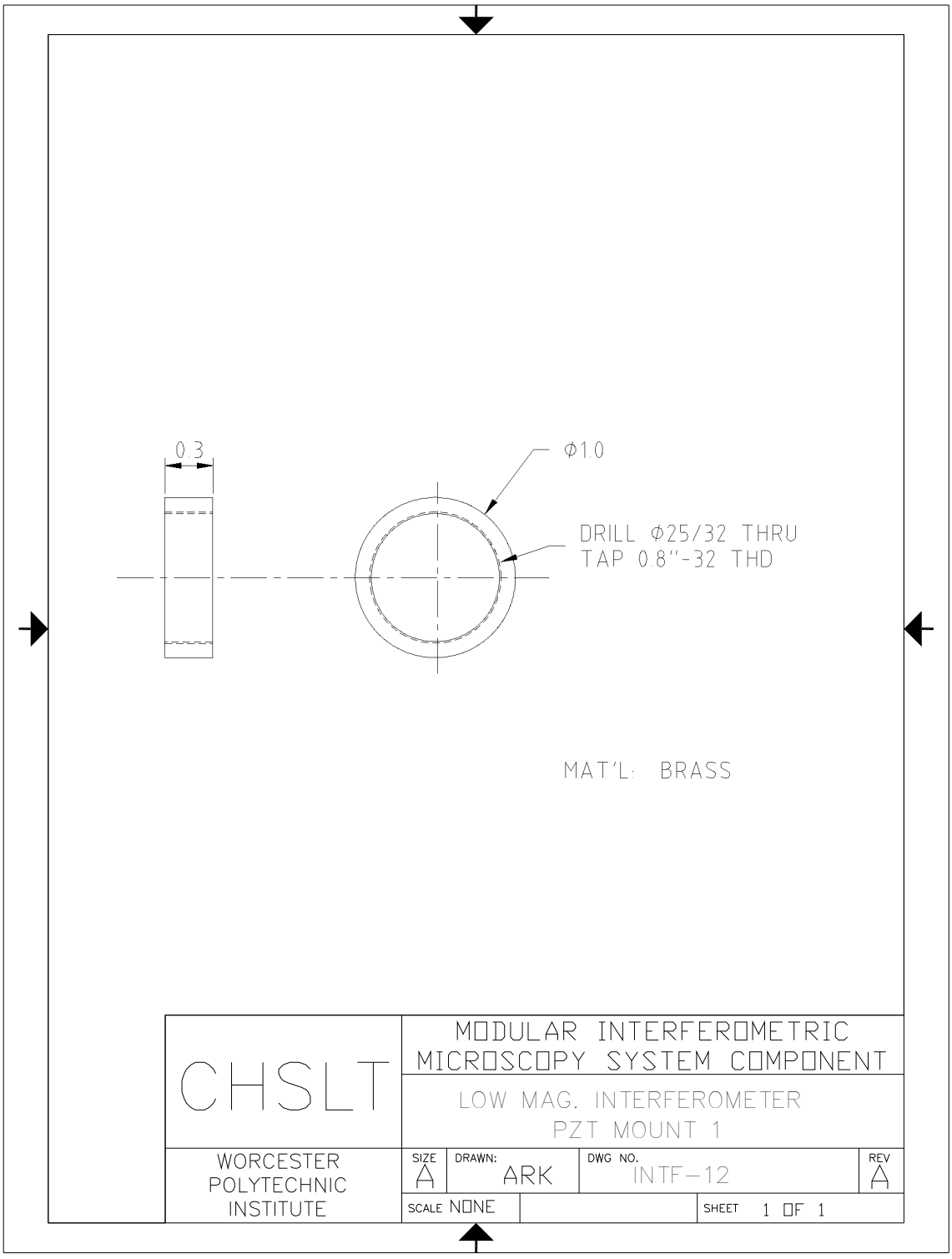

Fig. C.12. Low magnification interferometer PZT mount 1.

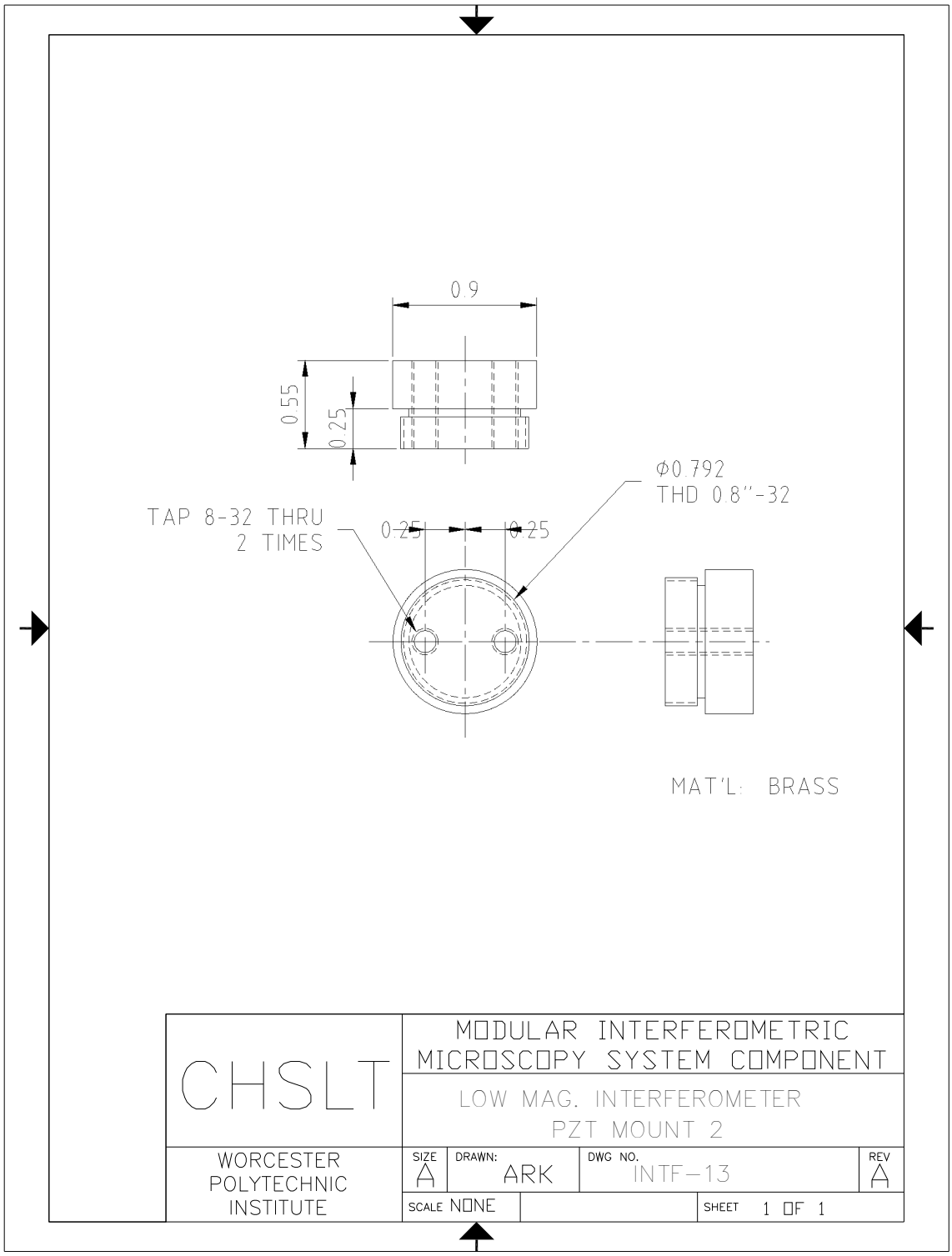

Fig. C.13. Low magnification interferometer PZT mount 2.

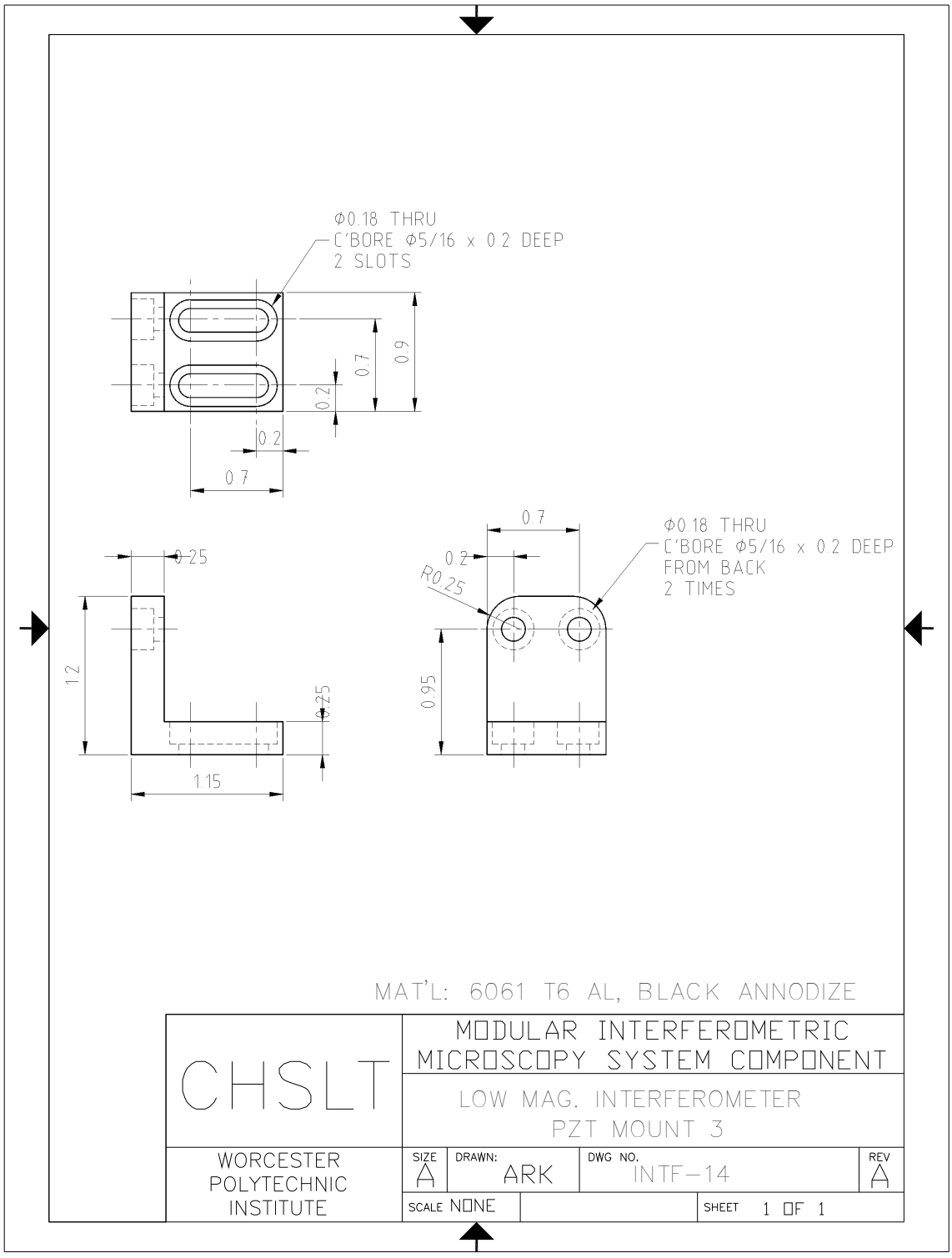

Fig. C.14. Low magnification interferometer PZT mount 3

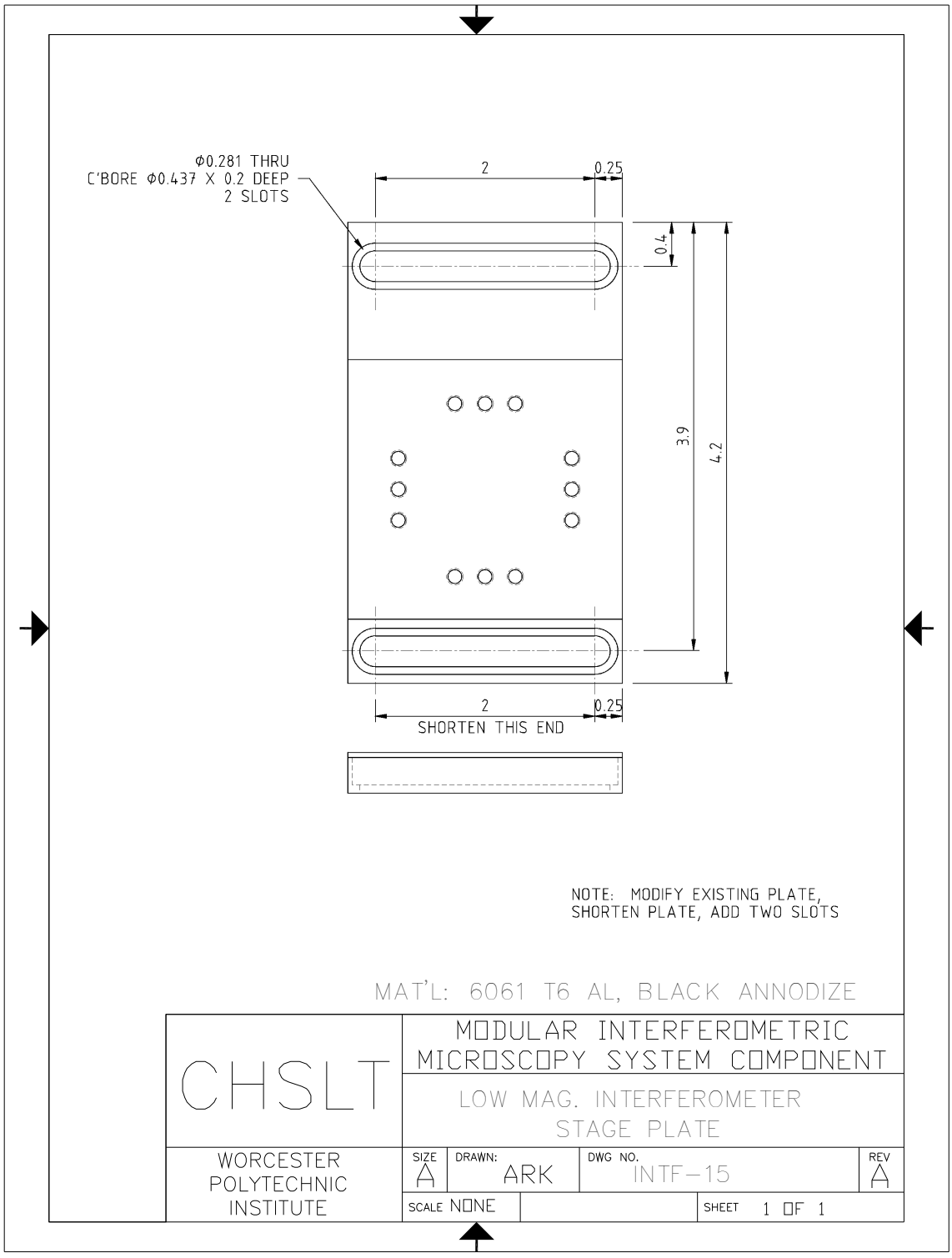

Fig. C.15. Low magnification interferometer stage plate.

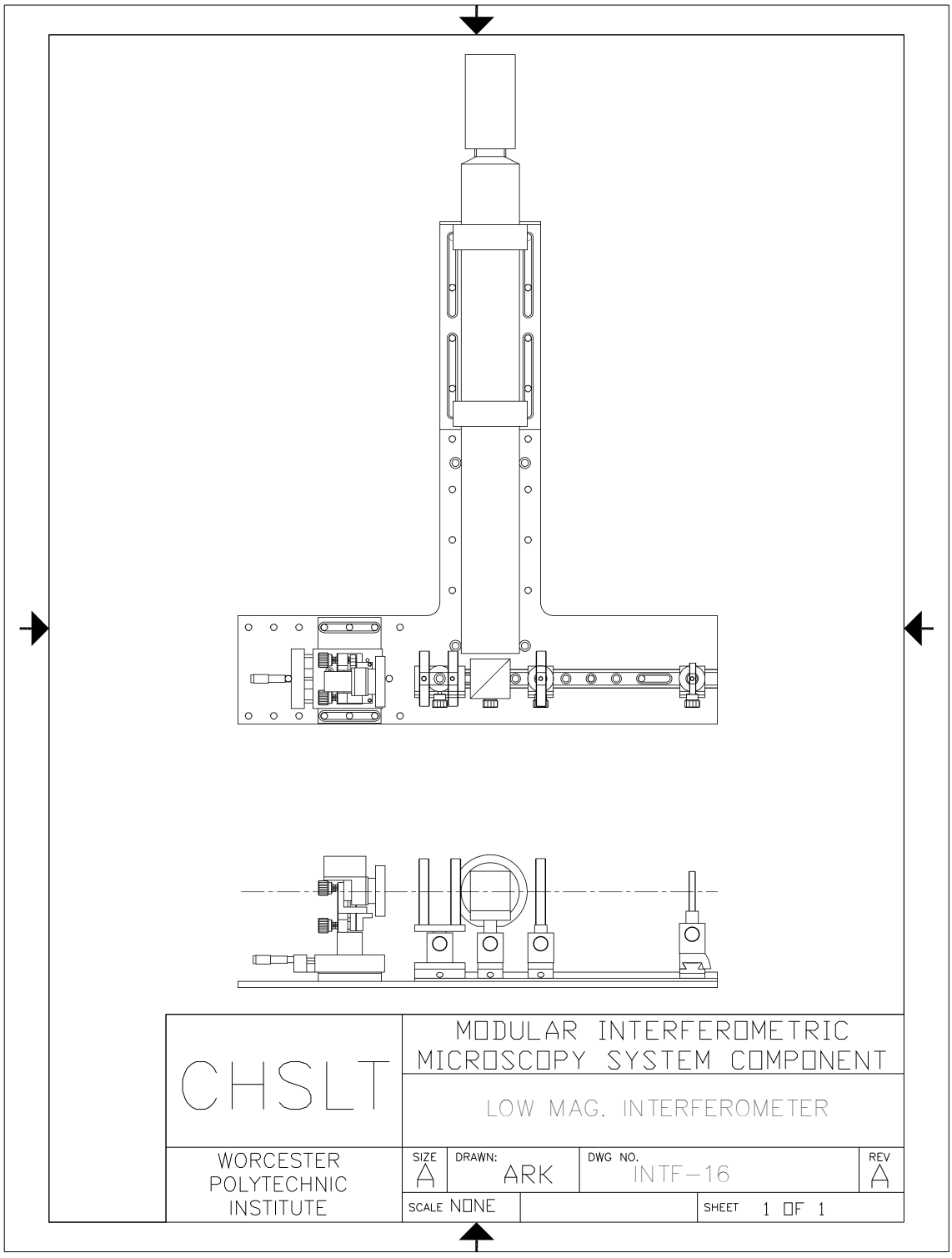

Fig. C.16. Low magnification interferometer assembly.

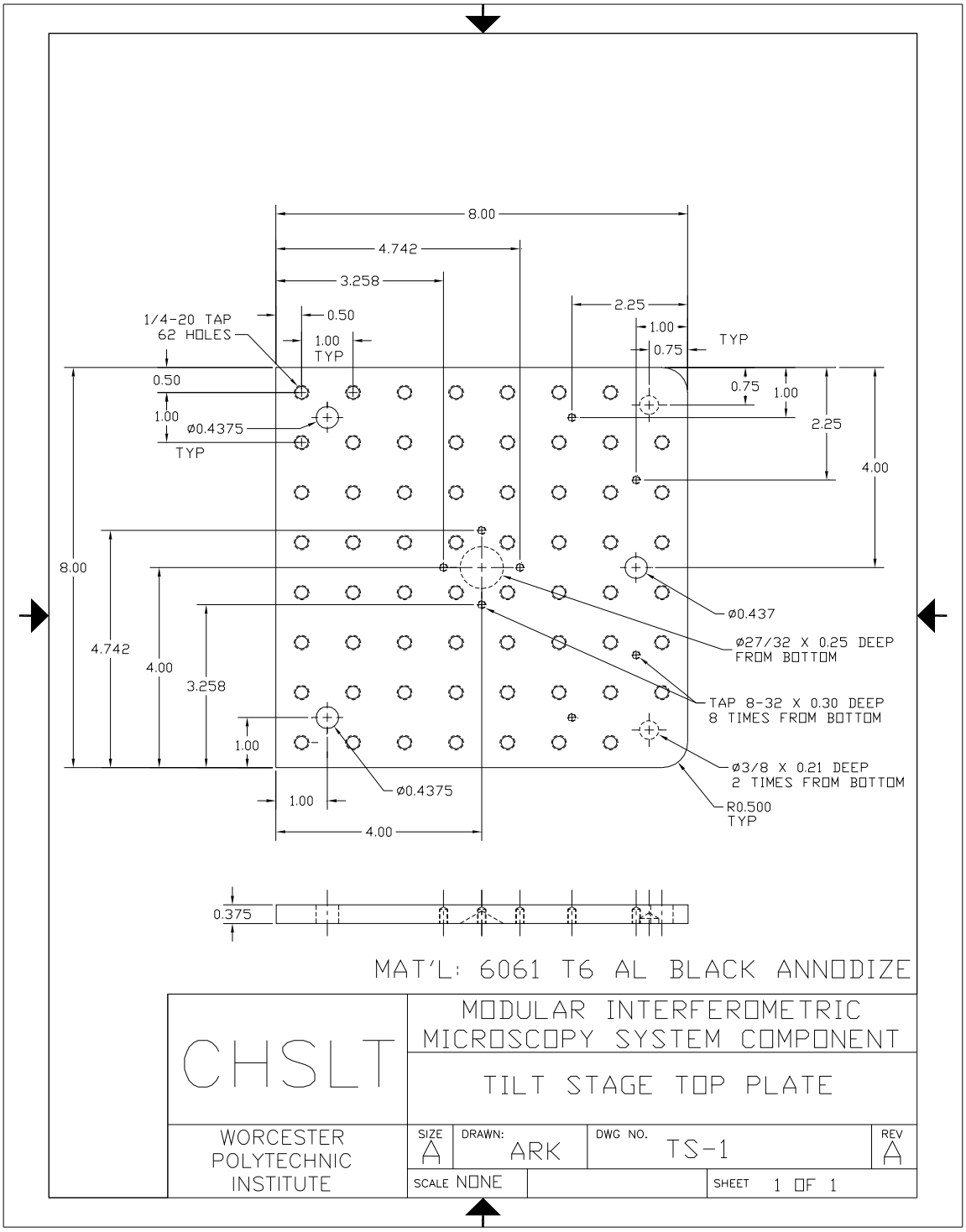

Fig. C.17. Tilt stage top plate.

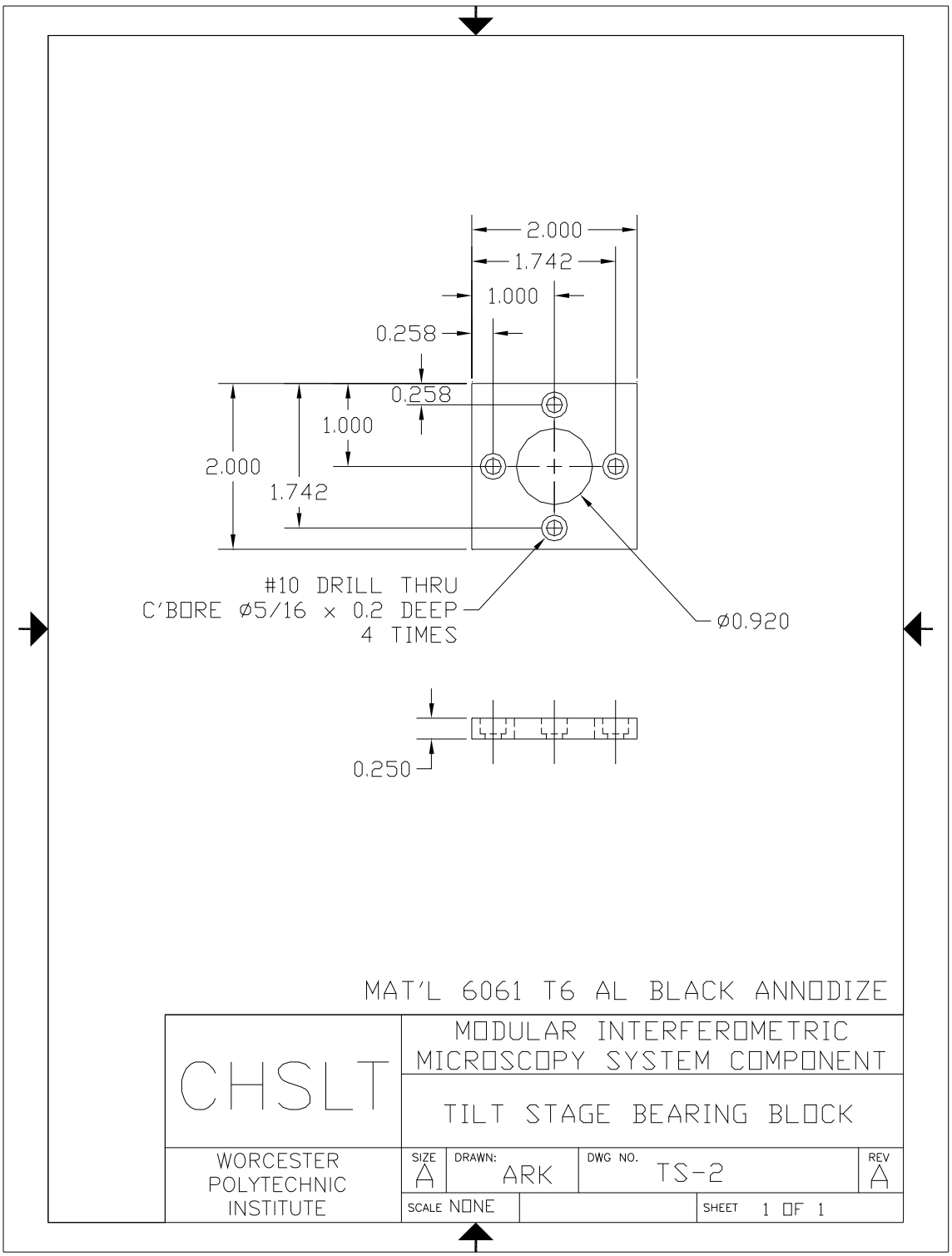

Fig. C.18. Tilt stage bearing block.

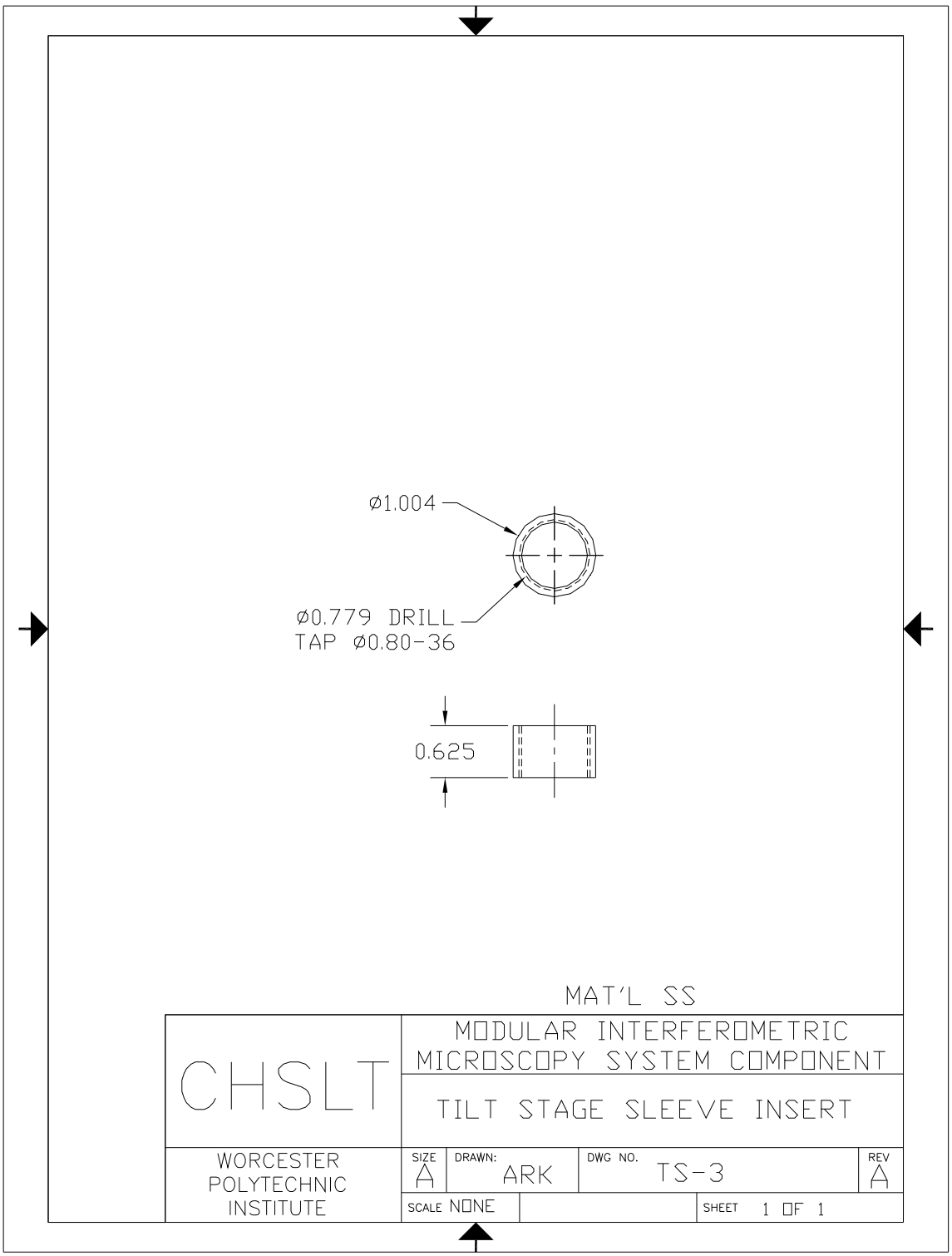

Fig. C.19. Tilt stage sleeve insert.

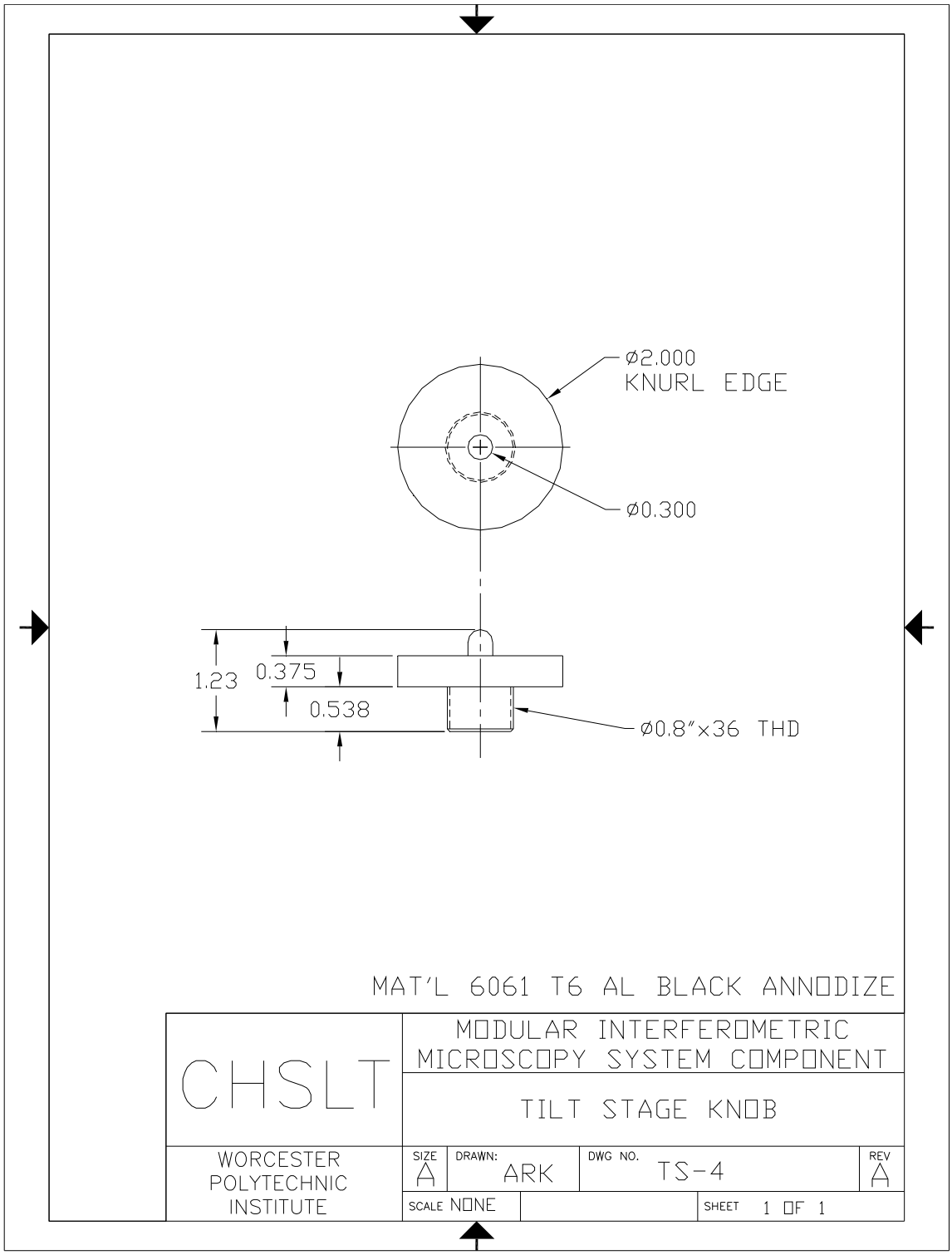

Fig. C.20. Tilt stage knob.

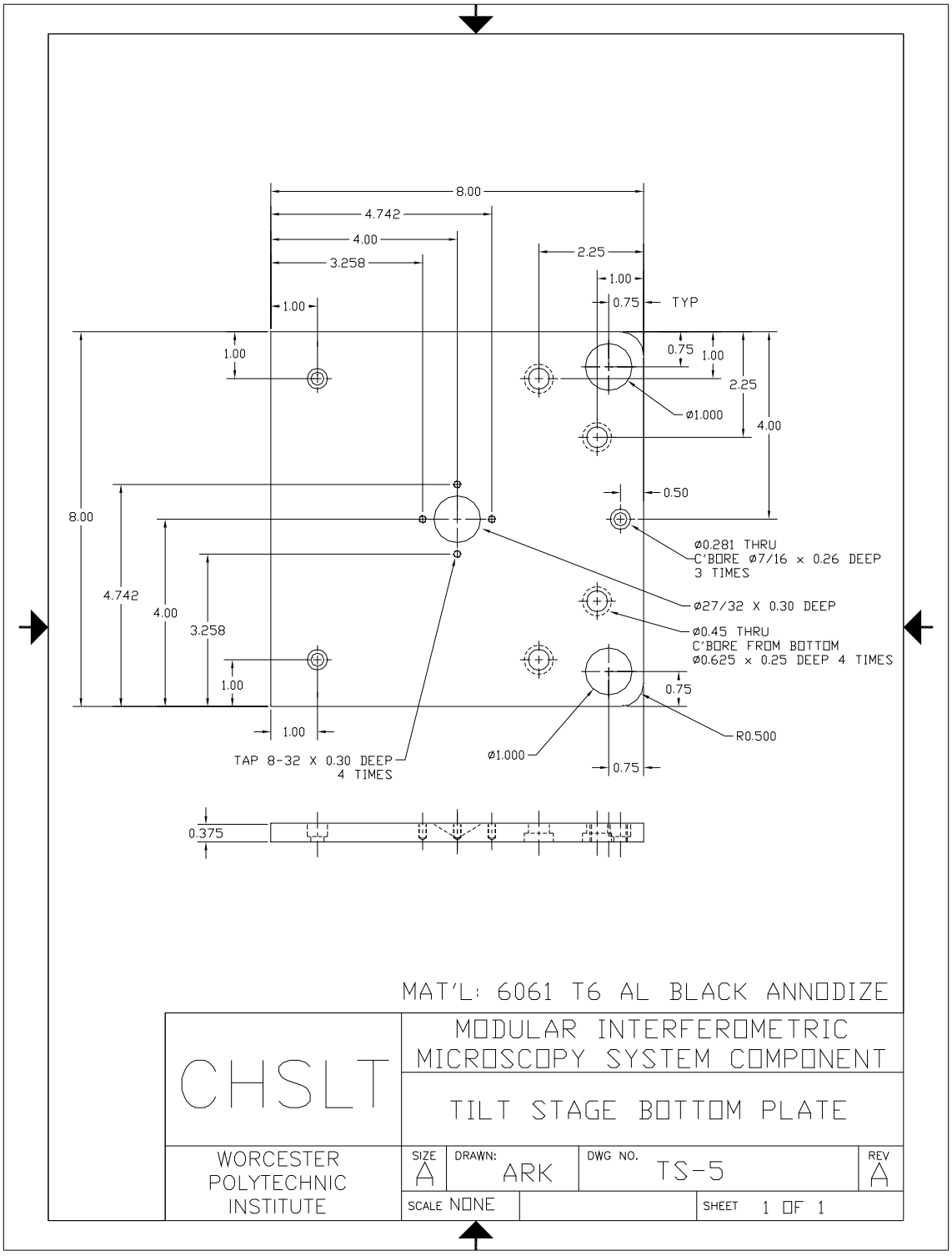

Fig. C.21. Tilt stage bottom plate.

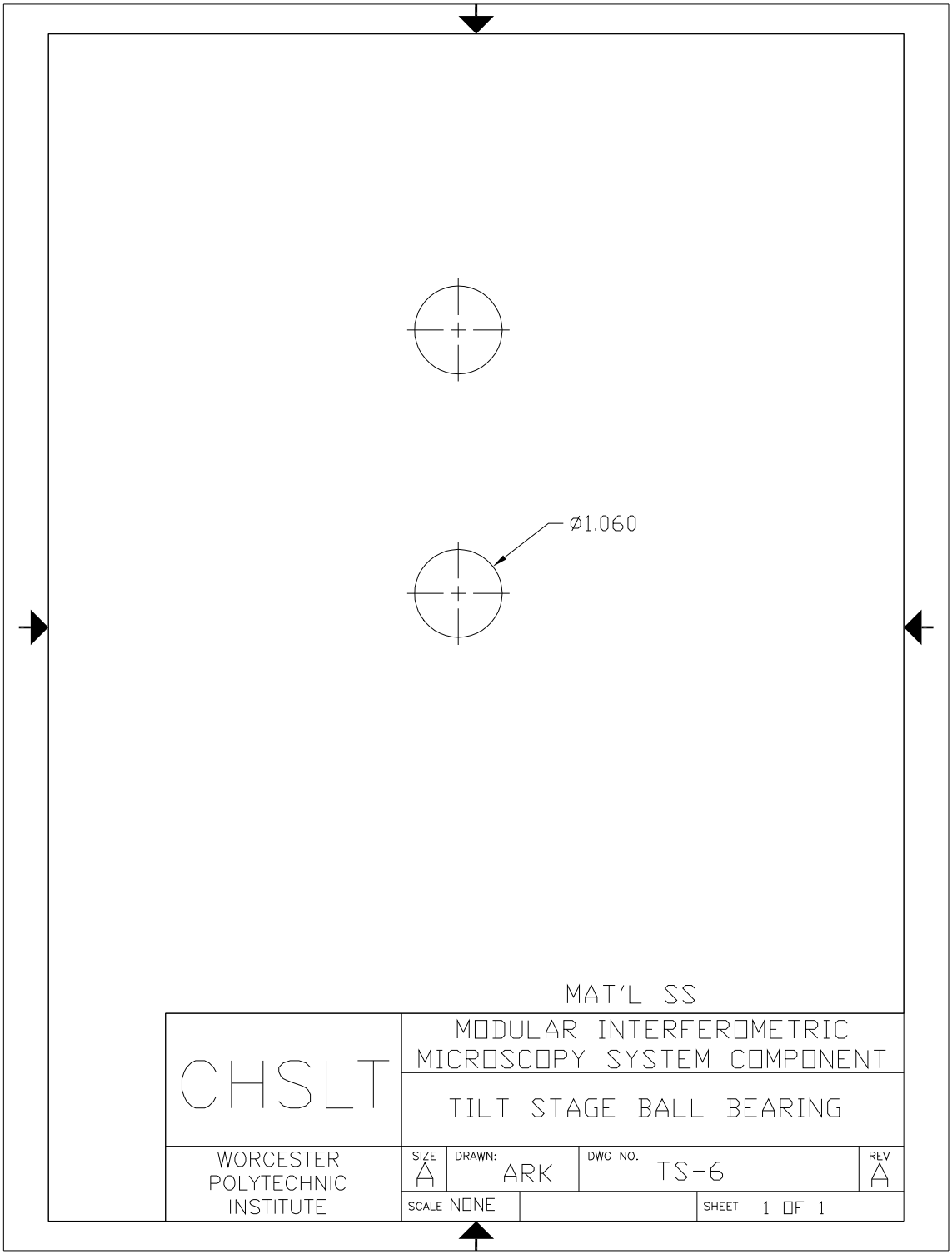

Fig. C.22. Tilt stage bearing.

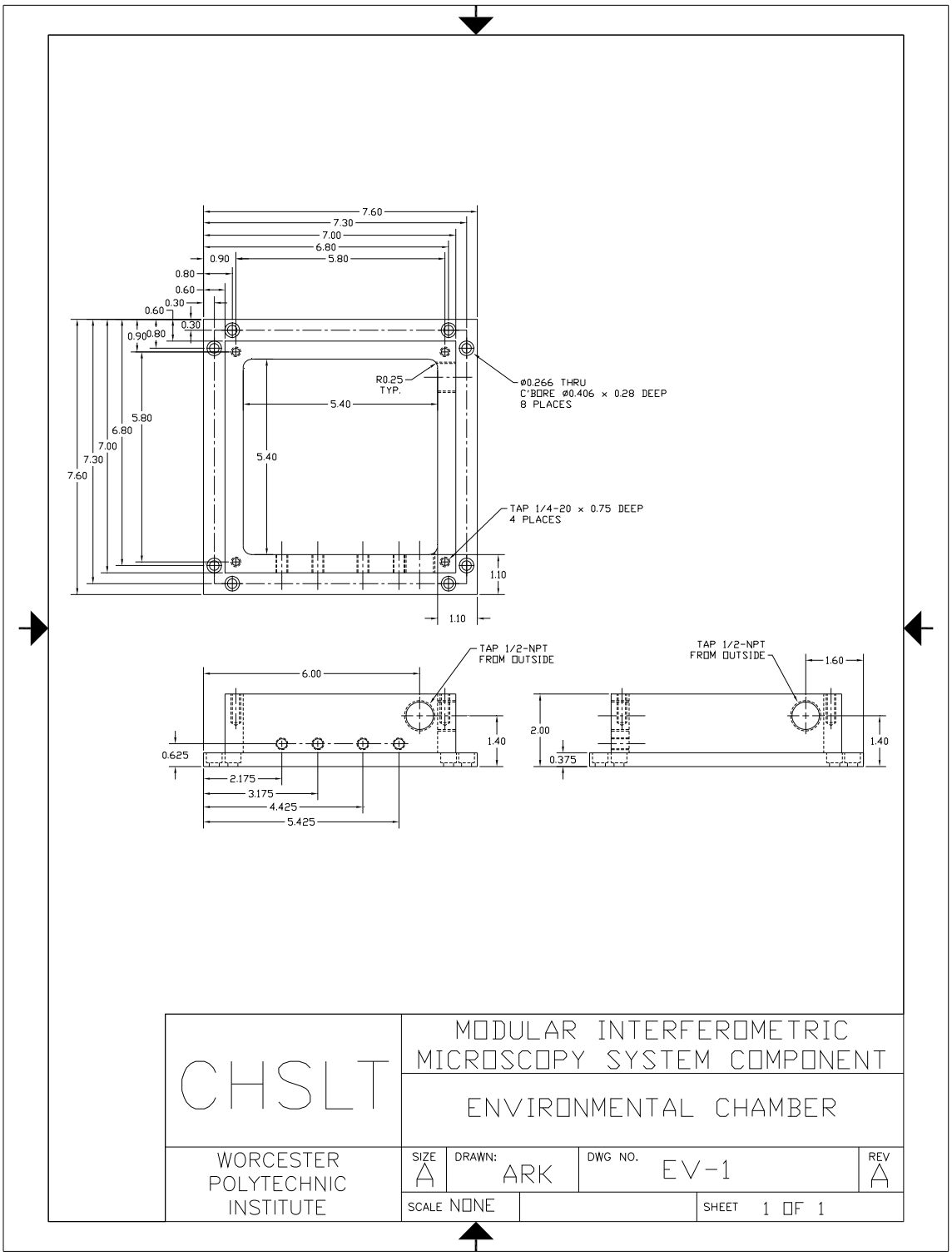

Fig. C.23. Environmental chamber.

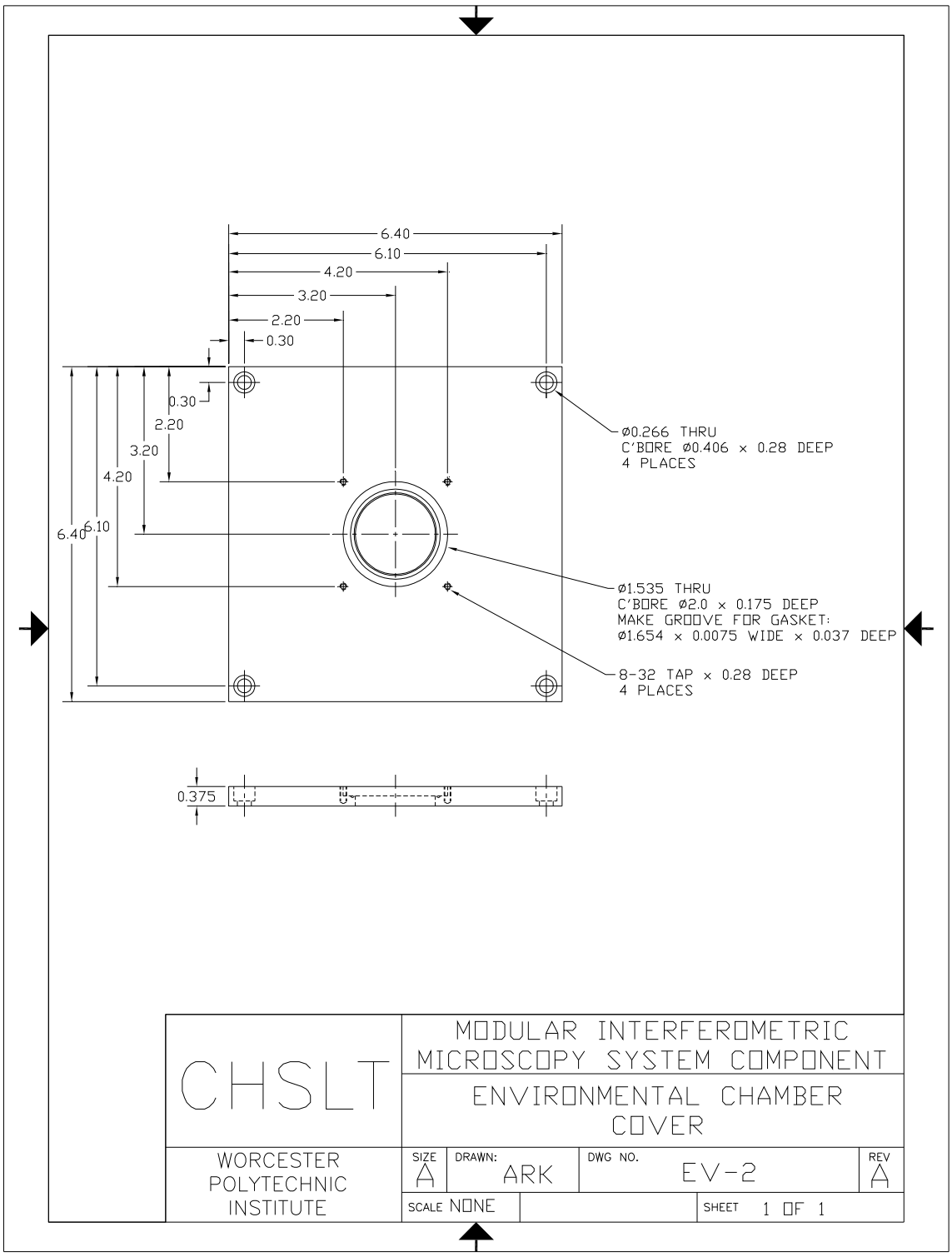

Fig. C.24. Environmental chamber cover.

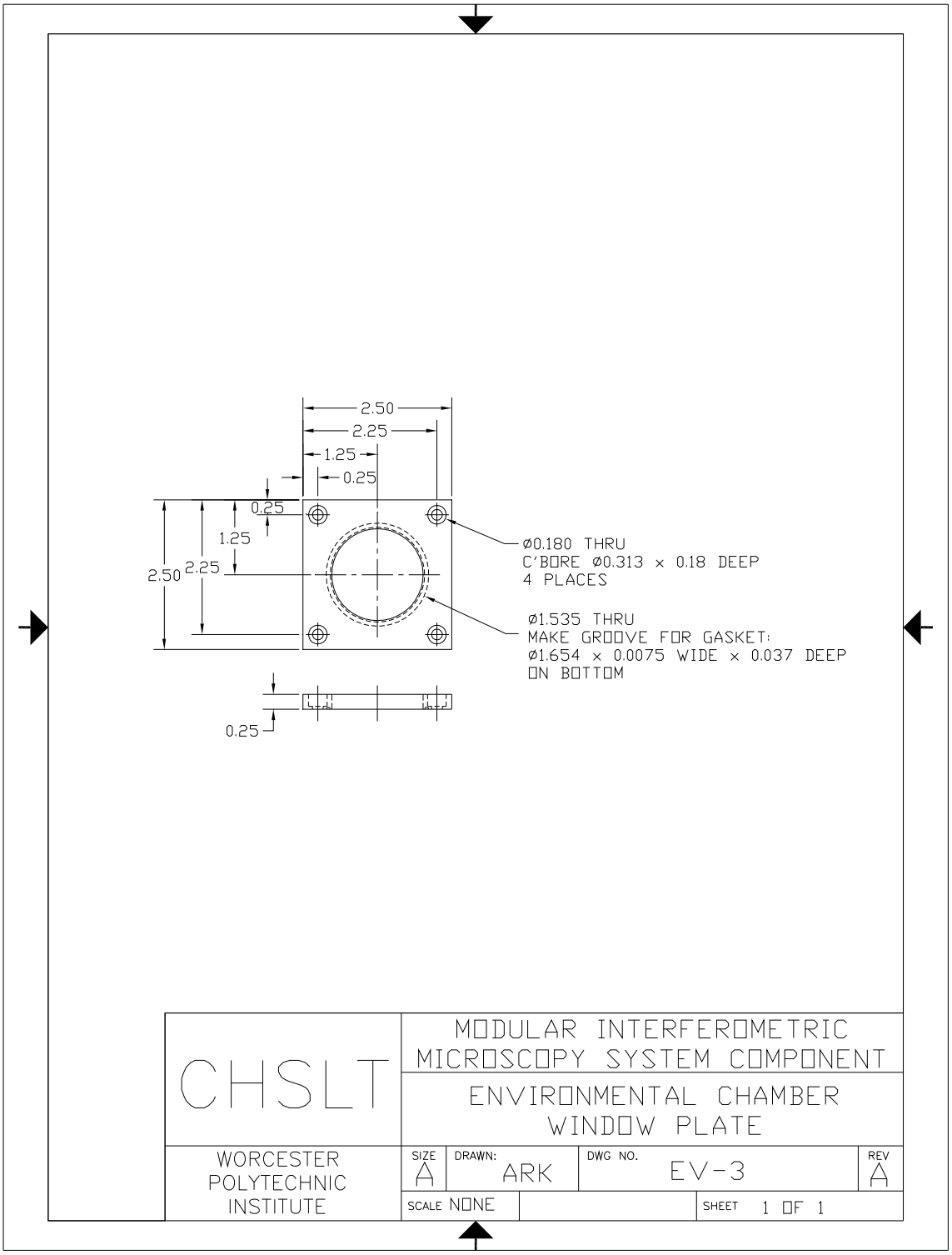

Fig. C.25. Environmental chamber window plate.

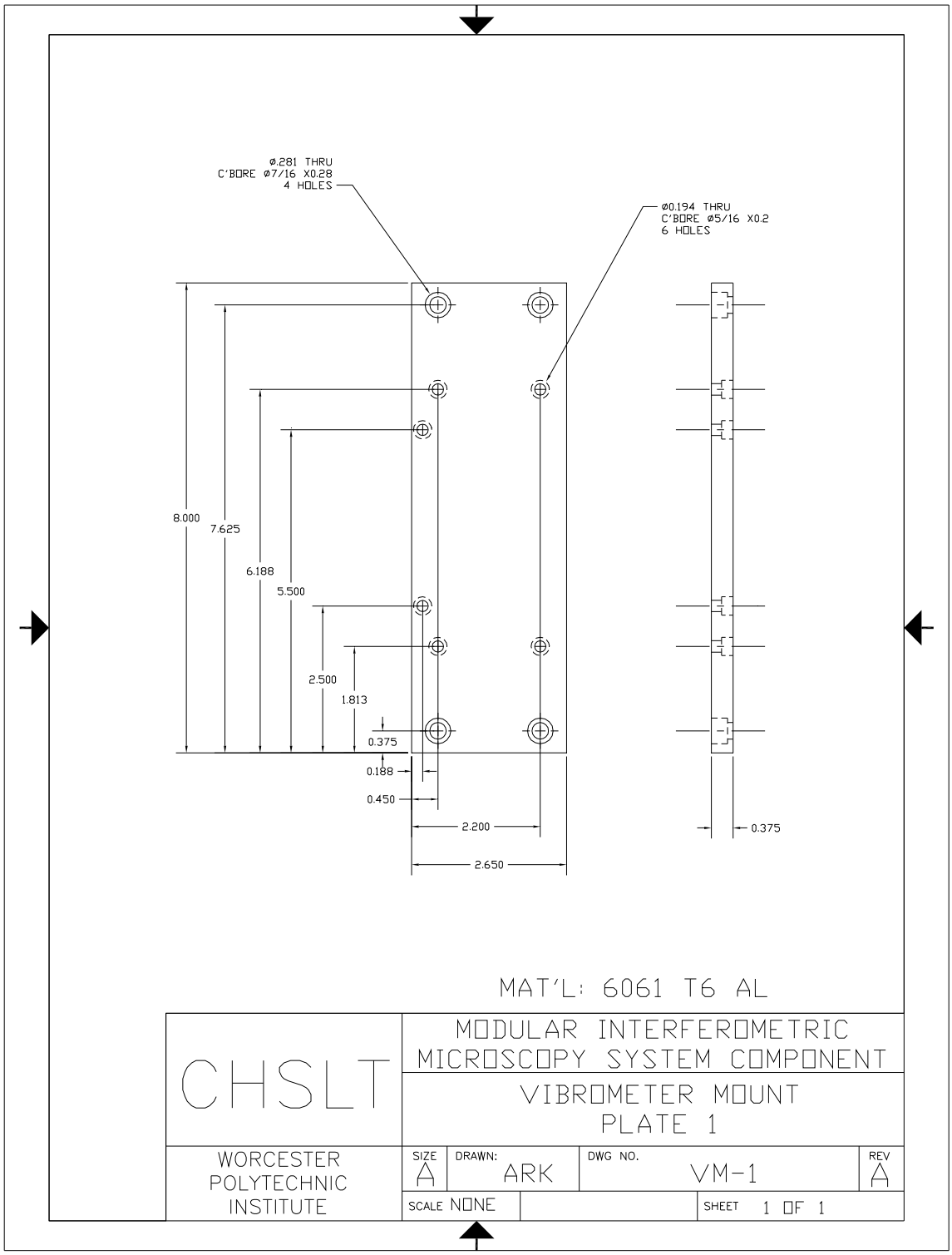

Fig. C.26. Vibrometer mount plate 1.

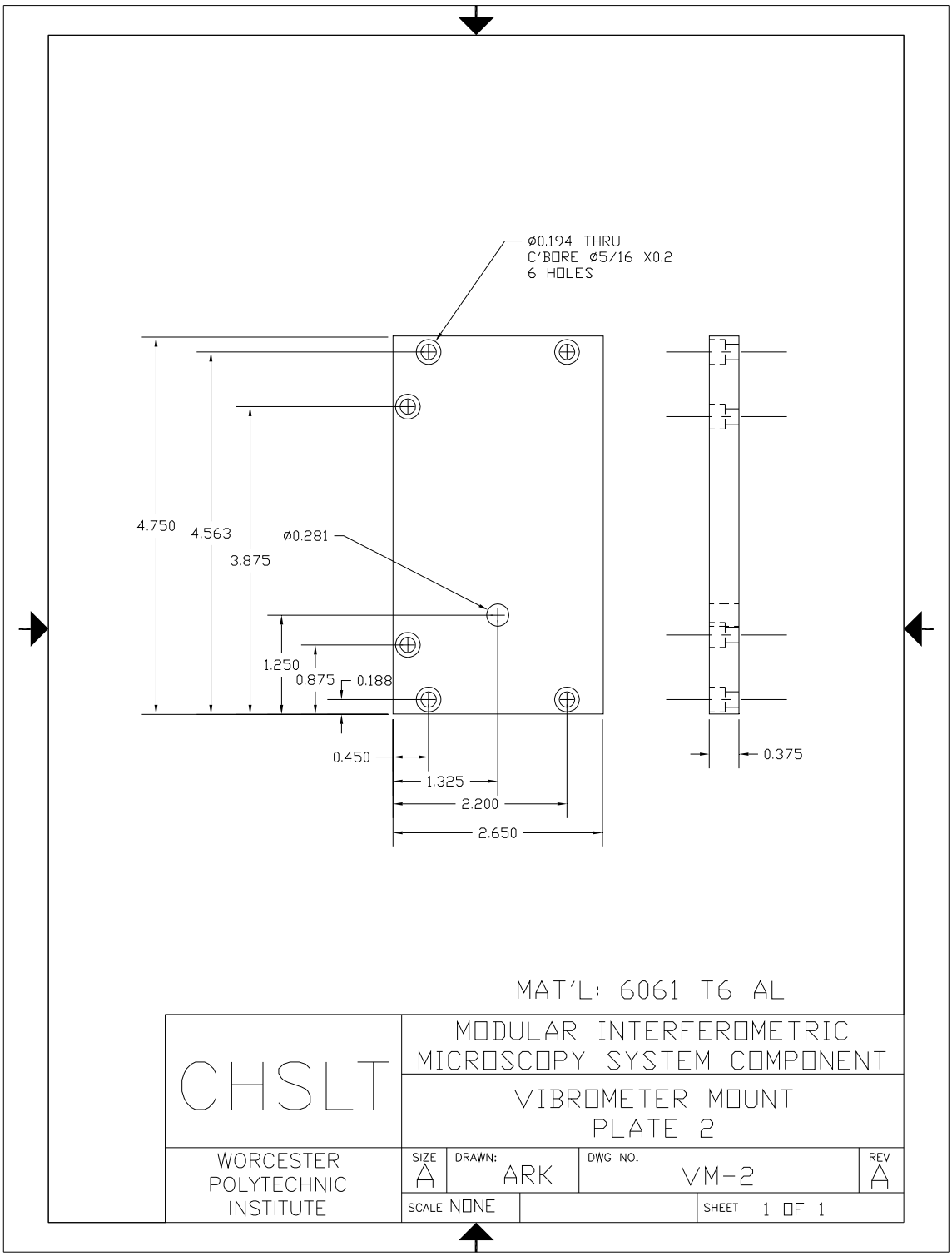

Fig. C.27. Vibrometer mount plate 2.

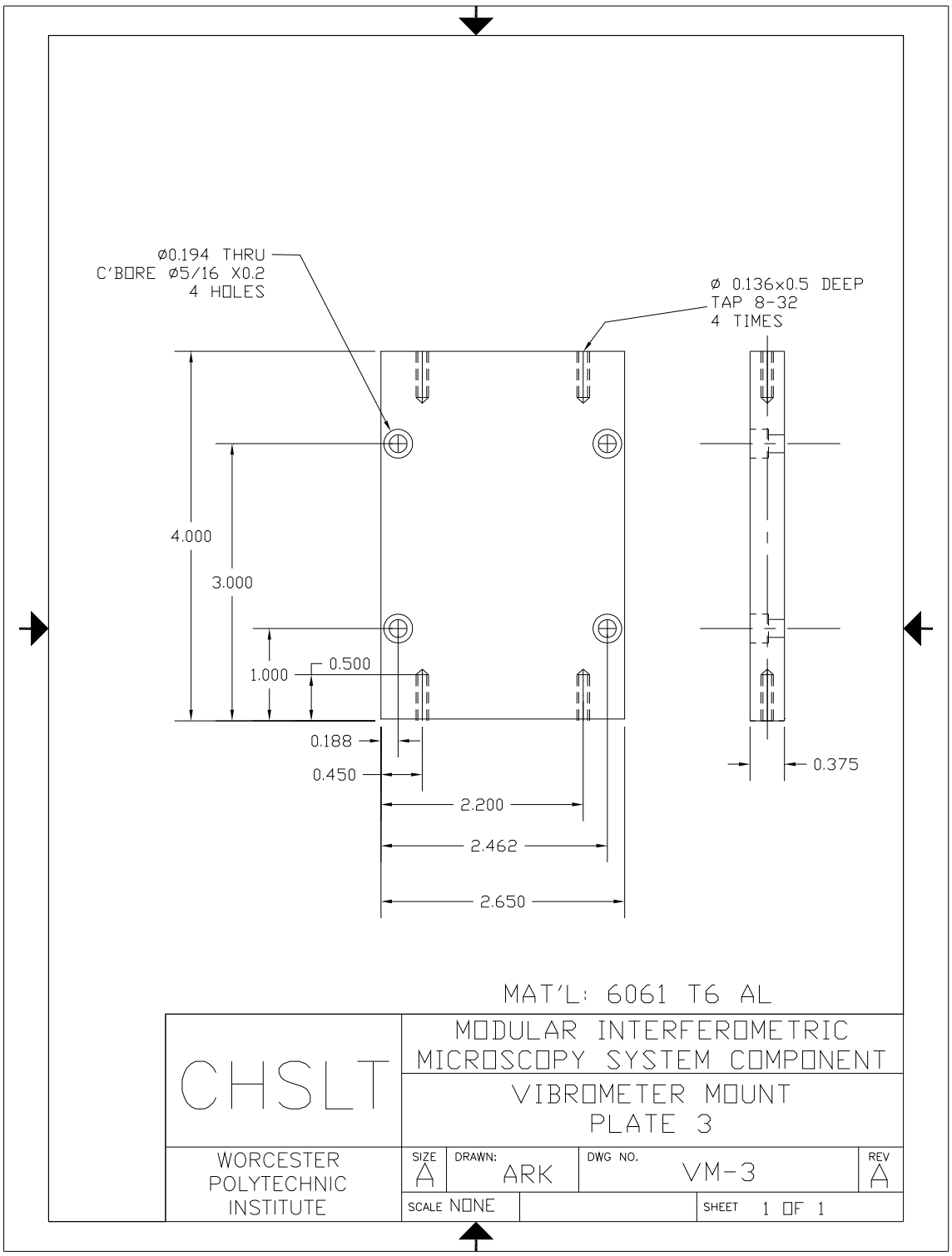

Fig. C.28. Vibrometer mount plate 3.

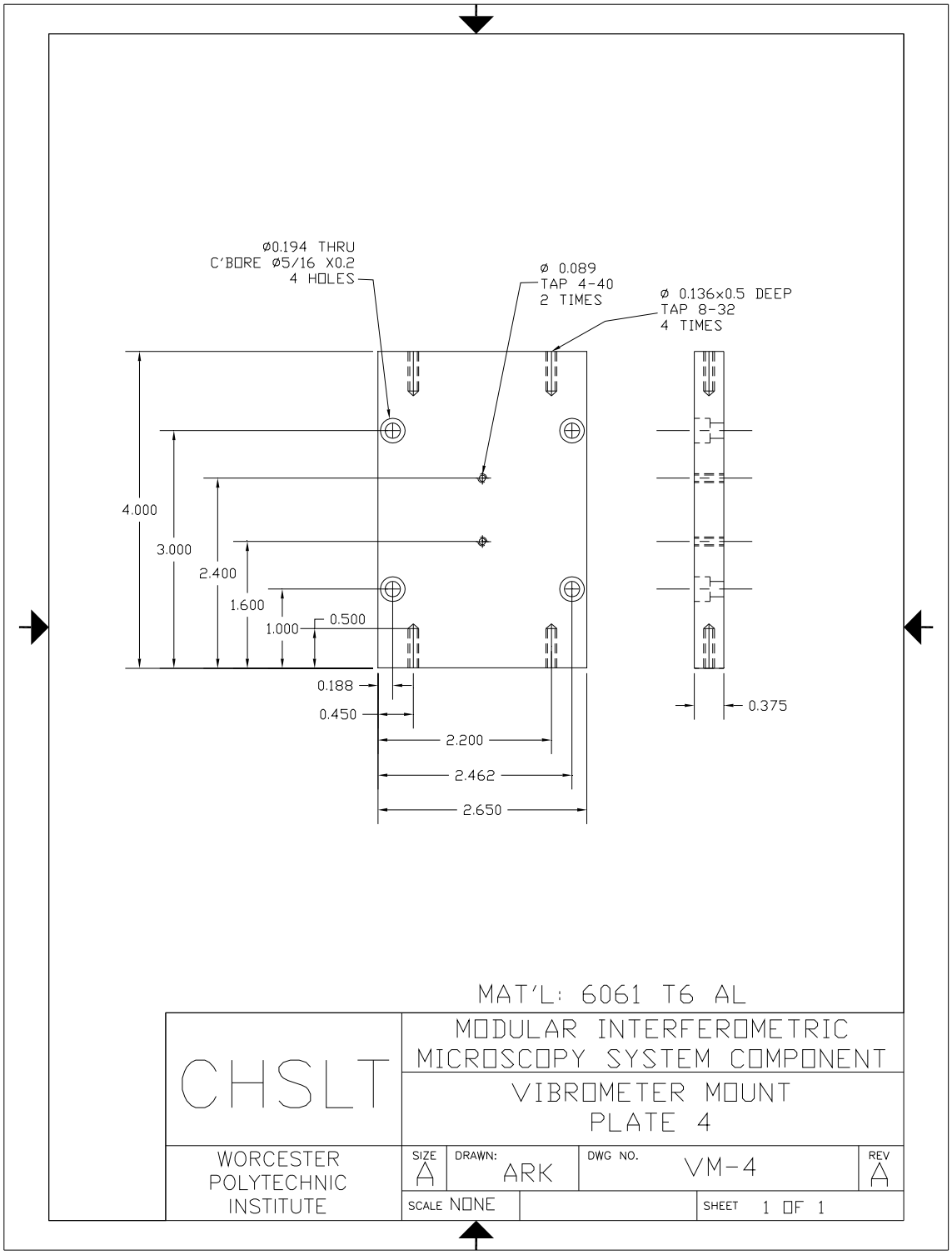

Fig. C.29. Vibrometer mount plate 4.

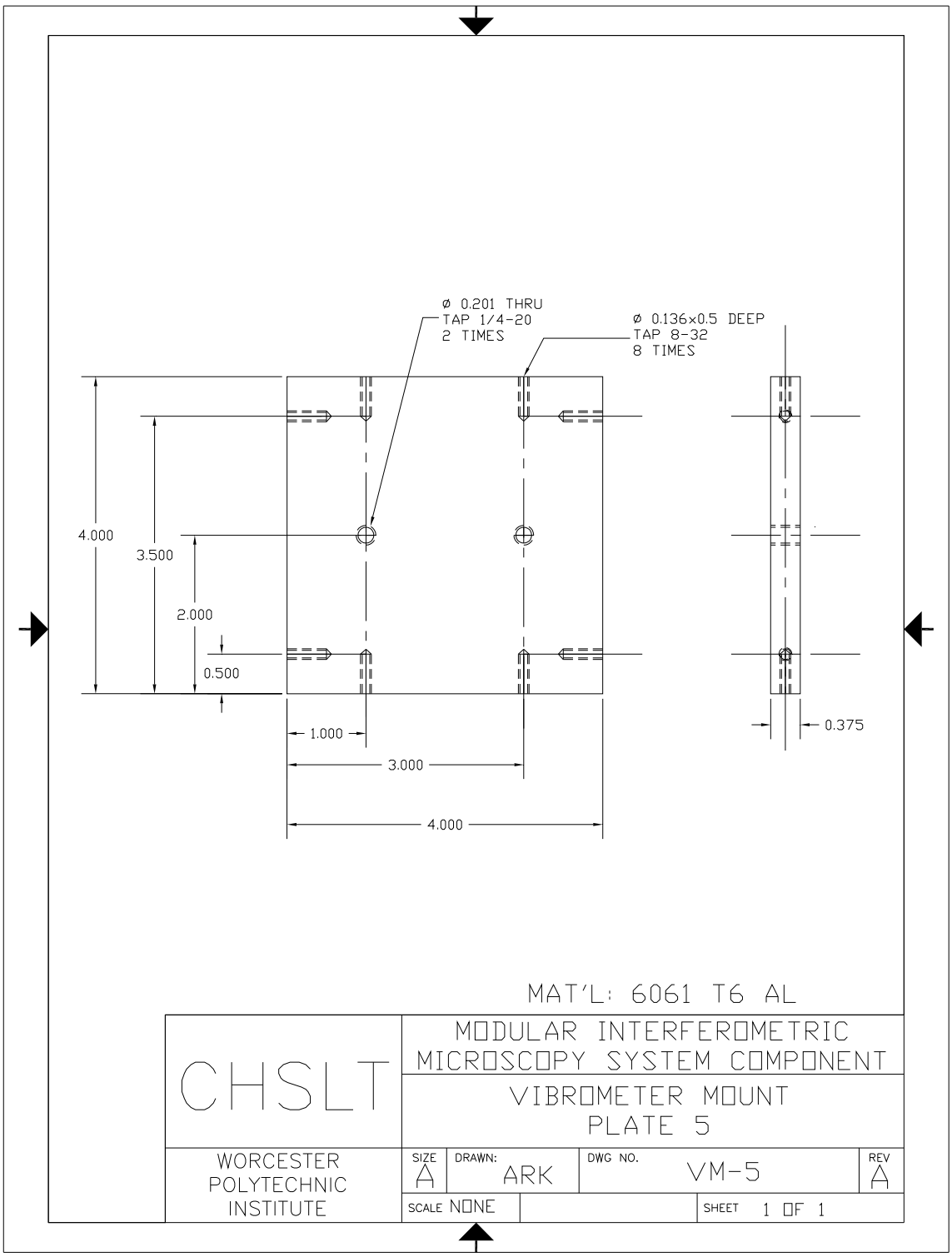

Fig. C.30. Vibrometer mount plate 5.

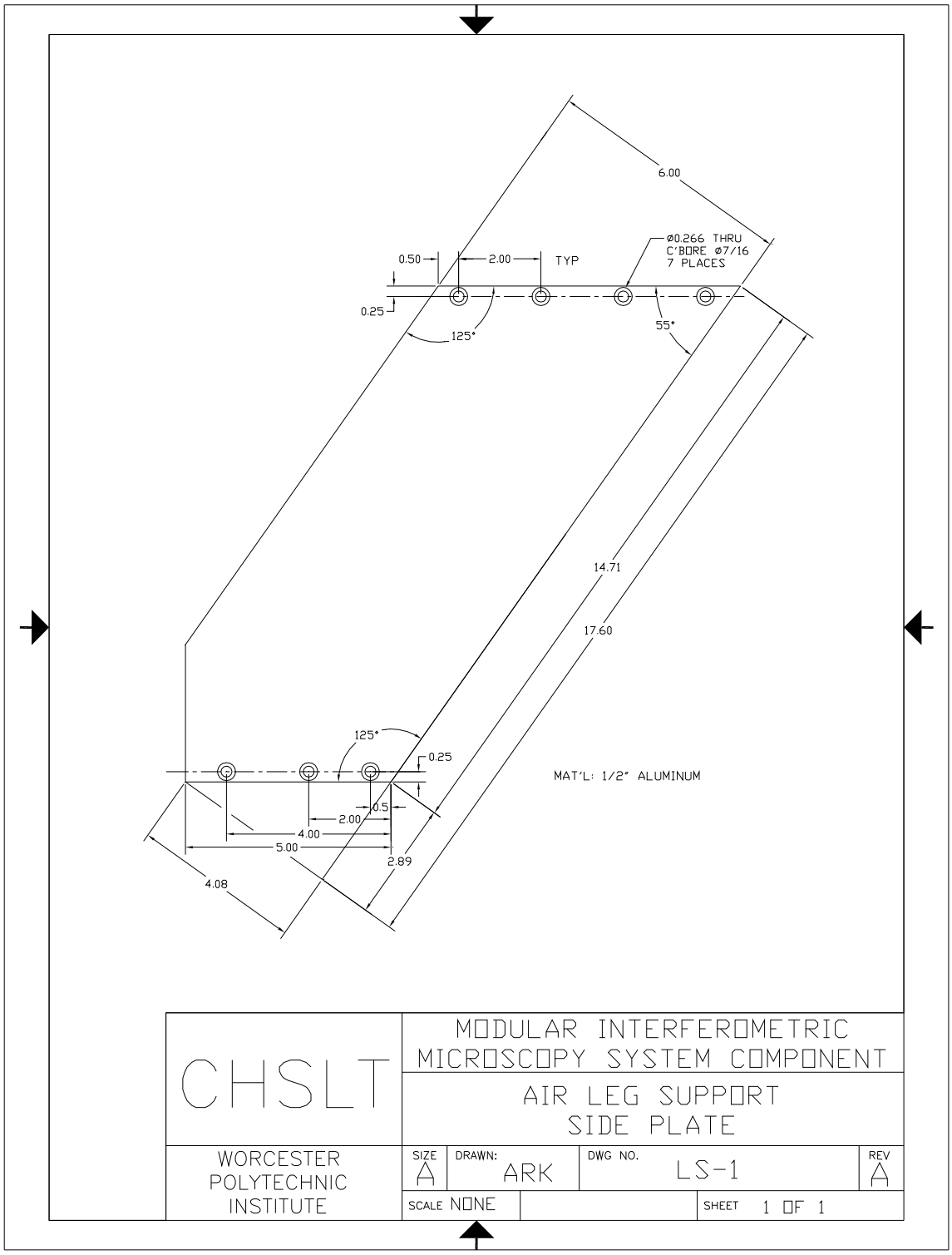

Fig. C.31. Air leg support side plate.

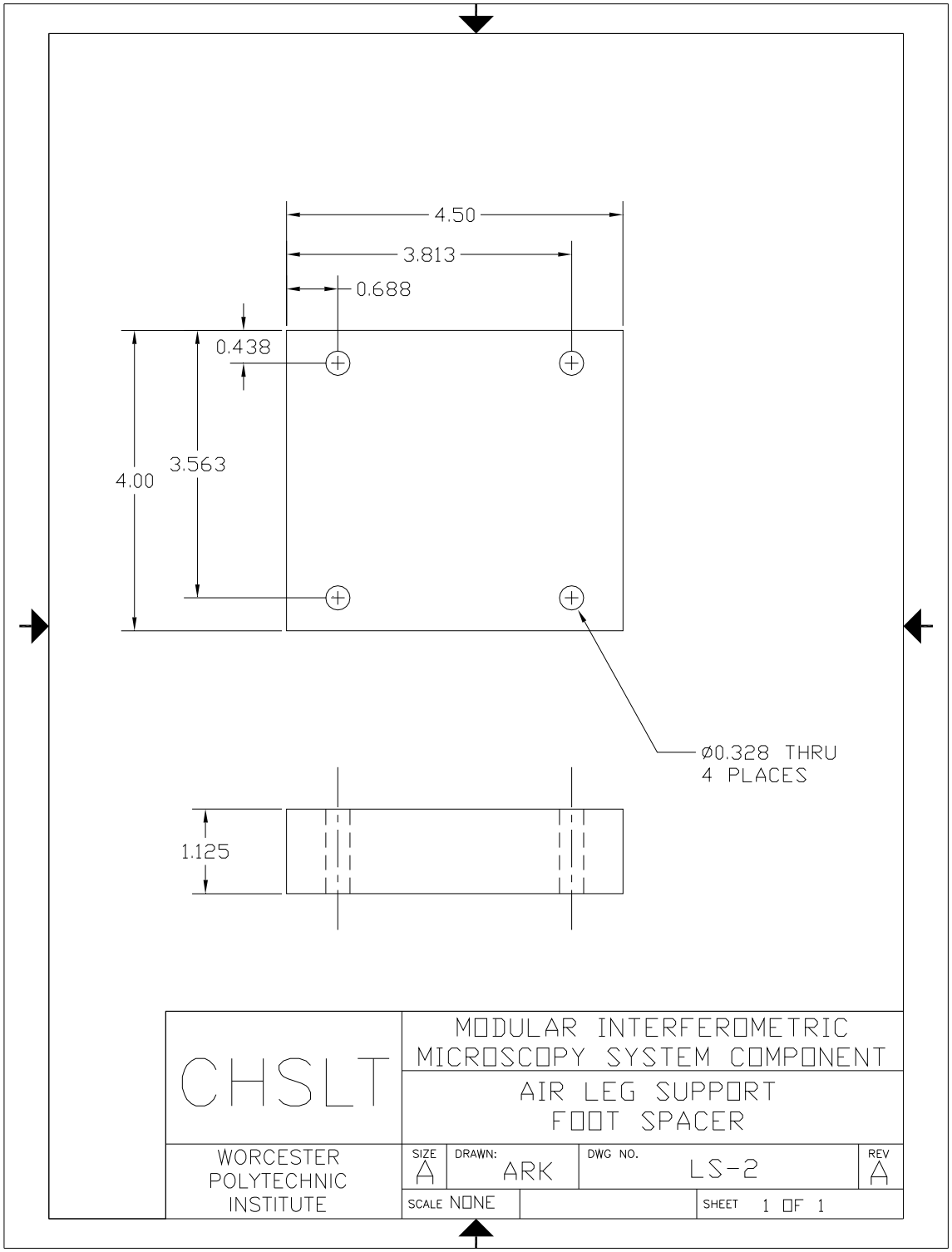

Fig. C.32. Air leg support foot spacer.

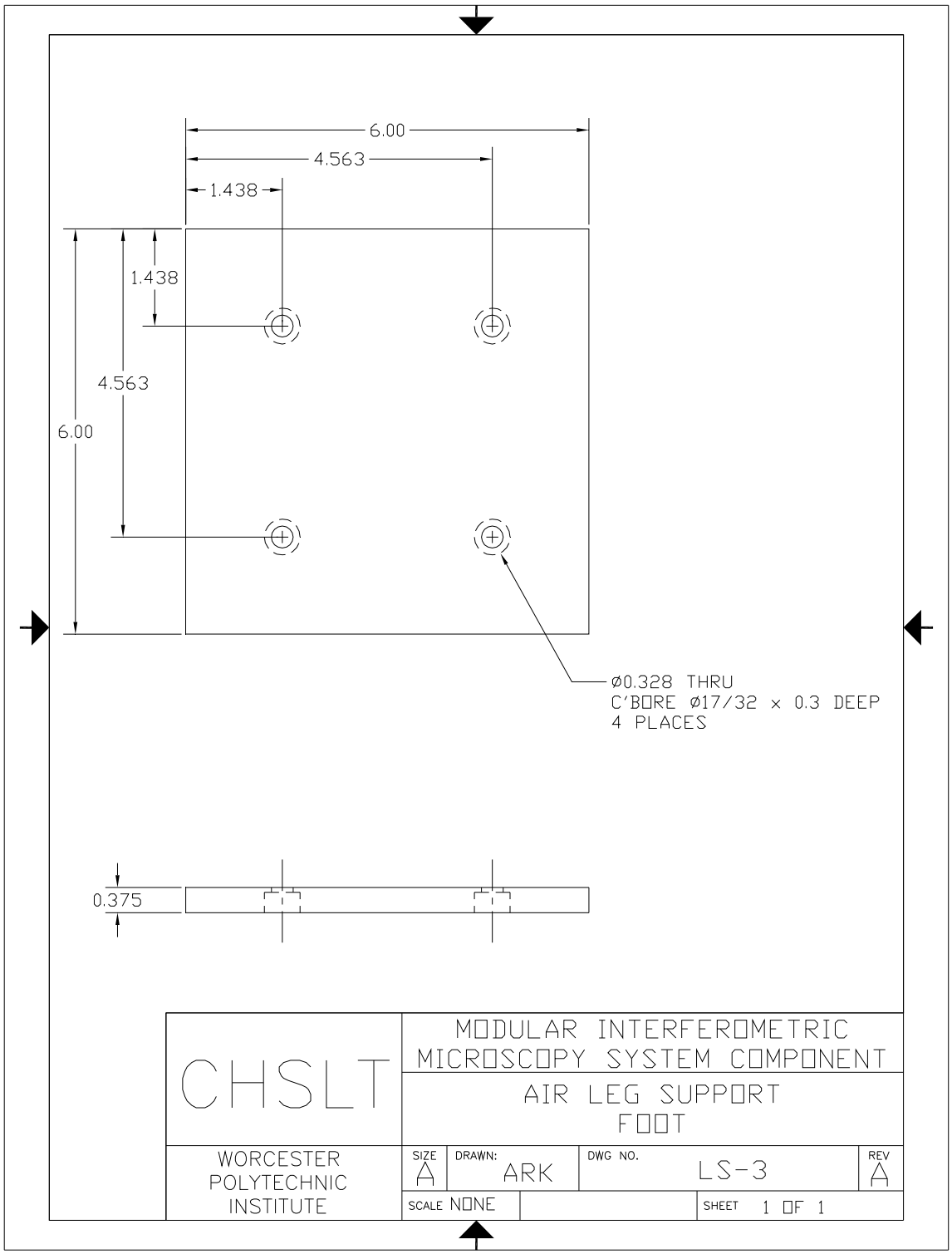

Fig. C.33. Air leg support foot.

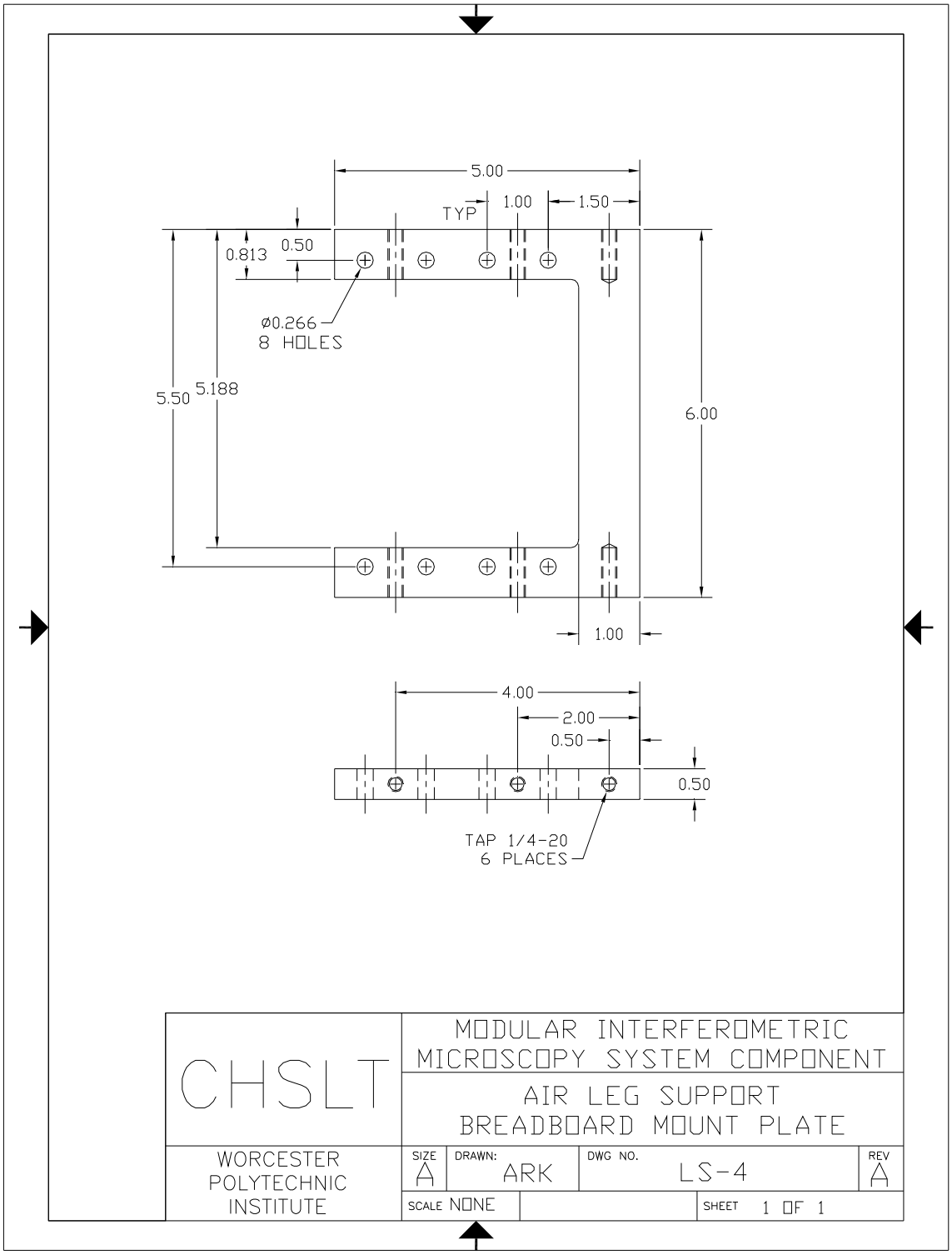

Fig. C.34. Air leg support breadboard mount plate.

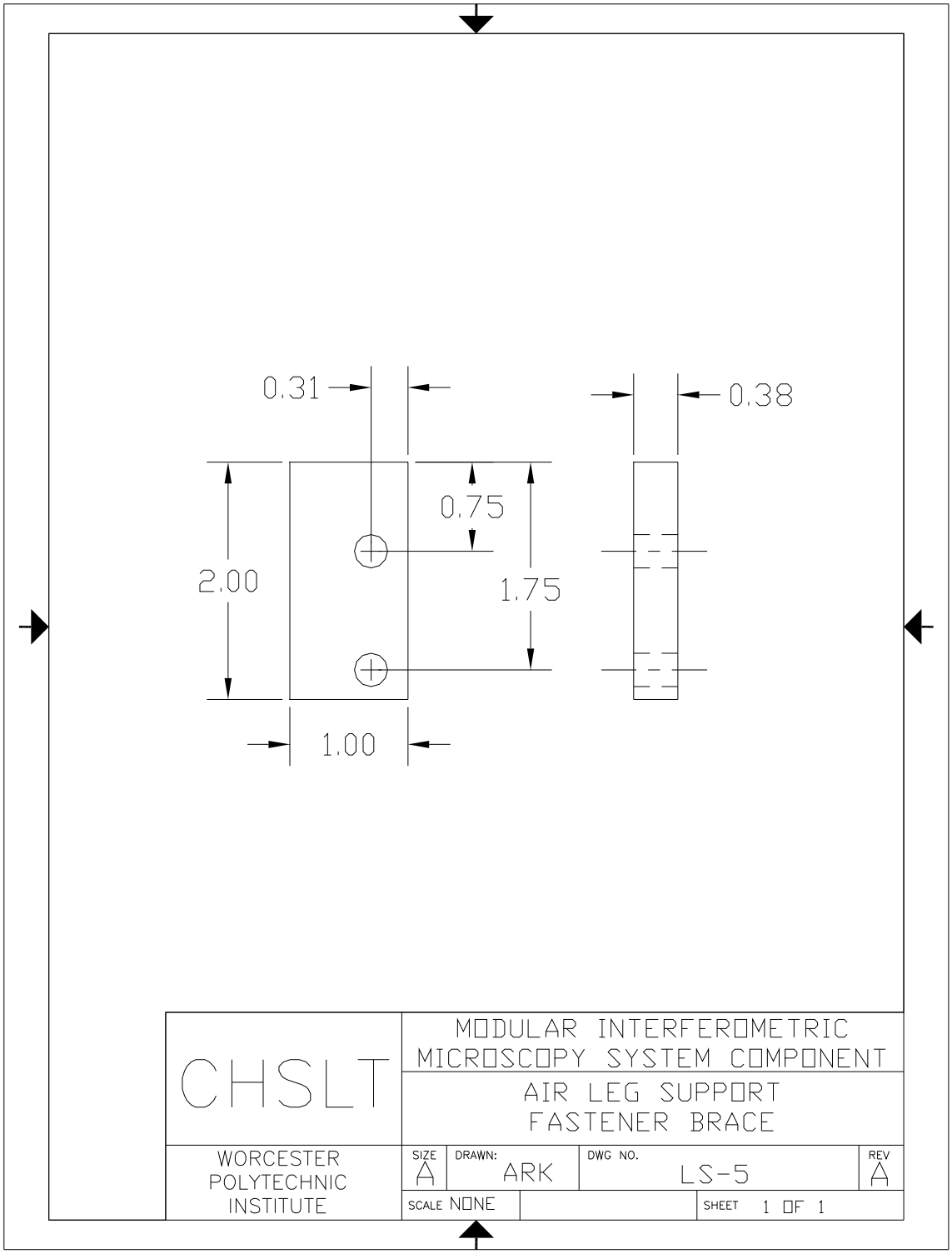

Fig. C.35. Air leg support fastener brace.

APPENDIX D. TILT STAGE CALCULATIONS

This Appendix shows calculations used to design the tilt stage. The tap used to make the threaded sleeves is a custom made tap, unlisted on standard tapping diagrams, requiring the tap drill size to be calculated. Also, the resolution of the stage is estimated.

Tilt stage design

Tap drill size calculation for 0.8" x 36 thread, pg 1900 of Machinery's Handbook

$Dia := 0.8in$ Basic major diameter

$PFT := 0.75$ Percent full thread, 55-75% typical, higher values for ductile mat'l

$TPI := 36 \cdot \frac{1}{in}$ Threads per inch

$Hole\_size := Dia - \frac{1.0253 \cdot PFT}{TPI}$ $Hole\_size = 0.779\,in$

Calculation of the tilting resolution of the stage:

$Rotation := 1.0deg$ Manual rotation amount of the tilting screw

$D_{SP} := 4.6in$ Distance from tilting screw to pivot

$360deg = \frac{1}{36}in$ $1deg = \left(\frac{1}{36}in\right) \cdot \frac{1}{360}$

$Screw\_travel := \left(\frac{1}{36}in\right) \cdot \left(\frac{1}{360deg}\right) \cdot Rotation$ $Screw\_travel = 0.077\,mil$

$Screw\_travel = 1.96\,\mu m$

The angular resolution of the tilting stage, assuming the smallest manual rotaton possible of 1 degree:

$Tilt\_angle := \tan\left(\frac{Screw\_travel}{D_{SP}}\right)$ $Tilt\_angle = 9.611 \times 10^{-4}\,deg$

Applying this angle to a typical MEMS device of characteristic length of 100 μm, the minimum out of plane height difference controllable by tilting:

$L_c := 100\mu m$

$H\_min_{MEMS} := \tan(Tilt\_angle) \cdot L_c$ $H\_min_{MEMS} = 1.677\,nm$

If one fringe indicates a tilt of about 320nm, then the tilt is controlable to approximately 1/200th of a fringe on a 100 μm long MEMS.

APPENDIX E. TAS STEADY STATE RESULTS OF COOLED CHAMBER

Section 6.3.2 deals with the design of the environmental chamber and describes the FEA model developed with TAS to simulate the thermal response of the TEC and liquid HEX controlled chamber. This Appendix includes the steady state results of the temperature profile of the chamber, Fig. E.1. Figure E.2 shows a cross section of the simulated liquid HEX in which -15°C fluid was pumped through. The model indicates slight warming of the fluid by the time it exits the HEX.

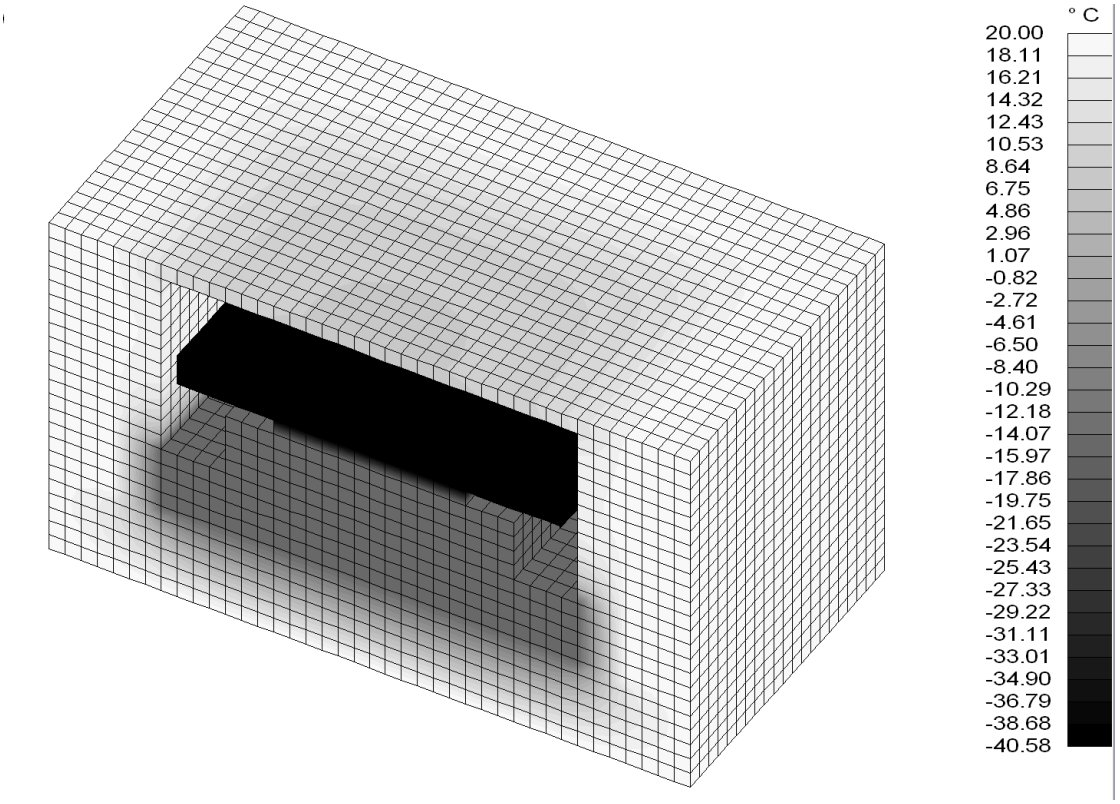

Fig. E.1. Steady state simulation results of chamber cooling (cross section).

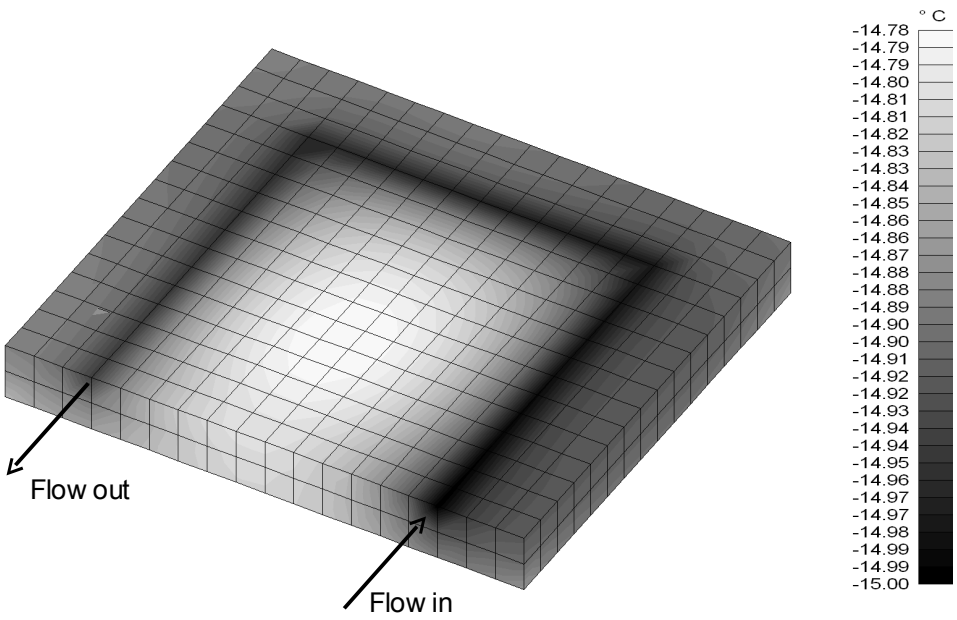

Fig. E.2. Cross section of the liquid HEX showing thermal gradient of flowing fluid.

APPENDIX F. LED CALIBRATION DATA

This Appendix is intended to be an operator's "quick-reference" guide to determine the actual wavelength being output by a LED module. Please note that as the driving current changes, the wavelength output does also, correspondingly. Use the linear plots to determine the correct wavelength to input for data analysis.

Figures F.1 through F.6 are calibration data plots for LEDs "B", "C", and "D". Each LED has two corresponding plots, one showing the optical spectrum at a nominal power output, and the other shows the wavelength dependence on driving current. The latter is more critical to know when performing routine measurements.

LED “B”

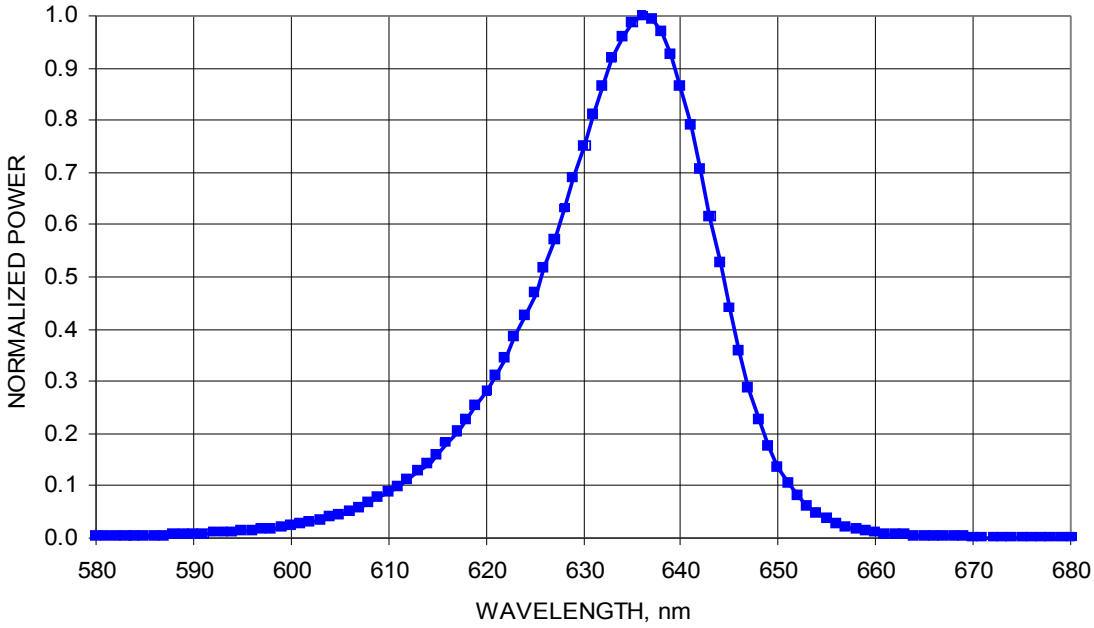

Fig. F.1. A typical normalized optical spectrum of LED "B".

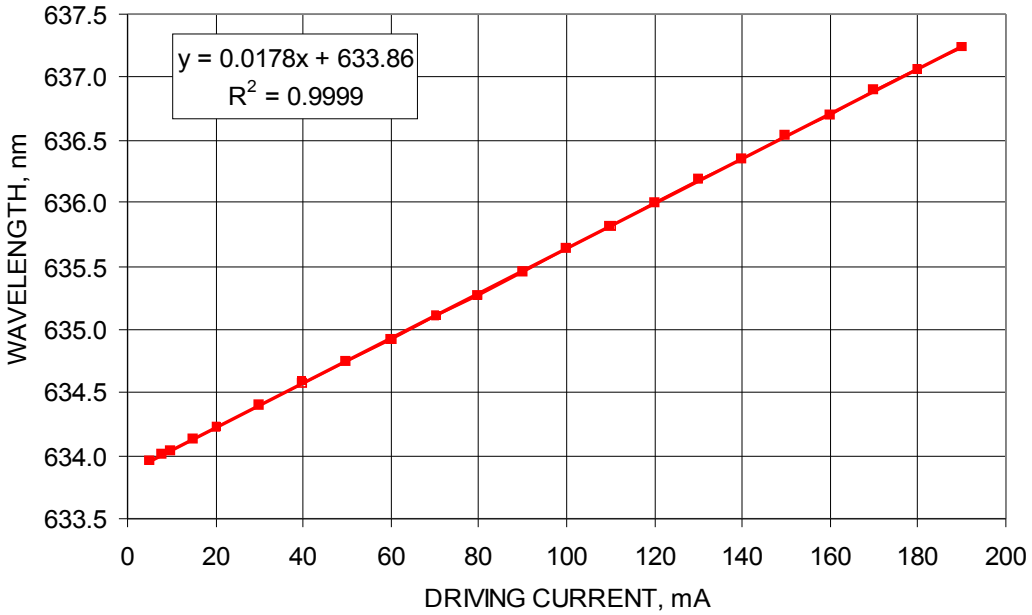

Fig. F.2. Peak wavelength of LED "B" as a function of driving current.

LED “C”

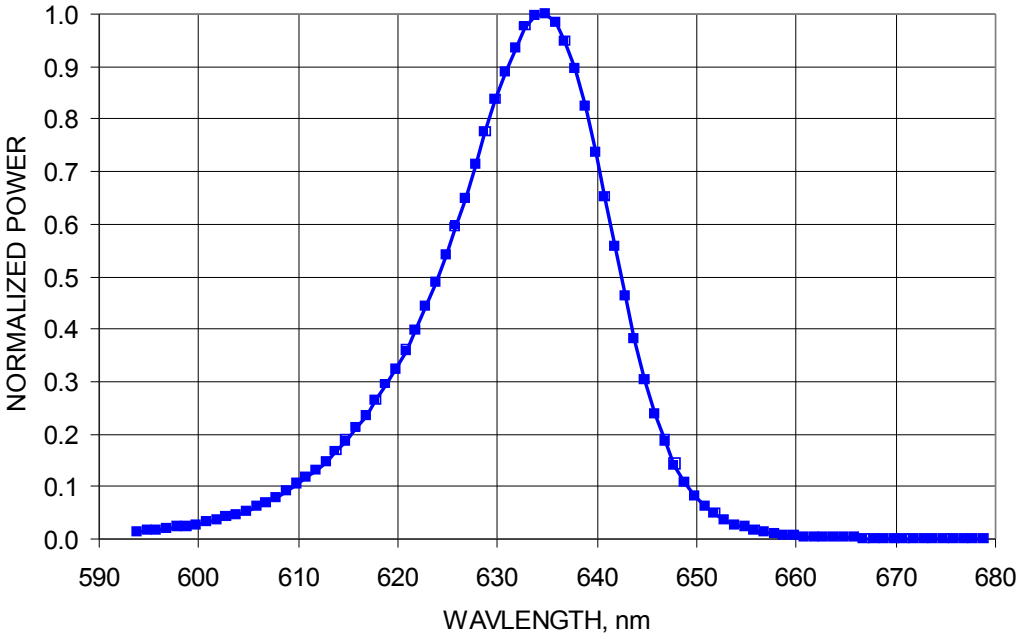

Fig. F.3. A typical normalized optical spectrum of LED "C".

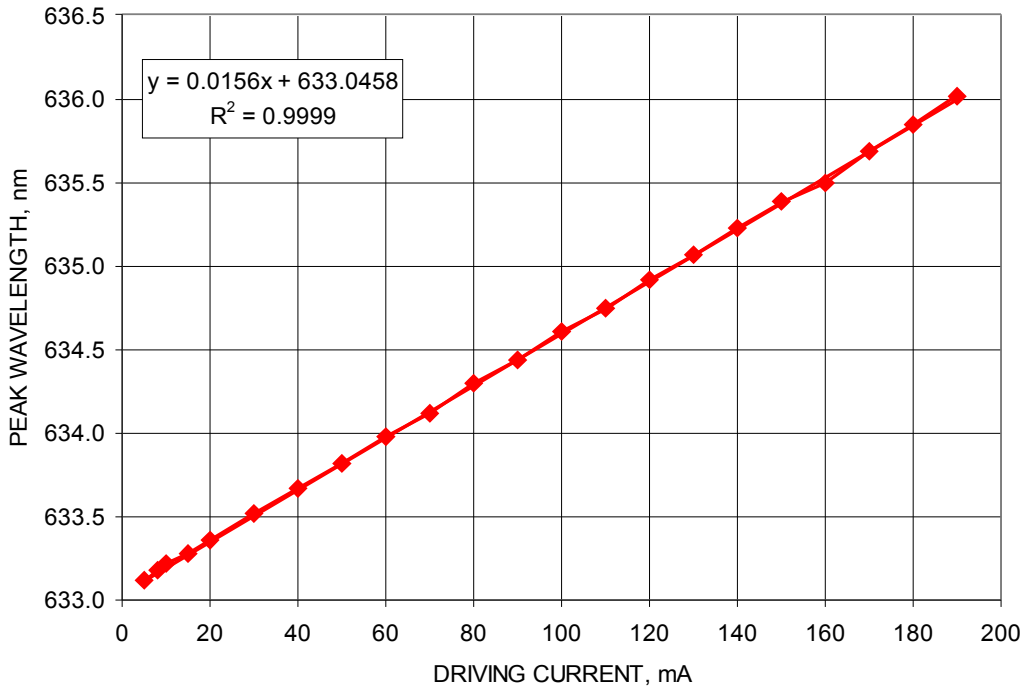

Fig. F.4. Peak wavelength of LED "C" as a function of driving current.

LED “D”

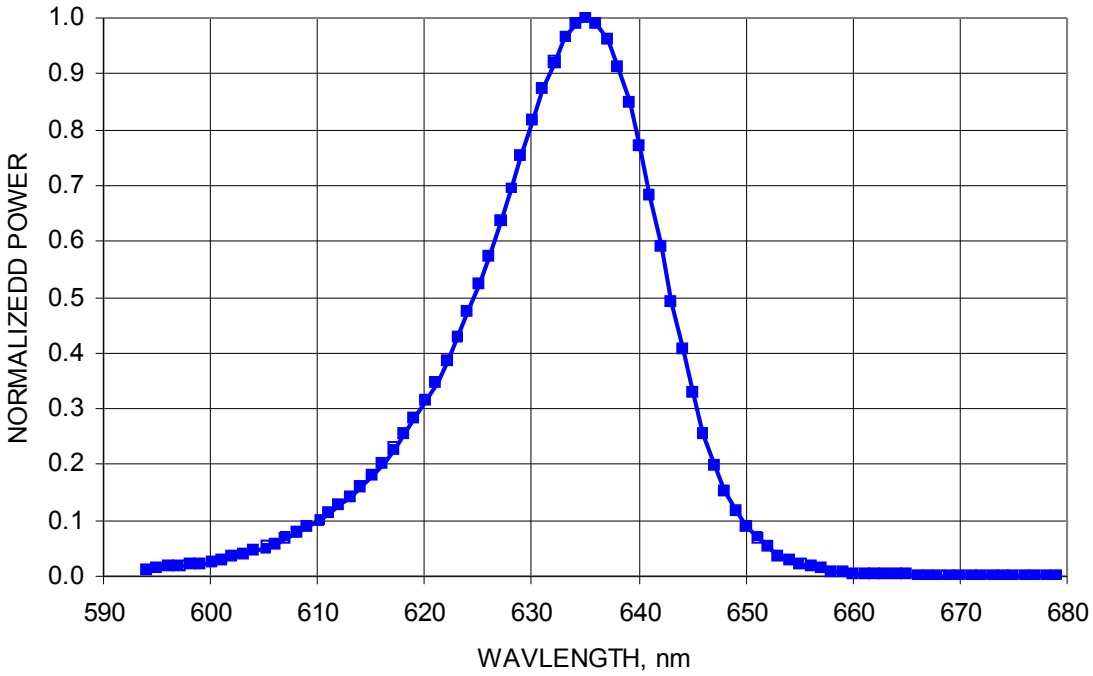

Fig. F.5. A typical normalized optical spectrum of LED "D".

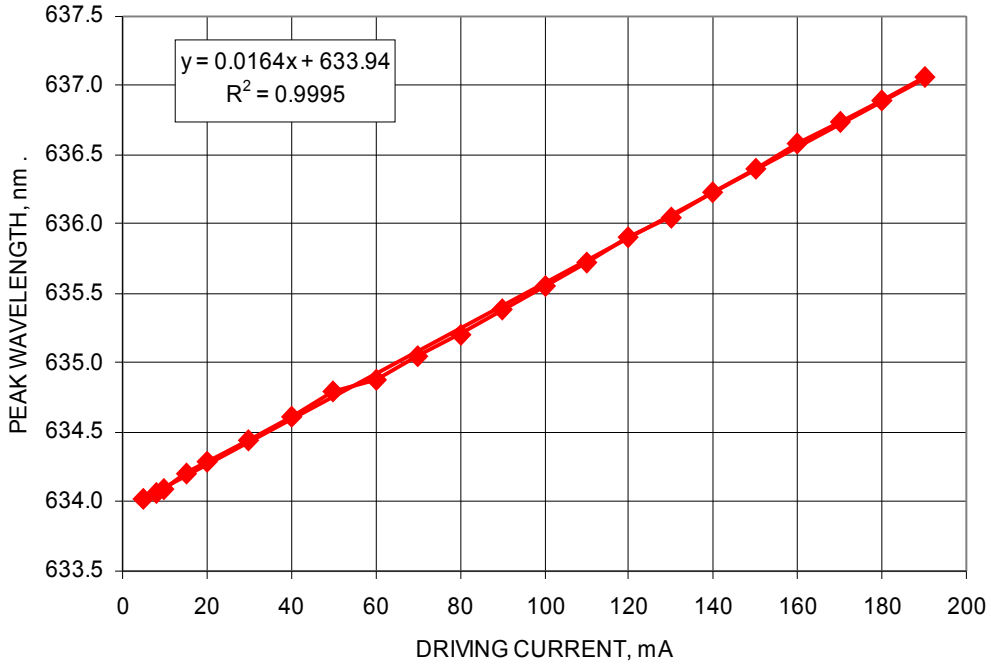

Fig. F.6. Peak wavelength of LED "D" as a function of driving current.

APPENDIX G. EXCITATION PZT FREQUENCY RESPONSE

This Appendix is intended to be an operator's "quick-reference" guide to be consulted when setting up vibrational experiments. Please ensure that the correct PZT module is chosen for the intended measurement range.

The PZT calibration data presented herein were obtained by sweeping sinusoidal driving function to each of the four PZT modules, and the response of each was measured with the Vibrometer. Three ranges were chosen based on the instrumentation that we commonly utilize for experiments: 0 to 20 kHz is the audio range where high-power audio amplifiers can be utilized to drive the PZTs; 0 to 100 kHz is approximately the range in which the LEDs can strobe; and 0 to 1 MHz is the maximum expected range that a response will be achieved by any of the PZTs. Figures G.1 through G.12 represent the measured velocity response of all of the PZT modules over various frequency ranges.

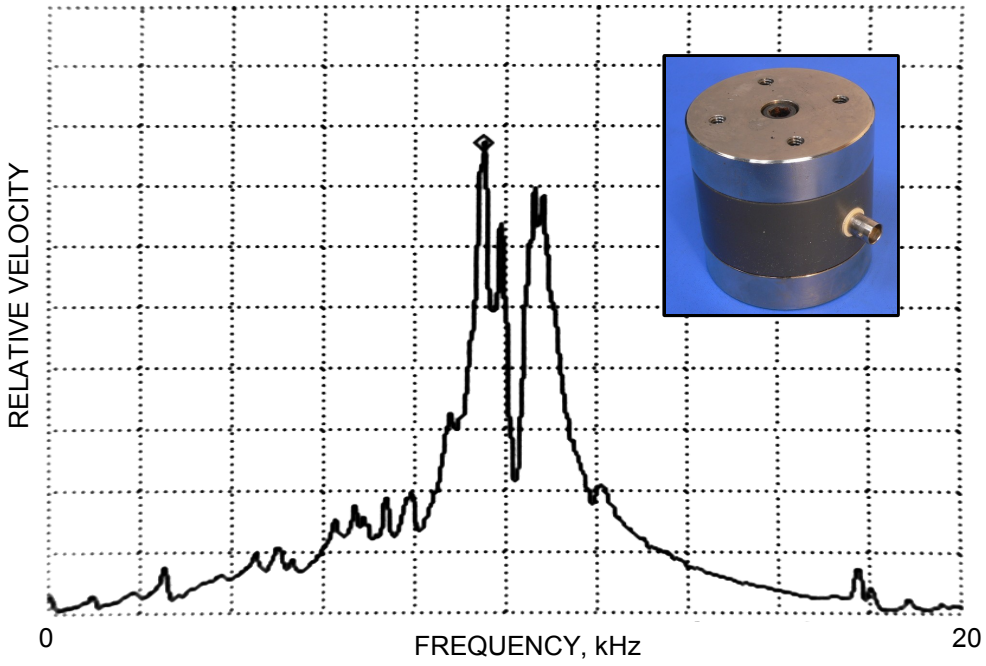

Fig. G.1. 0 to 20 kHz response of PZT1, a Jodon *EV-100* (insert).

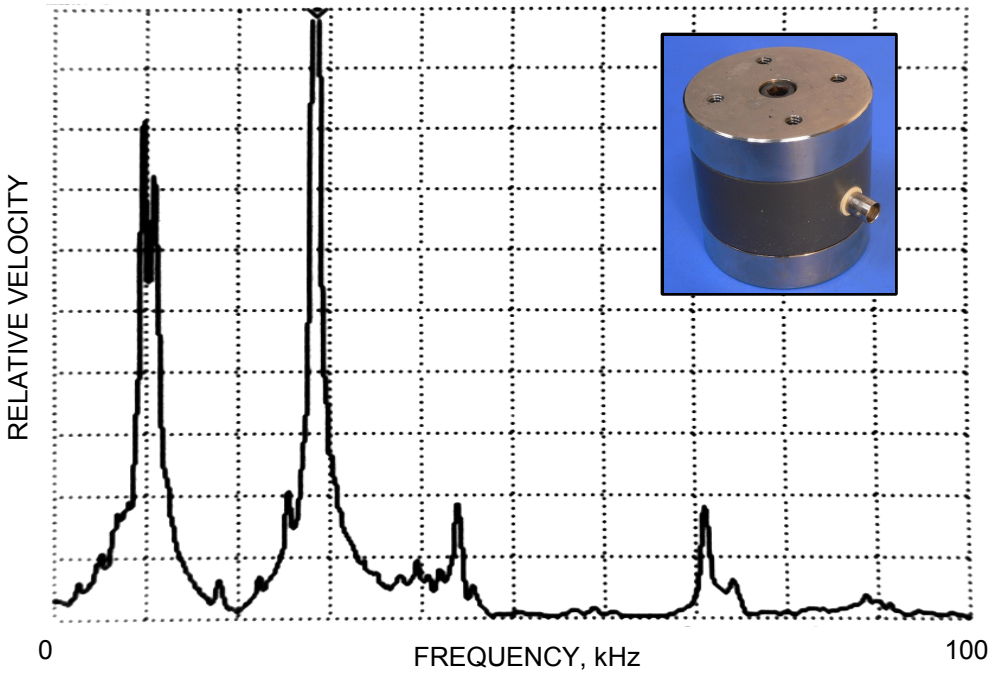

Fig. G.2. 0 to 100 kHz response of PZT1, a Jodon *EV-100* (insert).

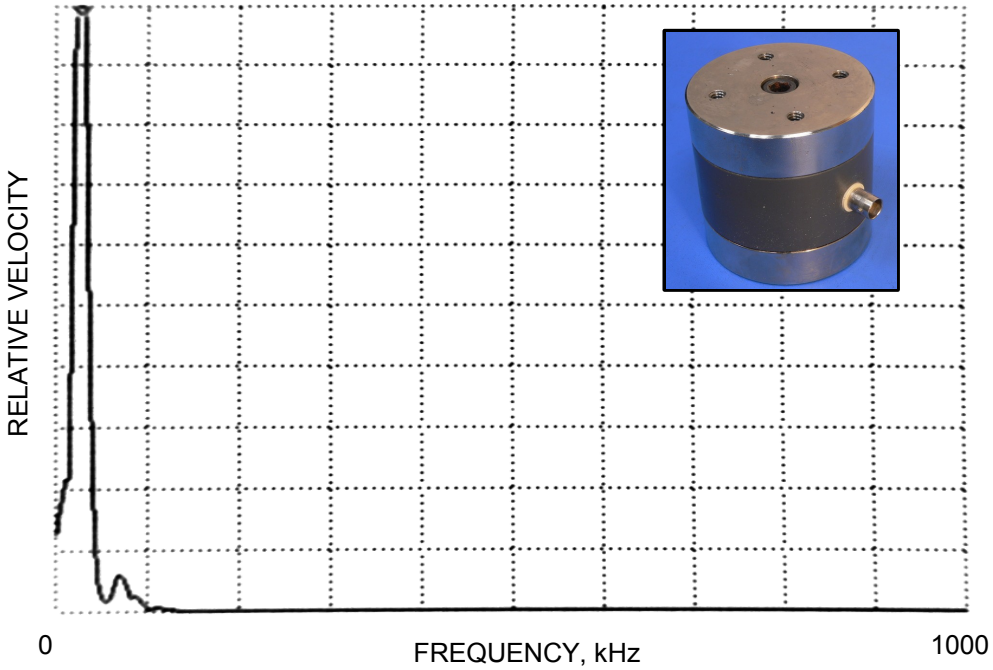

Fig. G.3. 0 to 1 MHz response of PZT1, a Jodon *EV-100* (insert).

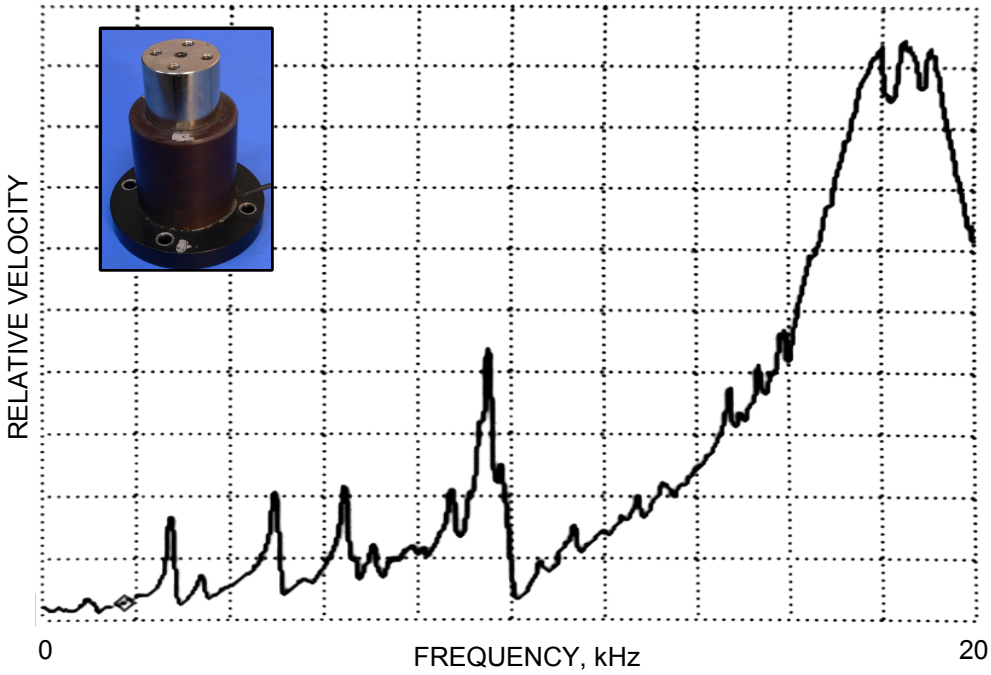

Fig. G.4. 0 to 20 kHz response of PZT2, a Jodon *EV-30* (insert).

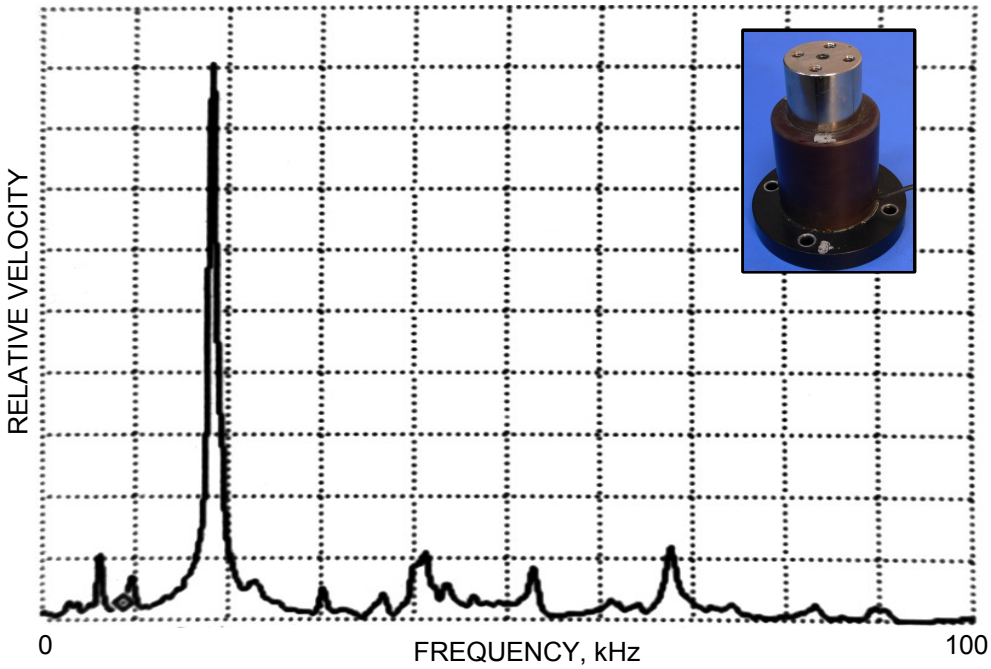

Fig. G.5. 0 to 100 kHz response of PZT2, a Jodon *EV-30* (insert).

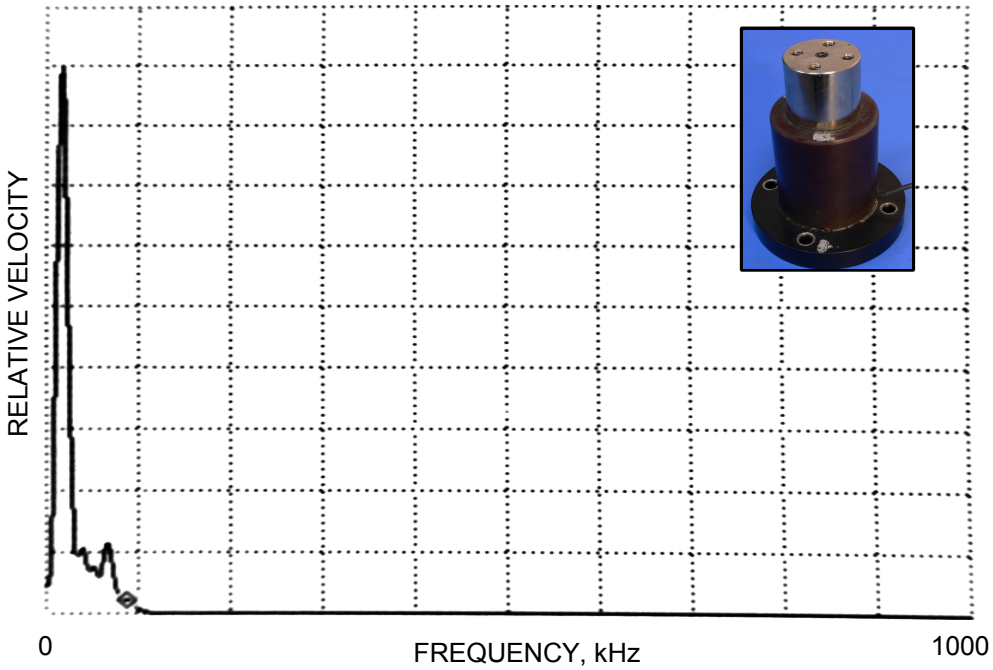

Fig. G.6. 0 to 1 MHz response of PZT2, a Jodon *EV-30* (insert).

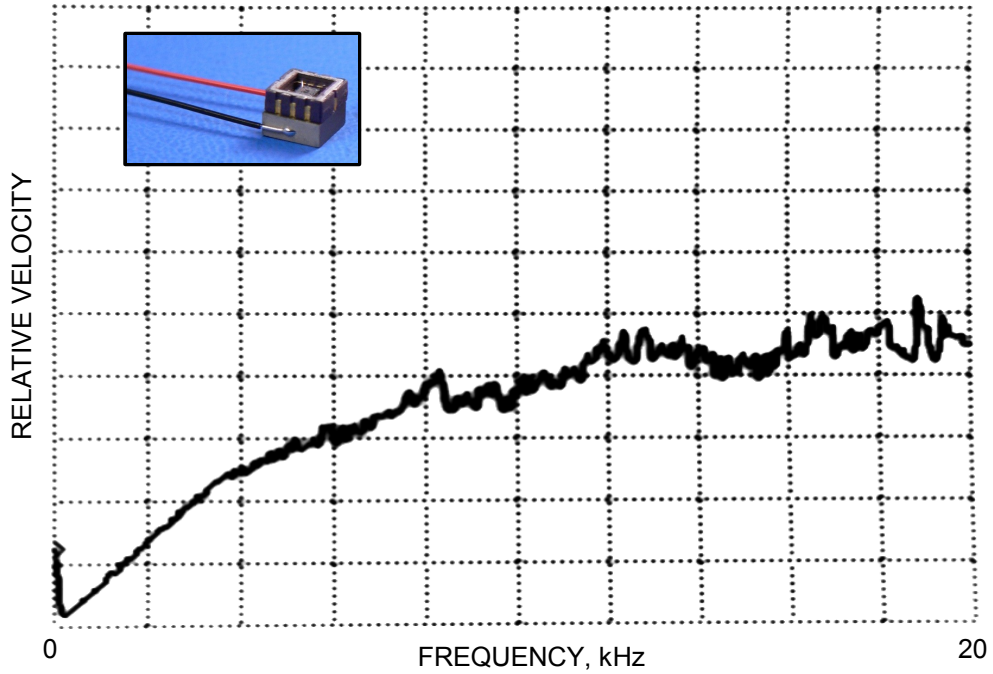

Fig. G.7. 0 to 20 kHz response of a PZT chip, a P.I. *PL055.30* (insert).
Note: PZT was measured without MEMS attached

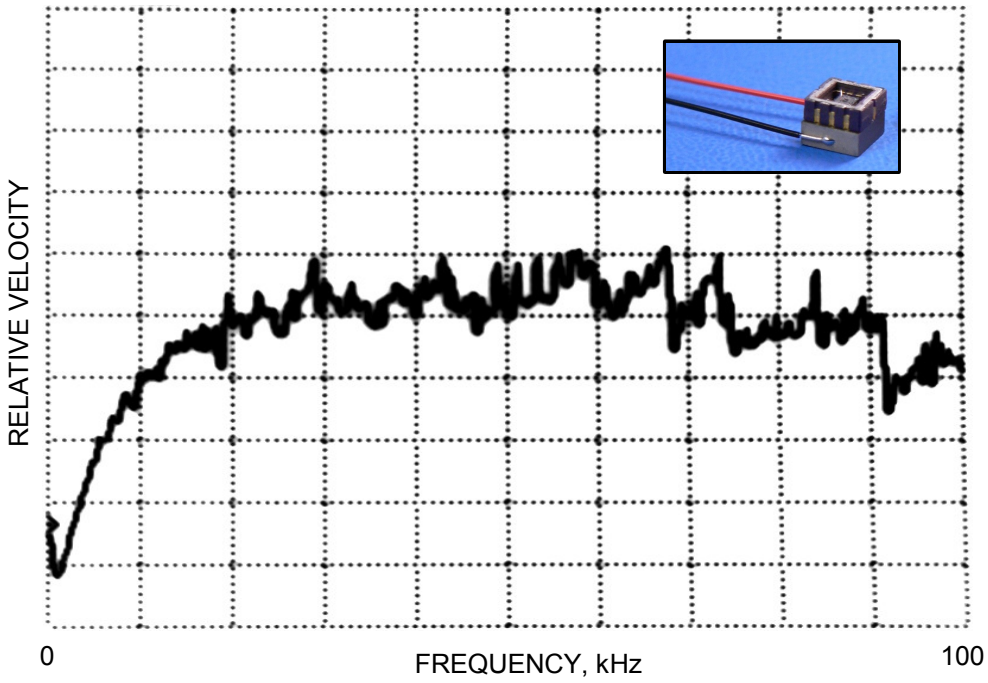

Fig. G.8. 0 to 100 kHz response of a PZT chip, a P.I. *PL055.30* (insert).
Note: PZT was measured without MEMS attached

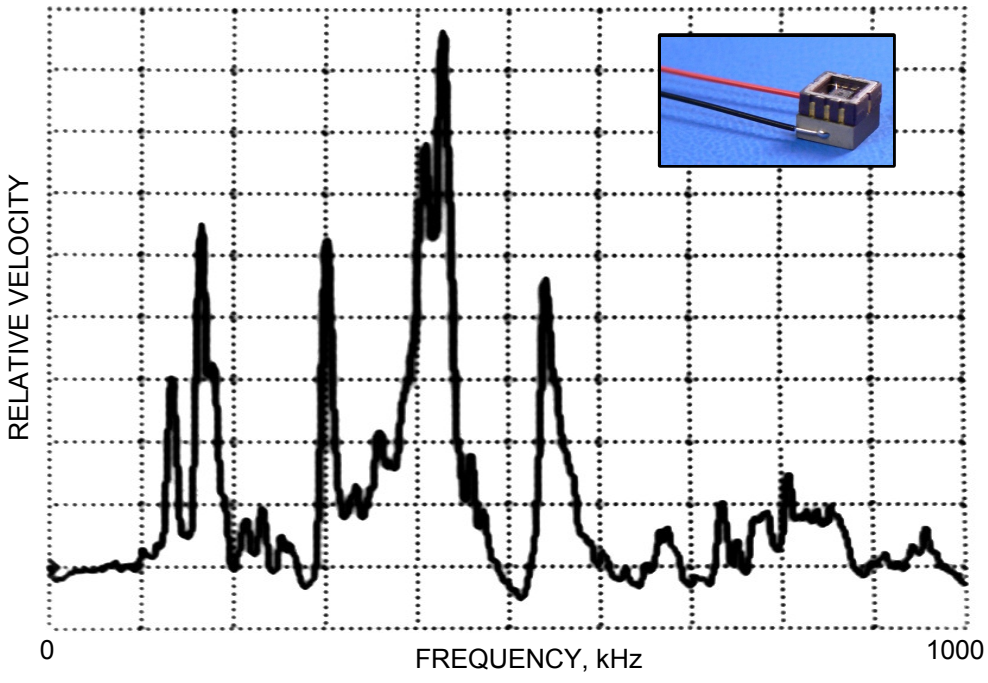

Fig. G.9. 0 to 1 MHz response of a PZT chip, a P.I. *PL055.30* (insert).
Note: PZT was measured without MEMS attached

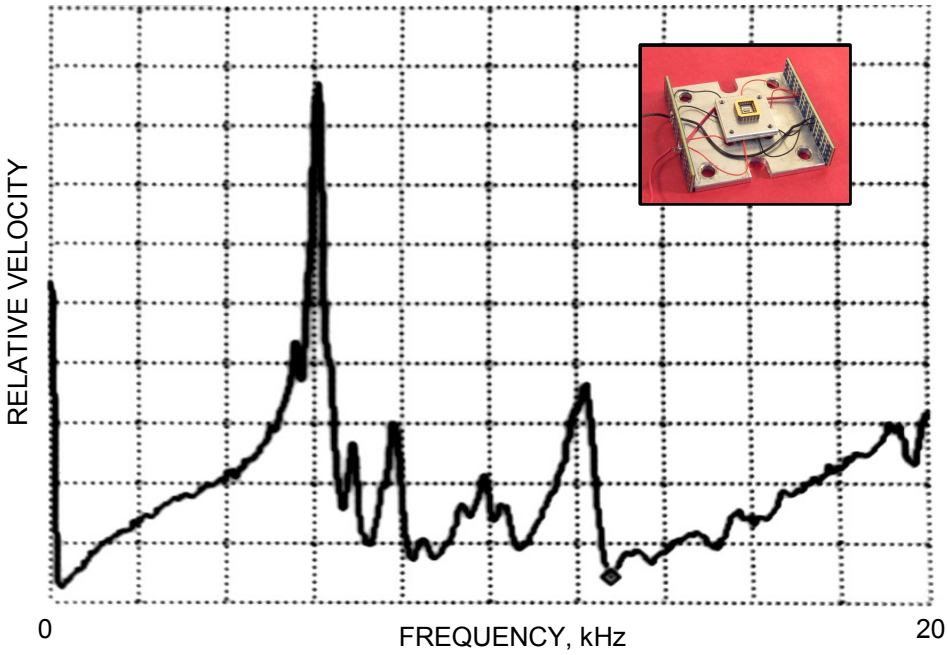

Fig. G.10. 0 to 20 kHz response of the low profile PZT module (insert).
Note: PZT was measured without MEMS attached

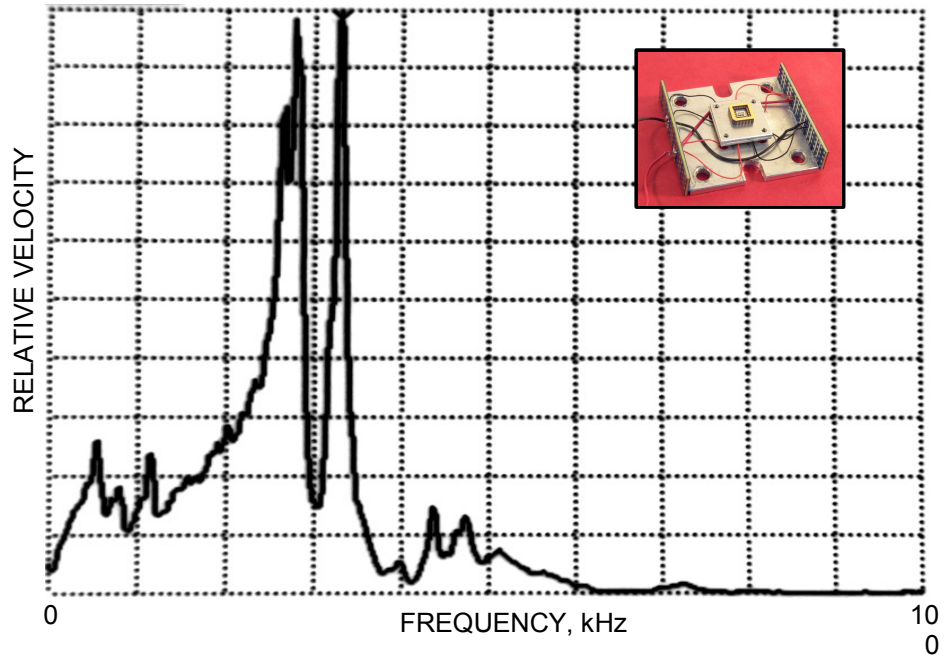

Fig. G.11. 0 to100 kHz response of the low profile PZT module (insert).
Note: PZT was measured without MEMS attached

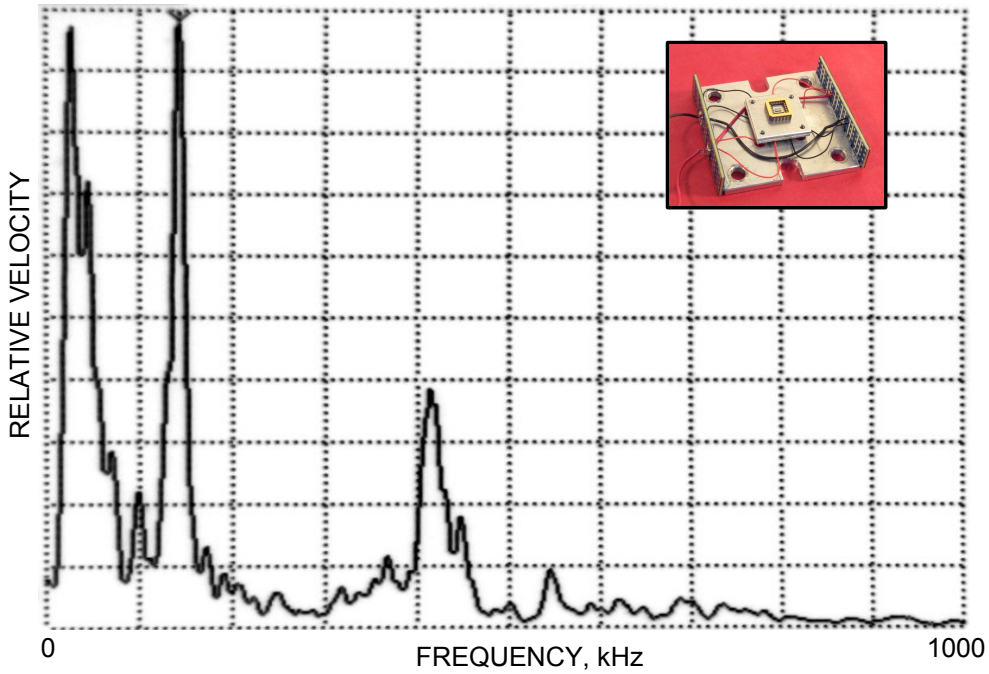

Fig. G.12. 0 to 1 MHz response of the low profile PZT module (insert).
Note: PZT was measured without MEMS attached

APPENDIX H. INTERFEROMETER MODULE SELECTION GUIDE

This Appendix is an interferometer module selection guide that gives an easy to follow flow chart, Fig. H.1, for determination of which interferometer module should be installed for a given experiment.

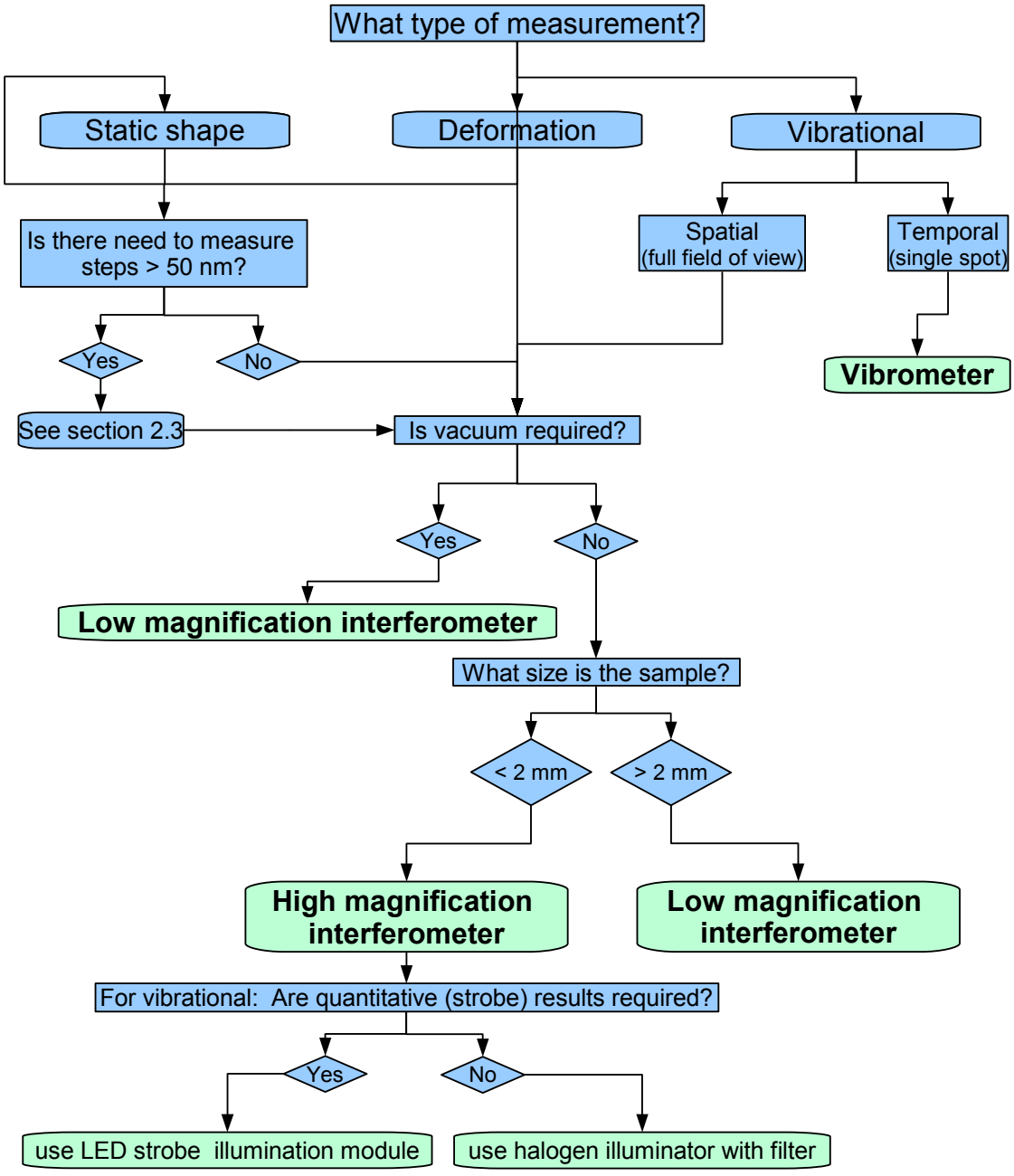

Fig. H.1. Interferometer module selection guide.

APPENDIX I. LOADING DEVICE SELECTION GUIDE

This Appendix is a loading device selection guide that gives an easy to follow flow chart, Fig. I.1, for determination of which loading devices should be installed for a given experiment.

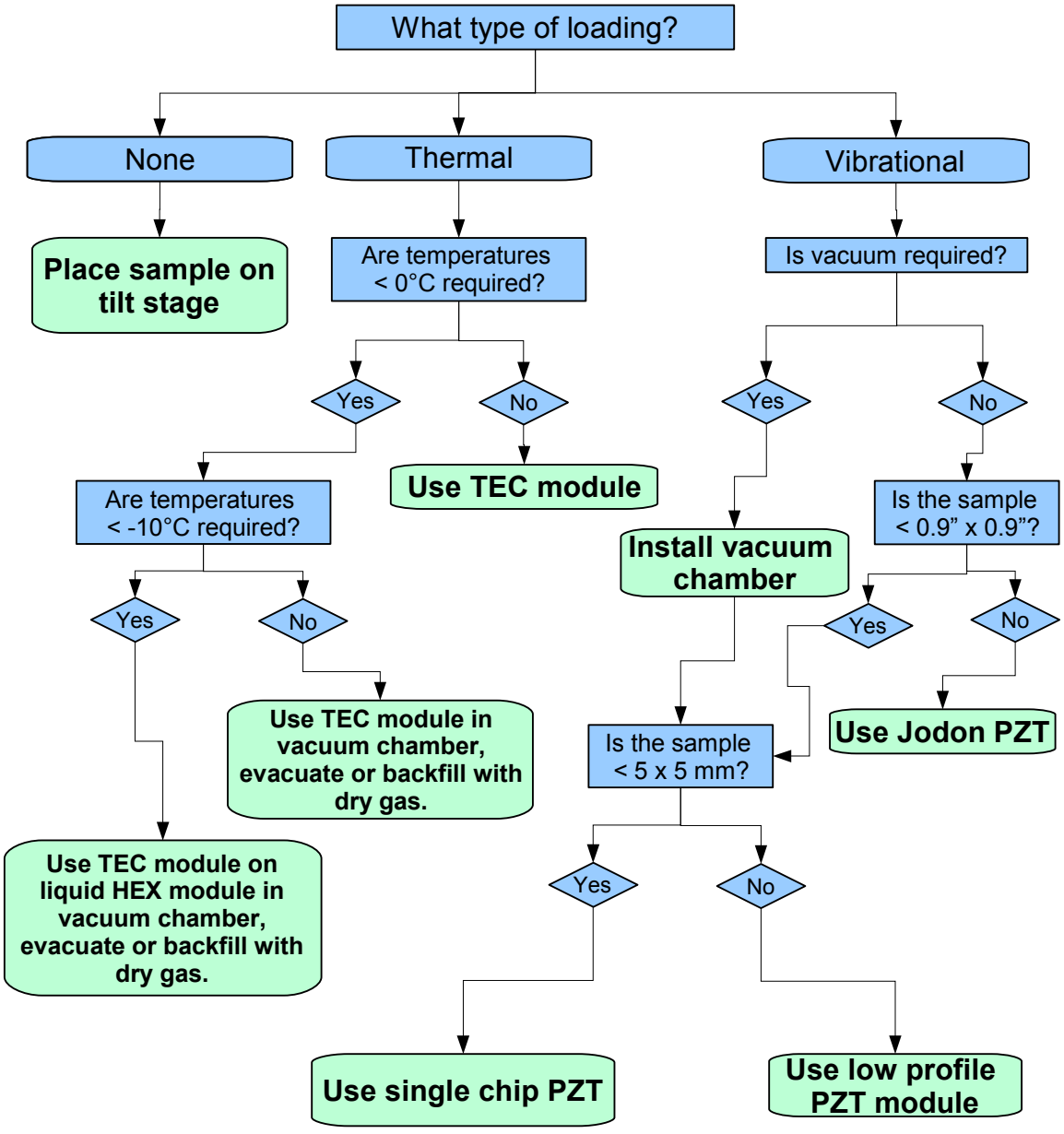

Fig. I.1. Loading device selection guide.